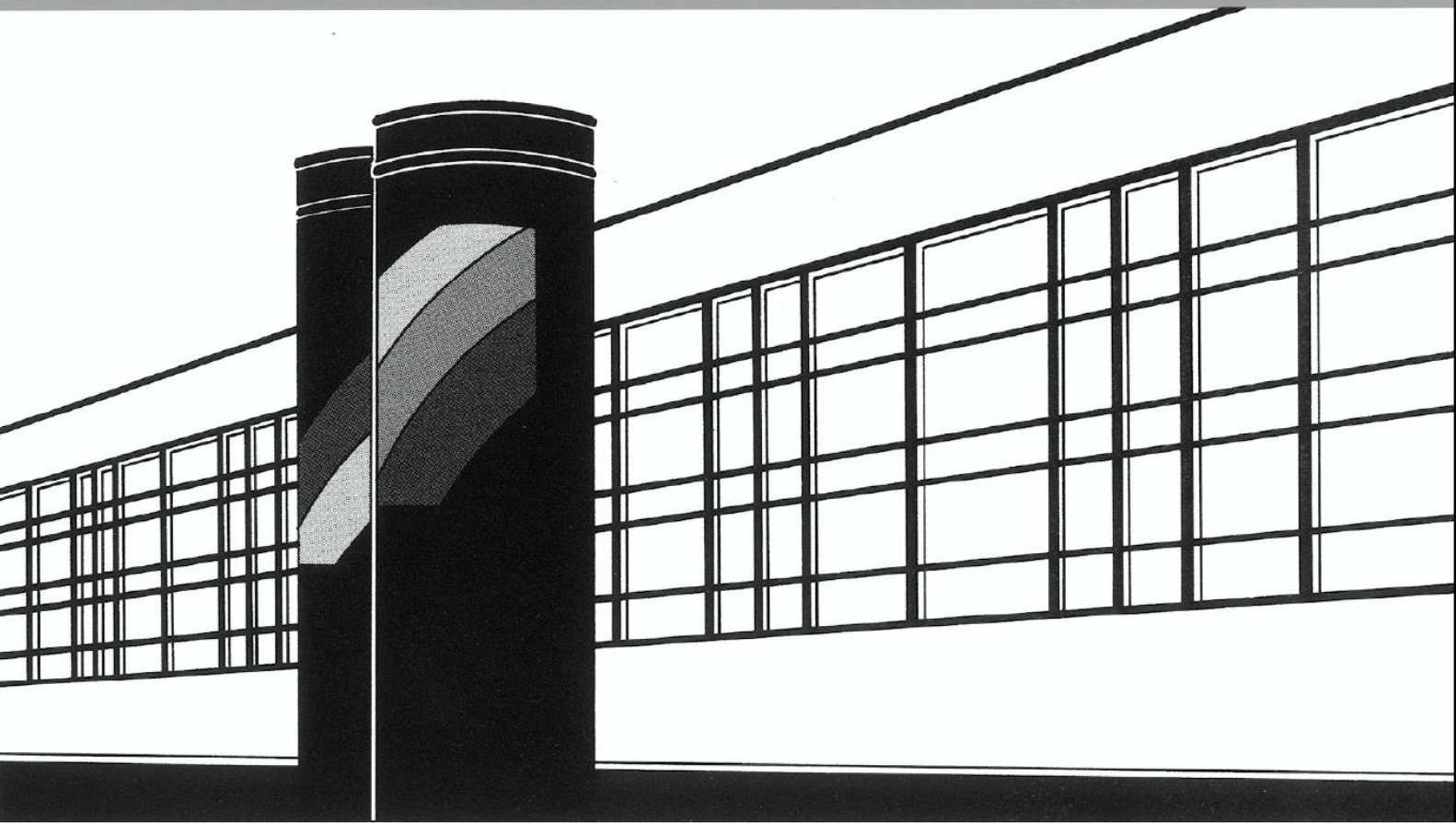


Universität Stuttgart



Institut für Wasser- und Umweltsystemmodellierung

Mitteilungen



Heft 237 Klaus Philipp Nuske

Beyond Local Equilibrium —

Relaxing local equilibrium assumptions
in multiphase flow in porous media

Beyond Local Equilibrium

Relaxing local equilibrium assumptions in multiphase flow in porous media

von der Fakultät Bau- und Umweltingenieurwissenschaften der
Universität Stuttgart zur Erlangung der Würde eines
Doktor-Ingenieurs (Dr.-Ing.) genehmigte Abhandlung

vorgelegt von

Klaus Philipp Nuske

aus Berlin

Hauptberichter: Prof. Dr.-Ing. Rainer Helmig
Mitberichter: Prof. Dr. Ir. Majid Hassanizadeh
Prof. Dani Or, PhD
Prof. Dr.-Ing. Joachim Groß

Tag der mündlichen Prüfung: 13. Oktober 2014

Institut für Wasser- und Umweltsystemmodellierung
der Universität Stuttgart
2014

Heft 237 Beyond Local Equilibrium

Relaxing local equilibrium
assumptions in multiphase flow
in porous media

von
Dr.-Ing. Klaus Philipp Nuske

D93 Beyond Local Equilibrium — Relaxing local equilibrium assumptions in multiphase flow in porous media

Bibliografische Information der Deutschen Nationalbibliothek

Die Deutsche Nationalbibliothek verzeichnet diese Publikation in der Deutschen Nationalbibliografie; detaillierte bibliografische Daten sind im Internet über <http://www.d-nb.de> abrufbar

Nuske, Klaus Philipp:

Beyond Local Equilibrium — Relaxing local equilibrium assumptions in multiphase flow in porous media, Universität Stuttgart. - Stuttgart: Institut für Wasser- und Umweltsystemmodellierung, 2014

(Mitteilungen Institut für Wasser- und Umweltsystemmodellierung, Universität Stuttgart: H. 237)

Zugl.: Stuttgart, Univ., Diss., 2014

ISBN 978-3-942036-41-2

NE: Institut für Wasser- und Umweltsystemmodellierung <Stuttgart>: Mitteilungen

Gegen Vervielfältigung und Übersetzung bestehen keine Einwände, es wird lediglich um Quellenangabe gebeten.

Herausgegeben 2014 vom Eigenverlag des Instituts für Wasser- und Umweltsystemmodellierung

Druck: Document Center S. Kästl, Ostfildern

Danksagung

Wie jede wissenschaftliche Arbeit, ist auch diese Dissertation nicht im luftleeren Raum entstanden, sondern konnte nur durch die Vorarbeit, Hilfe und Unterstützung vieler Menschen abgeschlossen werden. Daher möchte ich die Gelegenheit nutzen, einigen davon zu danken.

Zuallererst danke ich Kathérina: Ohne Dich hätte ich das alles nicht geschafft.

Ich möchte auch meiner Familie danken. Ihr wart eine großartige Unterstützung, Abwechslung und habt mir immer wieder neue Perspektiven eröffnet. Danke Vati, Du hast mir unter anderem gezeigt, dass die Uhrzeit nicht so wichtig ist, wenn man etwas fertig bekommen will. Und danke Ulla, für das fulminante Büfett!

Mein Dank gilt auch denjenigen Menschen, die direkteren Anteil an der Entstehung dieser Arbeit hatten. Vahid Joekar-Niasar stellte mir sein Porennetzwerk Modell zu Verfügung und erweiterte es sogar nach meinen Wünschen. Dani Or lieh uns die Infrarotkamera seiner Arbeitsgruppe für fünf sehr intensive Tage. Dank gilt natürlich Nikos Karadimitriou: You are the most relaxed and enjoyable experimenter, imaginable. Pieter Kleingeld war unsere Rettung in Entwurf und Durchführung des Experiments. Bei der Auswertung des Experiments half uns zunächst Olaf Ronneberger, um dann sogar als Koautor zu uns zu stoßen: Vielen Dank für die unkomplizierte und effiziente Zusammenarbeit. Rainer Helmig hat mir durch seinen Enthusiasmus und seine Begeisterungsfähigkeit viel beigebracht, vielen Dank dafür. Majid Hassanizadeh hat mir den wunderbaren Forschungsaufenthalt im schönen Utrecht ermöglicht, wofür ich dankbar bin.

Meine Bürokollegen und unsere vielen vielen gemeinsam genossenen Kaffees haben durch Ablenkung, Anregung und Unterstützung beim Weiterarbeiten und vor allem Entspannen geholfen. Natürlich möchte ich mich hier insbesondere bei Nicolas und Benjamin bedanken. Dank gebührt selbstverständlich auch Frau Lawday, die mir oft geholfen hat selbst die seltsamsten Formulare auszufüllen und auch sonst immer wusste, was zu tun war.

Majid Hassanizadeh, Dani Or und Joachim Groß danke ich für die Übernahme der Gutachten. Außerdem danke ich der DFG und dem Ministerium für Wissenschaft, Forschung und Kunst Baden-Württemberg für die Finanzierung dieser Arbeit, insbesondere für den Forschungsaufenthalt an der Utrecht University.

Contents

List of Figures	ix
List of Tables	xiii
Notation	xv
Abstract	xxi
Zusammenfassung	xxv
1 Introduction	1
1.1 Motivation	1
1.2 Structure of the Thesis	3
2 Conceptual Model	5
2.1 Basic Definitions	5
2.1.1 Phase, Component, Capillary Pressure	5
2.1.2 Density, Viscosity	7
2.1.3 Int. Energy, Enthalpy, Heat Capacity, Thermal Conductivity	8
2.1.4 Mole Fractions	8
2.1.5 Mixture Properties	9
2.2 System Properties	9
2.2.1 Scales	10
2.2.2 Quantities on the Macro Scale	11
2.3 Equilibrium	19
2.3.1 Mechanical Equilibrium	20
2.3.2 Thermal Equilibrium	20
2.3.3 Chemical Equilibrium	21
2.3.4 Relaxing Equilibrium Assumptions / State of the Art	25
3 Mathematical & Numerical Model	29
3.1 Non-Equilibrium Mass Conservation	30
3.1.1 Phase Presence	34

Contents

3.1.2	Limitations of Non-Equilibrium Mass Conservation	35
3.2	Non-Equilibrium Energy Conservation	37
3.2.1	Limitations of Non-Equilibrium Energy Conservation	42
3.3	Momentum Description in Multiphase Flow in Porous Media	43
3.4	Numerical Model	45
3.4.1	Temporal Discretization	45
3.4.2	Spatial Discretization	46
3.4.3	Numerical Framework	47
3.5	Sustainability and Code Accessibility	48
3.6	Summary	49
4	Discussion of Interfacial Area Balance	51
5	Non-Equilibrium: An Evaporation Example	55
5.1	Generation of Constitutive Relations	55
5.1.1	Pore-Network Model	57
5.1.2	Capillary Pressure – Saturation Relation	59
5.1.3	Non-Wetting – Wetting Surface	60
5.1.4	Non-Wetting – Solid Surface	62
5.2	Simulating Evaporation on the Macro Scale	64
5.2.1	Motivation	64
5.2.2	Setup	64
5.2.3	Initial and Boundary Conditions	66
5.2.4	Results	68
5.2.5	Convergence	74
5.3	Summary	76
5.4	Outlook	77
6	Estimating Transfer Coefficients: Experimental Setup & Measurement	79
6.1	Experimental Setup and Procedure	80
6.1.1	Micro-Model Design	80
6.1.2	Flow Visualization	83
6.1.3	Flow and Temperature Control	86
6.1.4	Experimental Procedure	87

6.2	Image Processing	87
6.2.1	Temporal Correlation	87
6.2.2	Spatial Correlation	88
6.2.3	Phase Segmentation	89
6.3	Results	92
6.3.1	Preparation and Removal of Entrapped Air	92
6.3.2	Influence of Velocity on Temperature Distribution	93
6.3.3	Temperature as Flow Path Indicator	94
6.3.4	Stationary Temperature Distributions	95
6.4	Summary & Conclusion	96
7	Estimating Transfer Coefficients: Simulation of the Experiment	99
7.1	Input Parameters	100
7.1.1	Material & Fluid Properties	100
7.1.2	Micro-Model Properties	101
7.2	Image Analysis	102
7.2.1	Thin Plate Spline Warping	102
7.2.2	Segmentation	103
7.2.3	Estimation of Macro-Scale Quantities	105
7.2.4	Implementation Details & Code Availability	107
7.3	Constitutive Relations	107
7.4	Experimental & Modelling Setup	109
7.4.1	Balance Equations	109
7.4.2	Initial and Boundary Conditions	110
7.4.3	Implementation of Heat Loss	111
7.5	Simulation & Experiment	112
7.5.1	Line Averaging of Temperature	112
7.5.2	Matching Simulation Results to Experimental Observations .	113
7.5.3	Limitations of the Chosen Boundary Conditions	122
7.6	Summary & Conclusion	123

8	Forced Evaporation: Model Comparison for a Non-Isothermal System	125
8.1	Mathematical Models	128
8.1.1	Fully Coupled Model	128
8.1.2	Two-Phase Mixture Model in Local Thermal Non-Equilibrium	129
8.1.3	Common Features and Differences	131
8.2	Numerical Solution	135
8.2.1	Numerical Solution Fully Coupled Model	135
8.2.2	Numerical Solution TPMM-LTNE	136
8.2.3	Differences in Numerics	141
8.3	Problem Setup & Boundary Conditions	141
8.4	Results and Discussion	144
8.4.1	Analytical Outlet Temperature	144
8.4.2	Results and Model Comparison	145
8.5	Summary & Conclusion	151
9	Final Remarks	153
9.1	Summary	153
9.2	Future Research	155
9.3	Conclusion	156
	List of Publications	159
A	Forced Evaporation: Compositional Effects	161
A.1	Component Properties	162
A.2	Fluidsystem	162
A.3	Simulation Results of the Two-Component Evaporation	163
A.3.1	Grid Convergence	164
A.3.2	Composition	164
A.3.3	Composition in the Two-Phase Region: Factors of Influence	166
A.3.4	Varying Heat Fluxes	168
A.4	Summary & Conclusion	172
	Bibliography	173

Lebenslauf

189

List of Figures

1.1	Closing the loop.	3
2.1	A water droplet on two different surfaces.	7
2.2	Construction of an REV. Adapted from Helmig (1997).	10
2.3	Multiphase flow: micro scale and macro scale	12
2.4	Qualitative capillary pressure – saturation relationship.	13
2.5	Capillary pressure – saturation relationships.	15
2.6	Relative permeability – saturation relationships.	16
2.7	Sketch: wetting – non-wetting / wetting – solid interfacial area. . .	18
2.8	Sketch: non-wetting – solid / total solid interfacial area.	19
2.9	Conceptual sketch of a local thermal non-equilibrium situation. . . .	20
2.10	Conceptual sketch of a chemical non-equilibrium situation.	21
3.1	Schematic sketch of an invasions process.	42
3.2	Conceptual sketch of the box method.	47
4.1	Schematic depiction of interfacial area production.	52
4.2	Schematic depiction of distinction between destruction and flow. . .	53
4.3	Thought experiment regarding interfacial velocity.	53
5.1	Principle of the used pore-network model.	56
5.2	42 realizations and the mean value of the $p_c - S_w$ data.	58
5.3	Plot of 42 realizations of $a_{wn} - S_w$ and $a_{ns} - S_w$ data.	59
5.4	Averaged pore.network results with fit $p_c - S_w$ function.	60
5.5	Averaged data points from pore-network simulation, fit surface. . .	61
5.6	Averaged data points from pore-network simulation, fit surface. . .	63
5.7	Sketch of the simulation setup.	67
5.8	$S_w, T_n, x_n^{H_2O}$ after 1 d and 4 d simulated time.	68
5.9	Liquid water in the porous medium, different $f_e = f_m$	71
5.10	Liquid water in the porous medium, different f_e, f_m	71
5.11	Equilibrium, actual mole fractions of water component in gas phase.	72
5.12	Equilibrium, actual mole fractions of water component in gas phase.	73

List of Figures

5.13	Different grids that were used in the convergence study.	74
5.14	Global indicator for convergence.	75
5.15	Local indicator for convergence.	76
6.1	Drawing of the flow network.	81
6.2	Image of the micro-model.	83
6.3	Schematic representation of the imaging setup.	84
6.4	The imaging setup.	85
6.5	Optical and thermal image of the micro-model.	88
6.7	Raw optical and segmented image.	90
6.8	Segmented temperature fields of the two fluids and the solid phase.	91
6.9	Saturating the micro-model with Fluorinert.	92
6.10	Invasion of hot water: primary drainage at two different flow rates.	93
6.11	Two stages during secondary drainage.	94
6.12	This figure shows two successively reached temperature distributions.	95
7.1	Landmarks: Model and recorded image.	103
7.2	Optical and segmented image (phases).	104
7.3	Optical and segmented image (interfaces).	106
7.4	Measured data points, fit k_r, p_c functions.	108
7.5	Measured data points with fit a_{wn}, a_{ns} functions.	108
7.6	Boundary conditions as well as model abstraction of the simulation.	110
7.7	Visualization of line averaging.	112
7.8	Overlay of low-rate temperature and optical information.	114
7.9	Temperature line averages: low-rate.	114
7.10	Simulation of the experiment, low-rate, $f_e = 0.1$	116
7.11	Simulation of the experiment, low-rate, $f_e = 0.5$	116
7.12	Simulation of the experiment, low-rate, $f_e = 1$	117
7.13	Simulation of the experiment, low-rate, $f_e = 10$	117
7.14	Overlay of high-rate temperature and optical information.	119
7.15	Temperature line averages: high-rate.	119
7.16	Simulation of the experiment, high-rate, $f_e = 0.1$	120
7.17	Simulation of the experiment, high-rate, $f_e = 0.5$	120
7.18	Simulation of the experiment, high-rate, $f_e = 1$	121

7.19	Simulation of the experiment, high-rate, $f_e = 10$.	121
7.20	Pressure distribution in the simulated experiment.	122
8.1	Schematic of a burner.	126
8.2	Heat transfer function in the two-phase region.	136
8.3	Macroscopic phase boundaries.	139
8.4	Γ_h and Pe : transition between two-phase and super-heated region.	139
8.5	Problem setup and boundary conditions for the two models.	142
8.6	Comparison between Solver 1, fully coupled model and Shi.	146
8.7	Comparison between Solver 1, fully coupled model and Shi.	147
8.8	Saturation of the water phase.	148
8.9	Influence of smoothing Γ_h .	149
8.10	Influence of heat transfer coefficient on solution.	150
9.1	Closing the loop in this work.	157
A.1	Grid convergence: saturations and mole fractions.	165
A.2	Phase diagram of the heptane–dodecane mixture.	166
A.3	Gas phase: composition, saturation, pressure, temperature.	167
A.4	Influence of varying compositions at the inflow.	169
A.5	Influence of scaling capillary pressure.	170
A.6	Varying heat fluxes.	171

List of Tables

3.1	Dimensionless numbers for mass transfer, meaning and definition. . .	33
3.2	Dimensionless numbers for heat transfer, meaning and definition. . .	40
3.3	Accessibility of used source code.	48
5.1	Medium sand properties taken from Stingaciu et al. (2010).	57
5.2	Fit Brooks and Corey (1964) parameters for a medium sand.	59
5.3	Fit parameters (Equation 5.1) for a realization of medium sand. . .	61
5.4	Fit parameters (Equation 5.2) for a realization of medium sand. . .	63
5.5	Parameters for the “free-flow” and the porous-medium part.	64
5.6	Fluid parameters.	66
5.7	Fluid parameters cont.	66
7.1	Fluid properties.	100
7.2	Material properties of the solid phase (PDMS, Mark (1999)).	101
7.3	Intrinsic properties of the micro-model.	102
7.4	VAN GENUCHTEN parameters of p_c and k_r fits.	108
7.5	Fit parameters and coefficients of determination.	108
7.6	Initial conditions & extraction rates.	111
8.1	Conservation equations of the fully coupled model.	129
8.2	Conservation equations of the TPMM-LTNE model (Shi).	130
8.3	Properties of the porous medium.	143
8.4	Main fluid properties as used in both models.	143
8.5	Comparison of the outlet fluid-temperatures.	146
A.1	Heptane, dodecane properties.	163
A.2	Parameters of the simulated scenarios.	163
A.3	Comparison: Simulation results and values from phase diagram. . .	168

Notation

Greek Symbols

α	VAN GENUCHTEN parameter ($1/m$)
β_0	VAN GENUCHTEN parameter (temperature scaling) (K)
Γ_h	effective diffusion coefficient (m^2/s)
γ_h	advection correction coefficient (-)
η_r	relative passability (-)
Θ_c	contact angel (-)
λ	BROOKS-COREY parameter (-)
λ	thermal conductivity (W/mK)
μ	chemical potential (J/mol)
μ_g	grain size (m)
μ	mixture dynamic viscosity (Pa s)
μ_α	phase dynamic viscosity (Pa s)
μ_p	mean (of pore size distribution) (m)
ν	mixture kinematic viscosity (m^2/s)
ν_α	phase kinematic viscosity (m^2/s)
ρ_α	phase density (kg/m^3)
ρ_k	kinetic density (kg/m^3)
σ_p	standard deviation (of pore size distribution) (m)
σ	surface tension (N/m)
τ	tortuosity (-)
ϕ	porosity (-)

Latin Symbols

A	area (m^2)
a_i	fitting coefficient (according)

Notation

\mathbf{a}_i	position in recorded image (m)
a_{ns}	volume-averaged interfacial area: non-wetting and solid phase (m^2/m^3)
a_s	volume-averaged total surface of the solid phase (m^2/m^3)
a_{wn}	volume-averaged interfacial area: wetting and non-wetting phase (m^2/m^3)
a_{ws}	volume-averaged interfacial area: wetting and solid phase (m^2/m^3)
$b_{\alpha\beta}$	borderline between phases α, β (-)
\mathbf{b}_i	position in reference image (m)
c	specific heat capacity ($\text{J}/\text{kg K}$)
c_F	FORCHHEIMER coefficient (-)
D	diffusion coefficient (m^2/s)
d_p	characteristic size of porous medium (m)
\dot{e}	energy flux (J/s)
E_{wn}	production / destruction term of interfacial area ($\text{m}^2/\text{m}^3 \text{s}$)
f	hindrance function (-)
f_a	local attenuation function (-)
f_e	factor kinetic energy transfer (-)
f_m	factor kinetic mass transfer (-)
\mathbf{g}	gravity vector (m/s^2)
G_σ	GAUSSIAN smoothing kernel (-)
h	specific enthalpy (J/kg)
H	HENRY coefficient (Pa)
H	volumetric enthalpy of fluid mixture (J/m^3)
$\bar{h}_{s\alpha}$	mean heat transfer coefficient of solid and α -phase ($\text{W}/\text{m}^2 \text{K}$)
Δh_v	enthalpy of vaporization ($\text{J}/\text{kg K}$)
I	image (-)
I'	warped image (-)
\mathbf{j}	diffusive mass flux (kg/s)
J	LEVERETT J-Function (-)
\mathbf{K}	permeability tensor (m^2)

\mathbf{k}	local position (m)
k_r	relative permeability (-)
L	characteristic length (m)
m	mass (kg)
M	molar mass (kg/mol)
m	VAN GENUCHTEN parameter (-)
M_α	mask for obtaining phase α (-)
n	VAN GENUCHTEN parameter (-)
\dot{n}	mole flux (mol/s)
p	mixture pressure (Pa)
p_α	phase pressure (Pa)
p_c	capillary pressure (Pa)
$p_{c\max}$	fitting parameter, see Section 5.1.3 (Pa)
p_d	entry pressure (Pa)
p_{vap}^κ	vapor pressure of component κ (Pa)
Q	heat (J)
q	source/sink (mass/energy) (kg/m ³ s, J/m ³ s)
\dot{q}_{boil}	heat transfer under boiling conditions (W/m ³)
\dot{q}_{sf}	solid to fluid energy transfer (W/m ³)
R^2	coefficient of determination (-)
r	radius (m)
r	relative humidity (-)
S_α	saturation of phase α (-)
\mathbf{T}	warping function (-)
T	temperature (K)
T_{boil}	boiling temperature (K)
T_{ref}	reference temperature (K)
t	time (s)
u	specific internal energy (J/kg)

Notation

V	volume (m^3)
\mathbf{v}_α	phase velocity (m/s)
\mathbf{v}	mixture velocity (m/s)
\mathbf{v}_{un}	velocity of interfacial area (m/s)
W	work (J)
\mathbf{x}	position (m)
x_α^κ	mole fraction of component κ in phase α (mol/mol)

Subscripts

α	general phase
eff	effective quantity
equil	under equilibrium conditions
f	fluid (wetting <i>and</i> non-wetting phase)
i	discrete point i
i	initial
n	non-wetting phase
pm	in porous medium
ref	reference
r	residual
s	solid phase
v	void space
w	wetting phase

Superscripts

H_2O	water
κ	general component
N_2	nitrogen
n	time level

Dimensionless Numbers

Nu	NUSSELT number
Pe	PECLET number
Pr	PRANDTL number
Re	REYNOLDS number
Sc	SCHMIDT number
Sh	SHERWOOD number

Abstract

One of the most basic assumptions in the field of multiphase flow in porous media is that of local equilibrium. This work is a contribution to the study and understanding of this assumption. Assuming local equilibrium basically means that heat and mass transfer processes between phases take place instantaneously. For a number of applications, this assumption is questionable for various reasons. In the following, two of these reasons are illustrated by examples.

Supply of Non-Equilibrium If there are sources present in the porous medium which unbalance the system, assuming local equilibrium for all phases is a very strong assumption in need of justification. Practically, this source can be the supply of non-equilibrated, i.e. not fully water saturated, air bypassing soil. The assumption that the air immediately becomes fully vapor-saturated might be a serious oversimplification.

Heat sources in porous media are another reason to doubt the applicability of local equilibrium assumptions. An evident example is the cooling of severely damaged nuclear reactor cores. In this case, the solid phase continuously provides energy and complex phase-change processes occur.

Insufficient Equilibration Time If the considered porous medium is thin, for example paper during drying processes, the short residence time of air makes the idea of immediate equilibration far-fetched.

Another case of questionable applicability of local equilibrium assumptions comes from the field of steam-assisted subsurface remediation. In order to predict remediation success, the correct description of the high flow velocities as well as large temperature gradients that occur are crucial.

What the systems described above have in common is that studying them experimentally is hard and/or expensive. Therefore, simulation technologies can be an important tool in this context. This work is a contribution to the study and understanding of such (non-) equilibrium situations in multiphase flow in porous media.

Abstract

In this work, a model free of local equilibrium assumptions is developed and explained in depth. The model describes multiphase flow in porous media on a volume-averaged basis. It is, mathematically as well as numerically, formulated in general terms, allowing it to be applied to very different scenarios, as shown in this thesis. The numerical implementation is accomplished in DuMu^x, a free and open-source simulator. We have also developed ways of making all the source code used in this work, be it for flow simulations or image analysis, freely available.

In a first application of the non-equilibrium model developed here, a parameter study, motivated by evaporation from a porous medium, is conducted. In order to obtain the necessary input parameters (volume-averaged interfacial areas) a pore-network model is adapted and constitutive relations derived. Varying an unknown model parameter (scaling factor) within a range of values results in the physically expected behavior of the system.

In order to put the study of non-equilibrium effects in multiphase flow in porous media on an experimental basis, a new platform is developed in collaboration with colleagues from the University of Utrecht. The experimental setup allows us to study thermal equilibration and immiscible displacement processes simultaneously in a transparent micro-model. This is accomplished by a setup which includes both an optical as well as an infrared camera, recording the same invasion process. Both the versatility and feasibility of the platform are demonstrated in qualitative findings and observations.

Building on this, two different experimental runs are simulated by means of the model developed previously. In order to be able to use the non-equilibrium model, a new image-analysis procedure had to be developed for the determination of constitutive relations. As the proposed scaling factor of heat transfer is still unknown, it had to be calibrated to the experimental observations. Remarkably, both simulations find that the same scaling factor results in the best reproduction of the experimental observations.

In another effort to increase confidence in the model, a code intercomparison study is conducted. In this regard, the same technical application, a metallic evaporator, is simulated by two simulators developed independently. These are the model

developed in this work and a model describing multiphase flow in porous media based on a mixture description. Although both models are different in terms of mathematics, numerics and the simulation environments employed, they produced very similar results. This was taken as a validation of the developed model.

In summary, three things are accomplished in this thesis: a toolbox of models and methods allowing the study of local non-equilibrium effects in multiphase flow in porous media in a volume-averaged sense is developed and successfully applied to a number of different applications. Secondly, new procedures for sustainable software development and source code accessibility are developed. Thirdly, different ways to determine constitutive relations are developed and successfully applied.

Zusammenfassung

Eine grundlegende Annahme in der Mehrphasenströmung in porösen Medien ist die des lokalen Gleichgewichts. Diese Arbeit leistet einen Beitrag dazu, diese Annahme zu untersuchen und zu verstehen. Lokales Gleichgewicht anzunehmen bedeutet im Wesentlichen, dass Energie- und Massentransfer unendlich schnell stattfinden. Diese Annahme ist, aus unterschiedlichen Gründen, für verschiedene Problemstellungen fragwürdig. Im Folgenden werden zwei dieser Gründe anhand von Beispielen erläutert.

Kontinuierliches Aus-Dem-Gleichgewicht-Bringen Wenn es Quellen in einem porösen Medium gibt, die das System aus dem Gleichgewicht bringen, so ist es eine starke Annahme, die begründet werden sollte, davon auszugehen, dass sich das System im lokalen Gleichgewicht befindet. Ein Beispiel für eine solche Situation ist nicht zu 100% mit Wasserdampf gesättigte Luft, die über Erdreich streicht. Die Annahme, dass die Luft sofort wassergesättigt ist, sobald sie in Kontakt mit dem porösen Medium Erde kommt, kann eine folgenschwere, zu starke Vereinfachung sein.

Ein weiterer Grund, die Annahme des lokalen Gleichgewichtes in Frage zu stellen, sind Wärmequellen im porösen Medium. Dies ist zum Beispiel der Fall bei der Kühlung eines nuklearen Reaktorkerns nach einem schweren Reaktorunfall. Hier befindet sich eine starke Wärmequelle in der Feststoffphase, die auch Verdampfungsprozesse verursacht.

Ungenügende Ausgleichszeit Wenn das poröse Medium relativ dünn ist, wie zum Beispiel im Falle von Papier in der Papierherstellung, macht die kurze Verweilzeit des Trocknungsmediums die Annahme von lokalem Gleichgewicht abwegig.

Ein weiteres Beispiel in diesem Zusammenhang ist die Dampfinjektion in den Untergrund zur Altlastensanierung. Um den Sanierungserfolg richtig vorherzusagen, müssten die hohen Strömungsgeschwindigkeiten und Temperaturgradienten korrekt abgebildet werden.

Zusammenfassung

Die beschriebenen Systeme haben eine Gemeinsamkeit: experimentelle Untersuchungen sind schwer und/oder teuer. Daher können Simulationstechnologien hier einen wichtigen Beitrag leisten. Diese Arbeit entwickelt Werkzeuge zur Untersuchung solcher Sachverhalte und leistet einen Beitrag zum besseren Verständnis von solchen (nicht-) Gleichgewichtsprozessen.

In dieser Arbeit wird ein Modell entwickelt und erklärt, welches keine lokalen Gleichgewichtsannahmen trifft. In diesem Modell wird eine volumengemittelte Beschreibung von Mehrphasenströmung in porösen Medien verwendet. Sowohl mathematisch als auch numerisch ist das Modell zunächst so generell wie möglich gehalten. Dadurch kann es, wie in dieser Arbeit gezeigt, für sehr unterschiedliche Problemstellungen verwendet werden. Die numerische Implementierung erfolgt als freie Software in DuMu^x, einer Simulationsumgebung für Strömung und Transport in porösen Medien. Im Zuge dessen, wurden auch neue Möglichkeiten entwickelt, Software im Rahmen von DuMu^x zur Verfügung zu stellen. So kann alle Software, die in dieser Arbeit verwendet wurde, sei es für Strömungssimulation oder zur Bildverarbeitung, frei eingesehen, überprüft und weiterentwickelt werden.

Im ersten Anwendungsfall für das entwickelte nicht-Gleichgewichtsmodell wird eine Parameterstudie, motiviert durch Evaporation aus dem Boden, durchgeführt. Eine wichtige Eingangsgröße für das Modell sind volumengemittelte Phasengrenzflächen. Durch die Weiterentwicklung eines Porennetzwerk Modells können diese Konstitutivbeziehungen abgeleitet werden. Die Variation eines unbekanntes Modellparameters (Skalierungsfaktor) führt zu dem physikalisch erwarteten Verhalten des Systems.

Um die Untersuchung von nicht-Gleichgewicht in der Mehrphasenströmung in porösen Medien auf eine experimentelle Grundlage zu stellen, wurde in einer gemeinsamen Arbeit mit Kollegen von der Universität Utrecht eine neue experimentelle Plattform entwickelt. Mit Hilfe dieses Versuchsaufbaus kann man gleichzeitig thermische Ausgleichsprozesse und nicht-mischbare Verdrängungsprozesse in einem transparenten Mikromodell beobachten. Hierzu werden mit einer optischen und einer Infrarotkamera Bilder des nicht-isothermen Verdrängungsprozesses im Mikromodell gemacht. Die praktische Verwendbarkeit & Nutzbarkeit des beschrie-

benen Versuchsaufbaus wird durch eine Reihe von qualitativen Beobachtungen demonstriert.

Aufbauend auf den Versuchsergebnissen, werden zwei unterschiedliche Versuchsdurchläufe mit dem entwickelten nicht-Gleichgewichtsmodell simuliert. Zur Quantifizierung von Konstitutivbeziehungen wurden neue Bildverarbeitungs-Algorithmen entwickelt und angewendet. Da der oben erwähnte Skalierungsfaktor nach wie vor unbekannt ist, muss er kalibriert werden. Es ist bemerkenswert, dass bei beiden Simulationen der gleiche Skalierungsfaktor die beste Übereinstimmung zwischen Modell und Beobachtung geliefert hat.

Um das Vertrauen in das entwickelte Modell zu erhöhen, wurde eine Software Vergleichsstudie durchgeführt. Hierzu wurde die gleiche technische Anwendung mit zwei unabhängig entwickelten Simulationsprogrammen abgebildet. Das in dieser Arbeit entwickelte nicht-Gleichgewichtsmodell wurde einem Modell, das Mehrphasenströmung in porösen Medien auf Grundlage eines Mischungsansatzes beschreibt, gegenüber gestellt. Obwohl die beiden Modelle unterschiedliche mathematische und numerische Ansätze verwenden und in unterschiedlichen Simulationsumgebungen implementiert sind, haben sie zu sehr ähnlichen Ergebnissen geführt. In diesem Sinne wurden die Ergebnisse als Modellvalidierung aufgefasst.

Zusammenfassend wurden drei Dinge in dieser Arbeit erreicht: Es wurden Modelle und Methoden, um lokales nicht-Gleichgewicht in der Mehrphasenströmung in porösen Medien auf Grundlage einer volumengemittelten Beschreibung zu untersuchen entwickelt. Diese Modelle wurden erfolgreich auf sehr unterschiedliche Problemstellungen angewendet. Zweitens wurden neue Verfahren entwickelt, um die Software Entwicklung nachhaltiger zu gestalten und den verwendeten Quellcode zugänglich zu machen. Drittens wurden unterschiedliche Methoden entwickelt, um Konstitutivbeziehungen herzuleiten.

1

Introduction

1.1 Motivation

At the core of any model of reality are the assumptions and decisions on which this model is built. The reasons for making these assumptions need to be well founded and testable. If there is doubt about the applicability or correctness of an assumption, it needs to be loosened and replaced by a suitable one.

One of the most prominent assumptions in the field of multiphase flow in porous media is the assumption of local equilibrium. Basically, this means that energy and mass transfer between phases take place instantaneously.

This work provides tools and methods for checking the validity of these assumptions in porous media systems. This is done by developing a model which is free of local equilibrium assumptions and studying consequences and implications thereof.

Pure scientific curiosity is, of course, known to boost general progress, but there are also a number of practical applications which put the question of the applicability of local equilibrium assumptions on the agenda:

Subsurface Remediation by Steam Injection One effective cleanup-technology for contaminated sites is the injection of hot steam into the subsurface. This process involves temperature differences and flow velocities which are high compared with other flow processes in porous media. The prediction of contaminant behavior in this highly non-isothermal setting is crucial for solving environmental problems instead of creating new ones.

1 Introduction

Reactions, Industry In the chemical industry, reactions take place in biochemical reactors with multiple fluid phases as well as a solid phase present. Describing phase temperatures correctly gives control over the reactions taking place.

Reactions, In-Situ Combustion During in-situ combustion, heavy oil is partly oxidized in the reservoir in order to decrease its viscosity for mobilization, and ultimately production. If the temperatures of the individual phases are not correctly described, undesired reactions may take place. Or even worse: too much oil could be burnt instead of being produced.

Debris Cooling After a severe nuclear accident, the core might collapse and can be treated as a porous medium. It is of paramount importance to have a good understanding of the subsequent events in order to be able to orchestrate a fast cooling without causing any further (H_2) explosions.

Drying In the case of drying thin porous media for industrial applications (pulp and paper) local equilibrium assumptions are at least questionable. Better models will lead to a better allocation of resources in the production process.

Evaporation At the interface between the subsurface and the atmosphere, two very different compartments share a boundary: the land surface. Here, evaporation takes place if the subsurface provides liquid water and the atmosphere can take up water vapor. However, flow velocities in the atmosphere can be very high and the exact interaction processes are not yet fully understood.

What all these examples have in common is that they do not only involve temperature differences but also phase change-processes. In other words, heat and mass transfer are strongly coupled phenomena which need to be treated and understood together. Therefore, a model allowing the combined description of local chemical as well as thermal non-equilibrium is developed in this work. The detailed structure of this thesis is given in the next section.

1.2 Structure of the Thesis

To analyze local equilibrium assumptions in multiphase flow in porous media, I use the classic scientific method extended by simulation, see Figure 1.1. In today's research, simulation has established itself as a crucial third pillar beside theoretical and experimental work. It demands a thorough foundation in physics, mathematics and numerics on the one hand and, on the other, it gives guidance and allows the efficient allocation of resources.

I start by giving a concise introduction to physical definitions and conventions in Chapter 2. All quantities relevant in order to describe the multiphase flow in porous media processes covered in this work are briefly introduced. I emphasize the volume-averaged description of quantities, which will be built upon later when employing these concepts in order to derive input parameters from numerical and actual experiments. The main part of this chapter is, of course, the explanation and discussion of local thermal and chemical equilibrium in multiphase flow in porous media.

In Chapter 3, a macro-scale non-equilibrium model is developed. Limitations as well as numerical solution techniques are also briefly discussed.

Chapter 4 gives a quick explanation of why an interesting and promising approach, the balancing of interfacial area on the macro scale, can as of now not be used for

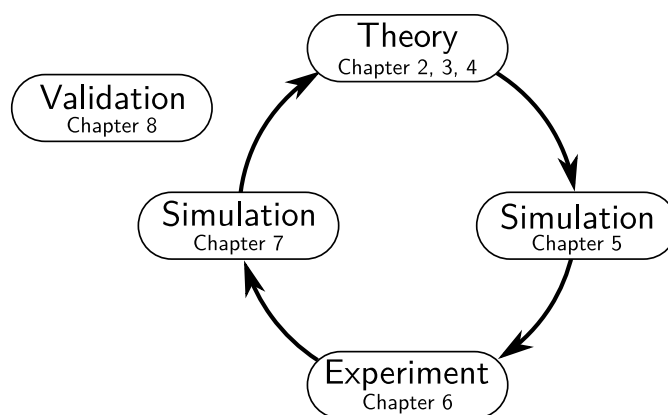


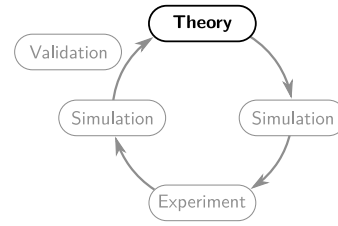
Figure 1.1: Closing the loop.

1 Introduction

volume-averaged macro-scale models. This is extremely unfortunate as the interfacial area approach has the potential to loosen assumptions about the knowledge of the history of a system.

The macro-scale non-equilibrium model is put to use in Chapter 5. There, a parameter study is conducted, delimiting ranges of an unknown model parameter, the scaling factor of heat and mass transfer. In the model, this parameter is essential for actually describing heat and mass transfer in multiphase flow in porous media. In order to estimate that parameter, an experimental setup and qualitative findings are presented in Chapter 6. A model calibration conducted in Chapter 7 gives an estimate of that formerly unknown parameter.

The other possibility, besides experimental testing, to increase confidence in numerical models is the cross-validation with independently developed models. This ansatz is adopted in Chapter 8 by means of a comparison between two different numerical models simulating a technical system. I conclude in Chapter 9.



2 Conceptual Model

Numerical simulation, first of all, demands the development of a conceptual model. This includes the proper selection of relevant processes as well as the decision regarding the level of detail necessary to capture the characteristics of the system. The focus of this work is the description and study of non-equilibrium processes. Therefore, special attention is given to the definition of equilibrium.

We start this chapter by giving definitions of standard thermodynamic quantities followed by a short introduction to the scales of interest which will be useful in the scope of this work. This process gives rise to new quantities which are only defined on higher scales. Finally, the respective equilibria are introduced.

2.1 Basic Definitions

In this section, terms and definitions which are essential to this work, are presented. These definitions are kept as short as possible and the reader is referred to the literature – which was the basis for this section – for in depth discussions (Atkins and Julio, 2006; Reid et al., 1987).

2.1.1 Phase, Component, Capillary Pressure

A *phase* (α) is a region with continuous physical and chemical properties. In other words, a phase is defined by the fact that it has a sharp interface with another

2 Conceptual Model

phase. Three different phases are typically distinguished: solid, liquid and gas phase. In the scope of this work, all phase states occur. The grains of the porous medium are solid and considered immobile and rigid. Within the void space, liquid and gas phases can move. In this work, only two mobile phases are considered, although three phase flow can also occur (e.g. Class et al., 2002). We consider also phase transitions between liquid and gas states. These processes can be highly non-isothermal and are therefore strongly coupled with energy conservation.

The term *component* refers to chemical species (like water or nitrogen) which constitute a phase. A phase can be comprised of multiple components. We do not consider chemical reactions but the chemical composition of phases can change as the individual components can move within a phase and across phase boundaries.

In the presence of two separate fluid phases the phenomenon of *capillarity* occurs. Fluids tend to minimize their surface, in order to reach a state of minimum energy. If the area (A) of an interface between two fluids is changed, work (W) either needs to be supplied or is freed according to

$$dW = \sigma dA, \quad (2.1)$$

with the surface tension σ as a material property of any combination of two fluids. This minimization of surface area can lead to curved surfaces, which are associated with a pressure difference across the interfaces. The difference in pressure (p) between the fluid phases can be described by the so called *Young-Laplace-Equation*

$$\Delta p = \sigma \left(\frac{1}{r_1} + \frac{1}{r_2} \right), \quad (2.2)$$

with r_1 and r_2 as the two principal radii of curvature of the considered interface. The pressure on the concave side of the interface is always the bigger one.

However, in the scope of this work, we also consider the presence of a solid phase (index s). In this case, the pressure difference across an interface is given by

$$\Delta p = \sigma \cos \Theta_c \left(\frac{1}{r_1} + \frac{1}{r_2} \right), \quad (2.3)$$

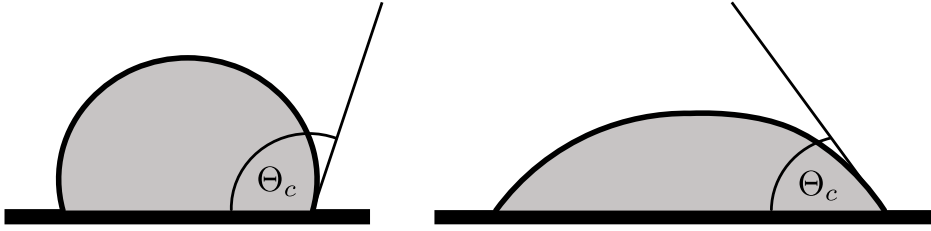


Figure 2.1: A water droplet on two different surfaces. **Left:** Water is the non-wetting phase. **Right:** Water is the wetting phase.

with Θ_c as the contact angle of a phase with respect to a considered solid phase. A contact angle of $0^\circ < \Theta_c < 90^\circ$ defines a *wetting phase*, as it tends to cover the solid phase. Phase specific properties of the wetting phase are denoted with a subscript w in this work. Contact angles of $90^\circ < \Theta_c < 180^\circ$ define the so called *non-wetting phase*, subscript n , see Figure 2.1. A water droplet is the non-wetting phase with respect to e.g. a Teflon[®] surface (left) and the wetting phase with respect to a glass surface (right). In general, wettability is defined by the combination of fluids and solid phase. It can even change over time (e.g. Wessolek et al., 2009). However, in the scope of this work, wetting properties are considered constant.

The surface tension between phases is mainly a function of temperature. Thus, the pressure difference across an interface between two fluid phases is also a function of temperature, decreasing up to the critical point where the discrimination between phases ceases to be possible.

2.1.2 Density, Viscosity

The ratio of mass (m) to occupied volume (V) of a phase α is called its *density*, ρ_α . In general, density is a function of pressure, temperature and composition. In the case of gases, the pressure dependence is much stronger than for liquids. The density of the solid phase is generally assumed constant in this work.

Applying a shear stress to a fluid results in a movement of the fluid with the maximum velocity at the point where the shear stress is applied. In the scope of this work, all fluids are assumed to behave as *Newtonian* fluids. Therefore, the proportionality factor relating the shear stress to the gradient in velocity is

2 Conceptual Model

viscosity, μ . In that sense, viscosity can be considered a measure for the internal fluid friction opposing any change of fluid motion.

2.1.3 Internal Energy, Enthalpy, Heat Capacity, Thermal Conductivity

The total amount of energy contained in a given mass of a substance is given by its *mass specific internal energy*, u . However, when moving substance, energy is also needed for making space for it. Therefore, a further characteristic quantity is introduced, *mass specific enthalpy*, h . It is different from the internal energy by the contribution of volume changing work

$$h = u + \frac{p}{\rho}. \quad (2.4)$$

The ratio of supplied heat (Q) to the resulting change in temperature (ΔT) of a substance is called its *heat capacity*. This change can either happen at constant pressure or constant volume leading to isobaric and isochoric heat capacities, respectively. However, in the scope of this work, the heat capacity will be only used for characterizing solid and liquid phases which are assumed incompressible. Therefore, discrimination between isobaric and isochoric heat capacities is not necessary in the scope of this work and the symbol c will be used for the mass specific heat capacity.

Two systems at different temperatures which are in contact with one another will exchange energy. The proportionality factor which relates the heat flux and the temperature gradient in a homogeneous medium is called *heat conductivity*, λ (Atkins and Julio, 2006). It is a material property of a phase.

2.1.4 Mole Fractions

As mentioned above, the coexisting phases are not necessarily pure, i.e. they can consist of multiple chemical species of varying composition. In the scope of this

work, we will only deal with two components per phase at the most, as this is the simplest configuration allowing the study of the coupled phenomenon of phase change.

The composition of the respective phases is given by the mole fractions x_α^κ of the components κ in a phase α . Mole fractions are defined by the relation of the amount of the species κ in a phase to the total amount of substance in a phase. In an existing phase, mole fractions always add up to unity:

$$\sum_{\kappa} x_\alpha^\kappa = 1. \quad (2.5)$$

2.1.5 Mixture Properties

When mixing two or more components, properties of the mixture arise which are not necessarily a pure linear combination of the original properties. Interactions between the molecules of the pure components lead to an additional contribution, the so called *excess quantities*. However, in the scope of this work, we will assume *ideal mixtures* and ignore excess contributions. In other words, we assume that the interaction of molecules in a mixture are uniform, no matter which types of molecules are interacting. The considered properties of phases are therefore calculated as simple mole fraction weighted sums, e.g. for the molar density of a phase consisting of two components a and b :

$$\varrho_\alpha^{(n)} = x_\alpha^a \varrho^{(n)a} + x_\alpha^b \varrho^{(n)b}. \quad (2.6)$$

Here, ϱ^κ stands for the density of the pure substance at the current pressure and temperature and ϱ_α for the density of the resulting mixture.

2.2 System Properties

In the previous section, the properties of pure substances, their mixtures and the interaction of two fluid phases were introduced. In this section, the interaction

2 Conceptual Model

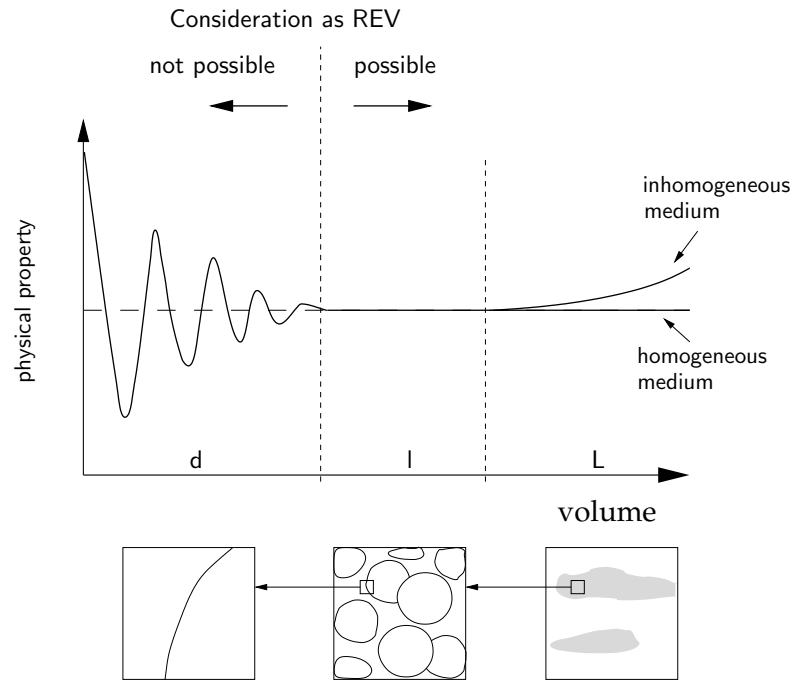


Figure 2.2: Construction of an REV. Adapted from Helmig (1997).

with the solid phase as well as the scales utilized in this work will be explained. This will also give rise to new quantities which are not defined on all scales or have different meanings on different scales.

2.2.1 Scales

Up to now, reasoning took place on a scale where the individual phases were resolved. This scale will be called *micro scale*. Although this scale might be helpful for principal understanding and developing conceptual models, in most cases and for real life applications it is not feasible to describe multiphase flow in porous media on the micro scale.

Obtaining the geometry of a porous medium is typically associated with prohibitively high costs. An alternative to obtaining real geometries is to use pore-network models (Joekar-Niasar, 2010). They exhibit certain features of a porous medium without reproducing exact geometries (see Section 5.1). Even in those cases where

geometries are obtained, simulation can only take place on small samples due to computational limitations.

Therefore, the description of multiphase flow in porous media systems typically involves an averaging step (Whitaker, 1999), see Figure 2.2 for a depiction of the process. Averaging properties over some volume initially leads to strong fluctuations of the averaged quantity (d in Figure 2.2). However, after reaching a certain averaging volume, the averaged quantity ceases to fluctuate (l in Figure 2.2). The scale on which these constant properties can be observed will be called *macro scale*. The volume for which it is possible to observe non-fluctuating properties will be called *representative elementary volume, REV*. In the case of an inhomogeneous porous medium, further increasing the averaging volume (L in Figure 2.2) will lead to a non-constant averaged quantity.

The goal of this work is to describe non-equilibrium in multiphase flow in porous media on the macro scale. As the body of literature in this area is sparse, necessary input parameters for the macro-scale model have to be derived from micro-scale considerations, see Figure 2.3. In Section 5.1 a pore-network model will be employed in order to obtain effective volume-averaged quantities and in Chapters 6 and 7 observations of and measurements from a micro-model experiment are presented.

2.2.2 Quantities on the Macro Scale

In the described averaging process the detailed micro-scale information is lost, see Figure 2.3. It is represented by averaged quantities which will be introduced in the following.

Matrix Properties

A porous medium consists of the solid phase which acts as a skeleton for the void space in between. The ratio of void space to the space occupied by the REV is called *porosity*, ϕ :

$$\phi = \frac{\text{volume of void space}}{\text{volume of REV}}. \quad (2.7)$$

2 Conceptual Model

The reciprocal of the resistance exerted by the porous medium on the movement of a fluid phase is called *permeability*, \mathbf{K} . Resistance to flow is in general a directional property and therefore a tensor. However, in the scope of this work, it will be treated as a scalar.

Multiphase Properties

Saturation The volume fraction of the void space of a porous medium which is occupied by a phase α is called *saturation*, S_α , of that phase:

$$S_\alpha = \frac{\text{volume of fluid } \alpha}{\text{volume of void space}}. \quad (2.8)$$

Figure 2.3 shows on the left-hand side the micro-scale configuration with solid grains and a wetting and a non-wetting phase. On the right-hand side the macro-scale representation is shown. Here, only the information about respective volume fractions is retained.

Capillary Pressure In Section 2.1.1 the capillary pressure on the micro scale was introduced. In Equation 2.3 it was defined as the difference of pressures across a curved interface.

On the macro scale, the information about individual interfaces is not available. There are only volume-averaged quantities defined. Therefore, the *macro-scale capillary pressure* p_c is defined as the difference in pressures of the wetting and

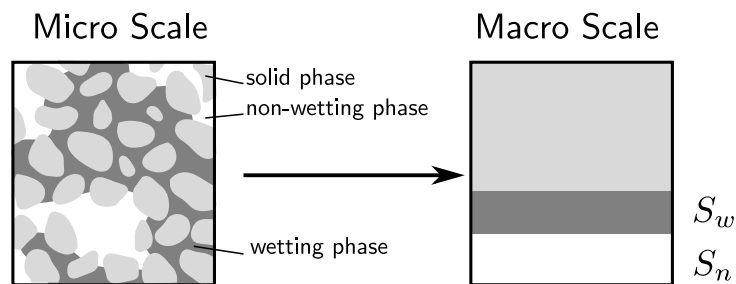


Figure 2.3: Micro-scale configuration (**left**) and macro-scale representation (**right**) of a multiphase flow situation.

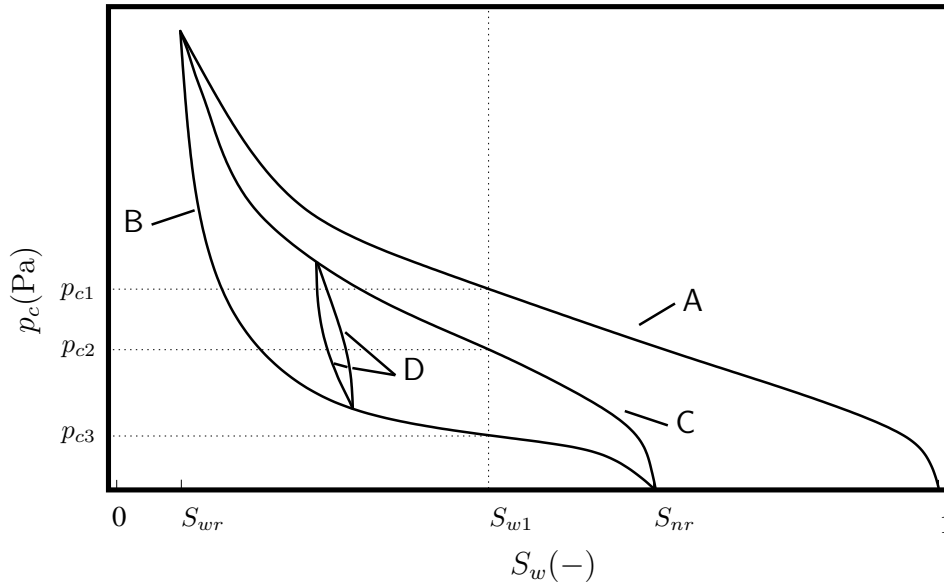


Figure 2.4: Qualitative observation of capillary pressure – saturation relationship.

non-wetting phase in an REV. It is related to the saturation of a phase, usually the wetting phase.

In a typical experiment for establishing the relation between wetting phase saturation and macro-scale capillary pressure a sample of a porous medium is first fully saturated with a wetting phase and placed horizontally in order to minimize the influence of gravity. One side of the sample is in contact with a non-wetting phase and the other side allows the wetting phase to leave the sample. The pressure difference between these two sides is identified as macro-scale capillary pressure.

Raising the non-wetting phase pressure and letting the sample equilibrate leads to a new saturation and a non-zero capillary pressure. Repeating this procedure incrementally up to the point where no (mobile) wetting phase is left in the sample establishes a series of points which uniquely relate the wetting phase saturation and the macro-scale capillary pressure. As the process of non-wetting phase replacing a wetting phase is called *drainage*, this curve is called *primary drainage curve*, A in Figure 2.4.

However, reversing the process leads to a new series of p_c - S_w couples, B in Figure 2.4. As the process of wetting phase replacing non-wetting phase is called imbibition, this

2 Conceptual Model

curve is called primary imbibition curve. Switching again to drainage establishes yet another path, C in Figure 2.4, which is called *main drainage curve*. Further switching between drainage and imbibition will lead to so called *scanning curves*, D in Figure 2.4, between the primary imbibition and the main drainage curve. S_{wr} and S_{nr} are the residual saturation of wetting and non-wetting phase respectively. These are the saturations at which the respective phases become immobile and thus cannot be reduced any further by hydromechanical processes. In summary, it can be stated that only knowing the saturation of a porous medium does not uniquely give its macro-scale capillary pressure. Saturation S_{w1} in Figure 2.4 allows any capillary pressure between p_{c1} and p_{c3} .

Systems behaving like this, with the state of the system not clearly defined by state variables but also by the systems history, are said to inhibit *hysteresis*. The word hysteresis was coined by Sir ALFRED EWING (Bates, 1948) who studied magnetization. It is derived from ancient Greek $\nu\sigma\tau\acute{\epsilon}\rho\eta\sigma\iota\zeta$ which means “lagging behind” or “deficiency” (in the meaning of scarcity).

Many empiric parametrizations of the above described curves exist. The two most commonly used functions are according to Helmig (1997):

$$\text{BROOKS\&COREY: } p_c = p_d S_{w\text{eff}}^{-1/\lambda} \quad \text{and} \quad (2.9)$$

$$\text{VAN GENUCHTEN: } p_c = \frac{1}{\alpha} \left(S_{w\text{eff}}^{-1/m} - 1 \right)^{1/n} \quad (2.10)$$

where m, n, α are VAN GENUCHTEN (van Genuchten, 1980) and p_d, λ are BROOKS & COREY (Brooks and Corey, 1964) parameters. In fact, the VAN GENUCHTEN approach has only two parameters, as $m = 1 - 1/n$ is a necessary assumption in its derivation, see van Genuchten (1980). $S_{w\text{eff}}$ is the *effective wetting phase saturation* defined by

$$S_{w\text{eff}} = \frac{S_w - S_{wr}}{1 - S_{wr}}. \quad (2.11)$$

The functions presented in Equations 2.9 and 2.10 are depicted in Figure 2.5. Additionally, that figure depicts the temperature dependence of the capillary pressure saturation relationship according to Grant (2003).

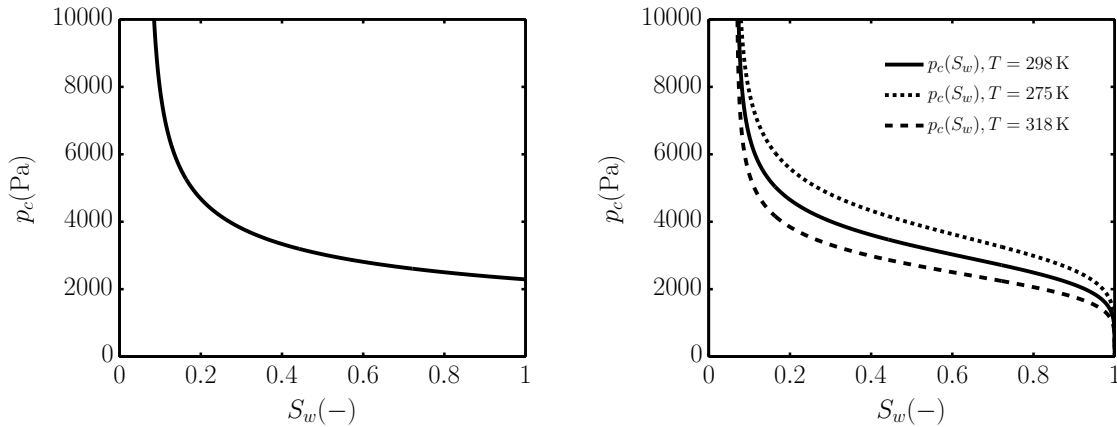


Figure 2.5: Left: Capillary pressure – saturation relationship according to BROOKS & COREY, $\lambda = 2.74$, $p_d = 2300$ Pa, **right:** Capillary pressure – saturation relationship according to VAN GENUCHTEN, $\alpha = 3.3 \cdot 10^{-4}$ 1/Pa, $n = 5.4$. The scaling according to Grant (2003) for the temperatures of 298 K (reference, solid), 275 K (dotted) and 318 K (dashed) are also depicted, scaling parameter $\beta_0 = -413.4$ K.

The temperature dependence of surface tension is well understood and industry standard equations of state are readily available for common systems like water and air (IAPWS, 1994). However, Grant (2003) shows that the variation with temperature of the macro-scale capillary pressure in porous media cannot be explained by the variation of surface tension alone. Therefore, he proposes a scaling of the capillary pressure relationship:

$$p_c = \frac{\beta_0 + T_{\text{ref}}}{\beta_0 + T} \frac{1}{\alpha} \left(S_w^{\text{eff}^{-1/m}} - 1 \right)^{1/n}, \quad (2.12)$$

with T and T_{ref} as the current and reference temperature, respectively. The parameter β_0 of this relationship is characteristic for the given porous medium and combination of fluids, it should not be used outside its fitting range. Within that range, however, Grant (2003) shows that the above equation can be fit to many natural and artificial porous media as well as combinations of fluids. Two examples are shown in Figure 2.5 (right).

However, all of these functions uniquely relate saturation and capillary pressure, i.e. they can describe one of the curves A, B, C, D in Figure 2.4. Extensions in order to capture the hysteretic behavior of the system could be accomplished e.g. by inclusion of a phenomenological scaling approach e.g. *play-type* hysteresis (Visintin,

2 Conceptual Model

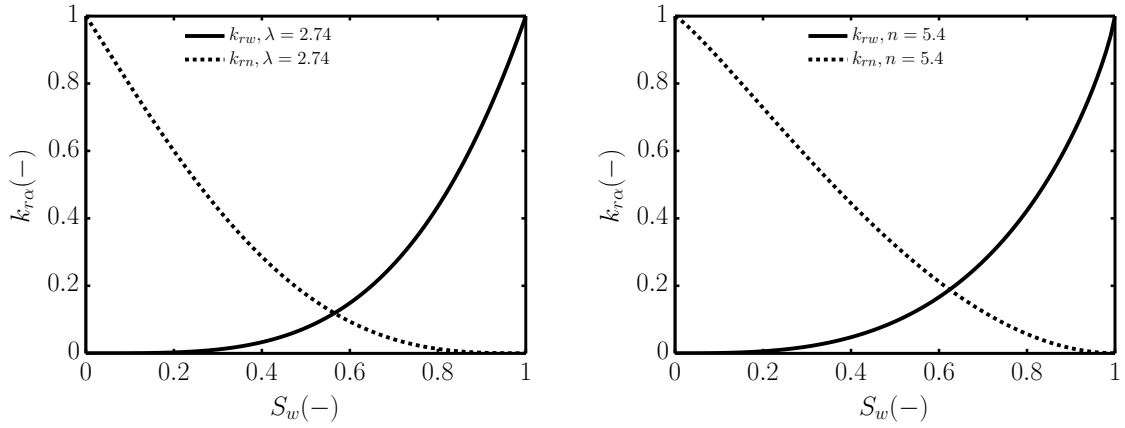


Figure 2.6: **Left:** Relative permeability–saturation relationship according to BROOKS&COREY, **right:** relative permeability – saturation relationship according to VAN GENUCHTEN.

1994) or *Parker Lenhard* hysteresis (Parker et al., 1987). For other approaches, including the relaxation behavior of the phase pressure difference, we refer to the literature, e.g. Mantney et al. (2005).

In Chapter 4 a short introduction into an approach (and its limitations) which tries to describe macro-scale capillary pressure uniquely by introducing an additional state variable will be given. For the sake of brevity we will abbreviate “macro-scale capillary pressure” by capillary pressure in the rest of this work.

Relative permeability In a multiphase setting, the resistance to flow is changed compared to the single-phase case. In other words, the presence of one fluid phase does have an influence on the flow behavior of the other fluid phase. This influence is described by so-called *relative permeabilities*. They are also parametrized as functions of saturation ($k_r(S_w)$).

Of course, relative permeabilities are also a function of the configuration of the respective phases and therefore inhibit hysteresis as explained above. However, this will not be covered in this work. For an example where this phenomenon is of interest, see Juanes et al. (2006) who applied a concept of Land (1968).

Independent measurements of relative permeabilities are most informative and therefore preferable for characterizing the behavior of the system at hand. In their

absence, Helmig (1997) explains how the relative permeability functions can be approximated from knowledge about p_c - S_w parameters.

Concepts from Burdine (1953) in conjunction with the BROOKS&COREY approach lead to the relative permeability functions:

$$k_{rw} = S_{w \text{ eff}}^{\frac{2+3\lambda}{\lambda}}, \quad (2.13)$$

$$k_{rn} = (1 - S_{w \text{ eff}})^2 \left(1 - S_{w \text{ eff}}^{\frac{2+\lambda}{\lambda}}\right), \quad (2.14)$$

visualized in Figure 2.6 (left). The VAN GENUCHTEN approach with Mualem (1976) leads to another set of relative permeability functions:

$$k_{rw} = \sqrt{S_{w \text{ eff}}} \left(1 - \left(1 - S_{w \text{ eff}}^{\frac{1}{m}}\right)^m\right)^2 \quad (2.15)$$

$$k_{rn} = (1 - S_{w \text{ eff}})^{\frac{1}{3}} \left(1 - S_{w \text{ eff}}^{\frac{1}{m}}\right)^{2m}, \quad (2.16)$$

visualized in Figure 2.6 (right).

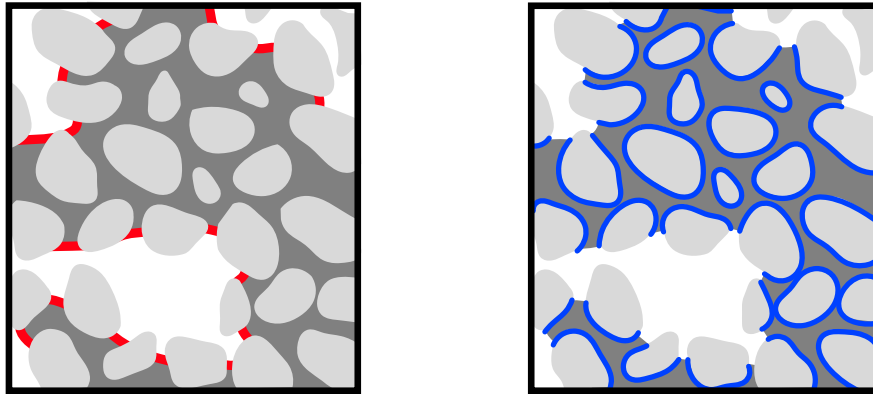


Figure 2.7: Conceptual sketch of the wetting – non-wetting (**left**) and wetting – solid (**right**) interfacial area in a multiphase flow in porous media situation.

Interfacial Area

This work deals with the description of transfer processes between phases. An important quantity in order to describe such processes is the cross-sectional area actually available to the transfer process.

In the case of mass transfer (and in the absence of sorption) the corresponding quantity is the interfacial area between the fluid phases, see Figure 2.7 (left). In the case of heat transfer, the solid phase also needs to be taken into account. There is potentially heat transfer between the fluid phases as well as fluid and solid phases, see Figures 2.7 (right) and 2.8 (left) for a depiction of the corresponding interfacial areas. Only one of the two interfacial areas between the solid and fluid phases need to be determined, as the other one can be calculated as the difference between the solid surface (Figure 2.8, right) and the respective other interfacial area.

As explained before, the volume-averaged description of flow processes in this work takes place on the macro scale. Therefore, not the actual interfaces, depicted in Figures 2.7 and 2.8 (in the unit of m^2), but their volume averages (in the unit of m^2/m^3 or $1/\text{m}$) are used. Therefore, the quantities employed in this work will actually be the *volume-averaged interfacial areas*, a_{wn} , a_{ws} and a_{ns} between the respective phases as indicated by the subscripts. For the sake of brevity, these terms will be called interfacial areas.

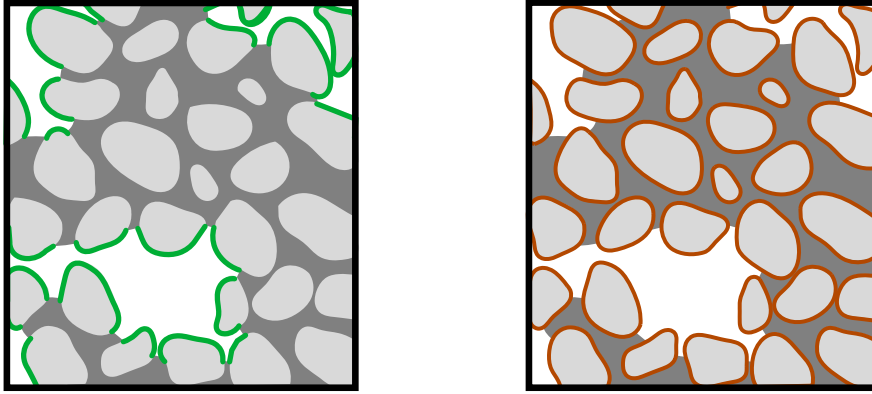


Figure 2.8: Conceptual sketch of the non-wetting – solid (**left**) and total solid (**right**) interfacial area in a multiphase flow in porous media situation.

Although being non-standard constitutive relations, interfacial areas can be determined by several techniques. These techniques are pore-network modelling (e.g. Reeves and Celia, 1996, and Section 5.1 of this work), Lattice-Boltzmann simulation (e.g. Ahrenholz et al., 2011), optical observation (e.g. Karadimitriou, 2013, and Chapter 7 of this work), X-ray computed tomography (e.g. Wildenschild et al., 2002) or interfacial tracer (e.g. Chen and Kibbey, 2006).

2.3 Equilibrium

At the core of this work is the study of equilibrium assumptions. Therefore, we first of all need to precisely define what this term means. To be more precise, we need to distinguish between *local equilibrium* and *global equilibrium*. In general, local equilibrium means that a sufficiently small surrounding of a point is equilibrated, i.e. a sufficient number of collisions of particles has taken place, allowing the definition of intensive state variables such as temperature.

However, in the scope of this work, the term will be used in a slightly different notion. Due to the volume-averaged description (see Figure 2.3), mathematically, there are potentially several phases present at the same point. If these phases do not fulfill the subsequently given criteria for equilibrium, the system is said to be in local non-equilibrium. With the given definition, we find that in this context

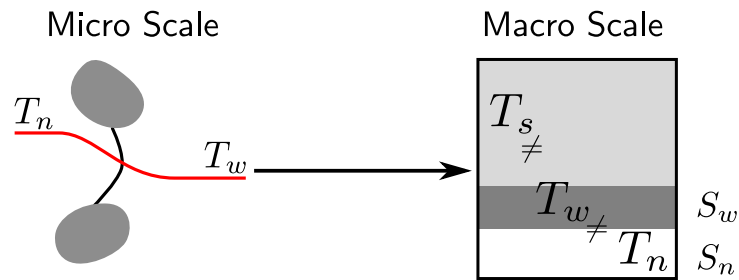


Figure 2.9: Conceptual sketch of a local thermal non-equilibrium situation. The two fluid phases and the solid phase do not have the same temperature.

there is little danger of confusion. Global equilibrium, on the other hand, means that the subsequently given criteria are fulfilled throughout the whole system.

A system is said to be in full or thermodynamic equilibrium if all of the three subsequently defined equilibria are given.

2.3.1 Mechanical Equilibrium

A system is said to be in mechanical equilibrium if the sum of all forces sum up to zero. This is usually the case for multiphase flow in porous media processes as flow velocities are typically sufficiently small for neglecting inertial effects. This is also a necessary assumption for applying the momentum equations presented in Section 3.3. The assumption of mechanical equilibrium will be kept in this work.

2.3.2 Thermal Equilibrium

Two systems that have the same temperature are said to be in thermal equilibrium. These systems could either be adjacent points or phases (mathematically) present at the same point. If these systems do not have the same temperature, the former would imply global thermal non-equilibrium, while the latter will be called local thermal non-equilibrium.

Figure 2.9 gives a conceptual impression of a thermal non-equilibrium situation. However, it has to be kept in mind that the left-hand side of that figure is merely

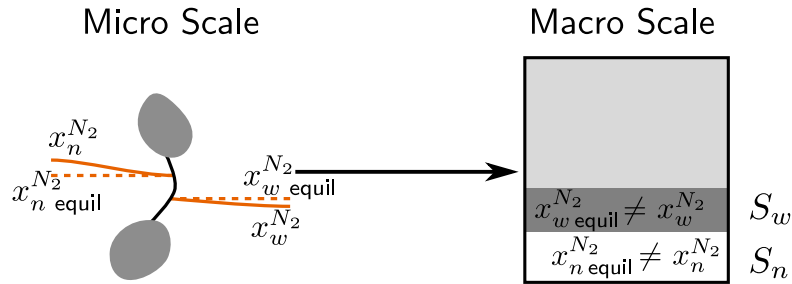


Figure 2.10: Conceptual sketch of a chemical non-equilibrium situation. The figure shows an interface between two grains. While the mole fractions *on the interface* are related via equilibrium relations, they need not be in equilibrium in the bulk phase. Only the quantities with regard to the N_2 component are shown, a similar sketch can be drawn for the other component.

a mental tool. As explained in Section 2.2, we are describing multiphase flow in porous media on the macro scale, without knowledge about individual interfaces. Figure 2.9 shows the different temperatures in the respective phases. As long as the temperatures have not equilibrated, energy exchange between the phases will occur. This process will be called *kinetic energy transfer*.

Without making the assumption of local thermal equilibrium, all phases need to be attributed individual temperatures on the macro scale. It has to be noted that although allowing local thermal non-equilibrium, we keep the assumption that within a given REV each phase has a uniform temperature.

2.3.3 Chemical Equilibrium

Chemical equilibrium is a state at which a system is at a local minimum of GIBBS free energy. Atkins and Julio (2006) elegantly show that (for the other equilibria fulfilled) this is only the case if the derivative of GIBBS free energy with respect to number of particles (the *chemical potential*, μ) is constant.

If this state is not yet reached, either reaction will take place or a change in composition by other processes will occur. As reactions are not covered in this work, the remaining equilibrating processes are mass fluxes within a phase (*diffusion*) or across phase boundaries (*phase change*). In the scope of this work, only phase

2 Conceptual Model

change between fluid phases is considered, i.e. neither sorption nor dissolution of the solid phase are described.

Diffusion can be described by many different kinds of gradients like pressure (pressure diffusion), temperature (thermal diffusion) or external force fields (forced diffusion). In this context, only diffusion caused by gradients in mole fraction are considered (Poling et al., 2001). Of course this is already a simplifying assumption from what is considered to be the true driving force of diffusion: the gradient in chemical potential (Ghai et al., 1973). This assumption is especially good for binary gases at moderate pressures but is commonly made in the scope of multiphase flow in porous media systems. The mathematical description of diffusion, employed in this work, will be given in Section 3.1.

If two fluid phases, present in the same REV, do not have the same chemical potential, we call this *local chemical non-equilibrium*. In the REV considered in Figure 2.10, the present fluid phases do not have the same chemical potentials and are therefore not in chemical equilibrium. Conceptually, it is still assumed that on the interface chemical equilibrium prevails. But this is merely a mental tool for constructing the quantitative description of the equilibration process, i.e. the phase change or *kinetic mass transfer*. Phase change will take place until equal chemical potentials of all components in all phases are reached. It has to be stressed that the goal of this work is to study non-equilibrium on the macro scale. On that scale, no information about individual interfaces is available. The assumption of equal chemical potentials on the interface is incorporated into the macro-scale description by means of the volume-averaged interfacial area, see Section 3.1. Although allowing local chemical non-equilibrium, we keep the assumption that each phase within a given REV has a uniform chemical potential.

Similar to the process of diffusion, which is described by means of gradients in mole fractions, the endpoint of phase change is usually described by means of equilibrium relations. Equilibrium relations connect the mole fractions of contacting phases. This allows to identify the state up to which phase change will occur. These relations give information about the chemical composition of phases which were in contact for sufficiently long time at a given pressure and temperature. In the

following, the two most prominent examples for air–water systems are presented. They have the benefit of simplicity and being applicable in many environmental systems. If systems over wider ranges of pressure and temperature are to be described, more complex relations have to be employed, see e.g. Duan and Sun (2003) for a description of a CO_2 –water system.

Raoult's Law

The French chemist *François Marie Raoult* (1830 – 1901) provided the foundation for relating vapor pressures of components in mixtures, their mole fractions in the liquid phase and the pressure in the overlying gas phase. The general form of RAOULT's law can be obtained by an approach of equal chemical potentials of one component in both phases.

For an almost pure main component of an ideal mixture with an ideal gas phase RAOULT's law (Baehr, 2005) is

$$p_{\text{vap}}^{\kappa} x_{w \text{ equil}}^{\kappa} = p_n x_{n \text{ equil}}^{\kappa}, \quad (2.17)$$

with p_{vap}^{κ} as the saturation vapor pressure of the component κ and the non-wetting phase being gaseous. The index `equil` illustrates that this relation only holds in an equilibrium situation. In other words, for a given pressure and temperature the composition after equilibration can be determined.

The consideration of the gas phase to behave ideally is valid in most cases if a pressure of ≈ 0.1 MPa is not exceeded. Even for pressures of up to 1 MPa deviations from ideal behavior may not be large according to Baehr (2005).

It has to be kept in mind that this simplification is only valid if the mixture consists almost exclusively of one component and the gas phase can be considered ideal. Otherwise deviations from ideal behavior occur.

Henry's Law

In the last section, it was shown how the composition of the liquid phase and of the gaseous phase can be related easily if the component of interest is the main component of the liquid mixture. In the case of a mixture of water and air, the mole fractions of air in the gas and liquid phases cannot be calculated by Equation 2.17, as the component of interest in the liquid phase is in very low concentration. The described case, of one component having a very low mole fraction, is relevant for many applications, mostly gases dissolved in liquids.

The English chemist *William Henry* (1774 – 1836) studied dissolution of gases in liquids. He found that the mole fraction of a dissolved gas in a liquid is related to the mole fraction of the gas in the mixture's vapor (Baehr, 2005).

Following a similar rationale of simplifying the general **RAOULT's** law, a simplified version of **HENRY's** law can be obtained:

$$H^\kappa x_w^\kappa \text{equil} = p_n x_n^\kappa \text{equil} . \quad (2.18)$$

Here, H^κ is the *Henry coefficient* of the component κ and the non-wetting phase is gaseous. Precisely like in the case of **RAOULT's** law, the given relation holds after equilibration, as indicated by the subscript **equil**.

According to Baehr (2005), **HENRY** coefficients do not vary strongly with pressure but are mainly a function of temperature. By means of Equation 2.18 the mole fraction in the liquid phase of one or more dissolved gases can be calculated if the individual **HENRY** constants, mole fractions and pressure in the gas phase are known.

Let us reconsider Figure 2.10 in the light of the above introduced equilibrium relations. The system of air and water is captured by two phases and two components, with nitrogen representing the air phase (exponent N_2). In order to determine the endpoint of kinetic mass transfer, the equilibrium composition needs to be calculated. With two components in two phases, this state is characterized by the four mole fractions.

With Equations 2.5 (for each phase), 2.17 and 2.18 this state is uniquely defined for a given set of constitutive relations (vapor pressure, HENRY coefficient) and boundary conditions (temperature and pressure). This way, the equilibrium composition, denoted by an index *equil*, can be calculated. Kinetic mass transfer will occur as long as the actual mole fractions do not equal the equilibrium composition in the fluid phases (or a phase is depleted).

Dalton's law

Partial pressures p_n^κ are defined as the product of gas phase pressure and mole fraction (if the non-wetting phase is gaseous)

$$p_n^\kappa = x_n^\kappa p_n . \quad (2.19)$$

In this work, gases are assumed to behave ideally. Therefore, the pressure of the gas phase can be calculated as the sum of the individual partial pressures

$$p_n = \sum_{\kappa} p_n^\kappa . \quad (2.20)$$

This relation is known as DALTON's law.

2.3.4 Relaxing Equilibrium Assumptions / State of the Art

In the following, a brief literature review of chemical and thermal non-equilibrium in multiphase flow in porous media is given. Reasons for loosening the local thermodynamic equilibrium assumption include slow transfer processes or the presence of internal "sources" of mass or energy. This is the case for heat input by radiation, for nuclear debris cooling (Fichot et al., 2006) after a severe nuclear accident or for in-situ combustion in porous media (Oliveira and Kaviany, 2001) which prevent a system from reaching local thermodynamic equilibrium. In Chapter 5, the continuous supply of comparatively fast dry air, bypassing a porous medium, as a cause for non-equilibrium will be studied.

2 Conceptual Model

In the case of air-water systems, it is common to assume local chemical equilibrium and to use **RAOULT's** and **HENRY's** law for describing the composition of the coexisting fluid phases (Helmig, 1997; Atkins and Julio, 2006). In the field of groundwater remediation, for example, it can be important to describe the temporal course of the mass transfer process of contaminants between the liquid and the gas phase as opposed to just assuming that mass is transferred instantaneously. Armstrong et al. (1994) find that a standard model for multiphase flow in porous media, which assumes local chemical equilibrium, overestimates the mass transfer between the phases. However, Falta (2000) argues that this observation is just an apparent kinetic effect. He attributes the observed non-equilibrium to the formation of air channels in the water-saturated porous medium.

Berning et al. (2010) describe kinetic mass transfer on the cathode side of a fuel cell. In that case, the reason for non-equilibrium is air, quickly bypassing water droplets in the free flow channel. However, their model only captures stationary states, exhibits some rough approximations with respect to the distribution of the liquid phase and is restricted to the description of kinetic mass transfer of the water component.

Similarly to the discussion of local chemical equilibrium above, local thermal equilibrium might not be a good assumption in the case of processes causing a lot of heat transfer –like evaporation of water– or in the presence of a heat source – e.g. if the cooling of a technical system is to be modeled.

In order to capture the relevant physics, the idea of modeling such situations as several temperatures in the same REV has been developed (Anzelius, 1926; Schumann, 1929). This means that the temperature distribution of each coexisting phase is described by individual energy conservation equations. Today, local thermal non-equilibrium for the case of *single-phase* flow in porous media is covered in textbooks, see Nield and Bejan (2006) and references therein. Local thermal non-equilibrium might be caused by transient effects, like the injection of a hot fluid into a cold domain or vice versa (Rees et al., 2008), the heat generation due to chemical (Li et al., 2007) or nuclear (Baytas and Pop, 2002) reaction or very strong contrast in thermal properties (Truong and Zinsmeister, 1978).

The body of literature covering local thermal non-equilibrium in the case of *multi-phase* flow in porous media, on the other hand, is very limited. There are approaches (Crone et al., 2002) which assign the same temperature to both fluid phases, but acknowledge that those might be different from the solid temperature. They also capture the fact that grains might have a non-uniform temperature and describe the temperature distribution as a function of grain size.

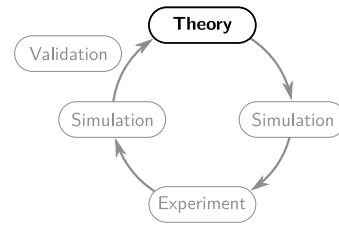
Models which also allow the fluid phases to have different temperatures are mostly motivated by nuclear safety research, concerning post-accident nuclear debris cooling.

In the case of a severe nuclear accident the nuclear core may collapse and the debris will form a debris bed at the bottom of the reactor vessel. This has e.g. happened in the Three Mile Island Accident (Tolman et al., 1988). The debris bed can be treated as a porous medium. There is ongoing research concerning the modeling (Bürger et al., 2006; Fichot et al., 2006) and the experimental (Schäfer et al., 2006; Rashid et al., 2012) investigation of this situation.

Here, the cause for local thermal non-equilibrium is the high initial temperature as well as the heat source in the solid phase. Other authors use three energy equations to describe the thermal equilibration process (along with compositional effects) of a two-phase invasion process into a porous medium (Ahrenholz et al., 2011). In that work, only invasion processes are studied. Quite naturally, equilibration is quick because this is a purely asymptotic process. Therefore, the non-equilibrium situation can only be shown for early times, i.e. the first moments of an invasion process.

Nonetheless, the balance equations therein capture both phenomena, local thermal and chemical non-equilibrium at the same time. Therefore, these are the starting point for the equations used in this work.

The work of Ahrenholz et al. (2011) and this work are to the best of my knowledge the only ones that describe the coupled phenomena of local thermal and chemical non-equilibrium in multiphase flow in porous media on the macro scale. This work is the first to experimentally estimate heat transfer coefficients, which are necessary for describing local thermal non-equilibrium between fluid phases.



3

Mathematical and Numerical Model¹

In this chapter, first the mathematical description of mass and energy conservation, as well as possible momentum descriptions employed in this work will be explained. Building on the mathematical description, the numerical discretization and solution techniques will be briefly outlined.

Although the presented concepts are extendible to multiple components, we present a two-phase – two-component system for the sake of simplicity. This means that the only components considered are water and nitrogen (as the main component of air). In this context, we need to describe the different components (nitrogen and water with the respective superscripts N_2 , H_2O) in the wetting (subscript w) and non-wetting (subscript n) phases because we are interested in the non-equilibrium transition of components between phases, see Section 5.2 for an example in the context of evaporation. In Chapters 7 and 8 special cases of the presented systems of equations are employed, namely the cases of an immiscible system and a single-component system.

¹The mathematical description presented in this chapter is largely based on Nuske, P., Joekar-Niasar, V., and Helmig, R. (2014a). Non-equilibrium in multiphase multicomponent flow in porous media: An evaporation example. *International Journal of Heat and Mass Transfer*, 74(0):128–142

3.1 Non-Equilibrium Mass Conservation

Following the discussion in Section 2.3.3, we will present a mathematical model capable of describing local chemical non-equilibrium. In this context, this amounts to the components in the different phases of the same REV not necessarily being connected via equilibrium relations. As the knowledge about the composition of one phase does therefore not allow direct calculation of the composition of the other phase, we need to balance each component *in each phase*. Similar to the standard set of balance equations (Helmig, 1997) there is a storage term, a flux term and a source term. Each of these terms has to be given for each component in each phase, leading to four balance equations for the case of a two-phase two-component system. This approach builds on the work presented in Ahrenholz et al. (2011) with a refined mass exchange term. The described concept amounts to the following set of equations:

3.1 Non-Equilibrium Mass Conservation

$$\begin{aligned} \frac{\partial (\phi S_w \rho_w x_w^{H_2O})}{\partial t} + \nabla \cdot (\rho_w x_w^{H_2O} \mathbf{v}_w + \mathbf{j}_w^{H_2O}) &= q_w^{H_2O} \\ &\underbrace{- \rho_n f_m \text{Sh}(\text{Re}, \text{Sc}) a_{wn} \frac{D_n^{H_2O}}{L} (x_n^{H_2O} - x_n^{H_2O})}_{-\dot{n}_{wn \rightarrow n}^{H_2O}} \end{aligned} \quad (3.1a)$$

$$\begin{aligned} \frac{\partial (\phi S_w \rho_w x_w^{N_2})}{\partial t} + \nabla \cdot (\rho_w x_w^{N_2} \mathbf{v}_w + \mathbf{j}_w^{N_2}) &= q_w^{N_2} \\ &\underbrace{+ \rho_w f_m \text{Sh}(\text{Re}, \text{Sc}) a_{wn} \frac{D_w^{N_2}}{L} (x_w^{N_2} - x_w^{N_2})}_{\dot{n}_{wn \rightarrow w}^{N_2}} \end{aligned} \quad (3.1b)$$

$$\begin{aligned} \frac{\partial (\phi S_n \rho_n x_n^{H_2O})}{\partial t} + \nabla \cdot (\rho_n x_n^{H_2O} \mathbf{v}_n + \mathbf{j}_n^{H_2O}) &= q_n^{H_2O} \\ &\underbrace{+ \rho_n f_m \text{Sh}(\text{Re}, \text{Sc}) a_{wn} \frac{D_n^{H_2O}}{L} (x_n^{H_2O} - x_n^{H_2O})}_{\dot{n}_{wn \rightarrow n}^{H_2O}} \end{aligned} \quad (3.1c)$$

$$\begin{aligned} \frac{\partial (\phi S_n \rho_n x_n^{N_2})}{\partial t} + \nabla \cdot (\rho_n x_n^{N_2} \mathbf{v}_n + \mathbf{j}_n^{N_2}) &= q_n^{N_2} \\ &\underbrace{- \rho_w f_m \text{Sh}(\text{Re}, \text{Sc}) \frac{D_w^{N_2}}{L} a_{wn} (x_w^{N_2} - x_w^{N_2})}_{-\dot{n}_{wn \rightarrow w}^{N_2}} \end{aligned} \quad (3.1d)$$

$$\text{with: } p_n - p_w = p_c(S_w) , \quad (3.1e)$$

$$a_{wn} = a_{wn}(S_w, p_c) . \quad (3.1f)$$

3 Mathematical & Numerical Model

The storage terms represent the change of a component's mass for a given point. The flux terms have two contributions: an advective and a diffusive part. There are also two contributions to the source terms. Either from an external source (injection / reaction) or from exchange between the phases.

As explained above, any system strives towards full equilibrium. The underlying assumption in this context is that, conceptually, *on the fluid-fluid interface*, the mole fractions exist according to local chemical equilibrium ($x_{\alpha}^{\kappa \text{equil}}$), see Figure 2.10. The actual mole fractions (x_{α}^{κ}) on the other hand, are independent variables. They are not necessarily defined by equilibrium relations but are in principle free to assume any value. Driven by the difference in actual mole fraction and equilibrium mole fraction, exchange between the residing phases will take place approaching equilibrium.

This means that there will be mass transfer from the interface towards the bulk phase until the equilibrium mole fraction ($x_{\alpha}^{\kappa \text{equil}}$) is reached in bulk phase, too. The equilibrium mole fractions are uniquely defined via equilibrium relations (for the case of an ideal consideration of water and nitrogen: HENRY's and RAOULT's law), phase pressures (p_{α}), phase temperature (T_{α}) and closure relations.

Constitutive relations (Equations 3.1e and 3.1f), are needed in order to close the system. In this work, the determination of such relations from experimental measurements (see Chapter 7) and pore-network modeling (see Section 5.1) will be demonstrated. The pressure difference between the phases equals capillary pressure p_c (i.e. local mechanical equilibrium is established), which is a function of S_w alone, because the system of interest is assumed to follow a primary drainage curve, i.e. there is knowledge about the history of the system, see the discussion on hysteresis in Section 2.2.2.

$\mathbf{j}_{\alpha}^{\kappa}$ is the molar diffusive flux of the κ -component in the α -phase. In this work a *Fickian* ansatz is employed

$$\mathbf{j}_{\alpha}^{\kappa} = -\varrho_{\alpha} D_{\alpha}^{\kappa} \nabla x_{\alpha}^{\kappa}. \quad (3.2)$$

In other words, the gradient in the chemical potential of a species, which drives

3.1 Non-Equilibrium Mass Conservation

Table 3.1: Dimensionless numbers for mass transfer, meaning and definition.

Symbol (Name)	Definition	Meaning	Purpose
Re (REYNOLDS)	$\frac{\mathbf{v}L}{\nu}$	$\frac{\text{inertia}}{\text{viscosity}}$	flow regime
Sc (SCHMIDT)	$\frac{\nu}{D}$	$\frac{\text{momentum diffusion}}{\text{mass diffusion}}$	fluid characterization
Sh (SHERWOOD)	$\frac{\beta L}{D}$	$\frac{\text{convective mass transfer}}{\text{diffusive mass transfer}}$	mass transfer

diffusion, is approximated by a gradient in mole fraction. The porous diffusion coefficients $D_{\alpha \text{pm}}^{\kappa}$ are calculated from the binary diffusion coefficients (D_{α}^{κ}) and tortuosity (τ) according to the model of Millington and Quirk (1960):

$$D_{\alpha \text{pm}}^{\kappa} = \tau \phi S_{\alpha} D_{\alpha}^{\kappa} \quad (3.3)$$

$$\text{with: } \tau = \frac{(\phi S_{\alpha})^{2/3}}{\phi^2} .$$

\mathbf{v}_{α} is a cross section specific velocity in a porous medium. In Section 3.3 DARCY and FORCHHEIMER velocity descriptions will be presented for its calculation.

The rightmost expression in the above system of equations approximates the rate of mass transfer of a component into a phase. A standard ansatz for describing the rate of mass transfer between the phases is chosen: The *Sherwood* number (Sh) is a function of the flow regime (*Reynolds* number, Re) and the fluid properties (*Schmidt* number, Sc). Definitions for these parameters are given in Table 3.1. In there, β is the mass transfer coefficient and $\nu = \mu/\rho$ is the kinematic viscosity defined as the ratio of dynamic viscosity and density. L is a characteristic length to the system (e.g. mean pore or grain size).

However, no Sh for the case of multiphase flow in porous media could be found in the literature. Therefore, single-phase relations for flow in porous media are used (Wakao and Kagei, 1982)

$$\text{Sh} = 2 + 1.1 \text{Sc}^{1/3} \text{Re}^{0.6} . \quad (3.4)$$

Because these dimensionless correlations do not exactly apply to the given situation,

3 Mathematical & Numerical Model

the factor f_m allows scaling of the used relation in order to study the influence of the magnitude of the mass transfer. In a second step, the results can be compared to experiments and an appropriate factor f_m for the given situation can be applied. A study investigating the influence of this scaling factor is conducted in Section 5.2.

Mass conservation with respect to transfer is ensured by a straight forward assumption. The interface is considered a lower dimensional object, i.e. it has no thickness. Therefore, what leaves one phase has to arrive in the other phase (shown by braces and mole fluxes $\dot{n}_{w \rightsquigarrow \alpha}^\kappa$ in Equations 3.1a/3.1c and 3.1b/3.1d). q_α^κ finally stands for the component κ which can be supplied to phase α via external sources and sinks.

The standard approach to mass balance of compositional multiphase flow in porous media uses the same set of balance equations with one exception: local chemical equilibrium of the individual components in the respective phases is assumed. Thus, the set of Equations 3.1a to 3.1d is simplified because equilibrium relations for the mole fractions can be employed and the mass balances of each component in the respective phases can be summed up leading to one balance equation *per component* (Helmig, 1997).

3.1.1 Phase Presence

Not all quantities presented in the mass balance equations are necessarily always defined. Nonetheless, saturation is typically taken as a primary variable. In the case of that phase not being present at a given point, it is not defined. Therefore, the standard fully implicit (see Section 3.4.1) description of miscible multiphase flow in porous media usually includes some sort of variable switching (Class et al., 2002). Depending on the presence of a phase, either saturation or mole fractions are used as primary variables. This switching of variables can lead to oscillations and bad convergence behavior.

Therefore, this work builds on non-linear constraints as formulated by Lauser et al. (2011). Essentially, the idea boils down to demanding, by additional equations, that either the saturation of a phase be zero (the phase is not present) or the mole

3.1 Non-Equilibrium Mass Conservation

fractions of that phase sum up to one (the phase is present). Mathematically, this can be formulated for each fluid phase α at each point as follows

$$S_\alpha \left(1 - \sum_{\kappa} x_\alpha^\kappa \right) = 0. \quad (3.5)$$

As a phase must be either present or not, this equation is always fulfilled and no switching between variables is necessary. Although the added equations are non-linear in nature, they do not need additional boundary conditions as they do not include flux terms.

3.1.2 Limitations of Non-Equilibrium Mass Conservation

The described model for non-equilibrium mass conservation in multiphase multi-component flow in porous media has four main limitations. The first three are unique to the non-equilibrium description while the last one is shared with the standard model.

Resistance to Transfer In the above system of equations the mass transfer quantities $\dot{n}_{wn \rightsquigarrow w}^{N_2}$ and $\dot{n}_{wn \rightsquigarrow n}^{H_2O}$ (Equations 3.1b, 3.1c) are calculated. In order to ensure mass conservation, these quantities are inserted into the remaining mass balance equations (Equations 3.1a, 3.1d).

This is a good engineering approximation; a particle that is transferred to a phase has to originate from the other phase. However, a potentially important piece of information is lost during this replacement: the resistance to transfer “on the other side of the interface”. Especially in the case of considering more components and slow transfer this can be important. In the presented case, $\dot{n}_{wn \rightsquigarrow n}^{H_2O}$ is surely bigger than $\dot{n}_{w \rightsquigarrow wn}^{H_2O}$, as diffusion in the gas phase is orders of magnitude bigger than in the liquid phase. Therefore, the presented model is an upper limit to the possible rate of kinetic mass transfer of the water component.

A possible remedy, accounting for the resistances to mass transfer in both phases, is to calculate all transfer quantities (without making replacements) and ensure

3 Mathematical & Numerical Model

mass conservation by additional balance equations for each conserved component. For the above system of equations this would amount to the additional equations

$$\dot{n}_{wn \rightsquigarrow w}^{H_2O} + \dot{n}_{wn \rightsquigarrow n}^{H_2O} = 0 \quad (3.6)$$

$$\dot{n}_{wn \rightsquigarrow w}^{N_2} + \dot{n}_{wn \rightsquigarrow n}^{N_2} = 0 \quad (3.7)$$

Boiling Conditions When the boiling temperature of a pure phase is reached, the mole fraction of the respective component in the gas phase is exactly one (see Equation 2.17). Although this is correct, it leads to a situation, where no more mass can be transferred according to the presented mass transfer concept even if there is liquid phase present. The actual and the equilibrium mole fraction remain identically one, even if more energy is added. As a consequence, temperatures can rise above the boiling temperature with liquid phase present, which is unphysical.

This behavior is a limitation of the chosen mass transfer approximation. It can be circumvented, by employing the true driving force behind mass transfer which is a gradient in chemical potential. With a proper description of a component's chemical potential, mass transfer would continue until equal potentials are reached or a phase is depleted.

Condensation The current description of mass-transfer focuses on the exchange between the bulk phases. Mass is exchanged via the common wetting – non-wetting interface. However, during condensation, mass could also be transferred towards the solid – non-wetting interface.

This mechanism can be especially important in a very dry hydrophilic porous medium, see Berning et al. (2010) who employ a concept from Nam and Kaviany (2003) in the scope of water management in fuel cells.

However, in the scope of this work, we focus on intermediate saturation ranges and evaporation. Therefore, no dedicated condensation model is employed.

Super Critical State This limitation is shared with the standard description of multiphase multicomponent flow in porous media. If the main component of the liquid phase in a gas-liquid system reaches its critical point, the distinction between liquid and gas phase ceases to be possible. Therefore, all descriptions which build on relating mole fractions in liquid and gas phases (i.e. standard and non-equilibrium) are not applicable any more.

A possible solution could be based on a variable switch based on pressure and temperature conditions.

3.2 Non-Equilibrium Energy Conservation

Following the explanations of Section 2.3.2, the possibility to capture local thermal non-equilibrium is given by allowing individual temperatures in all phases in the same REV. Therefore, each phase is attributed an individual energy balance. The caloric state variables internal energy (u_α) and enthalpy (h_α) are defined by the contributions of the components in the (ideal) mixture of a phase.

The formulation of energy balance equations for the individual phases follows a similar train of thought than the balance equations for the components in the respective phases: The phases do not have the same temperature, exchange between the phases is described via a standard heat transfer ansatz. Similar to the mass balance equations presented above, we build on the work of Ahrenholz et al. (2011).

Again, we have a storage, a flux and a source term. The flux terms have three contributions: the advective and the diffusive contribution move energy associated with the moved mass. However, the transported quantity is different from the stored quantity. Because we also need to make room for the transported internal energy, the flux quantity is enthalpy. The third flux-contribution originates from a different transport mechanism: conduction does transport energy without moving mass. The fraction occupied by a phase is taken as a first approximation to the cross-sectional area available to conduction.

3 Mathematical & Numerical Model

The source terms of the fluid phase energy balances have four contributions: Energy can either be introduced associated to a mass injection or without injecting mass, e.g. via heating. Each phase can exchange energy with the other two phases via two mechanism: due to different temperatures (conduction) or due to mass exchange and the associated energy transfer.

Energy conservation is different from mass conservation in the fact that, although the solid matrix is conceptualized as rigid, it can still take part in the energy exchange. Therefore, a third balance equation is needed for the case of two fluid phases (Equation 3.8c). In that equation, the storage term captures the change of energy via the heat capacity (c) and the change of temperature (T_s). The only flux possible in the solid phase is conduction. There are three possible source terms to the solid phase: it can either be supplied with heat from external sources or from conductive heat exchange from other phases.

The described system amounts to the following set of balance equations for three phases:

3.2 Non-Equilibrium Energy Conservation

$$\begin{aligned}
\frac{\partial (\phi \varrho_w S_w u_w)}{\partial t} + \nabla \cdot \left(\varrho_w \mathbf{v}_w h_w + \sum_{\kappa} \mathbf{j}_w^{\kappa} h_w^{\kappa} \right) - \nabla \cdot (\phi S_w \lambda_w \nabla T_w) = \\
\sum_{\kappa} h_w^{\kappa} q_w^{\kappa} + q_w^{\text{energy}} \\
+ \underbrace{f_e \text{Nu}(\text{Re}, \text{Pr}) a_{wn} \frac{\bar{\lambda}_{wn}}{L} (T_n - T_w)}_{\dot{e}_{n \rightsquigarrow w}} + \underbrace{f_e \text{Nu}(\text{Re}, \text{Pr}) a_{ws} \frac{\bar{\lambda}_{ws}}{L} (T_s - T_w)}_{\dot{e}_{s \rightsquigarrow w}} \\
+ \sum_{\kappa} \dot{n}_{wn \rightsquigarrow w}^{\kappa} h_w^{\kappa} \quad (3.8a)
\end{aligned}$$

$$\begin{aligned}
\frac{\partial (\phi \varrho_n S_n u_n)}{\partial t} + \nabla \cdot \left(\varrho_n \mathbf{v}_n h_n + \sum_{\kappa} \mathbf{j}_n^{\kappa} h_n^{\kappa} \right) - \nabla \cdot (\phi S_n \lambda_n \nabla T_n) = \\
\sum_{\kappa} h_n^{\kappa} q_n^{\kappa} + q_n^{\text{energy}} \\
- \underbrace{f_e \text{Nu}(\text{Re}, \text{Pr}) a_{wn} \frac{\bar{\lambda}_{wn}}{L} (T_n - T_w)}_{-\dot{e}_{n \rightsquigarrow w}} + \underbrace{f_e \text{Nu}(\text{Re}, \text{Pr}) a_{ns} \frac{\bar{\lambda}_{ns}}{L} (T_s - T_n)}_{\dot{e}_{s \rightsquigarrow n}} \\
+ \sum_{\kappa} \dot{n}_{wn \rightsquigarrow n}^{\kappa} h_w^{\kappa} \quad (3.8b)
\end{aligned}$$

$$\begin{aligned}
\frac{\partial ((1 - \phi) \varrho_s c T_s)}{\partial t} - \nabla \cdot ((1 - \phi) \lambda_s \nabla T_s) = q_s^{\text{energy}} \\
- \underbrace{f_e \text{Nu}(\text{Re}, \text{Pr}) a_{ws} \frac{\bar{\lambda}_{ws}}{L} (T_s - T_w)}_{-\dot{e}_{s \rightsquigarrow w}} \\
- \underbrace{f_e \text{Nu}(\text{Re}, \text{Pr}) a_{ns} \frac{\bar{\lambda}_{ns}}{L} (T_s - T_n)}_{-\dot{e}_{s \rightsquigarrow n}} \quad (3.8c)
\end{aligned}$$

Each phase can be supplied with energy by a heat flux ($q_{\alpha}^{\text{energy}}$). Additionally, the fluid phases can be supplied with energy if a component is supplied to the phase (q_{α}^{κ}).

The conductive heat transfer between the phases is captured by the expressions

3 Mathematical & Numerical Model

Table 3.2: Dimensionless numbers for heat transfer, meaning and definition.

Symbol (Name)	Definition	Meaning	Purpose
Re (REYNOLDS)	$\frac{\mathbf{v}L}{\nu}$	$\frac{\text{inertia}}{\text{viscosity}}$	flow regime
Pr (PRANDTL)	$\frac{c_p\mu}{\lambda}$	$\frac{\text{momentum diffusion}}{\text{thermal diffusivity}}$	fluid characterization
Nu (NUSSELT)	$\frac{\alpha L}{\lambda}$	$\frac{\text{convective heat transfer}}{\text{conductive heat transfer}}$	heat transfer

marked with underbraces. A well-known engineering approach is chosen: the heat transferred is equal to a dimensionless number times the (volume-averaged) cross-sectional area (a_{wn}, a_{ws}, a_{ns}) available to the heat flux, times the averaged heat conductivity times the driving temperature difference between the respective phases divided by a characteristic length of the system, L . The concept of differing temperatures at the same point was introduced in Figure 2.9. In detail, a_{wn} stands for the volume-averaged interfacial area between wetting and non-wetting phase, a_{ws} stands for the volume-averaged interfacial area between the wetting and solid phase and a_{ns} stands for the volume-averaged interfacial area between the non-wetting and solid phase, see Figures 2.7 and 2.8. In Sections 5.1 and 7.3 constitutive relations between the above quantities and saturation and capillary pressure are developed from pore-network modeling and experimental measurements, respectively.

The dimensionless number for the case of heat transfer is the *Nusselt* number which is a function of the flow regime – Re – and the fluid-specific *Prandtl* number – Pr, see Table 3.2. In there, c_p stands for heat capacity at constant pressure, α is the heat transfer coefficient.

However, in the setting of compositional flow, there is one more mechanism for the transfer of energy from one phase to another. Each particle entering a phase carries the enthalpy it had in the originating phase. This mechanism is captured by the last term on the right-hand side in Equation 3.8a and 3.8b.

Of course, the enthalpies of a component differ with respect to the phase it resides in: there is the latent heat of vaporization / enthalpy of vaporization. This enters the balance equations in the following way: a component brings the enthalpy it had before transfer from the other phase. After transfer, it is accounted for in the

3.2 Non-Equilibrium Energy Conservation

storage term of the new phase, with the enthalpy of the phase it newly belongs to. In order for the energy balance to be fulfilled, the temperature has to adopt, i.e. it has to drop for vaporization and rise for condensation.

The fact that the interfaces are conceptualized as sharp interfaces means that they cannot store energy. Therefore, the amount of energy leaving one phase has to equal the amount of energy entering another phase. This has already been included in the equations, by the braces showing the individual energy fluxes \dot{e} .

Similar to the case of mass transfer, no Nu correlations for the case of multiphase flow in porous media could be found in the literature. Again, single-phase relations are employed (Wakao and Kagei, 1982)

$$Nu = 2 + 1.1Pr^{1/3}Re^{0.6}, \quad (3.9)$$

and a scaling factor f_e is assigned, allowing the study of the influence of the heat transfer on evaporation. In Section 5.2, a detailed investigation of this scaling factor's influence is conducted. Ultimately, f_e needs to be determined experimentally. A first approximation is established in Chapter 7 by calibrating the presented macro-scale model to experimental observations.

Although the system of Equations 3.8a - 3.8c looks quite daunting, it can be reduced easily to the standard energy balance applied in multiphase non-isothermal flow in porous media (e.g. Class et al., 2002). Assuming local thermal equilibrium of the phases leads to $T_w = T_n = T_s = T$. This allows to sum up the three equations with the right-hand side terms canceling one another and leading to one energy balance equation.

Formulating individual energy equations for the respective phases (Equations 3.8a-3.8c) makes it possible to describe the processes of energy transfer between the phases and the “path to equilibration”. In this context this means that e.g. the influence of the resistance to energy transfer on evaporation rates can be studied (see Section 5.2), the process of equilibration between a hot invading and a cold residing phase can be described (see Chapter 7) or the influence of energy transfer can be studied if an energy source is restricted to an individual phase (see Chapter 8).

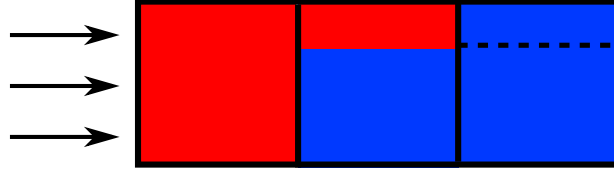


Figure 3.1: Schematic sketch of an invasions process.

3.2.1 Limitations of Non-Equilibrium Energy Conservation

Resistance to Transfer As explained for the case of the local chemical non-equilibrium mass conservation equations, energy conservation is forced by calculating transfer fluxes into one phase and inserting that quantity into the balance equation for the respective other phase. This neglects the fact that resistance to energy transfer is potentially different for the involved phases. The error made in the context of energy conservation is probably smaller compared to the respective error in the case of mass conservation: Thermal conductivities typically do not vary as strongly as diffusion coefficients e.g. between gas and liquid. A similar procedure as suggested for mass conservation is possible if both resistances are to be captured. All transferred quantities have to be calculated and additional balance equations have to be fulfilled

$$\dot{e}_{w \rightsquigarrow n} + \dot{e}_{n \rightsquigarrow w} = 0 \quad (3.10)$$

$$\dot{e}_{w \rightsquigarrow s} + \dot{e}_{s \rightsquigarrow w} = 0 \quad (3.11)$$

$$\dot{e}_{n \rightsquigarrow s} + \dot{e}_{s \rightsquigarrow n} = 0. \quad (3.12)$$

Capturing Volume Changing Work with Phase Specific Energy Balances The second limitation is probably of less importance, however so far no solution was found. Figure 3.1 schematically depicts an invasion process. Some fraction of the middle cell has just been invaded by the red phase, while blue phase has left to the right cell.

As mentioned before, in an energy balance for fluid flow, the transported quantity is enthalpy while the stored quantity is internal energy. Equations 3.8a-3.8c formulate energy conservation *phase specifically*. In the depicted setup, this leads to a situation

where “red” enthalpy has entered the middle cell, but only “red” internal energy is stored. The difference (volume changing work) has left with the blue phase. In order for the energy conservation to be fulfilled, this must lead to a temperature peak in the red phase at the invasion front: The energy of the volume changing work has to be conserved and goes into a temperature rise. However, this is only observable for fine grids (see Section 3.4.2 for a discussion of the applied spatial discretization techniques) with sharp invasion front. A possible circumvention is to neglect volume changing work. In the standard description of energy conservation in multiphase flow in porous media this behavior does not occur, because the enthalpy fluxes are summed up.

3.3 Momentum Description in Multiphase Flow in Porous Media

On the macro scale, the flow of fluid phases within a porous medium is commonly described by *Darcy’s law*. Darcy (1856) observed that the volumetric water flux through a fully water saturated column filled with sand linearly depends on the applied pressure gradient.

DARCY was concerned with single-phase (or saturated) flow conditions. Such situations occur in a number of relevant settings: In groundwater flow DARCY’s law is the well-established standard for describing fluid flow in porous media (Freeze and Cherry, 1979). However, it has also been successfully applied to different other fields, such as technical filtration processes (Rushton et al., 2000) or flow in biological tissue (Støverud et al., 2012).

Beyond the original scope of application, DARCY’s law has been empirically extended to the so-called “extended DARCY’s law” in order to describe multiphase flow (e.g. Helmig, 1997; Class et al., 2002)

$$\mathbf{v}_\alpha = -\mathbf{K} \frac{k_{r\alpha}}{\mu_\alpha} (\nabla p_\alpha - \rho_\alpha \mathbf{g}) . \quad (3.13)$$

3 Mathematical & Numerical Model

Here, \mathbf{g} is the vector of gravity. \mathbf{v} is a cross-sectional-area specific velocity, known as *Darcy velocity*. In other disciplines it is known as superficial velocity.

With more than one fluid phase present in a porous medium, the non-linearity of the system is drastically increased: phase pressures differ (capillary pressure) and the presence of one phase inhibits the movement of the other phase (relative permeability). In addition, both relations are strongly non-linear functions of saturation, see Section 2.2.2.

The extended DARCY's law is established as the standard for the multiphase flow in porous media macro-scale momentum description of such diverse applications as remediation of contaminated sites, CO₂ storage and modeling of the cathode side of fuel cells (Class and Helmig, 2002; Class et al., 2009; Acosta et al., 2006). Although the theoretical foundation and correctness of the extended DARCY's law is the subject of ongoing scientific debate (e.g. Joekar-Niasar and Hassanizadeh, 2011), its application is largely justified by satisfactorily reproducing experimental data and field scale measurements.

However, DARCY's law only applies for viscous-dominated flow regimes. According to Nield and Bejan (2006) DARCY's law is only valid for REYNOLDS numbers $\lesssim 1$. Beyond that threshold, drag forces start to become important, demanding for a different relation for the description of momentum in porous media flow. For REYNOLDS numbers between 1 and 500 a non-linear extension can be applied. This was first conducted by Forchheimer (1901). However, Ward (1965) was the first to suggest that the pre-factors of the non-linear term depend on permeability and density

$$\nabla p_\alpha = \varrho_\alpha \mathbf{g} - K^{-1} \frac{\mu_\alpha}{k_{r\alpha}} \mathbf{v}_\alpha - K^{-1/2} \frac{\varrho_\alpha c_F}{\eta_{r\alpha}} \mathbf{v}_\alpha |\mathbf{v}_\alpha|. \quad (3.14)$$

The coefficient c_F is, in approximation, taken to assume a constant value of 0.55 (Nield and Bejan, 2006).

Similar to the case of DARCY's law and relative permeability, the extension to multiphase flow of the FORCHHEIMER relation has been performed by the ad-hoc introduction of a non-linear scaling factor, relative passability η_r . It is often

assumed to follow the same functional relationship as the relative permeability (Fichot et al., 2006). The multiphase FORCHHEIMER extension is used for describing relatively high velocity flow, e.g. in fractures (Wu, 2002) or during debris cooling of a damaged nuclear reactor (Schäfer and Lohnert, 2006).

The replacement of Equation 3.13 by 3.14 further increases the non-linearity of the system. Equation 3.14 cannot be solved analytically for velocity (except for one-dimensional flow). Therefore, it cannot be directly inserted into mass or energy conservation equations.

3.4 Numerical Model

The presented framework of local thermal and chemical non-equilibrium constitutes a transient problem and includes spatial derivatives. In the case of a two-phase two-component system with the phase presence determined by non-complimentary constraints, a set of seven partial differential equations along with two non-linear algebraic equations have to be solved. This cannot be accomplished by analytical methods but has to be approached numerically in space and time. Therefore, robust temporal and spatial discretization techniques are needed in order to solve the system.

3.4.1 Temporal Discretization

The above presented framework of conservation equations can be written as (Class, 2007)

$$\frac{\partial e}{\partial t} = Ae \tag{3.15}$$

with A as an operator holding coefficient functions, including the spatial derivatives, which are functions of the unknowns. In this formalism the following defines a *fully*

3 Mathematical & Numerical Model

implicit backward EULER scheme

$$\frac{e^{n+1} - e^n}{\Delta t} = A^{n+1} e^{n+1}. \quad (3.16)$$

In other words, all material parameters and constitutive relations are evaluated and all unknowns solved at the unknown time-level $n + 1$. The fully implicit scheme is used in the scope of this work.

Although resulting in big systems of linear equations, the fully implicit scheme has a number of advantages. It is unconditionally stable and therefore does not restrict time-stepping in terms of stability. In contrast to IMPES-like approaches, fully implicit schemes in combination with a Newton solver always provide converged solutions in terms of the non-linearity. Fully implicit schemes are robust and technically mature procedures which allow focusing on the physical phenomena of interest.

3.4.2 Spatial Discretization

In terms of space discretization, the box method (Huber and Helmig, 2000) is chosen in the scope of this work. The box method combines aspects of finite element and finite volume discretization. It is a vertex centered discretization scheme which assembles fluxes for local sub-domains around each node. In Figure 3.2 the principle of constructing the name-giving boxes is depicted. Weighting functions are chosen such that the residual can be assembled locally for each sub-control-volume B_i . The elements e associated with the node i each contribute a sub-control-volume B_i to the node i . Fluxes are assembled at the integration points of the sub-control-volume faces. This way, one can benefit from the local mass conservation, typical for finite volume techniques and the freedom to choose appropriate shapes of elements, typically provided by finite element techniques.

Advectively transported quantities are typically treated by a fully up-winding method, although the switch to central spatial weighting is easily feasible on the level of the problem definition in the code.

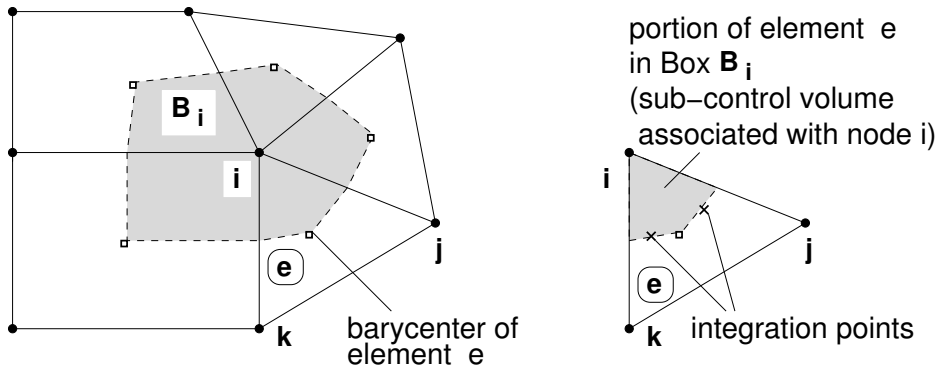


Figure 3.2: Conceptual sketch of the construction of the box method for spatial discretization (Helmig, 1997).

The discretized system of equations is highly non-linear and cannot be solved directly. A NEWTON-RAPHSON method is employed in order to solve the system. The resulting linear system of equations is solved either by the direct Super-LU solver (Li, 2005) or a preconditioned BiConjugateGradient method (van der Vorst, 1992). Depending on the convergence behavior of the NEWTON-RAPHSON method, the time step size is accordingly adjusted after each time step.

3.4.3 Numerical Framework

Building on the Distributed and Unified Numerics Environment DUNE (Bastian et al., 2008; Blatt and Bastian, 2007) the presented mathematical model is numerically solved in DuMu^x (Flemisch et al., 2011).

DuMu^x provides a free and open source numerical framework allowing the consistent treatment of flow and transport in porous media. All parts of the `dumux-stable` module are published under a GNU General Public License (GPL, Free Software Foundation, 1991). Source code as well as integrated documentation are readily available². This is not only motivated by the idea that (publically funded) knowledge belongs to society but also by the concrete possibility to facilitate collaboration and scientific exchange. The possibility for third parties to reproduce scientific results as well as to benefit and learn from developed algorithms (and the little but important

²<http://www.dumux.org>

Table 3.3: Accessibility of the employed source code.

application	source code
Chapter 5	<code>dumux-stable</code> , revision 11063
Chapter 7	<code>dumux-pub/Nuske-2014a</code>
Chapter 8	<code>dumux-stable</code> , revision 12744

details) is an additional advantage of free and open source software development. All development is conducted in the version control system subversion³ allowing collaborative working and documented, comprehensible improvements as well as transparent development.

To be more precise, the above system of equations was implemented as additional modules to the implicit *mpnc* model in DuMu^x. The modularized structure allowed the efficient implementation and testing of the newly developed numerical model. By means of the high degree of modularization a slim codebase and thus comparatively easy code maintenance is achieved. Additionally, modules can be easily combined: in Chapter 8, the standard mass conservation model is combined with a local thermal non-equilibrium model.

3.5 Sustainability and Code Accessibility

DuMu^x strives to conform to sustainable software development principles. A first step in this direction was the implementation of a continuous testing framework. This is a crucial tool for making sure that models do not break and results are not altered e.g. by seemingly unrelated changes to the code-base.

As two models presented in this work were newly developed, their test applications are simply the applications described in the respective chapters. They can be accessed as part of the freely available `dumux-stable` repository and the respective revision numbers, given in Table 3.3.

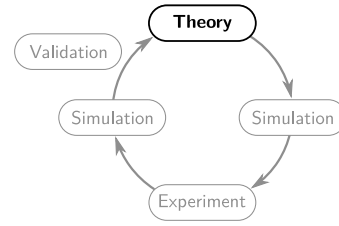
³subversion.apache.org/

However, `dumux-stable` itself is meant to be an as small as possible code-base. For each model, there is exactly one test application included. The work presented in Chapter 7 is the experimental application of the model introduced in this chapter and tested in Chapter 5. Therefore, new infrastructure was developed in order to make the employed DuMu^x code as well as the developed image analysis source code available to the public.

A new repository, `dumux-pub`, was implemented. Each publication, conducted with DuMu^x, can be published this way by means of a self-contained transparent archive binding to the ideas and principles of libre software (`table`). In this case, the image analysis code, raw images and the complete problem setup are included, see Table 3.3. Technically, a `table` is a DUNE module which only depends on `dumux-stable`. These `tables` are also freely published under a GPL license. This way a high degree of modularization on the one hand and transparency, testability and documentation on the other hand are achieved.

3.6 Summary

In this chapter, we explained the mathematical description of the developed non-equilibrium macro-scale model. Loosening the local chemical equilibrium assumption resulted in four balance equations for a two-phase two-component system. Loosening the local thermal equilibrium assumption led to three balance equations for two fluid phases and a solid phase. Limitations of the presented models and possible solutions were presented in each case. Subsequently, numerical tools allowing spatial and temporal discretization were briefly introduced. In an effort of sustainable and transparent software development, we explained how the used source code can be accessed. As this is considered an important aspect of simulation technology, new infrastructure was developed for this purpose.



4

Discussion of Interfacial Area Balance

In a series of publications, Hassanizadeh and Gray (e.g. 1980, 1990, 1993a,b) have suggested to include interfacial area (a_{wn}) as a state variable into a thermodynamically motivated description of multiphase flow in porous media. They show that this inclusion is thermodynamically consistent and standard description of multiphase flow in porous can be retrieved as limiting cases. The provided framework allows detailed understanding of the consequences of a given assumption. Additionally, it allows testing for the admissibility of constitutive relations by providing a rigorously derived formulation of the entropy inequality for multiphase flow in porous media.

The above mentioned work, conducted under the name *Rational Thermodynamics*, is considered fundamental and defining for the field of multiphase flow in porous media. Many researchers build on the general and clear derivations in that work.

One major expected practical outcome of the Rational Thermodynamics approach was the physically based (as opposed to heuristically) description of hysteresis in macro-scale models. It was expected, that the inclusion of interfacial area as an additional state variable would uniquely describe multiphase flow systems.

In the meantime, it has been shown (Reeves and Celia, 1996; Ahrenholz et al., 2011; Chen and Kibbey, 2006; Wildenschild et al., 2002) that the theoretically postulated dependence between interfacial area, saturation and capillary pressure exists on the micro scale and can be transferred by means of volume averaging to

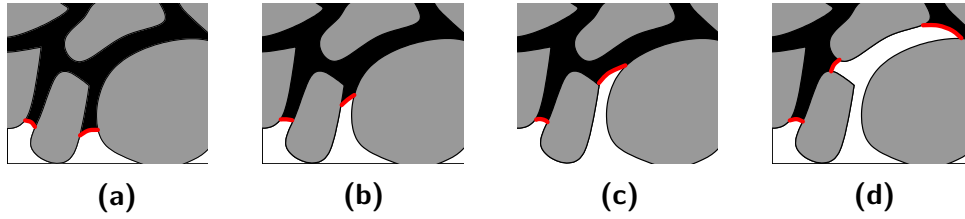


Figure 4.1: Schematic depiction of interfacial area production.

the macro scale. Building on these findings, a macro-scale model for balancing interfacial area has been suggested (Niessner and Hassanizadeh, 2008)

$$\frac{\partial a_{wn}}{\partial t} + \nabla \cdot (a_{wn} \mathbf{v}_{wn}) = E_{wn}. \quad (4.1)$$

In that equation, a_{wn} stands for the interfacial area separating wetting and non-wetting phases, \mathbf{v}_{wn} is the velocity of that interfacial area and E_{wn} is the production / destruction term of interfacial area. The driving idea is to model interfacial area on the macro scale by the presented additional balance equation and this way being able to capture hysteresis in a natural, physically motivated way.

First of all, it is important to understand the meaning of the presented terms in Equation 4.1. The right-hand side term is different from a standard source/sink term. It captures the possibility that interfaces might be produced or destroyed as depicted in Figure 4.1. It shows how the amount of interfacial area in an REV can change without the interfacial area being injected or passing borders. During the depicted invasion process, an interface moves (a to b). From b to c, the interface changes size and finally from c to d an interface splits in two. This behavior is fundamentally different from conserved quantities, like mass.

In Pop et al. (2009) an approximation for E_{wn} is suggested. However, it still uniquely relates saturation and capillary pressure. Therefore, it does not help in capturing hysteresis. In addition, the suggested approximation potentially violates the entropy inequality. In order for the E_{wn} approximation to be admissible, it would have to be shown that the difference in GIBBS energy between phases and interface needs to change sign simultaneously with the type of invasion process (imbibition / drainage) changing.

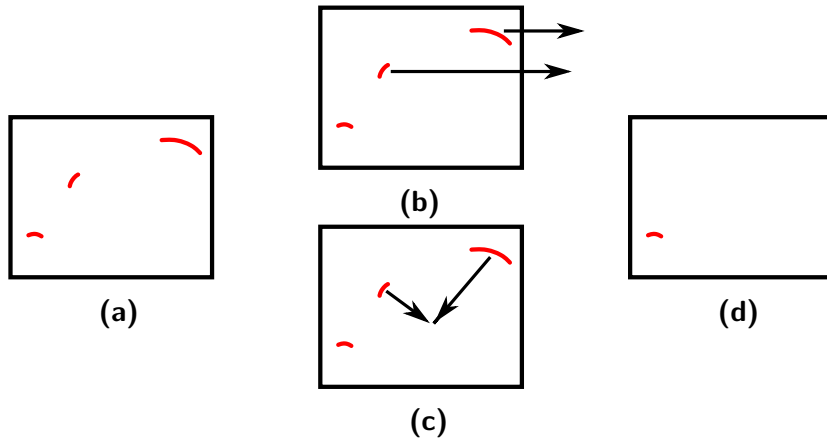


Figure 4.2: Schematic depiction of distinction between destruction and flow.

Although changes in interfacial area can be measured by pore-network modeling (Joekar-Niasar and Hassanizadeh, 2011) the differentiation between movement and production of interfacial area is tricky. Identifying the interfacial area velocity with the velocity of the center of mass of interfacial area might not be sufficient: The interfacial area that is formed by coalescence (or breakup) can change the center of mass of interfacial area without interfacial areas necessarily moving. In other words, it is not straightforward to decide whether the transition from Figure 4.2a to 4.2d happened via flow (Figure 4.2b) or destruction (Figure 4.2c).

A thought experiment (Figure 4.3) reveals another problem with the concept of equating interfacial area (red) velocity with the velocity of the center of mass of interfacial area: A straight, long pipe that is consecutively invaded by wetting (black) and non-wetting (white) phase has moving interfaces at the velocity of the bulk phases. The center of mass of interfacial area, however, is not moving.

In summary, it can be concluded that the Rational Thermodynamics approach has many merits especially in providing foundations and rigorous descriptions. The inclusion of an interfacial area balance on the macro scale is desirable and the

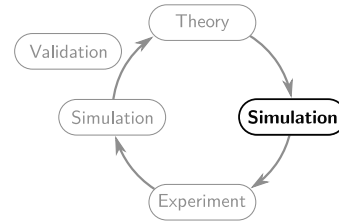


Figure 4.3: Thought experiment with interfacial velocity and non-moving center of mass of interfacial area.

4 Discussion of Interfacial Area Balance

physically based description of hysteresis would constitute substantial progress to the field. At the current state, however, the empirical approaches introduced in Section 2.2.2 have to be kept in service if hysteresis is to be described.

This work focusses on the description of local thermal and chemical non-equilibrium and the associated energy and mass transfer. For this, interfacial areas can be a limiting factor and are therefore explicitly included in the description of the transfer processes. For reasons explained above, they have to be obtained from constitute relations for the time being.



5

Non-Equilibrium: An Evaporation Example⁴

In this chapter, we use the previously developed macro-scale non-equilibrium model in order to simulate evaporation from a porous medium. Interfacial areas as well as capillary pressure – saturation relations are obtained from a pore-network model, presented in the first part of this chapter. We discuss the development and fitting of appropriate model functions and use the resulting constitutive relations as input for the macro-scale model. Eventually, the results of the macro-scale model, as a function of varying the scaling factors of heat and mass transfer, are discussed.

5.1 Generation of Constitutive Relations

One benefit of the presented kinetic model is its capability to capture the physics of heat and mass transfer across interfaces in multiphase flow in porous media. However, this capability stands or falls with the choice of appropriate constitutive relations. Namely the volume-averaged interfacial areas between the fluid phases (a_{wn}) and volume-averaged interfacial area between the non-wetting phase and the solid phase (a_{ns}) arise as new variables. The volume-averaged interfacial area

⁴The results presented in this chapter are published in Nuske, P., Joekar-Niasar, V., and Helmig, R. (2014a). Non-equilibrium in multiphase multicomponent flow in porous media: An evaporation example. *International Journal of Heat and Mass Transfer*, 74(0):128–142

5 Non-Equilibrium: An Evaporation Example

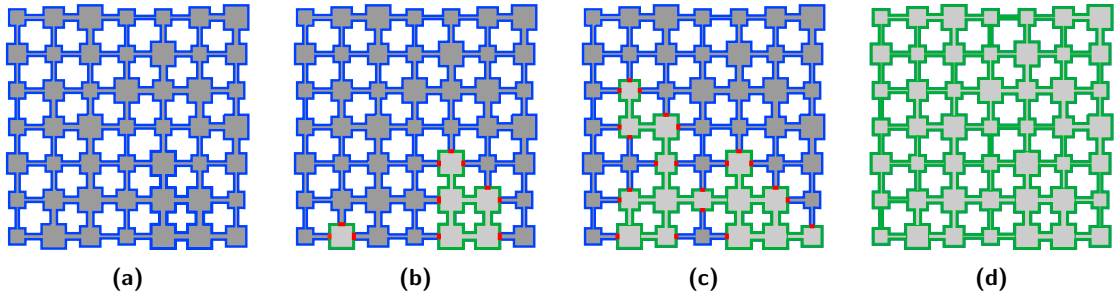


Figure 5.1: Principle of the used pore-network model. Depicted are four different pressure states as well as the interfacial areas between the fluid phases (red), non-wetting phase and solid phase (green) and wetting phase and solid phase (blue). The wetting phase is depicted in dark gray and the non-wetting phase is depicted in light gray.

between the wetting and solid phases (a_{ws}) can be obtained as the difference of the constant volume specific solid surface (a_s) and a_{ns} . Furthermore, the model needs capillary pressure as a function of saturation as input.

We employ a pore-network model in order to generate the required constitutive relations. From a “non-equilibrium” point of view, pore-network models can take equilibrium assumptions at the pore level into account (for example the validity of the YOUNG-LAPLACE equation for capillary pressure or the validity of equilibrium sorption in a single pore). As a consequence of upscaling to the network scale, they show non-equilibrium effects (for example, non-equilibrium capillary pressure, non-equilibrium relative permeabilities, or non-equilibrium sorption on the macro scale). In that sense, they indirectly support the approach of a non-equilibrium macro-scale approach. However, the pore-network presented in this chapter is used merely in order to generate constitutive relations for the macro-scale model. The following papers can be referred to for more information: Joekar-Niasar et al. (2010); Joekar-Niasar and Hassanizadeh (2011); Joekar-Niasar et al. (2012).

The challenge in this context is that interfacial areas between the fluid phases as well as the fluid phases and the solid phase are needed. So far, pore-network models have not been used to generate a_{ns} -data and an existing model had to be extended for providing this data. By employing a pore-network model, different constitutive relations representing different porous media can be obtained. The beauty of the method is that it only needs a pore size distribution and a set of rules

Table 5.1: Medium sand properties taken from Stingaciu et al. (2010).

μ_g (μm)	μ_p (μm)	σ_p (μm)	α ($1/\text{m}$)	n (-)
180 – 720	138	90	$3.3 \cdot 10^{-4}$	5.4

as input parameters. This is the motivation for briefly presenting the employed pore-network model in the following section. Afterwards we show the resulting input relations applied to the macro-scale model.

5.1.1 Pore-Network Model

The three dimensional, quasi-static pore-network of Joekar-Niasar et al. (2008) is extended by one capability: the determination of the interfacial area between solid surface and a fluid phase. Roughly, the pore-network model works as follows: First, the whole domain is filled with wetting phase: Figure 5.1a. Then, the pressure on one boundary of the domain is raised until the entry pressure of a pore is overcome: Figure 5.1b. Saturation, pressure difference (capillary pressure) and interfacial areas are recorded. Subsequently this step is repeated (Figure 5.1c) until the whole model domain is filled with non-wetting phase: primary drainage is complete (Figure 5.1d). Afterwards, the pressure on the boundary is lowered step by step, again recording the respective values until the pressure difference is back to zero: primary imbibition is complete.

It has to be kept in mind that the applied model is quasi static in nature. This means that not the flow process itself is captured but stable configurations of the phases are determined by rules. For detailed information please refer to Joekar-Niasar et al. (2008).

The input data for the pore-network model (pore body distribution information) is taken from Stingaciu et al. (2010), see Table 5.1. In there, μ_g stands for the grain size μ_p stands for the mean of the measured pore size distribution, σ_p stands for its standard deviation and α, n are the given parameters of a fitting van Genuchten (1980) function.

5 Non-Equilibrium: An Evaporation Example

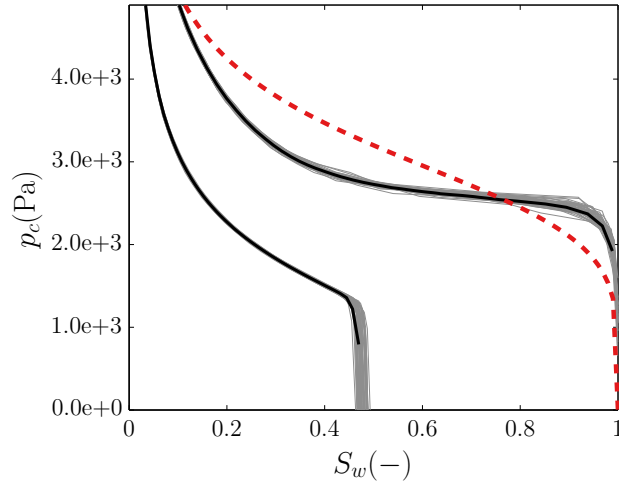


Figure 5.2: The figure depicts 42 realizations (gray) and the mean value (black) of the $p_c - S_w$ data generated by the pore-network model. The measured value of (Stingaciu et al., 2010) is plotted in red (dashed).

By means of the information given in Table 5.1 and the assumption of a log-normal distribution of the pore body sizes, pore body distributions could be generated. In order to ensure that different realizations of the same statistical properties result in comparable results, several simulation runs were conducted. The resulting $p_c - S_w$ primary drainage and primary imbibition data are shown in Figure 5.2. The dashed red line depicts the measured van Genuchten (1980) curve given in Stingaciu et al. (2010), the gray lines represent individual realizations and the black line their average.

The data originating from the described pore-network model generally shows a sharper transition between low and high capillary pressures. In other words, the $p_c(S_w)$ curve looks more similar to a well sorted sand. This can be explained by the structure of the input pore size distribution. The pore bodies are spatially uncorrelated and therefore it is probable that for some threshold p_c a small increase in p_c leads to drainage of large parts of the pore-network.

However, as the pore-network model was not calibrated by any means but merely the cited pore body distribution was given as an input, this is taken as good agreement. Furthermore, it can be seen that all realizations show the same principle behavior.

Figure 5.3 shows the generated $a_{wn} - S_w$ data (left) and the generated $a_{ns} - S_w$

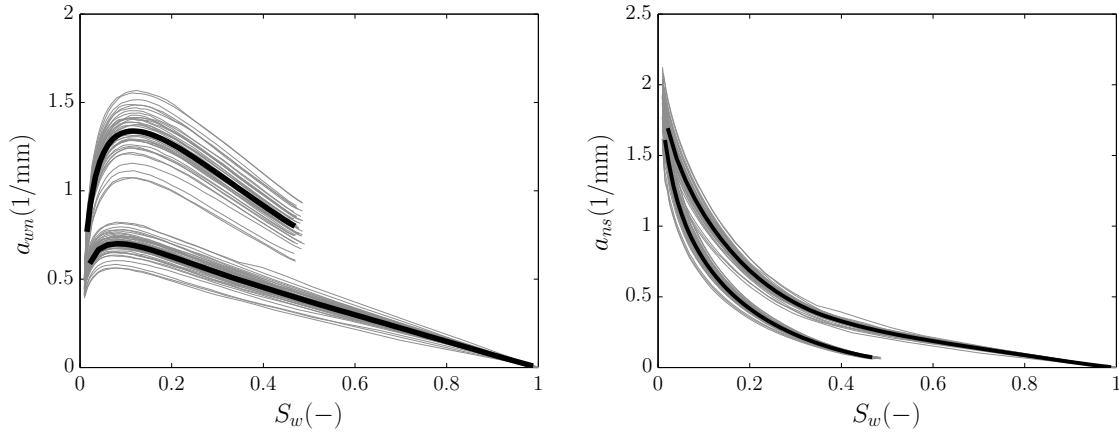


Figure 5.3: Plot of $a_{wn} - S_w$ (**left**) and $a_{ns} - S_w$ (**right**) data, 42 realizations of the pore-network results (gray) are shown. The mean value is depicted in black.

data (right) for 42 realizations of the pore-network undergoing primary drainage and primary imbibition. Again, gray lines stand for individual realizations and the black lines represent their average. Although these results scatter further, all in all this is taken as confirmation that the result of a model run is representative and one realization is chosen and used for input generation. Therefore, we show in the subsequent sections how the constitutive relations are fit to the respective data.

5.1.2 Capillary Pressure – Saturation Relation

As described in more detail in Section 5.2, the idea of this chapter is to describe the different flow domains in a mathematically as simple as possible way. Therefore, the Brooks and Corey (1964) (see Equation 2.9) model is chosen in order to relate saturation and capillary pressure. This way, the capillary pressure can easily be set to zero by setting the entry pressure, p_d , to 0 Pa in the “free flow” domain, see Section 5.2.

Table 5.2: Fit Brooks and Corey (1964) parameters for a realization of medium sand.

$p_d(\text{Pa})$	$\lambda(-)$	R^2
$2.29 \cdot 10^3$	2.74	0.99

5 Non-Equilibrium: An Evaporation Example

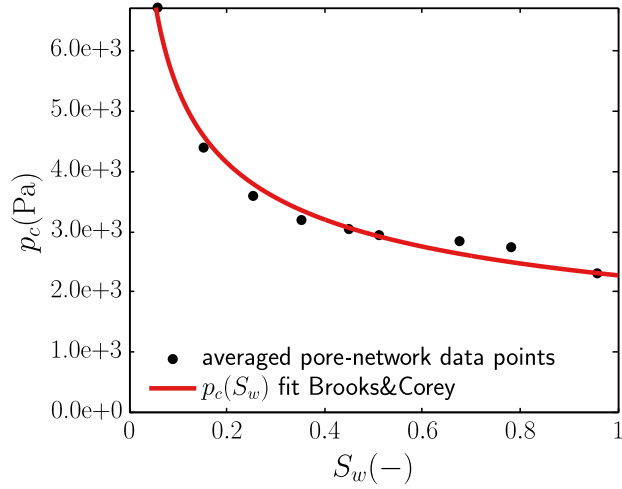


Figure 5.4: Averaged pore-network results with fit Brooks and Corey (1964) function.

In order to give each saturation range equivalent weight, the results obtained from the pore-network are first averaged. Subsequently the Brooks and Corey (1964) parameters are fit to the averaged data points by minimizing the sum of the squared distances to the model function. The averaged data points as well as the resulting fit are shown in Figure 5.4 and the corresponding parameters of Equation 2.9 are given in Table 5.2. The table also shows the coefficient of determination R^2 of the fit which would be one for a perfect fit.

5.1.3 Non-Wetting – Wetting Surface

So far, no generally accepted model function relating interfacial area, capillary pressure and saturation was established. Therefore, we felt free to design a model function that would fit the data as well as the physical constraints

$$a_{wn} = a_1(p_{c\max} - p_c)(1 - S_w) + a_2(p_{c\max} - p_c)^2(1 - S_w) + a_3(p_{c\max} - p_c)(1 - S_w)^2. \quad (5.1)$$

Equation 5.1 is chosen such that a_{wn} will always be zero for $S_w = 1$. Additionally, the equation ensures that the interfacial area is zero for the point where the maximum p_c value is reached. This choice is reasonable as it leaves more degrees of

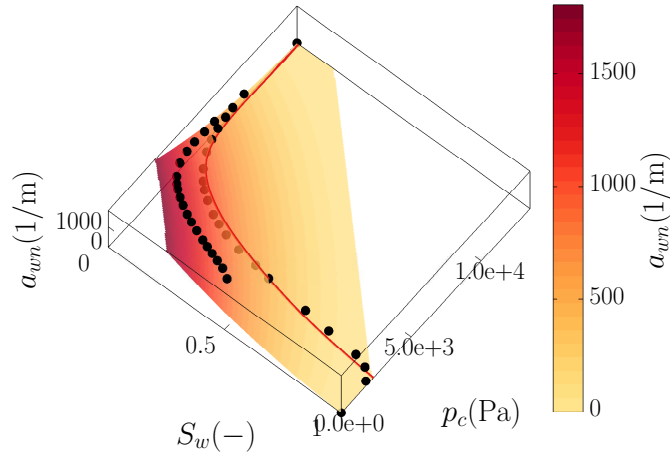


Figure 5.5: The figure shows the averaged data points obtained from the pore-network simulation as well as the resulting fit surface, see Equation 5.1. For parameters see Table 5.3. The solid (red) line is the fit (Brooks and Corey, 1964) function.

Table 5.3: Fit parameters (Equation 5.1) for a realization of medium sand.

a_1 (1/Pa m)	a_2 (1/Pa ² m)	a_3 (1/Pa m)	R^2
$-1.60 \cdot 10^{-1}$	$1.43 \cdot 10^{-5}$	$1.91 \cdot 10^{-1}$	0.91

freedom than demanding that the surface be zero for $S_w = 0$ and thus allows the description of the pore-network results by a macro-scale equation. As p_c is obtained as a function of S_w alone, it is in the end equivalent to demand that interfacial area be zero for $S_w = 0$ and that it be zero for $p_c = p_{c \max}$, because $S_w = 0$ can only be reached for $p_c = p_{c \max}$.

The maximum capillary pressure value $p_{c \max}$ is rather hard to define. Physically, one could define the maximum capillary pressure as the pressure difference for which the fluid phases start to be disconnected. However, this topological information is not available for a macro-scale model.

Here, a pragmatic approach – also chosen in DuMu^x – is followed: the capillary pressure curve is linearized at $S_w = 0.01$. This results in a maximum capillary pressure value when intersecting the ordinate. For further documentation, regarding the regularization employed in DuMu^x, we refer to the online documentation as

5 Non-Equilibrium: An Evaporation Example

well as the actual code.

Similar to the fitting of $p_c(S_w)$, the pore-network data points are averaged before Equation 5.1 is fit to it. The resulting primary drainage and primary imbibition $a_{wn} - p_c - S_w$ data points of one realization are taken. An averaging window is moved in the $p_c - S_w$ plane. All data falling in a window are represented by one averaged value, depicted as black points in Figure 5.5. Subsequently, the fitting algorithm calculated best fit a_i values. Furthermore, the fitting algorithm constrains the result such that for all data points a positive interfacial area is ensured.

Table 5.3 shows the fit coefficients as well as the coefficient of determination of the fit. Figure 5.5 shows the fit surface, averaged data points and the fit $p_c(S_w)$.

5.1.4 Non-Wetting – Solid Surface

In order to be able to describe the energy transfer not only between the fluid phases but also between the fluid phases and the solid phase, it is necessary to obtain constitutive relations describing the interfacial area between one fluid phase and the solid phase as a function of saturation and capillary pressure. The remaining interfacial area (between wetting phase and solid phase) can be determined algebraically because the total surface of the solid phase is a constant.

Here, the non-wetting phase is chosen for fitting according to

$$a_{ns} = a_1(1 - S_w) \exp(a_2 S_w) + a_3 p_c^3. \quad (5.2)$$

Equation 5.2 was chosen such that the physical constraints have to be met. In this case this means that the surface described by Equation 5.2 has to pass through $a_{ns}(S_w = 1, p_c = 0) = 0^{1/m}$ for all parameter values a_1, a_2, a_3 . The second physical constraint, $a_{ns}(S_w = 0, p_c(S_w = 0)) = a_s$ is not ensured by the structure of the fit function. However, the fit surface is for all observed cases very close to this value.

The fitting procedure is equivalent to the one described in Section 5.1.3. The resulting coefficients along with the coefficient of determination are shown in Table 5.4. The fit surface is depicted in Figure 5.6.

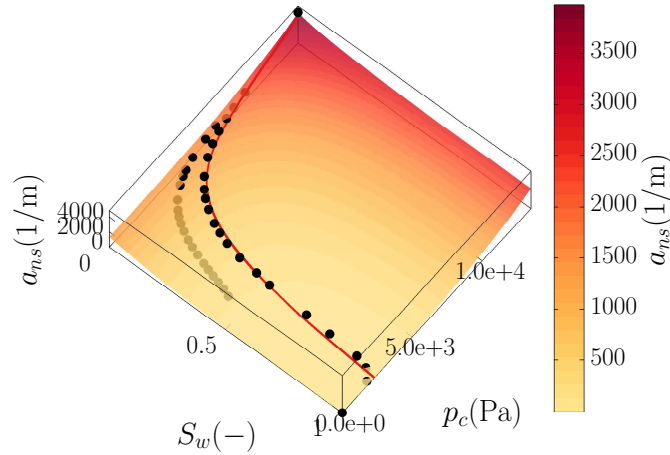


Figure 5.6: The figure shows the averaged data points obtained from the pore-network simulation as well as the fit surface, see Equation 5.2. For parameters see Table 5.4. The solid (red) line is the fit Brooks and Corey (1964) function.

Table 5.4: Fit parameters (Equation 5.2) for a realization of medium sand.

a_1 (1/m)	a_2 (-)	a_3 (1/Pa ³ m)	R^2
$1.37 \cdot 10^3$	-3.78	$1.06 \cdot 10^{-9}$	0.98

The interfacial area between the wetting phase and the solid phase is obtained by calculating the value for the non-wetting – solid interfacial area for a given saturation and capillary pressure and subtracting it from the volume-averaged total surface (a_s) of the solid phase

$$a_{ws}(S_w, p_c) = a_s - a_{ns}(S_w, p_c). \quad (5.3)$$

a_s is determined by obtaining the function value of $a_{ns}(S_w = 0, p_c(S_w = 0))$. Again, the value of $p_c(S_w = 0)$ is obtained by regularizing the Brooks and Corey (1964) function.

The presented model functions from Equations 5.2, 5.1, and 2.9 fit the data generated by the pore-network model very well. Therefore, the given parameters are taken as input for the macro-scale simulation described in the next section.

5.2 Simulating Evaporation on the Macro Scale

In this section, the macro-scale model presented in Chapter 3 with the constitutive relations developed in Section 5.1 is employed for the modeling of a simplified, academic evaporation setup. This way, we show the influence of non-equilibrium on the evaporation process. First, motivation for the setting, model setup as well as initial and boundary conditions are explained. Afterwards, simulation results and evidence for grid convergence are presented.

5.2.1 Motivation

In the case of evaporation from porous media two particularities appear that make the assumption of local thermal and chemical equilibrium questionable. First, it is quite common not to have a humidity of 100% in the atmosphere. In other words, the water component in the free-flow domain is not in chemical equilibrium.

Second, it happens that wind is blowing, in other words: flow processes in the free-flow domain can be comparatively fast due to forced convection. This could make the actual transfer processes between the phases the limiting step.

With these two effects occurring at the interface between free flow and porous medium, the setting of evaporation from porous media is an interesting system to study.

5.2.2 Setup

We want to simulate the coupled heat and mass transfer processes resulting from the evaporation of liquid water from a porous medium into a gas filled free-flow

Table 5.5: Intrinsic parameters for the “free-flow” and the porous-medium part.

	$K \text{ (m}^2\text{)}$	$\phi \text{ (-)}$
“free flow”	10^{-6}	0.99
porous medium	10^{-11}	0.4

5.2 Simulating Evaporation on the Macro Scale

domain. The gas in the free-flow domain is subject to forced convection. The focus, however, is on the non-equilibrium effects and not on the precise description of the coupling conditions as e.g. in Mosthaf et al. (2011).

Therefore, we choose the mathematically simplest possible model in order to get a first understanding of the relevance of non-equilibrium effects: The simulation domain is separated in two parts, the “quasi free flow” (denoted with “free flow” from now on) and the “porous medium”, see Figure 5.7. In the porous medium part, the generalized DARCY equation (e.g. Helmig, 1997) is used as momentum equation. Furthermore, individual mass balance equations for each component in each phase ensure mass conservation (Equations 3.1a-3.1d). Energy conservation is ensured by individual energy balances for the wetting, non-wetting and solid phase (Equations 3.8a-3.8c), see Chapter 3.

In the “free-flow” part, the same equations, with adopted parameters, are used. Of course this is not a precise description of the physical processes. Again, it has to be stressed that the presented work is a first step towards the non-equilibrium description of evaporation processes. The idea is to study the influence of the thermal and chemical non-equilibrium effects.

Besides the simplified description of momentum in the “free flow”, the second important missing mechanism is turbulence. In the case of turbulent flow the main resistance to evaporation originates from the laminar sublayer. In that layer the transport mechanism is still diffusion. However, the gradient driving the transport is drastically enhanced because outside of the sublayer the water vapor is removed by eddies (Bird et al., 2002). Therefore, turbulence in the “free-flow” domain would very efficiently move water vapor away from the porous medium – free flow interface.

In the chosen setup, the only mechanism available in order to remove vapor from the interface is diffusion, i.e. we are only considering laminar flow. This is a limitation of the presented model requiring further efforts. However, turbulence would tend to increase the amount of vapor removed from the interface and therefore increase any non-equilibrium effects. Thus, neglecting turbulence is a rather conservative approach with respect to the study of thermal and chemical non-equilibrium.

5 Non-Equilibrium: An Evaporation Example

Table 5.6: Fluid parameters.

	ρ_α (kg/m ³)	h_α (J/kg)	D_α^k (m/s)
water	Wagner et al. (2000)	Wagner et al. (2000)	Ferrell et al. (1967)
gas	ideal gas	Joback (1984)	Fuller et al. (1966)

In order to capture as much of the physical effects as possible, the following procedure is adopted: Choose the permeability and influx in the “free-flow” domain such that the resulting pressure gradients and velocities resembles the one obtained from a STOKES description of momentum (Mosthaf et al., 2011). Choose the porosity such that the “solid phase” has little influence in the “free-flow” domain. Choose the parameters for $p_c(S_w)$, $a_{wn}(S_w, p_c)$ and $a_{ns}(S_w, p_c)$ such that there is no capillary pressure and no interfacial area in the “free-flow” domain.

The parameters for the porous medium part are taken either from the fitting procedure described in Section 5.1 or taken as typical values for a medium sand, see Table 5.5. References for the fluid property relations employed are given in Tables 5.6 and 5.7.

5.2.3 Initial and Boundary Conditions

Figure 5.7 depicts the initial and boundary conditions for all conducted (two dimensional) simulations. Initial conditions amount to a fully water saturated porous medium and a gas filled “free-flow” domain.

Initially, there is atmospheric pressure. Temperatures are initially homogeneous through all phases and at 293 K in the whole domain. The chemical composition in the porous medium domain is according to chemical equilibrium as defined by

Table 5.7: Fluid parameters cont.

	μ_α (Pa s)	λ_α (W/mK)
water	Huber et al. (2009)	Huber et al. (2012)
gas	Poling et al. (2001)	Younglove (1982) (according to NIST)

5.2 Simulating Evaporation on the Macro Scale

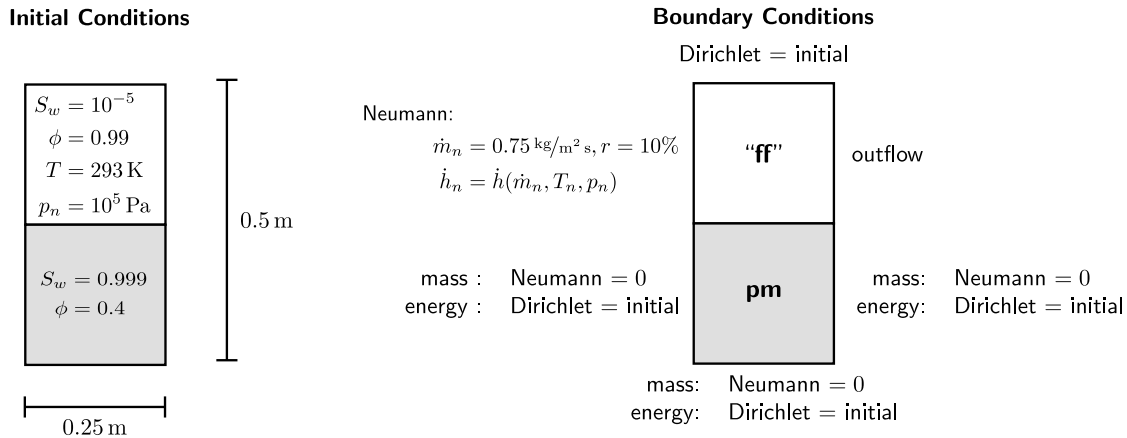


Figure 5.7: Sketch of the simulation setup.

pressure, temperature and equilibrium relations (namely HENRY’S and RAOULT’S law).

In the “free-flow” domain, the chemical composition is initially that one of the inflowing phase. The mole fraction of water in the gas phase is calculated to be 10% of the equilibrium relation. This means that there is chemical non-equilibrium in the “free-flow” domain and the inflow of dry gas continuously unbalances the system.

The boundary conditions are supposed to mimic the case of a sand box which is passed by dry air: The porous medium outer boundary is closed to mass flux by NEUMANN no-flow conditions while temperatures of all phases are fixed by DIRICHLET conditions. All primary variables are fixed by DIRICHLET conditions at the top of the “free-flow” domain. To the left there are NEUMANN conditions for mass inflow of gas. The gas phase has a relative humidity of $r = 10\%$. The heat influx is calculated according to the temperature, pressure and composition of the mass influx. To the right, outflow conditions for energy and mass let the primary variables develop in a natural way on the boundary.

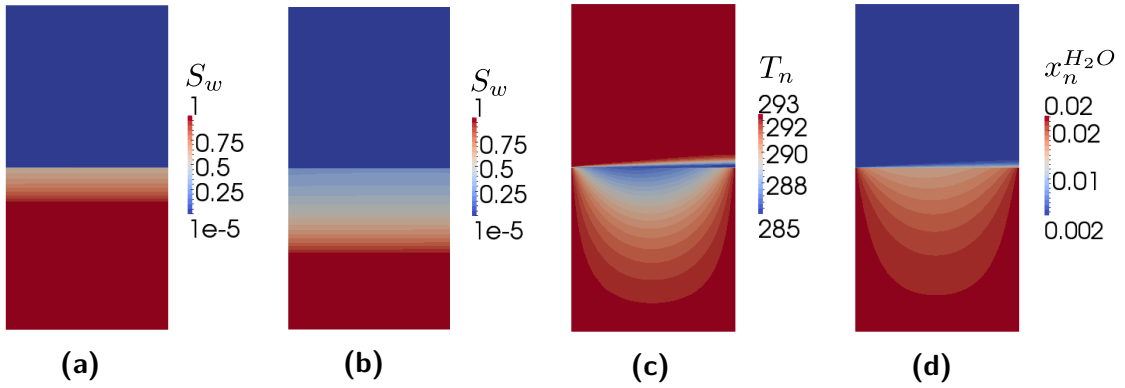


Figure 5.8: (a), (b): Water saturation after 1 d and 4 d simulated time. (c), (d): Gas temperature after 1 d and mole fraction of vapor in the gas phase after 1 d simulated time.

5.2.4 Results

In this section, we present simulation results of the above explained setup. All results in this and the next section are calculated on a 34×80 grid which is refined towards the interface (see Figure 5.13).

To give a general impression of the results, Figures 5.8a, b show the water distribution after one and four days of simulated time, the gas temperature after one day of simulated time (Figure 5.8c) and the water mole fraction in the gas phase after one day of simulated time (Figure 5.8d).

It can be seen how the drying front moves through the system, while water evaporates from the porous domain. The water evaporates because the inflowing gas is less than fully saturated leading to mass transfer from the liquid to the gas phase (see source term of Equation 3.1c). This mass transfer is accompanied by an evaporative cooling effect (heat of vaporization) leading to lower gas phase temperatures.

It has to be kept in mind that in the “free-flow” domain single-phase conditions prevail. Therefore, all non-equilibrium effects are confined to the porous medium part. Heat and mass transfer between “free-flow” and porous-medium domain take place exclusively via conduction and diffusion.

Influence on Evaporated Water

In this section, the influence of heat and mass transfer on the evaporated water from the porous medium is studied. Figure 5.9 shows the temporal development of the remaining liquid water in the domain. The porous medium boundaries are closed to mass flowing, therefore all lost water has to be evaporated. As explained in Chapter 3, there is some uncertainty associated with the dimensionless numbers characterizing heat and mass transfer, i.e. $Nu(Re, Pr)$ and $Sh(Re, Sc)$. Therefore, we varied the scaling factor f_e in front of Nu and the scaling factor f_m in front of Sh in order to get a better understanding about the behavior of the system.

It can be observed that the two highest factors result in very similar behavior. This is due to the equilibrium situation being an upper limit to heat and mass transfer from the porous medium. Further decreasing the scaling factors results in less and less water being removed from the porous medium.

Figure 5.10 shows the influence of only varying either f_e (left) or f_m (right). It can be seen that decreasing the heat transfer leads to an increase in evaporation. This can be explained in the following way: Mass gets transferred as long as the equilibrium concentration is not reached yet. However, a water particle only brings its liquid enthalpy into the gas phase and the temperature in the gas phase has to compensate for that in order for the energy balance to be fulfilled. This way, evaporation leads to cooling of the gas phase. However, if the heat transfer between gas and water phase is poor, the water phase gets cooled less efficiently and stays warmer. A warmer water phase has a higher vapor pressure which leads to a higher equilibrium mole fraction of water in the gas phase and thus to more efficient evaporation.

Figure 5.10 shows that the main influence on evaporation originates from the mass transfer. Varying f_m leads to almost the same variations in mass loss than varying both f_m and f_e . The smaller f_m gets, the lower is the mole fraction of water in the gas phase of the porous medium and therefore less water can reach the “free-flow” domain via diffusion.

This figure also explains the chosen range of the scaling factors. It can be seen that

5 Non-Equilibrium: An Evaporation Example

f_m was varied between the two extreme cases. The smallest value of f_m does not lead to any perceivable evaporation. The two highest values of f_m , on the other hand, do not lead to a difference in the amount of evaporated water. This shows that we span the range from no transfer to chemical equilibrium.

For now, the transfer coefficient for energy f_e was varied in the same range. An outline of future work enabling us to obtain estimates of that quantity will be given in the outlook.

With the given ranges for f_m and f_e , the conclusion that has to be drawn is that chemical non-equilibrium is of higher importance than thermal non-equilibrium for this application. This does not mean that the energy conservation equation can be omitted altogether. But the main features of the system seem to be captured with a local thermal equilibrium model. However, this conclusion is subject to the range of applied transfer coefficients which has to be substantiated.

In this section, the global implications of scaling f_m and f_e were studied. In the next section, the detailed distribution of temperatures and chemical compositions on the interface are analyzed.

5.2 Simulating Evaporation on the Macro Scale

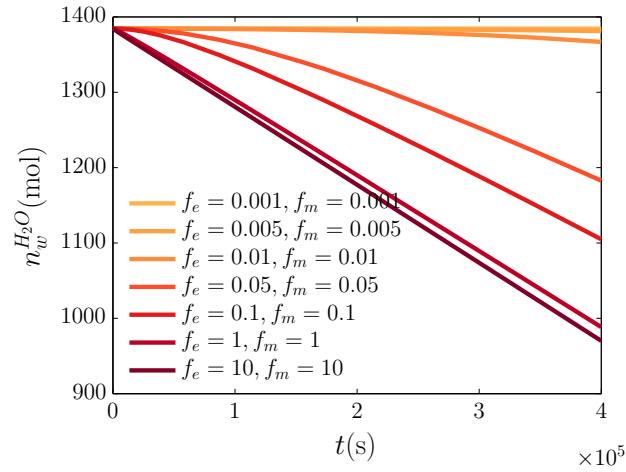


Figure 5.9: Liquid water in the porous medium over time as a function of different $f_e = f_m$.

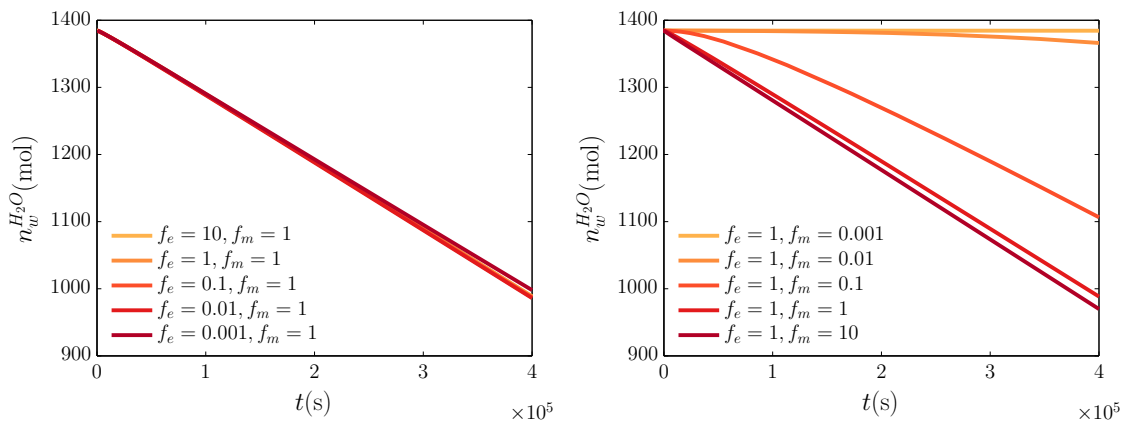


Figure 5.10: Liquid water in the porous medium over time. **Left:** Only f_e for heat transfer is varied and f_m for mass transfer is kept constant. **Right:** Only f_m for mass transfer is varied and f_e for energy transfer is kept constant.

5 Non-Equilibrium: An Evaporation Example

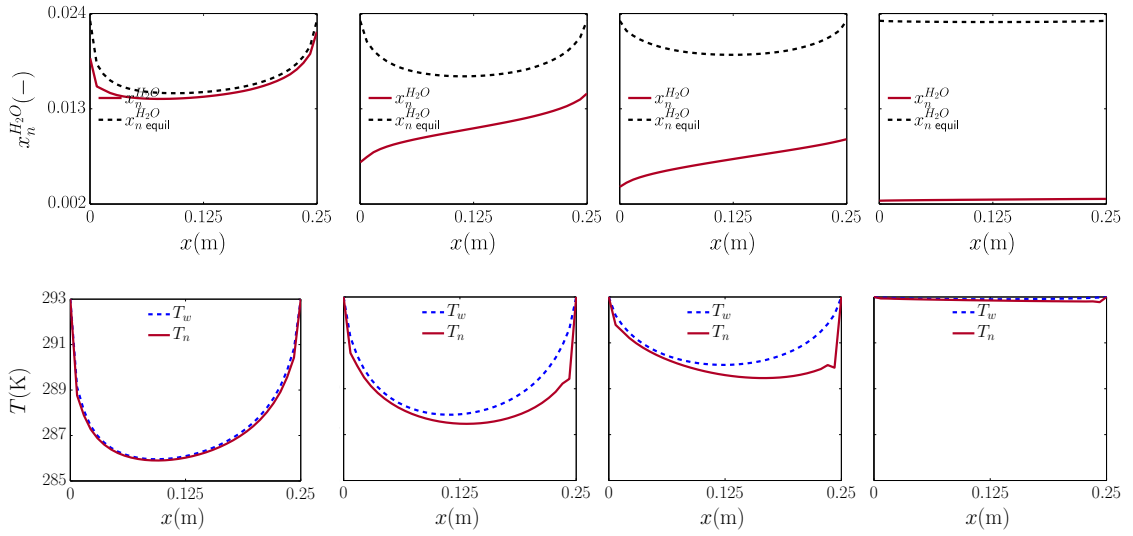


Figure 5.11: **Top:** Equilibrium (black, dashed) and actual (red, solid) mole fraction of water component in the gas phase. **Bottom:** water (blue, dashed) and gas (red, solid) temperature on the top of the porous medium. $f_e = f_m$ (from left to right): 1, 0.1, 0.05, 0.01, $t = 1$ d.

Situation on the Interface

The main achievement of the presented model is its capability to capture situations where there are locally non-equilibrium situations with respect to composition and temperature. For the given example of evaporation from a porous medium, this could happen on the top of the porous medium. Here, there is supply of dry inflowing gas as well as liquid, evaporating water as long as capillary forces can supply it.

Figure 5.11 shows in the top row the distribution of water in the gas phase on the top of the porous medium. The dashed black line shows the equilibrium mole fraction according to the given pressure and temperature. In red, the actual mole fraction of water in the gas phase is shown. From left to right the coefficients f_m, f_e decrease which leads to a more pronounced non-equilibrium situation. A coefficient of 1 (left) leads to almost immediate equilibration as soon as the gas phase enters the system. A coefficient of 0.01 (right) leads only to a very small step towards equilibration.

The bottom row of Figure 5.11 shows the distribution of the temperatures of the

5.2 Simulating Evaporation on the Macro Scale

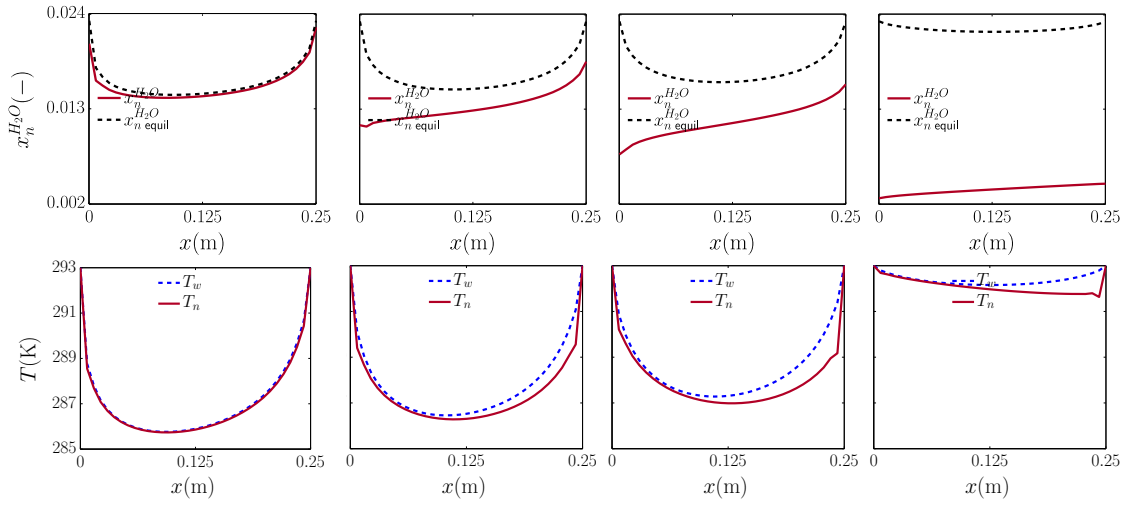


Figure 5.12: **Top:** Equilibrium (black, dashed) and actual (red, solid) mole fraction of water component in the gas phase. **Bottom:** water (blue, dashed) and gas (red, solid) temperature on the top of the porous medium. $f_e = f_m$ (from left to right): 1, 0.1, 0.05, 0.01, $t = 4$ d.

water (blue, dashed) and gas (red, solid) phase. Here, a similar trend can be recognized: the smaller the transfer the higher the temperature difference between the phases. However, for the smallest transfer coefficient, the cooling effect gets smaller (less water evaporates) and the difference between the temperatures of the fluid phases becomes smaller.

The asymmetrical shape of the temperature distributions can be explained by two competing effects. There is the continuous cooling by evaporation to the “free-flow” domain. This effect makes the temperature go down in the direction of flow. On the other hand there is heat conduction from the boundaries, where temperature is fixed. As the heat conduction in the water phase is higher than in the gas phase, the water phase is more efficient in conducting heat from the boundary. Therefore, the T_w distribution remains symmetrical with respect to the boundary.

Figure 5.12 shows the same variables as Figure 5.11, but after 4 d of simulated time. There is still liquid water in the upper part of the porous medium and the principle curve progression is equivalent. This shows clearly that the non-equilibrium effects are not an early time artifact but an inherent feature of the presented setup. However, the equilibrium situation is always enclosed in the

5 Non-Equilibrium: An Evaporation Example

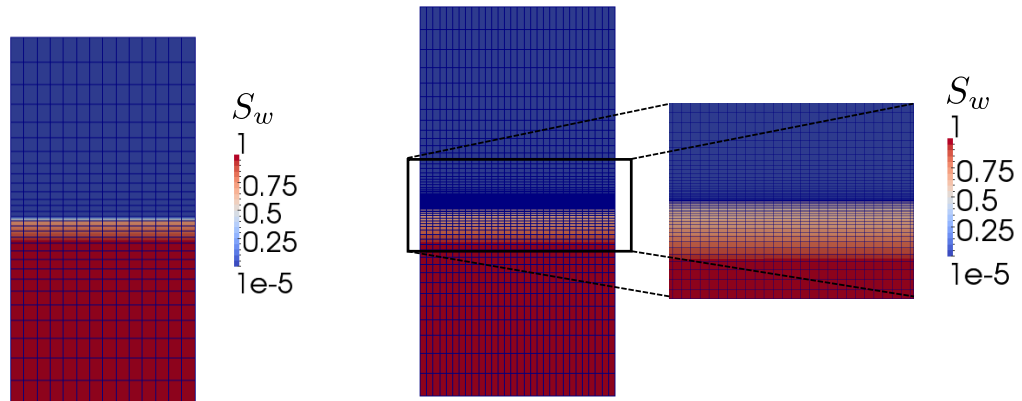


Figure 5.13: Different grids that were used in the convergence study (see Figure 5.14). The grid is gradually refined towards the interface between “free-flow” and porous-medium domain. From left to right: 14×30 grid, 30×70 grid and magnification of the interface between “free-flow” and porous-medium domain for the 30×70 grid. Depicted is the distribution of wetting phase saturation after 1 d of simulated time for $f_m = f_e = 1$.

non-equilibrium description. Using high transfer coefficients is equivalent to using a standard equilibrium model.

Now that the influence of the magnitude of heat and mass transfer on local thermal and chemical equilibrium was shown, we will briefly show evidence for the numerical convergence of the presented model.

5.2.5 Convergence

First, a convergence study is conducted, i.e. the above described model setup is run with different grid resolutions. The used grid is refined towards the interface in order to capture the important processes. Figure 5.13 shows two grids that were used in the convergence study. Even finer grids were used but could not be depicted.

As a global indicator of grid convergence, the liquid water left in the domain (i.e. not evaporated) is chosen. Figure 5.14 shows the liquid water left in the domain as a function of simulated time. Increasing grid resolution changes the result less and less. Finally, there is no visible difference between the 34×80 and the 38×90 grid.

5.2 Simulating Evaporation on the Macro Scale

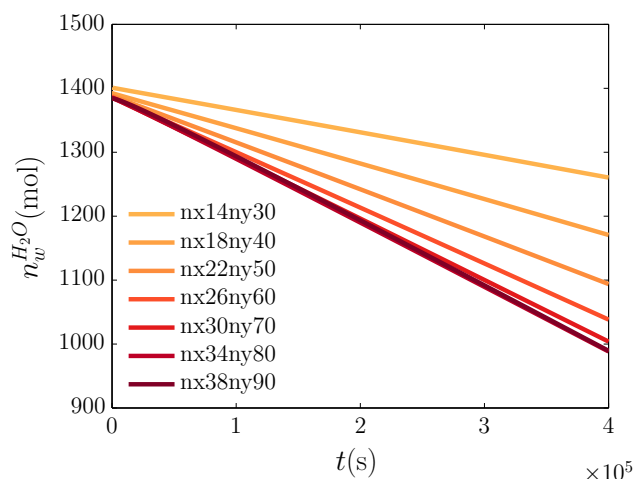


Figure 5.14: Global indicator for convergence: The liquid water left in the domain does not change for making the grid finer than 34×80 . The individual curves stand for the respective grids used.

Figure 5.14 shows some global indicator for convergence. In order to show locally that the model results are independent of the (sufficiently fine) discretization, the distribution of temperature and mole fraction as a function of grid resolution close to the interface are studied.

Figure 5.15 shows cuts through the porous domain at the interface ($x = 0.125$ m) –i.e. the middle of the domain– and the y-coordinate increasing towards the interface at $y = 0.25$ m. Although the spatial extend of the non-equilibrium situation reaches only approximately 2 mm into the porous medium domain, it can be seen that it is not a discretization artifact, as there are several elements in that region. Furthermore, it can be seen that the change in the depicted variables decrease with an increase in grid resolution up to the final grid resolution which does not result in any detectable change in the outcome any more.

5 Non-Equilibrium: An Evaporation Example

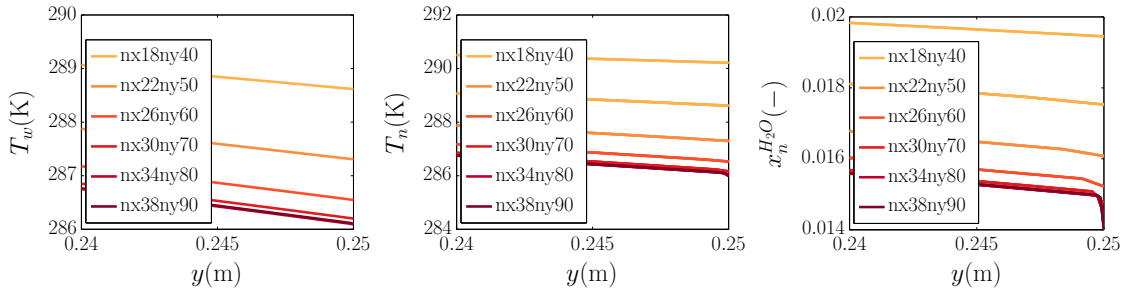


Figure 5.15: Local indicator for convergence: temperatures and mole fractions do not change any more for grids finer than 34×80 . Plots at $x = 0.125$ m, $y = 0.24 - 0.25$ m. The figures show the change of wetting phase temperature (**left**), non-wetting phase temperature (**middle**) and water vapor in the gas phase (**right**) for variable grid resolution and $f_e = f_m = 1$. The individual curves stand for the respective grids used.

5.3 Summary

In Chapter 3, a volume-averaged mathematical model for the description of multi-phase flow in porous media was developed. As opposed to standard models, this model allows locally chemical as well as thermal non-equilibrium. By these terms we mean that the different phases, present at the same point, may have different chemical potentials and temperatures. The respective balance equations exchange mass and energy via source terms.

These source terms include the crosssectional area available to transfer as a parameter. A pore-network model was extended in order to calculate the interfacial area between solid and non-wetting phase. It was shown that different realizations of the same pore-network model do result in comparable results and that the $p_c(S_w)$ was very close to the experimentally found parameters. Therefore, one realization was picked and a standard Brooks and Corey (1964) relation as well as newly developed $a_{wn}(S_w, p_c)$ and $a_{ns}(S_w, p_c)$ functions were fit with high correlation coefficients.

Using these correlations as input parameters, a macro-scale simulation of evaporation from a porous medium was conducted. This example was motivated by the fact that at the interface between free flow and porous medium high flow velocities (forced convection) and chemical non-equilibrium coincide. As a first step, extended

DARCY's law with adapted parameters was also employed in the "free-flow" domain. The parameters were chosen based on STOKES-flow simulation.

Unfortunately, no heat and mass transfer correlations for the case of multiphase flow in porous media are available. Therefore, single-phase correlations were employed and the sensitivity to simulation results were studied. For the varied ranges and setup it could be concluded that mass transfer is the limiting step and a local thermal equilibrium consideration is sufficient in order to capture the characteristics of the system. However, this could be different e.g. if the inflowing air had a different temperature than the present porous medium or if heat transfer coefficients were in different orders of magnitude.

In order to show convergence, a grid-convergence study was conducted which showed that the amount of water evaporated from the porous domain does not change any more above a certain discretization. It could also be shown that the spatial extend of thermal and chemical non-equilibrium does not change any more above some grid resolution.

5.4 Outlook

For the model to be used in a predictive sense, more experimental work is needed. Either new heat and mass transfer correlations need to be developed or the existing ones need to be calibrated to the multiphase-setting. In order to accomplish this, experimental investigations of the actual mole fractions and temperatures in the flowing phases need to be conducted.

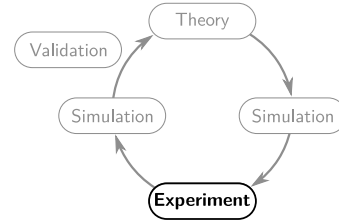
A first step in this direction is conducted in the next chapters by means of a micro-model under infrared as well as optical observation. Unlike in the work of e.g. Shahraeeni and Or (2011), this way phase specific temperature information can be gained. Detailed information about this experimental setup and simulation of that experiment are given in the following chapters.

The second important advancement of the presented model will be the incorporation of a more realistic momentum description in the free-flow domain on the one hand

5 Non-Equilibrium: An Evaporation Example

and the inclusion of a turbulence model on the other hand. In addition to that, the heterogeneity of realistic porous media needs to be incorporated in order to capture the phenomena observed in real evaporation processes.

Given that the remaining input parameters are obtained, this model can help in strengthening the confidence into the standard model and its range of applicability. If the local thermal and chemical equilibrium assumptions are violated, the presented model can give a better description of reality.



6

Estimating Transfer Coefficients: Experimental Setup, Measurements and Qualitative Results⁵

In the previous chapters, a macro-scale non-equilibrium model was developed and put to use in a parameter study, motivated by evaporation from porous media. Although parameter studies are valuable tools, functional relations ultimately have to be obtained from and tested by experiments. Therefore, we developed an experimental setup allowing the simultaneous thermal and optical observation of multiphase flow processes in a transparent micro-model. Details of the newly developed platform as well as qualitative findings are presented in this chapter.

A micro-model is an effective tool for the study of two-phase flow in a porous medium. The term usually refers to a transparent, artificial porous medium with known properties (Chang et al., 2009; Corapcioglu et al., 2009; Avraam et al., 1994; Baouab et al., 2007; Kumar Gunda et al., 2011; Zhang et al., 2011; Ferer et al., 2004; Grate et al., 2010; Gutiérrez et al., 2008; Hug et al., 2003; Huh et al., 2007; Cheng et al., 2004; Karadimitriou et al., 2012). An extensive review of micro-models used in two-phase flow studies (including fabrication, methods, materials

⁵The experimental setup and qualitative results presented in this chapter are published in Karadimitriou, N. K., Nuske, P., Kleingeld, P. J., Hassanizadeh, S. M., and Helmig, R. (2014). Simultaneous thermal and optical imaging of two-phase flow in a micro-model. *Lab Chip*, 14:2515–2524

and visualization techniques) can be found in Karadimitriou and Hassanizadeh (2012).

Up to now, micro-models have been used to study multiphase flow and transport in porous media (see e.g. Cheng et al. (2004); Karadimitriou et al. (2012); Kumar Gunda et al. (2011)) and colloid transport under two-phase conditions (see e.g. Zhang et al. (2013); Baumann and Werth (2004)). But, to the best of our knowledge, they have never been used to study heat exchange between phases. For this study, in addition to the need for imaging pore-scale temperature fields, we needed to visualize the pore-scale distribution of fluids under dynamic conditions. With the use of a novel imaging setup, thermal and optical pictures of the flow network during drainage and imbibition are taken at the same time and from the same part of the flow network. In this way, thermal and optical pictures can be correlated in time and space. Our micro-model setup makes it possible to experimentally determine phase specific temperature distributions during a dynamic process. In this chapter, we describe the setup, visualization and data processing details, present some qualitative results and explain how these results can be used in a kinetic heat transfer study.

6.1 Experimental Setup and Procedure

In this section, we explain the design and manufacturing of the employed micro-model. Afterwards, the experimental setup and procedure are described.

6.1.1 Micro-Model Design

The micro-model's flow network is based on DELAUNAY triangulation, as it has been reported to be a good approximation to a natural porous medium (Heiba et al., 1992). In DELAUNAY triangulation, first the number of points (here standing for the number of pore bodies) has to be chosen. Subsequently, the locations of the points are chosen such that each point is connected to its neighbors by non-intersecting bonds. Connected points form triangles that are as equilateral

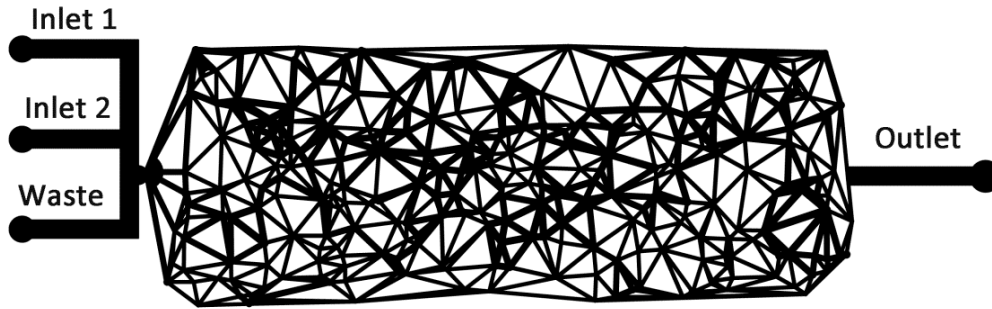


Figure 6.1: Drawing of the flow network with 300 pore bodies and 1000 pore throats, as well as channels for the introduction and removal of the fluids.

as possible. The triangulation points are considered to be the centers of the pore bodies. The connections between the triangulation points are considered as the pore throats.

We designed a flow-network with 300 pore bodies and approximately 1000 pore throats. The overall dimensions of the network are $14.4 \times 39 \text{ mm}^2$. Three channels for the introduction of the fluids, a waste line and an outlet channel were created. An image of the whole micro-model network is shown in Figure 6.1.

The pore-network has a quasi-two-dimensional nature. It comprises a two-dimensional network of pores, but each pore is a three-dimensional element, as it has depth. The pore throats have a parallelepiped shape (rectangular in both cross-section and planar view), pore bodies are cylindrical (rectangular in cross-section and circular in planar view). The coordination number, which is the average number of connections of a pore body, is 3.3 for our flow network. The sizes of pore bodies are assigned from a truncated log-normal distribution, even though, in the final design, they are strongly affected by the intersection of pore throats. The pore body sizes ranges from 340 microns to 440 microns, with a mean of 400 microns. The width of a pore throat is assigned such that it is always smaller than the diameters of two neighboring pore bodies, following a formula found in Joekar-Niasar et al. (2010). Special attention is paid to the fact that the statistical distribution of pore body sizes and pore throat sizes should overlap to some extent, as this is the case in natural porous media. All pores had a uniform depth of 100 microns.

With the use of LISP (LIST Processing), the network design is converted to an Autocad sketch. The conversion from the sketch to a mask is performed by CAD/Art Services (U.S.A.). The mask is a plastic transparency sheet on which the Autocad sketch is printed in actual dimensions, at a resolution of 1 micron/pixel . In the mask, the void space is transparent, and the solid phase was black.

With the use of the mask, optical and soft lithography are employed in order to produce the Polydimethylsiloxan (PDMS) micro-model. Then, a silanization process is used in order to make the micro-model uniformly and stably hydrophobic. The optical and soft lithography steps, as well as the bonding and silanization process, are fully described in Karadimitriou et al. (2013).

The only deviation from the procedure described in Karadimitriou et al. (2013) is as follows. A micro-model is commonly composed of two PDMS slabs, with approximately the same thickness. One slab contains the pore-network and inlet/outlet channels while the other, featureless, slab is used as a cover. This creates a closed network of pores. But, because we need to do thermal imaging with this micro-model, the cover slab has to be permissive to infrared wavelengths as well as optically transparent. More specifically, it has to be permissive to wavelengths between $7 \mu\text{m}$ and $14 \mu\text{m}$ for thermal imaging. For this purpose an infrared transmissive plastic film (KUBE Electronics, Switzerland), with a thickness of $100 \mu\text{m}$, is used as cover. This film has a high (83%) permittivity for thermal radiation.

In order to ensure uniform wettability of all pore walls and an effective bonding of the film with the other PDMS slab, the plastic film is spin-coated with PDMS, forming a very thin layer of 8 microns. In order for the spin coated PDMS to adhere to the film's surface and to be permissive to infrared radiation, the mixing ratio between the elastomer base and the curing agent is decreased from the usual 10 : 1 ratio to a ratio of 7.5 : 1. This ensures solidification of PDMS and increases its permeability to the desired wavelengths. The overall transmissivity of the covering slab is around 80% for wavelengths between $7 \mu\text{m}$ and $14 \mu\text{m}$ and close to 70% optically. In Figure 6.2, a picture of a complete micro-model is shown.

In the work of Gervais et al. (2006), the effect of liquids pressure on the deformation of shallow micro-fluidic channels is examined. Such deformation can, in turn, affect

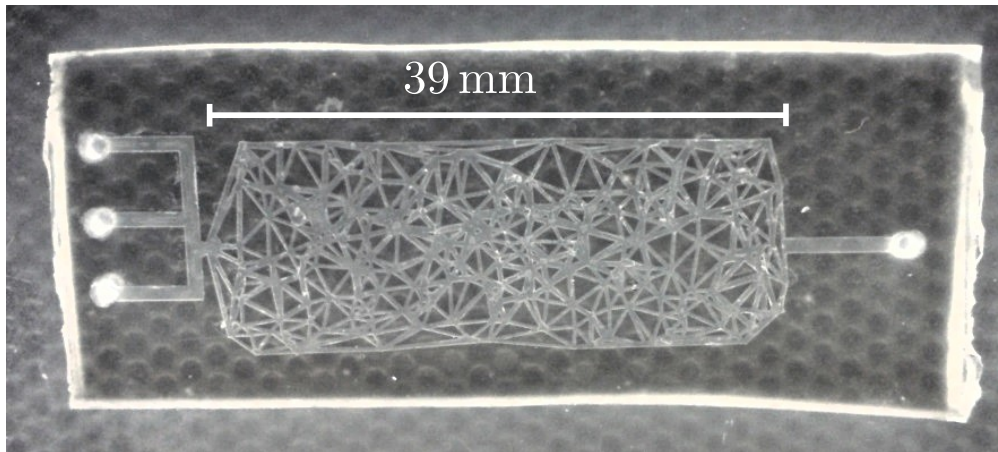


Figure 6.2: Image of the micro-model. The flow network is visible through a thin plastic covering slab, which is thermally and optically transparent.

the laminar flow profile and pressure distribution within the channels. They come up with a dimensionless number for assessing the significance of this deformation, depending on the pressure drop along a channel, its width and height and the YOUNG modulus of PDMS. Based on this dimensionless number, we determine that the deformation of PDMS in our experiments can be neglected.

6.1.2 Flow Visualization

In most micro-model studies, a microscope is used for visualization and a camera for recording images (see e.g. Cheng et al. (2004); Chang et al. (2009)). As explained above, the main objective of this work is to study thermal effects in two-phase flow by monitoring flow during transient experiments, both optically and thermally. A microscope would not offer the option of simultaneous thermal and optical monitoring at the highest possible spatial resolution.

The smallest pore size is dictated by the resolution of the thermal camera. In order to extract reliable data from the images, a feature of interest, such as a fluid-fluid interface, must be at least 10 pixels in size. The spatial resolution of the thermal camera is 30 microns per sensor pixel. This resolution is fixed, as the camera did not offer the option of a magnifying lens. This means that the actual size of a pore body has to be at least 300 microns. At the same time, it is important to keep the

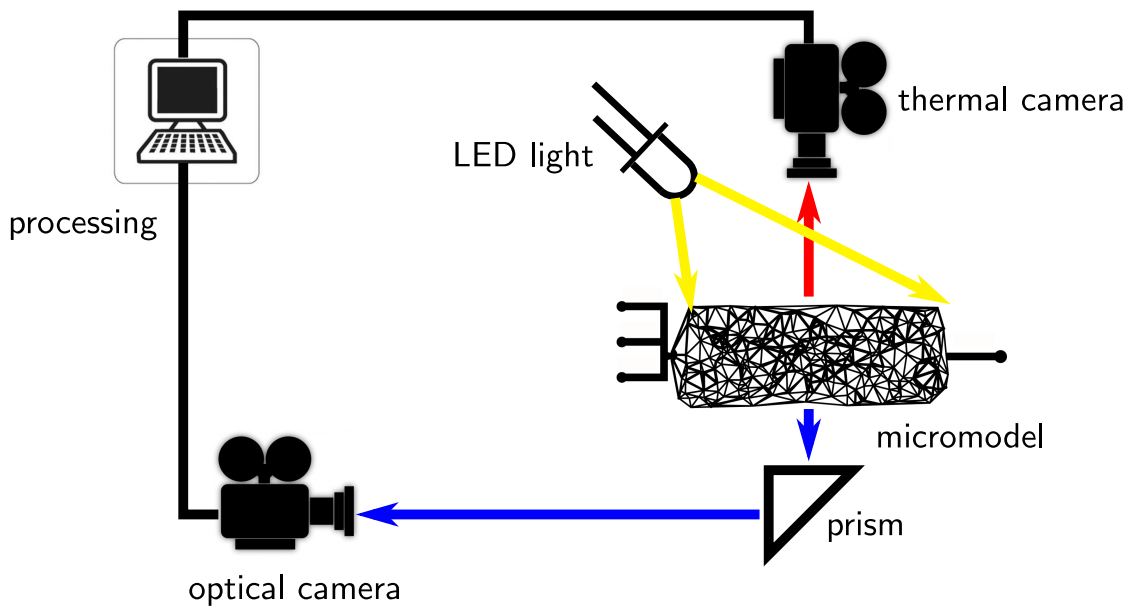


Figure 6.3: Schematic representation of the imaging setup.

pore size small enough for capillary effects to be relevant. Therefore, the mean pore size is set to 400 microns, with the smallest pore being 340 microns and the biggest being 440 microns.

The intrinsic resolution of the optical camera's sensor is 3.45 microns per pixel. If we had used the intrinsic resolution of the sensor, the area monitored by the optical camera had been much smaller than that of the thermal one. Therefore, we use a lens to reduce its resolution to 10 microns per pixel. This means that the image is shrunk in order to match the thermal camera image.

The experimental needs for simultaneous thermal and optical monitoring of flow through the micro-model, along with the restrictions of each monitoring method, led us to a new monitoring setup which is described below. This setup involves a light source, a prism, an objective lens with a long focal length, a high resolution optical camera, a camera able to take infrared pictures and a computer for data acquisition. A schematic representation of the main components is given in Figure 6.3 and a picture of the actual experimental setup is shown in Figure 6.4.

The micro-model is placed horizontally on a stage, with the side covered by the IR-transmissible film facing upwards. The thermal camera (ICI-7640P, Infrared

6.1 Experimental Setup and Procedure



Figure 6.4: The imaging setup. The image shows the optical and thermal cameras, the prism and the micro-model.

Cameras Inc.) is placed at a distance of 3 cm. For the optical imaging, an LED source, emitting at the wavelength of 570 nm, is used. The light source is chosen to be an LED one, so as to avoid any heating of the micro-model. It has to be placed under an angle at a relatively large distance from the micro-model (see Figure 6.3). This configuration is necessary due to the small focal length of the thermal camera (3 cm) which leaves little space for the light source to be put close to the sample. In order to obtain a comparative field of observation, the optical camera is placed at a distance of 38 cm from the micro-model. A prism is used to divert the light beam which passes through the micro-model and make it parallel to the optical table (see Figure 6.4).

An objective lens with a focal length of 135 mm is attached to a Prosilica GC-2450 (optical) camera for the purpose of reducing its resolution (as explained above). Both cameras are set to a constant frame rate of 10 frames per second. As explained in Section 6.2, measures are taken to ensure the synchronization of the two image streams. The cameras are connected to a computer so as to acquire and store the thermal and optical images.

6.1.3 Flow and Temperature Control

In order to exclude compressibility effects, two immiscible liquids are chosen as the two phases, namely Fluorinert (FC-43, 3M) as the wetting phase and water as the non-wetting phase.

Fluorinert is a colorless (refraction index, $n = 1.291$), fluorine based, inert liquid. It is 4.7 times more viscous ($\mu = 4.7 \cdot 10^{-3}$ Pa s) and 1.86 times heavier than water ($\rho = 1860$ kg/m³). The surface tension between water and Fluorinert is 58 mN/m. Fluorinert has an affinity towards PDMS which is additionally enhanced and stabilized by surface treatment. Therefore, Fluorinert serves as the wetting phase in our experiments.

In the first step, air is fully expelled from the micro-model by saturating it with the wetting phase. The goal of the experiment is to study the kinetic heat transfer between the two phases, i.e. we aim at temporally resolving the heat transfer process between the respective phases. Therefore, the invading phase has to reach the entrance of the flow network at the highest possible temperature, without causing a temperature rise in the surrounding area.

In order to accomplish this, the invading fluid (i.e. water) is heated by means of a two-walled counter-current heat exchanger up to the entry point of the micro-model (Inlet 2). The hot water flows from “Inlet 2” to “Waste” (see Figure 6.1) at a comparatively high flow rate (circulation flow rate). Actual invasion into the flow network is accomplished by sucking out wetting phase (Outlet). This diverts a fraction of the hot water into the flow network. The temperature of the invading phase can be controlled by the temperature and flow rate of the heat exchanger.

Inlet 1 was originally designed in order to counteract local heating by means of additionally circulating water at ambient temperature. This turned out not to be necessary in practice. These two strategies (heating up to the entry of the micro-model and bypassing of the entry of the flow-network) make sure that the highest possible temperature difference between invading and retreating phase is accomplished, without increasing the temperature of the whole micro-model.

6.1.4 Experimental Procedure

Initially, the micro-model and the resident wetting phase (i.e. Fluorinert) are at room temperature. The non-wetting phase (water) circulates, at a much higher temperature, from Inlet 2 to the waste at a high flow rate. Inflow into the flow network is initiated by withdrawing the wetting phase via the outlet, using a high precision syringe pump (Harvard Apparatus, Pump 11 Pico Plus Elite). The withdrawal rate is set to be much lower than the circulating flow rate of the non-wetting phase. In this way, only a small part of the bypassing water is diverted into the flow-network. At the end of this drainage step, the wetting phase is injected back into the flow network via the outlet channel. After this imbibition step, we perform several cycles of drainage and imbibition. During all steps, pictures were taken by the thermal and the optical camera at a rate of 10 pictures per second.

6.2 Image Processing

The acquired optical and thermal images have to be temporally and spatially correlated. This is done by the procedure described in the following sections.

6.2.1 Temporal Correlation

Temporal correlation is accomplished by holding an object, as a marker, in the monitoring frame of the two cameras, before the start of an experimental run. At a given time, this marker is removed. The first image from the two cameras where the marker is not visible is set to be the first frame of the image streams. This way, the start of the two image streams is synchronized.

Although both cameras are set to collect images at 10 frames per second, in practice there are some deviations. In order to account for this shortcoming, a simple nearest neighbor interpolation, based on the time stamps of the individual frames, is conducted. The applied algorithm is based on comparing the number of frames per second with the set frame rate (10 frames per second). If there are less frames

6 Estimating Transfer Coefficients: Experimental Setup & Measurement

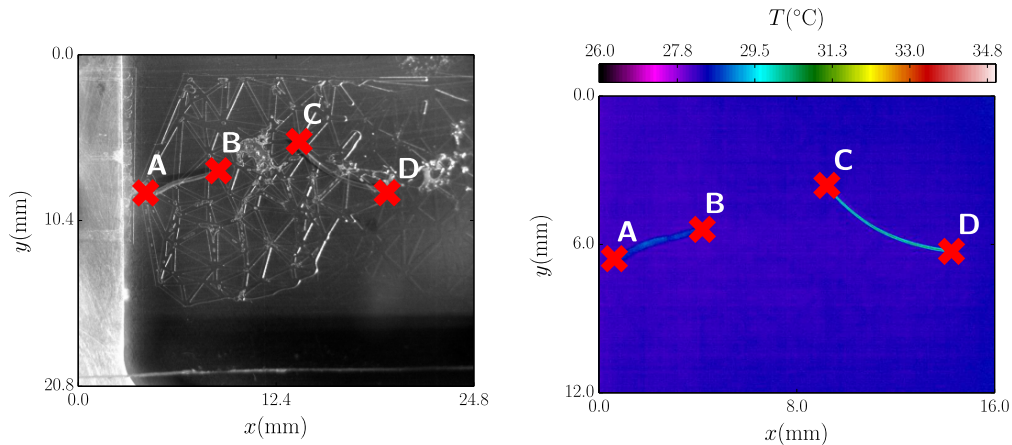


Figure 6.5: Optical image of the micro-model with the metallic wires on its surface (**left**) and thermal image of the same part of the micro-model (**right**). The wires have a different color than the background due to the difference in their thermal emissivities.

some frames are duplicated (i.e. the respective nearest neighbors are used) in order to achieve a constant frame rate. The opposite is done when the frame rate is higher than nominal (i.e. nearest neighbor frames are omitted). In this way, the two image streams are kept synchronized.

6.2.2 Spatial Correlation

The infrared and the optical images are taken independently. In order to gain information about the temperature of a specific phase at a specific point, the two images have to be correctly superimposed, i.e. spatially correlated. We make use of reference markers, which are physically put onto the micro-model and one image is taken by both cameras. These markers are metallic wires which have a different thermal emissivity than the micro-model. In a thermal image this is depicted as a temperature difference.

Figure 6.5 shows how the markers are visible both in the optical image (left) and infrared image (right). Corresponding reference points A to D are identified in the two images and a transformation matrix is calculated. The explained temporal and spatial correlation procedure allows us to superimpose images of the two cameras

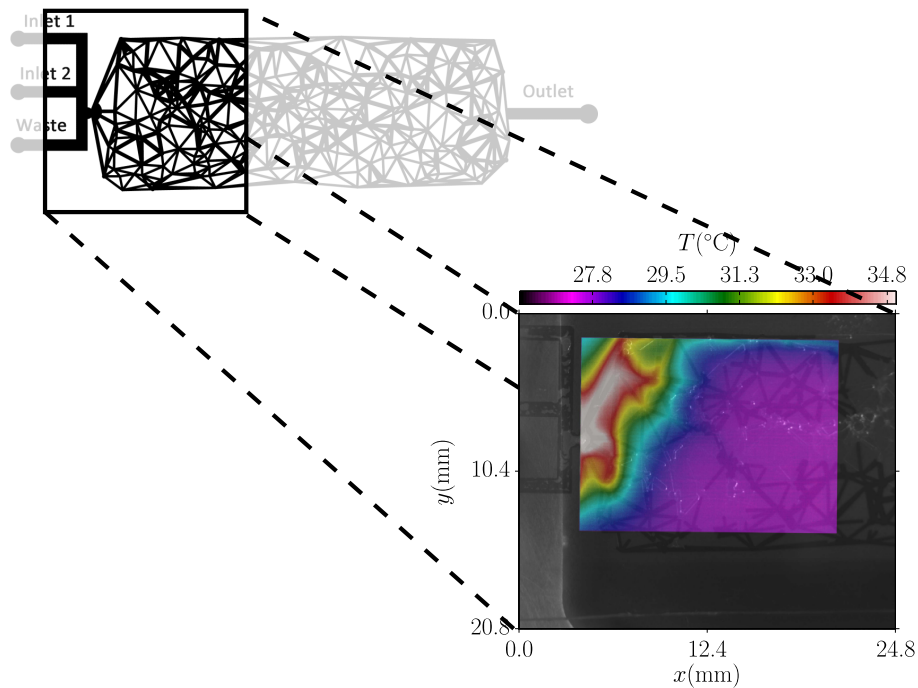


Figure 6.6: After temporal and spatial correlation, optical and thermal images are superimposed and presented in one image.

and to see both the temperature field and the phase configuration for a given point in time and space. A typical example of a composite image (with optical and thermal images superimposed) is shown in Figure 6.6.

6.2.3 Phase Segmentation

In order to attribute the observed temperature field to the wetting, non-wetting and solid phases, image segmentation is applied. The segmentation and attribution to the respective phases is a necessary prerequisite in order to assign the temperature field to the respective phases and, ultimately, derive heat transfer coefficients which is done in the next chapter. Image segmentation is conducted on the optical image. The information about phase presence is subsequently transferred to the infrared image, resulting in phase specific temperature distributions. The segmentation is conducted in two steps: first, delineation of the void space and, second, distinction between wetting and non-wetting phase. Information on the location of the solid

6 Estimating Transfer Coefficients: Experimental Setup & Measurement

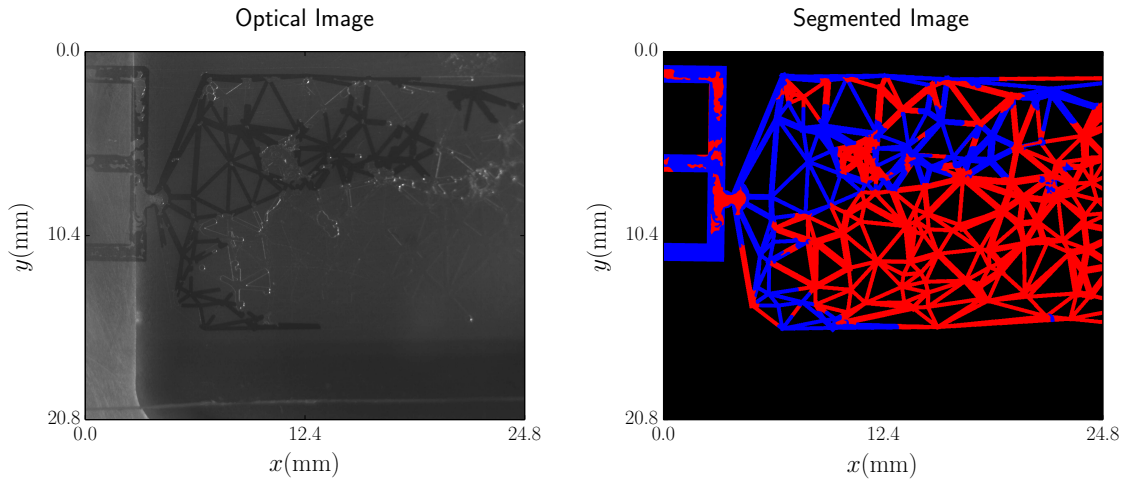


Figure 6.7: Raw optical image (**left**) and segmented image (**right**) acquired during a drainage process. In the segmented image, black stands for the solid phase, blue for the non-wetting phase and red for the wetting phase.

matrix (and thus also of the void space) is available from the original Autocad design (blueprint) of the flow network.

Correlation between the blue print and the optical image is achieved in the same way as for the correlation between the infrared and the optical images (see Section 6.2.2). The only difference being that the reference points are geometrical features rather than introduced markers.

The segmentation of wetting and non-wetting phases, however, is a more complicated process. The distinction between the phases is based on a thresholding approach, i.e. we compare the gray-level of a pixel to a threshold level. Depending on whether the gray-level is bigger or smaller than the threshold, we assign the pixel to the respective phase. In order to facilitate this process, the invading non-wetting (i.e. water) phase is dyed with ink.

The biggest challenge in the segmentation of the fluid phases is the low illumination quality. As explained before, the infrared camera has to be installed at the distance of 3 cm from the micro-model and there is little space for the light source. Therefore, the LED source is put at an angle, resulting in a dark optical image with a very narrow distribution of gray values, see Figure 6.7, left. This, in turn, makes the result of the segmentation very sensitive to slight variations in the thresholding

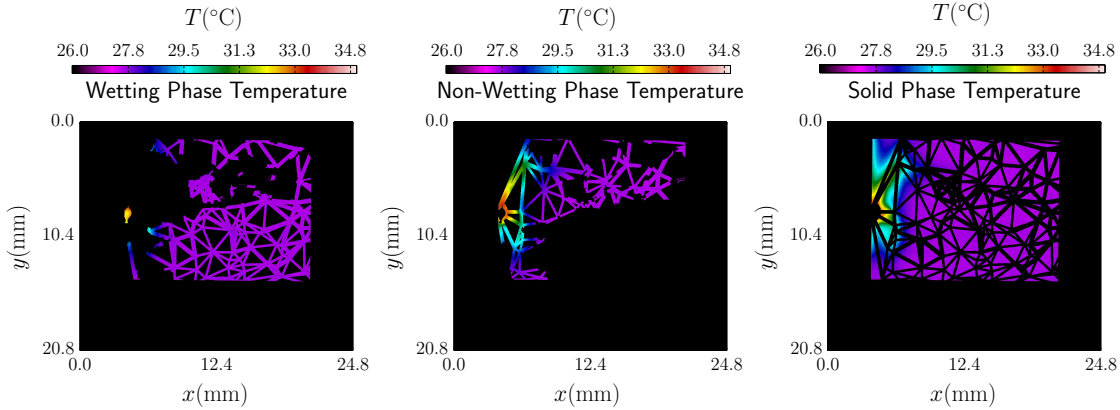


Figure 6.8: Segmented temperature fields of the two fluids and the solid phase, which correspond to the event shown in Figure 6.7.

level, slight intensity gradients over the optical image, as well as slight variations in illumination. Therefore, additional preprocessing of the optical image is necessary.

Mainly, we apply two measures in order to facilitate segmentation. First, the segmentation is not conducted on the optical image itself but on the difference between the optical image and a reference image. The reference image is chosen to be an image of the micro-model fully saturated with the wetting phase. This makes the result independent of background gradients in intensity, as only changes in gray-level caused by the phase distributions are detected. The second measure is intensity compensation. In order to compensate for temporal variations of light intensity, regions of the optical image are compared to the respective region in the reference image. If the intensity of the region of interest in the optical image is different from the reference intensity, this difference is counterbalanced in order to achieve constant light intensity of the optical images. This comparison is based on a GAUSS-filter (MATLAB, 2013).

With these two measures, a constant global threshold is manually selected for each experimental run. In a post processing step, image noise is eliminated by applying a 2D median filter with a size of 7 pixels. The unprocessed optical image from a drainage event and the corresponding segmented image are given in Figure 6.7. With the phase distributions known, the temperature field can be attributed to the respective phases, as shown in Figure 6.8.

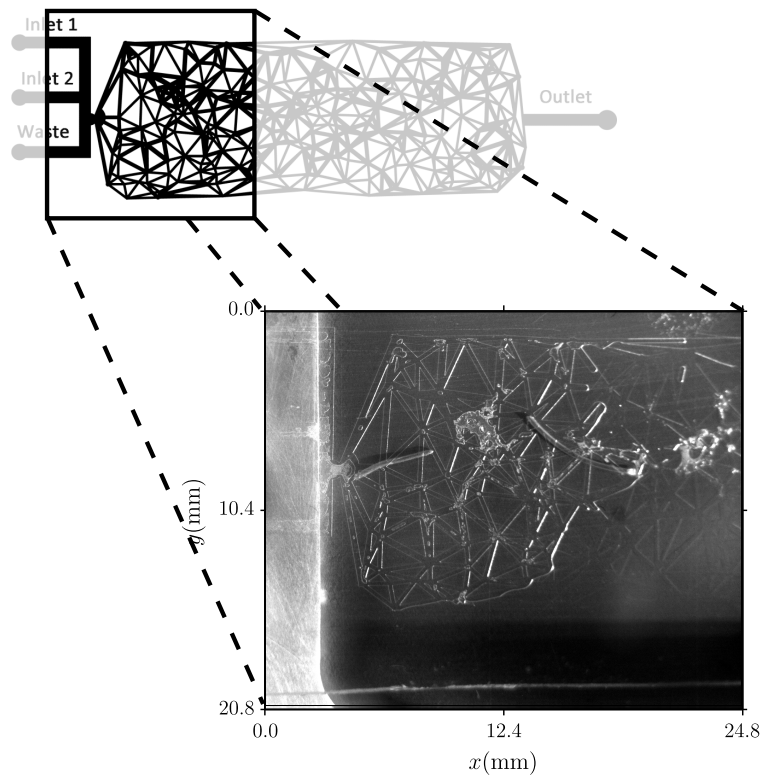


Figure 6.9: The initial step of the experimental procedure: saturating the micro-model with Fluorinert. In the accompanying movie ([Chapter6_1.avi](#)) Fluorinert replacing air is shown.

6.3 Results

In this section, we provide visualization results of a number of experiments and discuss how and what kind of information is extracted from them. Each example is accompanied by a movie, which is provided as ancillary material. These movies are important, as the very purpose of the experiment is to capture the dynamics of the system.

6.3.1 Preparation and Removal of Entrapped Air

Before the start of the experiment, the micro-model has to be saturated with the wetting phase displacing the air completely. Figure 6.9 shows an image from this

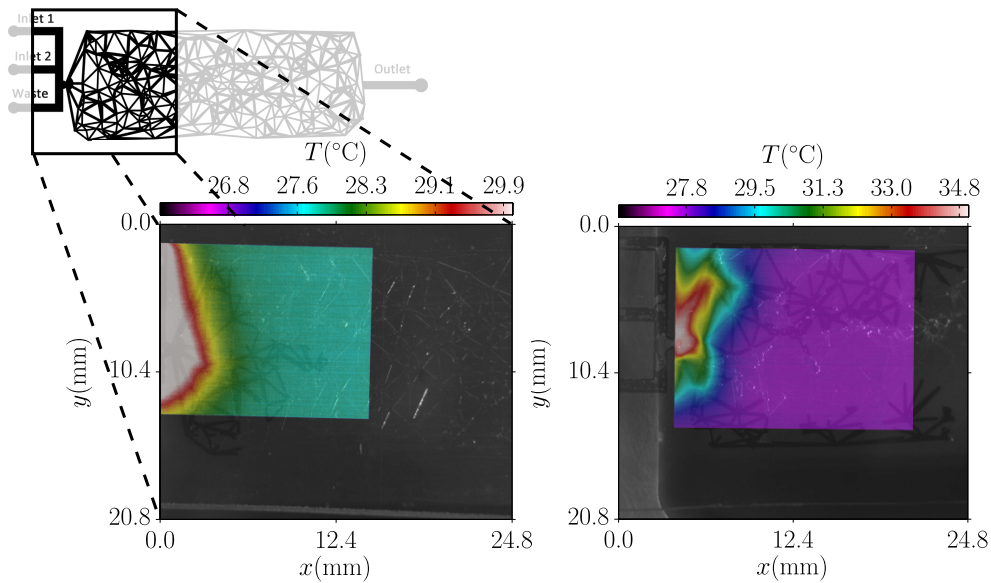


Figure 6.10: Invasion of hot water in a primary drainage process at two different flow rates. An extraction rate of 2.4 ml/h (**left**, shown in the accompanying movie `Chapter6_2a.avi`) leads to a much smoother temperature distribution than an extraction rate of 4.8 ml/h (**right**, shown in the accompanying movie `Chapter6_2b.avi`). Both images are taken at the same impingement time of 18 s.

step. The two pieces of wire visible are the markers used for image registration. The accompanying movie file `Chapter6_1.avi`, shows how some residual air bubbles are removed in order to obtain a fully Fluorinert saturated micro-model at the beginning of the actual experiment.

6.3.2 Influence of Velocity on Temperature Distribution

Figure 6.10 shows two primary drainage experiments with extraction flow rates of 2.4 ml/h (left) and 4.8 ml/h (right). The inflow temperature is the same in both experiments. Both images originate from primary drainage experiments. It can clearly be seen that the lower flow rate leads to a very smooth temperature distribution. In other words, non-equilibrium effects are much smaller. Additionally, with the higher flow rate, an increasing influence of geometry of the flow network on the temperature distribution can be observed. This is attributed to the more

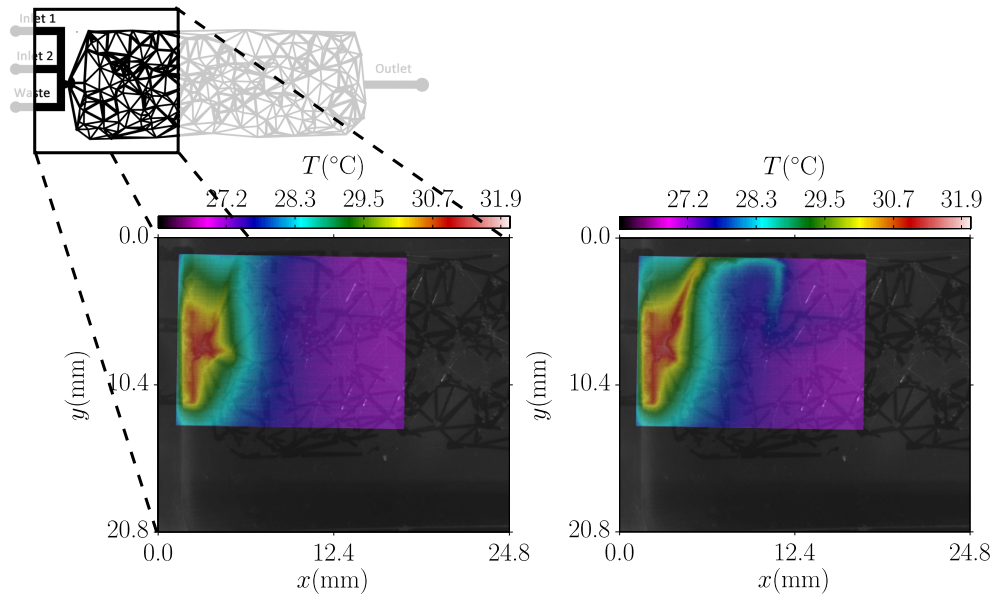


Figure 6.11: Two stages during secondary drainage. A stable temperature distribution is shown (**left**). Suddenly the temperature field changes (**right**), because a new flow path is established. This process can be nicely observed in the accompanying movie ([Chapter6_3.avi](#)).

pronounced difference between the phase temperatures. In other words: the heat transfer process shifts from being an equilibrium process to a kinetic process.

6.3.3 Temperature as Flow Path Indicator

Figure 6.11 shows two snapshots of a secondary drainage experiment, taken a moment apart, at an extraction flow rate of 2.4 ml/h . This can be nicely seen in the accompanying movie. The left figure originates from a stage during flow where stable temperature field and constant fluid distribution prevail. Without any change in the boundary conditions and phase distribution, suddenly the temperature field changes (right figure). We attribute the new temperature field to a newly established flow path.

This suggests that our experimental setup can be used in order to study which connected pathways are active, in the sense of actually conducting fluid, in a multiphase flow setting. This would not be possible by means of only optical

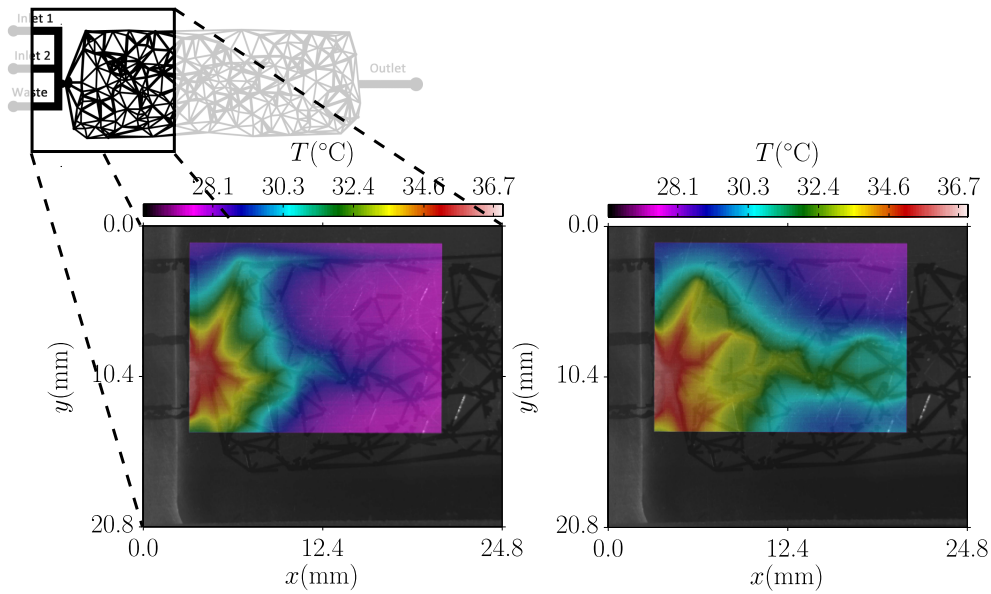


Figure 6.12: This figure shows two successively reached temperature distributions obtained at flow rates of $80 \mu\text{l}/\text{min}$ (**left**) and $200 \mu\text{l}/\text{min}$ (**right**). The interesting thing here is that the flow field and temperature distributions reach a steady states. The accompanying movie ([Chapter6_4.avi](#)) shows the respective stationary states.

observation, as optical observation merely shows phase presence and not whether it moves. Knowledge about active pores is important in order to calculate e.g. average residence time of particles in an REV.

After flow through the micro-model and the circulation of hot water at the inlet are both stopped, we can observe how the micro-model cools down. Expectedly, the large mass of water in the inlet area, compared to the flow network, leads to a bigger latency before reaching room temperature (please refer to the movie [Chapter6_3.avi](#) for this).

6.3.4 Stationary Temperature Distributions

Two successively reached stationary states for the extraction flow rates of $80 \mu\text{l}/\text{min}$ (left) and $200 \mu\text{l}/\text{min}$ (right) are shown in Figure 6.12. The most interesting aspect with this run is the fact that stationary states are reached for the respective

extraction rates. The temperature fields are stationary but not homogeneous in space because there is heat loss via the top and bottom of the micro-model.

Close observation shows that the temporal synchronization procedure is not fully successful: the optical stream is lacking behind the infrared stream. However, for those states which are stationary, this is not a problem as neither phase, nor temperature distribution change. This makes these runs highly valuable for deriving macro-scale heat transfer coefficients.

Apart from the stationary temperature distributions, the backflow of the cooled down water can be seen in the accompanying movie. As explained earlier, after the invasion of hot water is stopped, the flow process is reversed and the (now cooled down) fluid is re-injected. This can be seen as cool fingers moving from right to left in the later times of the accompanying movie (`Chapter6_4.avi`). Again, as shown in Section 6.3.3, local temperature information can serve as a flow path indicator.

6.4 Summary & Conclusion

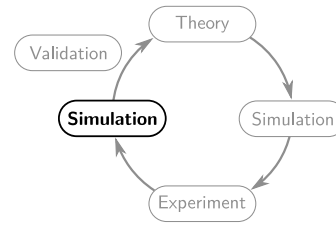
In this chapter, we presented a novel setup, consisting of a specially-designed micro-model and two cameras, which allows simultaneous optical and thermal imaging. This is the first time that a micro-model has been used in an integrated study of two-phase flow and heat transfer between phases.

The thermal and optical images acquired from this monitoring setup were temporally and spatially correlated. These images enabled us to draw conclusions on the interplay of flow and kinetic heat exchange between phases.

For future work, also the segmentation of the optical image into the wetting, non-wetting and solid phases is demonstrated. This will allow attributing the temperature fields to the respective phases. Our images clearly show that there are significant local differences in the pore-scale temperature of phases. The averaging of this information to macro-scale phase-average temperatures as well as further testing of the validity of the local thermal equilibrium assumption are conducted in the next chapter.

Additionally, we could show that temperature can be used as a flow path indicator. That is, the temperature information tells us which one of the pathways occupied by a phase actually takes part in the flow process. This information cannot be obtained from optical imaging alone.

The described setup had one major shortcoming: the cameras did not acquire images at the specified frame rates. This could be partly compensated by a simple nearest neighbor interpolation. But especially late time data were not synchronized temporally any more. An improvement of the experimental equipment would allow to have synchronized streams without post-processing. The macro-scale modeling of the described experimental setup as well as the estimation of heat transfer coefficients for the case of multiphase flow in porous media is demonstrated in the next chapter.



7

Estimating Transfer Coefficients: Simulation of the Experiment under Non-Equilibrium Conditions⁶

In this chapter, we want to take one further step towards the quantitative understanding and parameter estimation in the area of local thermal non-equilibrium in multiphase flow in porous media. To be more precise, we want to obtain an estimate of the heat transfer coefficient for a local thermal non-equilibrium model by means of parameter calibration. In order to accomplish this, we simulate two experimental runs of the experiment explained in Chapter 6 by means of the macro-scale local thermal non-equilibrium model presented in Chapter 3. By comparing simulation and experiment, we obtain a first-order approximation of the up-to-now unknown scaling parameter f_e .

The structure of this chapter is the following: In Section 7.1, input parameters needed for the macro-scale model are presented. Fluid and material parameters are straight forward to obtain. However, matrix properties and multiphase properties require some more effort (Section 7.1.2). The determination of interfacial areas, which are inevitable input parameters to the macro-scale model, require the development of a new image analysis algorithm, explained in Section 7.2. Building

⁶The macro-scale modelling of the micro-model experiment will be published in Nuske, P., Ronneberger, O., Karadimitriou, N. K., Helmig, R., and Hassanizadeh, M. (2014b). Modelling multiphase flow in a micro-model with local thermal non-equilibrium on the darcy scale. *Water Resources Research*. submitted

Table 7.1: Fluid properties.

	c_α (kJ/kgK)	ρ_α (kg/m ³)	λ_α (W/mK)	μ_α (Pa s)
Fluorinert ^a	1.1	1860	0.065	$4.7 \cdot 10^{-3}$
Water	4.2	1000	0.6	$1 \cdot 10^{-3}$
^a 3M (2013)				

on that information, macro-scale constitutive relations are fit to the obtained data in Section 7.3. Modelling choices and simulation setup are explained in Section 7.4. Employing these input parameters, the simulations of different experimental runs are presented in Section 7.5. We conclude in Section 7.6 and deduce future research goals.

7.1 Input Parameters

A model can only be as good as its input. Therefore, the simulation of complex systems, like multiphase flow in porous media systems, requires the detailed understanding of the parameters which are input to the model.

This is even more so for the case of a non-standard model, like the employed local thermal non-equilibrium model. In this case, in addition to fluid (Section 7.1.1) and matrix (Section 7.1.2) properties (and their interaction) the interfacial area available to heat transfer is a crucial input. The determination of all interfacial areas in a micro-model has not been accomplished so far and is therefore presented in detail in Section 7.2.

7.1.1 Material & Fluid Properties

In order to keep the model as simple as possible, we use constant fluid properties for Fluorinert and water, see Table 7.1. This is mostly justified by the fluids being both liquids and the comparatively moderate temperature differences during the experiment.

Table 7.2: Material properties of the solid phase (PDMS, Mark (1999)).

c_s (kJ/kgK)	ρ_s (kg/m ³)	λ_s (W/mK)
1.2	970	0.15

Although PDMS is in principle elastic, it will be modelled as a rigid, non-deforming (see Section 6.1.1) solid phase with the properties given in Table 7.2.

7.1.2 Micro-Model Properties

In order to measure intrinsic permeability, steady state flow measurements were conducted with the model and setup described above. The flow network is completely filled with the wetting phase (Fluorinert) and one reservoir is connected to a syringe pump. Upon reaching steady state, the pressure drop along the micro-model is recorded. With all remaining quantities known, intrinsic permeability can be calculated by using DARCY's law (see Equation 3.13). The procedure is repeated several times and an error of 2% of the intrinsic permeability measurements is calculated, see Table 7.3.

The capillary pressure – saturation curve is obtained from pressure controlled quasi-static measurements. Initially, the micro-model is fully saturated with the wetting phase. The non-wetting phase is introduced through sequential equilibrium pressure steps. For each step, an optical image of the distribution of fluids in the network is taken and the corresponding pressure difference between the reservoirs is recorded. Phase saturations are obtained by image processing. The equilibrium data points as well as a fit van Genuchten (1980) function are shown in Figure 7.4.

The porosity of the micro-model is also determined by image processing (Table 7.3). An image of the micro-model fully saturated with the wetting phase is used for this purpose. The measured value (58%) is close to the value expected from the design (60.5%).

Table 7.3: Intrinsic properties of the micro-model.

$K \text{ (m}^2\text{)}$	$\phi(-)$	$\mu_p \text{ (\mu m)}$
$2.3 \cdot 10^{-10}$ ^b	0.58 ^b	400 ^a
^a Karadimitriou et al. (2014)		
^b measurement		

7.2 Image Analysis⁷

We developed image analysis algorithms to extract saturation and interfacial areas from recorded images. In order to apply a consistent set of constitutive relations, the same set of images, recorded for the capillary pressure – saturation measurements (see above), is used.

The framework first maps each recorded image to a model image of the theoretical network. Then, it uses a threshold segmentation and basic morphological operations to compute the area of the wetting and the non-wetting phases in the image, as well as the border lengths between all areas. Using the scale of the model image, the areas and lengths in pixel coordinates are scaled to real-world units. In the final step, these areas and lines are multiplied with the depth of the micro-channels to obtain an estimate of the real volumes and the interfacial areas. The detailed image analysis pipeline is described in the following sections.

7.2.1 Thin Plate Spline Warping

The camera optics introduce some distortions to the image. To compensate for these distortions, and to bring each image to a standard coordinate system, we compute a mapping (warping) of the recorded image to the model image. This is done based on a set of manually defined landmark correspondences in the recorded image. The recorded image is denoted as $I : \mathbb{R}^2 \rightarrow \mathbb{R}; \mathbf{x} \mapsto I(\mathbf{x})$. We choose a rendered model of the micro-channel layout as reference image, see Figure 7.1, left.

⁷This section is the outcome of joint work with Olaf Ronneberger, University of Freiburg.

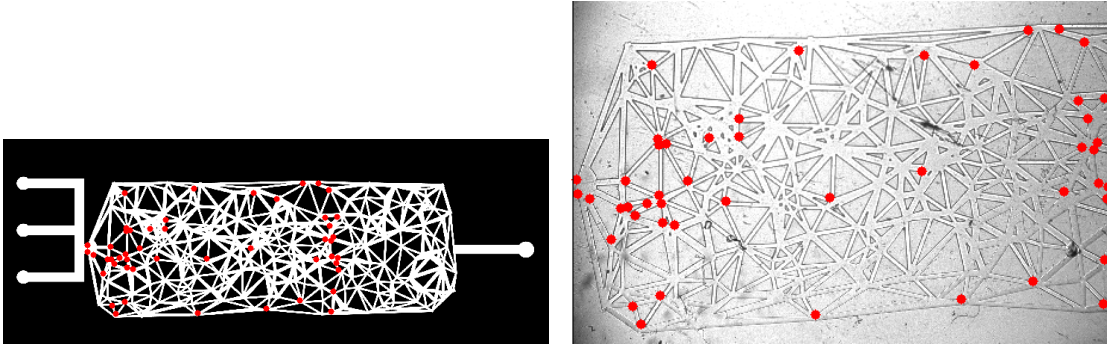


Figure 7.1: **Left:** Selected landmarks (red dots) in the model. **Right:** Identified landmarks in the recorded image.

In this rendered model, the mask selecting the void space is given by $M_v : \mathbb{R}^2 \rightarrow \{0, 1\}$. A function value of 1 denotes the void space (white in Figure 7.1, left) and 0 the solid phase (black in Figure 7.1, left). The landmark positions in the recorded image are denoted by $\mathbf{a}_i \in \mathbb{R}^2, i \in \{1, \dots, N\}$. The corresponding landmarks in the reference image are denoted as $\mathbf{b}_i \in \mathbb{R}^2, i \in \{1, \dots, N\}$. From these landmarks we compute a dense warping function $\mathbf{T} : \mathbb{R}^2 \rightarrow \mathbb{R}^2$ using thin plate spline interpolation (Bookstein, 1989), such that

$$\mathbf{a}_i = \mathbf{T}(\mathbf{b}_i) \quad \forall i \in \{1, \dots, N\}. \quad (7.1)$$

This transformation is applied to the recorded image to obtain the warped recorded image (I')

$$I'(\mathbf{x}) := I(\mathbf{T}(\mathbf{x})). \quad (7.2)$$

We added additional landmark pairs, until all micro-channel borders in the warped image were aligned to the borders of the model image.

7.2.2 Segmentation

To segment the warped recorded image into the different phases, we first apply a shading correction to compensate the inhomogeneous illumination and sensitivity of the optical system. The local attenuation function $f_a : \mathbb{R}^2 \rightarrow \mathbb{R}$ is estimated from the recorded intensities of the solid phase by a GAUSSIAN weighted averaging

7 Estimating Transfer Coefficients: Simulation of the Experiment

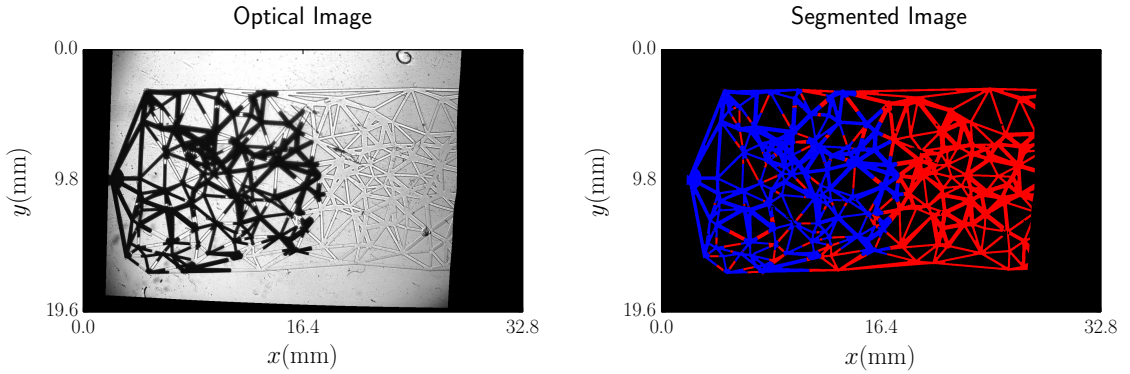


Figure 7.2: Left: Optical image of a quasi-static measurement point. Right: Segmented image, M_n is depicted in blue and M_w is depicted in red.

over the solid-phase-pixels in the local surrounding

$$f_a = \frac{(M_s \cdot I') * G_\sigma}{M_s * G_\sigma}, \quad (7.3)$$

where $G_\sigma(\mathbf{x}) = \frac{1\text{mm}}{\sqrt{2\pi}\sigma} \exp(-\frac{\mathbf{x}^2}{2\sigma^2})$ is the GAUSSIAN smoothing kernel (here $\sigma \approx 2.2\text{ mm}$), M_s is the mask selecting the solid phase pixels, and $*$ denotes a convolution. This mask is derived from M_v by inversion and morphological erosion to exclude the micro-channel borders by

$$M_s = (1 - M_v) \ominus \mathcal{C}_r, \quad (7.4)$$

where $\mathcal{C}_r \subset \mathbb{R}^2$ describes a disk-shaped structuring element with radius r , i.e. $\mathcal{C}_r = \{\mathbf{x} \in \mathbb{R}^2 \mid \|\mathbf{x}\| < r\}$. Here, we use an $r \approx 110\ \mu\text{m}$. The symbol \ominus denotes the morphological erosion, which is defined for a continuous function $f : \mathbb{R}^2 \rightarrow \mathbb{R}$ with a structuring element $\mathcal{S} \subset \mathbb{R}^2$ as

$$(f \ominus \mathcal{S})(\mathbf{x}) = \min_{\mathbf{k} \in \mathcal{S}} (f(\mathbf{x} + \mathbf{k})). \quad (7.5)$$

The estimated attenuation function f_a is then used to compensate for all attenuation effects in the image in order to perform the subsequent threshold segmentation. The pixels belonging to the non-wetting phase are found by

$$M_n = \left[\frac{I' * G_\sigma}{f_a} < 0.5 \right] \cdot M_v, \quad (7.6)$$

where G_σ is a small GAUSSIAN smoothing kernel with $\sigma \approx 11\mu\text{m}$ to avoid noisy borders in the obtained mask. Very small regions (< 10 pixels $\approx 4800\mu\text{m}^2$) are eliminated from this mask using a connected component analysis. The segmentation mask for the wetting phase is then found by

$$M_w = (1 - M_n) \cdot M_v . \quad (7.7)$$

The respective masks are graphically shown in Figure 7.2 for one equilibrium pressure step.

7.2.3 Estimation of Macro-Scale Quantities

We use the obtained segmentation masks M_w and M_n from each recorded frame to estimate the volume of the wetting and the non-wetting phase as well as the interfacial areas between them and the solid phase. The analysis of an empty image (containing only the wetting phase) at the beginning of the sequence is used to define a mask of erroneously assigned pixels, originating from scratches and dust particles on the sample. These pixels are excluded from further analyses.

The volume of the wetting and the non-wetting phases is computed from the area of the corresponding segmentation mask and the constant depth d of the channels as

$$V_w = d \int_{\mathbb{R}^2} M_w(\mathbf{x}) d\mathbf{x} \quad (7.8a)$$

$$V_n = d \int_{\mathbb{R}^2} M_n(\mathbf{x}) d\mathbf{x} . \quad (7.8b)$$

From this, the calculation of wetting phase saturation is straight forward:

$$S_w = \frac{V_w}{V_w + V_n} . \quad (7.9)$$

The interfacial areas appear as interface border lines in the 2d image. To measure the length of these borders, they were computed as lines with single pixel width using morphological operations on the segmentation masks (here all M denote the

7 Estimating Transfer Coefficients: Simulation of the Experiment

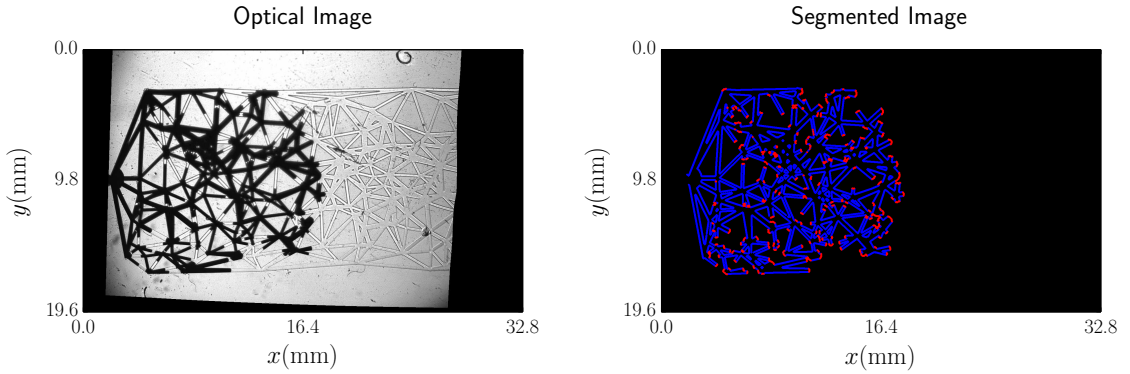


Figure 7.3: Left: Optical image of a quasi-static measurement point. Right: Segmented image, b_{ns} is depicted in blue and b_{wn} is depicted in red. Both borderlines are grown for visualization.

discretized masks) as

$$b_{wn} = (M_w \oplus \mathcal{N}) \cdot M_n \quad (7.10a)$$

$$b_{ws} = (M_w \oplus \mathcal{N}) \cdot (1 - M_v) \quad (7.10b)$$

$$b_{ns} = (M_n \oplus \mathcal{N}) \cdot (1 - M_v) \quad (7.10c)$$

with $\mathcal{N} = \left\{ \begin{pmatrix} -1 \\ 0 \end{pmatrix}, \begin{pmatrix} 1 \\ 0 \end{pmatrix}, \begin{pmatrix} 0 \\ 0 \end{pmatrix}, \begin{pmatrix} 0 \\ -1 \end{pmatrix}, \begin{pmatrix} 0 \\ 1 \end{pmatrix} \right\}$ describing the 4-neighborhood of a pixel, and \oplus denoting morphological dilation, which is defined correspondingly to the erosion (Equation 7.5) as

$$(f \oplus \mathcal{S})(\mathbf{x}) = \max_{\mathbf{k} \in \mathcal{S}} (f(\mathbf{x} + \mathbf{k})). \quad (7.11)$$

The calculated borderlines are shown in Figure 7.3.

To estimate the true length of the resulting lines, the centers between two adjacent pixels are connected to an open polygon. End pixels, corner pixels (at corners with an angle of 90° or more) and center pixels at line junctions are also added to that polygon. The measured length of such a polygon differs in the worst case approximately 3% from the true length of a straight line, which we consider precise enough for further evaluations.

The actual quantities of interest in this context are the volume specific interfacial areas (a_{wn} , a_{ns}). By means of the given measurements, they are actually straight

forward to compute from Equations 7.10. The respective lengths of the border lines need to be multiplied by the micro-model depth d and divided by the observed volume of the micro-model (V_{mm})

$$a_{wn} = \frac{d b_{wn}}{V_{\text{mm}}} \quad (7.12a)$$

$$a_{ns} = \frac{d b_{ns}}{V_{\text{mm}}}. \quad (7.12b)$$

7.2.4 Implementation Details & Code Availability

The image analysis pipeline is implemented in Matlab R2013a. The recorded images have a pixel size of $11 \mu\text{m}$, the model image was rendered with a pixel size of $21.9 \mu\text{m}$. The image analysis source code (along with the raw images) is provided to the scientific community as part of this work under the GPLv2. Please refer to Section 3.5 for details regarding the availability and documentation of image analysis as well as DuMu^x-code used in this chapter.

7.3 Constitutive Relations

Building on the data obtained by means of the above outlined image analysis procedure, we shortly present the fit constitutive relations. These constitutive relations are input to the non-equilibrium macro-scale model. They are therefore crucial to this work.

Capillary pressures are identified as the difference between the pressures on the boundaries of the flow network during quasi-static measurements. Wetting phase saturations, volume specific wetting – non-wetting and non-wetting – solid interfacial areas have been obtained in Section 7.2.

From these values, a van Genuchten (1980)-type curve was fit to the p_c - S_w data points. The measured data points as well as the fit function are shown in Figure 7.4. The resulting relative permeability curves are also shown in Figure 7.4.

7 Estimating Transfer Coefficients: Simulation of the Experiment

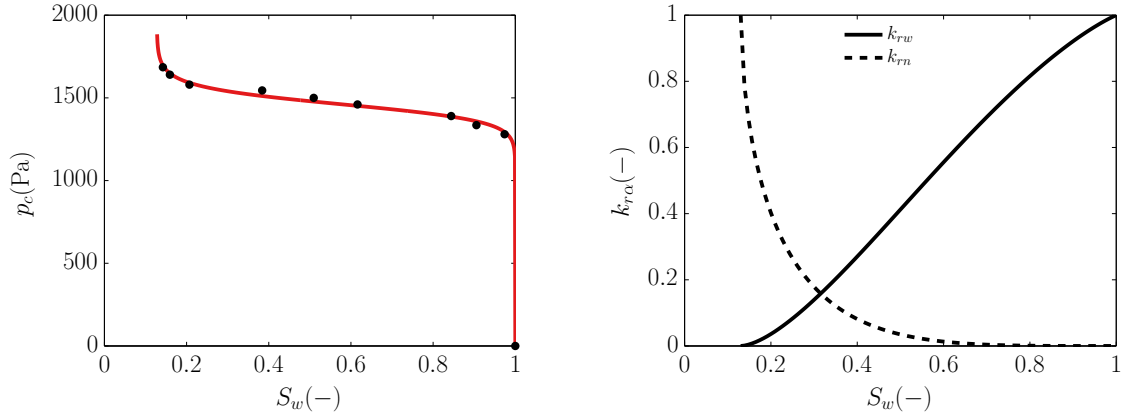


Figure 7.4: **Left:** Measured data points with fit VAN GENUCHTEN function. **Right:** Relative permeability function. The fit coefficients are given in Table 7.4.

Table 7.4: VAN GENUCHTEN parameters of the capillary pressure – saturation fit (index p_c) and relative permeability – saturation fit (index k_r), see Equations 2.10, 2.15 and Figure 7.4.

α_{p_c} (1/Pa)	n_{p_c} (-)	S_{wr}	$R_{p_c}^2$	m_{k_r}	$R_{k_r}^2$
$6.8 \cdot 10^{-4}$	28.2	0.13	0.99	1.70	0.92

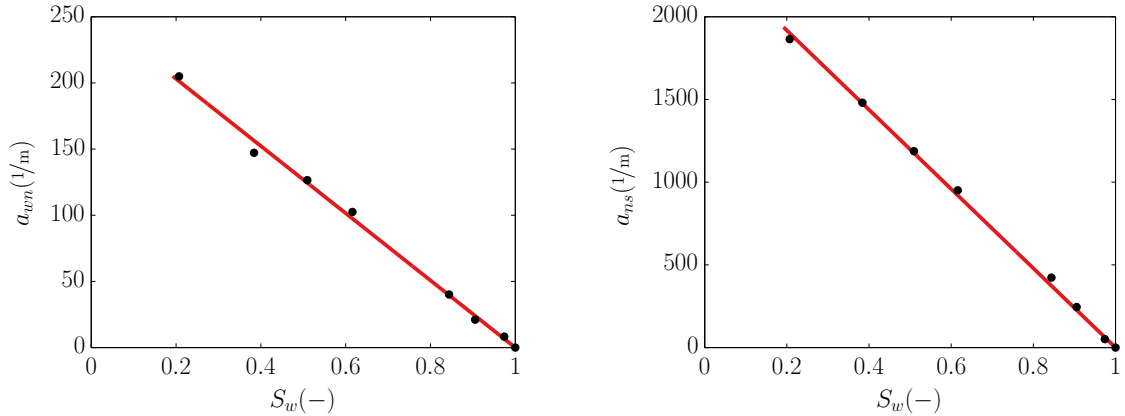


Figure 7.5: Measured data points with fit functions for $a_{wn}-S_w$ (**left**) and $a_{ns}-S_w$ (**right**) relations, see Equation 7.13a, 7.13b and Table 7.5. Both relations are a unique function of S_w because only data of a primary drainage process is fit.

Table 7.5: Fit parameters and coefficients of determination, see Equations 7.13a, 7.13b and Figure 7.5.

a_1	R_1^2	a_2	R_2^2
-253.85	0.99	-2397	0.99

Linear relations (Equations 7.13a, 7.13b) are fit to the volume specific interfacial area data, see Figure 7.5 and Table 7.5.

$$a_{wn} = a_1 S_w - a_1 \quad (7.13a)$$

$$a_{ns} = a_2 S_w - a_2 \quad (7.13b)$$

All fits were conducted by means of a non-linear least squares fitting tool (MATLAB, 2013).

Naturally, the interfacial area between the wetting and non-wetting phases needs to be zero for saturations of one and zero, respectively. However, the presented equations fit the obtained data very well. More research is needed with respect to the role of residual saturations and the associated interfacial areas during energy exchange processes. For the time being, we stick to the presented equation.

7.4 Experimental & Modelling Setup

The experimental setup has been exhaustively described in Chapter 6. Here, we will focus on the modelling decisions, made in order to simulate the experiment and ultimately calibrate heat transfer coefficients. The most basic decision is how to represent the physical setup which is to be simulated. We chose a one-dimensional model, as the process of interest has a dominant direction. The flow processes in the micro-model are represented by a macro-scale description: There is no detailed information about geometry, but the properties of the medium and the interaction with the fluid phases are represented on a volume-averaged basis (see Section 2.2.2).

7.4.1 Balance Equations

We employ the same balance equations as explained in Chapter 3. In the example presented in Chapter 5, temperature differences arose from evaporation processes. Here, temperature differences are externally applied. Therefore, we again choose to select an as simple as possible model. Solubility effects can be neglected, as

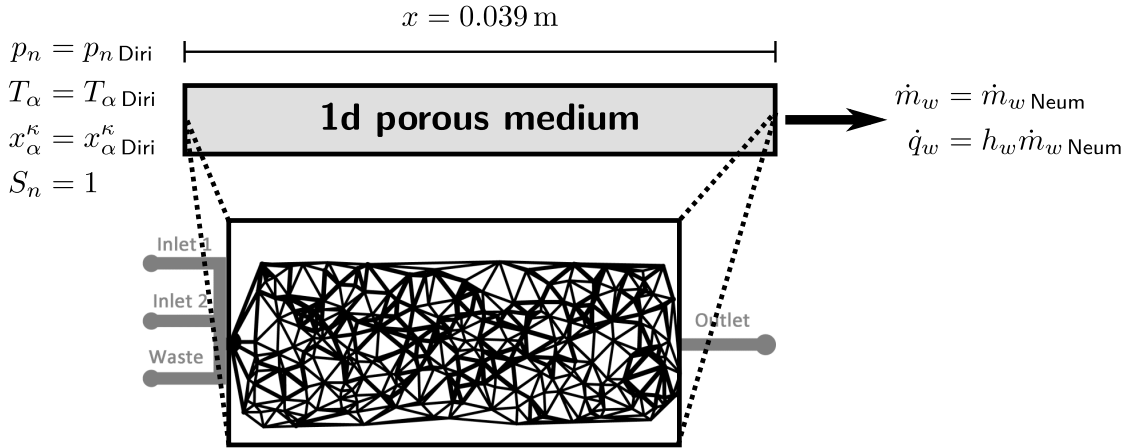


Figure 7.6: Boundary conditions as well as model abstraction of the simulation.

the chosen phases are virtually immiscible. Technically, this is implemented by setting the equilibrium, initial and injected mole fractions (x_{α}^{κ}) to zero and unity, respectively. This results in pure phases.

The micro-model was placed horizontally during all experiments. Therefore, gravitational effects do not play an important role and are neglected. All balance equations, constitutive relations and the thermodynamical framework are part of DuMu^x and are freely available, see Section 3.5 for details.

We kindly remind the reader that in this work the index w stands for the *wetting* (see Section 2.1.1) phase. With the solid phase being made of silanized PDMS (see Section 6.1.1), the wetting phase is *not* water but Fluorinert.

7.4.2 Initial and Boundary Conditions

Figure 7.6 shows the one-dimensional modelling concept as well as the chosen boundary conditions. Due to the high circulation flow rate (see Section 6.1.3) constant conditions are assumed at the inflow to the micro-model. Therefore, DIRICHLET values are set at the left-hand side of the modelling domain. On the right-hand side, NEUMANN values (\dot{m}_{Neum}) capture the withdrawal rates of fluid from the micro-model. Initial conditions are given in Table 7.6.

Table 7.6: Initial conditions and applied extraction flow rates for the simulations.

	$\dot{m}_w^{\text{Neum}}(\text{kg/s})$	$T_{\alpha \text{Diri}}(\text{K})$	$p_{ni}(\text{Pa})$	$S_{wi}(-)$	$T_{\alpha i}(\text{K})$
low-rate	$6.2 \cdot 10^{-7}$	307.65	$1 \cdot 10^5$	0.999	300.15
high-rate	$2.48 \cdot 10^{-6}$	308.65	$1 \cdot 10^5$	0.999	300.15

In this work, two experimental runs, mainly differing in the withdrawal rates imposed on the right-hand side, will be studied. The two experimental runs will be termed *low-rate* and *high-rate*, see Table 7.6 for the respective values.

7.4.3 Implementation of Heat Loss

As the micro-model is not placed in a complete vacuum, it exchanges energy with its surrounding. However, the topic of this work is the study and simulation of flow processes *in porous media*. Therefore, the exchange processes between micro-model and surrounding are not explicitly included but captured via boundary conditions.

We conceptualize the micro-model as a flat plate and use literature (McAdams, 1954) correlations for heat transfer coefficients (h_c) from a hot plate. Two contributions are assigned, heat loss from the top and from the bottom of a hot plate. At each vertex, with associated surface A , these losses occur according to

$$\dot{Q}_{\text{top}} = h_{c\text{top}}A(T_{\text{amb}} - T_s) \quad (7.14)$$

$$\dot{Q}_{\text{bottom}} = h_{c\text{bottom}}A(T_{\text{amb}} - T_s), \quad (7.15)$$

with the constant ambient temperature T_{amb} , chosen to be identical to the initial temperature. The heat losses are attributed exclusively to the solid phase because the outside of the micro-model consists of PDMS. Radiation losses are neglected due to low temperatures.

7.5 Simulation & Experiment

The goal of this work is to get a better understanding about the heat transfer between phases in multiphase flow in porous media processes. To be more precise, we want to estimate the unknown scaling parameter f_e , see Section 5.2.

In order to accomplish this, two experimental runs (**low-rate** and **high-rate**) are analyzed. They are simulated as explained above and the unknown scaling parameter f_e is selected by comparing simulation and experiment.

7.5.1 Line Averaging of Temperature

For comparing the measurements and the simulations, the information obtained during the simultaneous optical and thermal imaging experiment needs to be condensed. We choose to average the temperature information in y-direction. In other words: each point in x-direction, observed by the infrared camera, is assigned y-direction-averaged temperatures. In order to assign the temperature information to the respective phases, only those points where a phase resides are included in

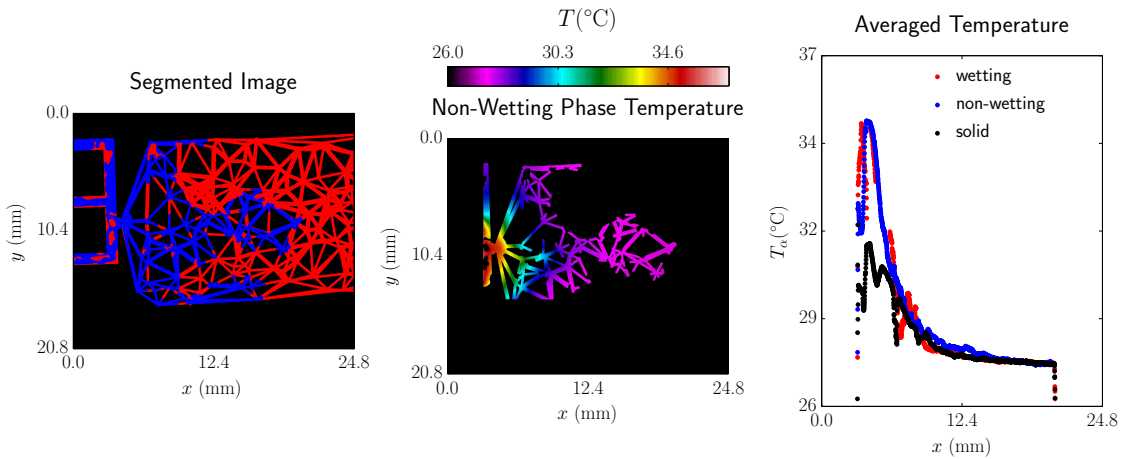


Figure 7.7: **Left:** The mask selecting the invading non-wetting phase is depicted in blue. **Middle:** The part of the infrared measurement attributed to the non-wetting phase. **Right:** Averages in y-direction of the respective phase temperatures, see movie `Chapter7_1.avi`.

the average. This information is obtained by means of the masks described in Section 6.2.3.

The procedure for obtaining the one dimensional line averages of T_w , T_n and T_s is shown in Figure 7.7. This condensed information is compared with simulation results in the next section.

7.5.2 Matching Simulation Results to Experimental Observations

First, we present the **low-rate** experiment and simulation. Figure 7.8 shows the micro-model experiment after 10s and 40s with temperature information superimposed.

Figure 7.9 shows the line averages of temperatures, explained above. In this figure, the beginning of the line average is moved to the left-hand side of the flow-network and the right-hand side of the plot is dictated by the right-hand side of the field of view of the infrared camera.

Figures 7.10, 7.11, 7.12, 7.13 show simulations of the **low-rate** experiment. The heat transfer scaling parameter f_e takes values of 0.1, 0.5, 1 and 10.

The temperature difference at the inflow after 10s is matched best in Figure 7.10. However, at both observed times, the temperature of the solid phase is not the lowest temperature, as it is observed in the experiment, see Figure 7.9. Figures 7.12 and 7.13 both show too small a temperature difference in the inflow region when comparing to the experiment.

We therefore conclude that simulating the experiment with a scaling coefficient of $f_e = 0.5$ matches the **low-rate** experiment best. However, two important experimental observations cannot be matched. First, in the experiment wetting and non-wetting temperature are close with the solid temperature being below. In the simulation, solid and wetting temperature are close with the non-wetting temperature above. Of course this can be explained by the interfacial area between wetting and solid phase (a_{ws}) being an order of magnitude bigger than the interfacial

7 Estimating Transfer Coefficients: Simulation of the Experiment

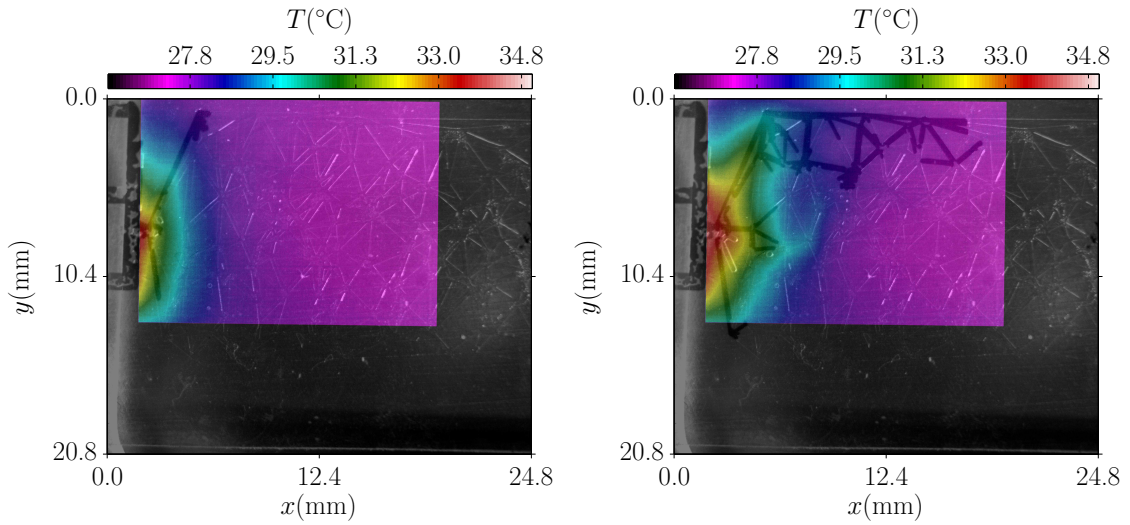


Figure 7.8: Overlay of low-rate temperature information and optical image after 10 s (**left**) and 40 s (**right**), see movie `Chapter7_2.avi` (showing a longer period).

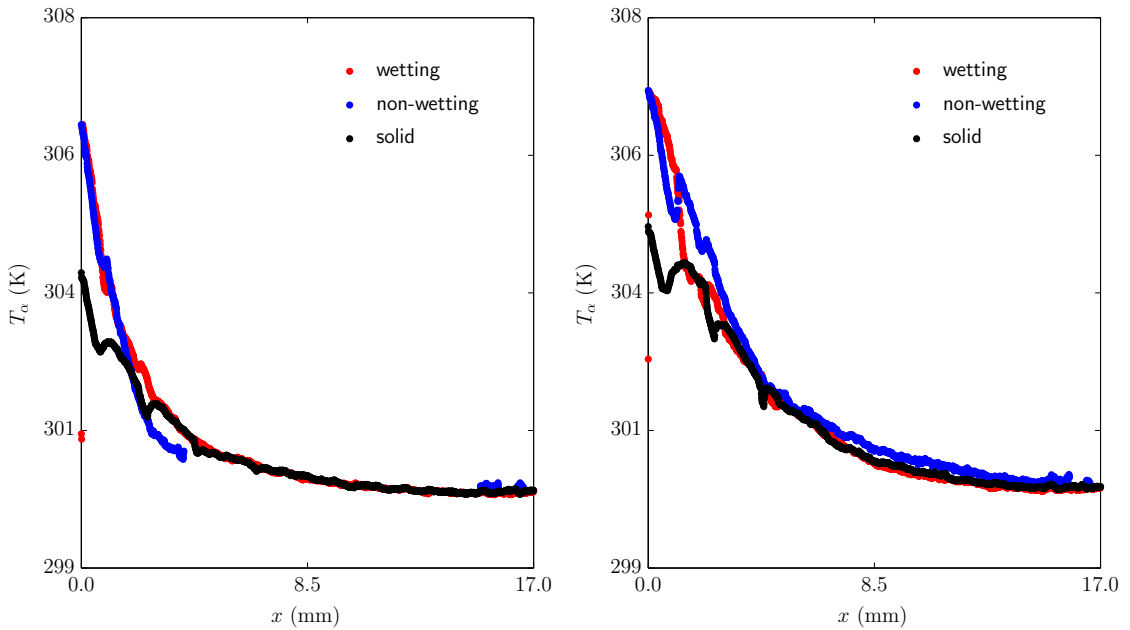


Figure 7.9: Experimental measurements, low-rate. **Left:** 10 s after start of invasion, **Right:** 40 s after start of invasion, see movie `Chapter7_3.avi`.

area between non-wetting and wetting phase (a_{wn}). However, this is a notable discrepancy between simulation and experiment.

Furthermore, the front velocity in the simulation is faster than in the experiment. In Section 7.5.3 an explanation for this observation is given.

7 Estimating Transfer Coefficients: Simulation of the Experiment

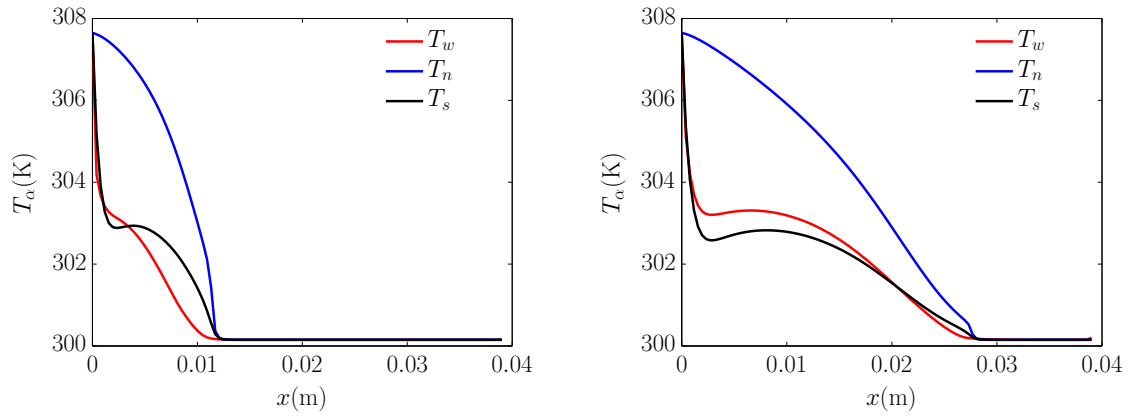


Figure 7.10: Simulation of the experiment, low-rate. **Left:** 10 s after start of invasion, **Right:** 40 s after start of invasion, $f_e = 0.1$.

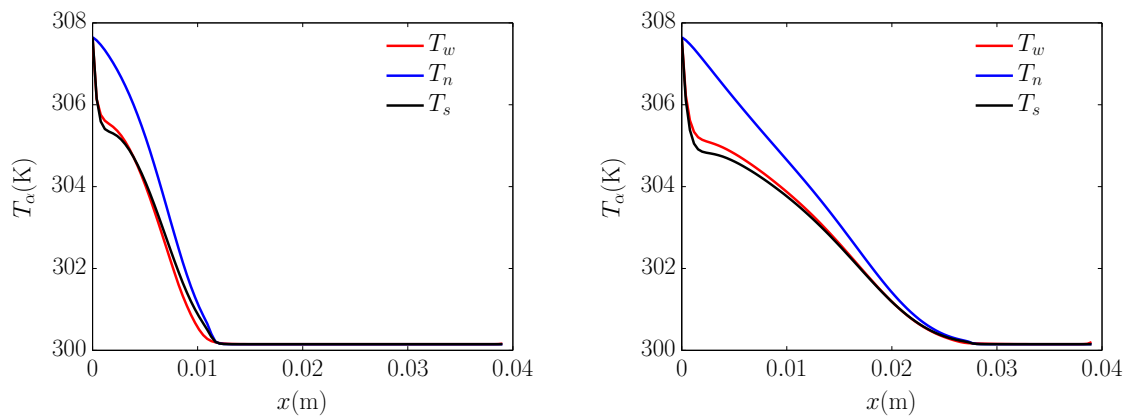


Figure 7.11: Simulation of the experiment, low-rate. **Left:** 10 s after start of invasion, **Right:** 40 s after start of invasion, $f_e = 0.5$.

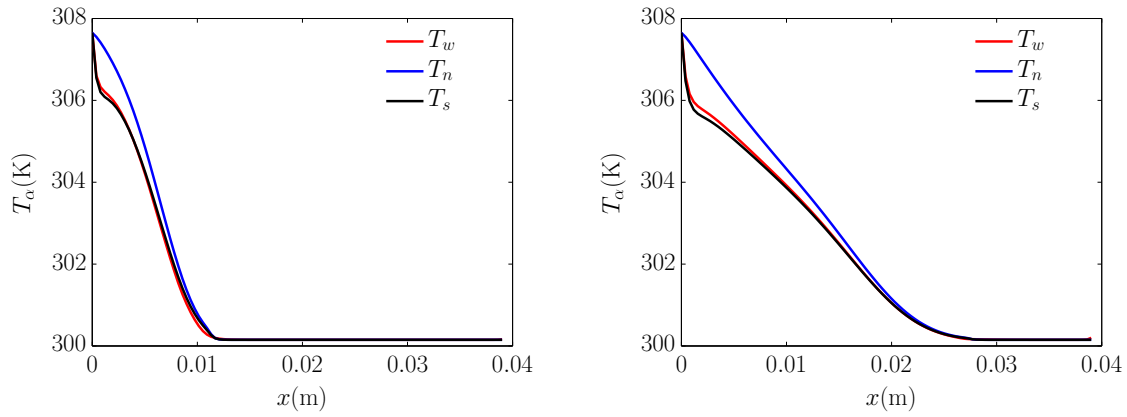


Figure 7.12: Simulation of the experiment, low-rate. **Left:** 10 s after start of invasion, **Right:** 40 s after start of invasion, $f_e = 1$.

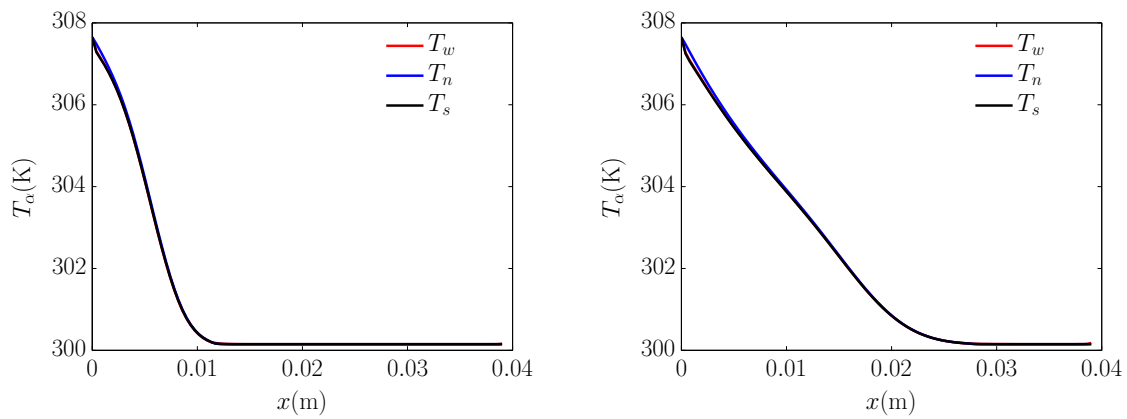


Figure 7.13: Simulation of the experiment, low-rate. **Left:** 10 s after start of invasion, **Right:** 40 s after start of invasion, $f_e = 10$.

7 Estimating Transfer Coefficients: Simulation of the Experiment

After having presented the matching of the **low-rate** experiment with simulation results, we present now experimental observations and simulations of the **high-rate** experiment.

Figure 7.14 gives an impression of the **high-rate** experiment after 5 s and 10 s and Figure 7.15 gives the line averages of the observed temperatures.

Figures 7.16, 7.17, 7.18, 7.19 show simulations of the **high-rate** experiment with heat transfer scaling factors f_e of 0.1, 0.5, 1 and 10, respectively.

Basically, the same reasoning as given for the **low-rate** experiment and simulation hold. This is in itself encouraging: The model behavior is consistent and behaves as expected with respect to a change in boundary conditions. We therefore conclude that for the given boundary conditions and variations of parameters, a heat transfer scaling factor of $f_e = 0.5$ is the best choice.

However, it has to be noted that the lowest $f_e = 0.1$ gives the best match for the temperature difference at the entrance. The incorrect behavior of the solid phase temperature can be attributed to too rough an approximation of the heat losses to the surrounding. Higher heat losses would decrease solid phase temperature, as observed in the experiment.

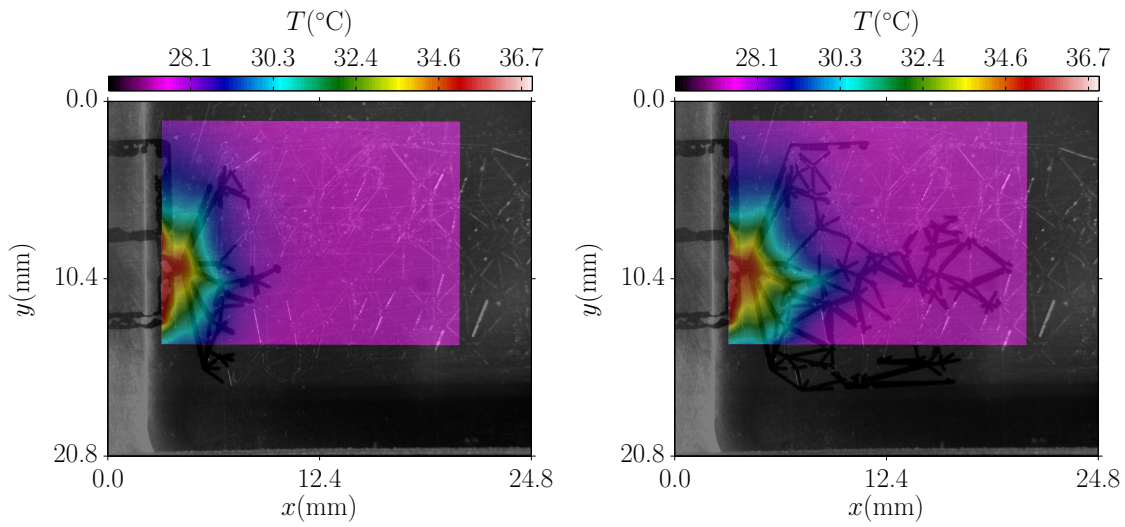


Figure 7.14: Overlay of high-rate temperature information and optical image after 5s (left) and 10s (right), see movie Chapter7_4.avi (showing a longer period)

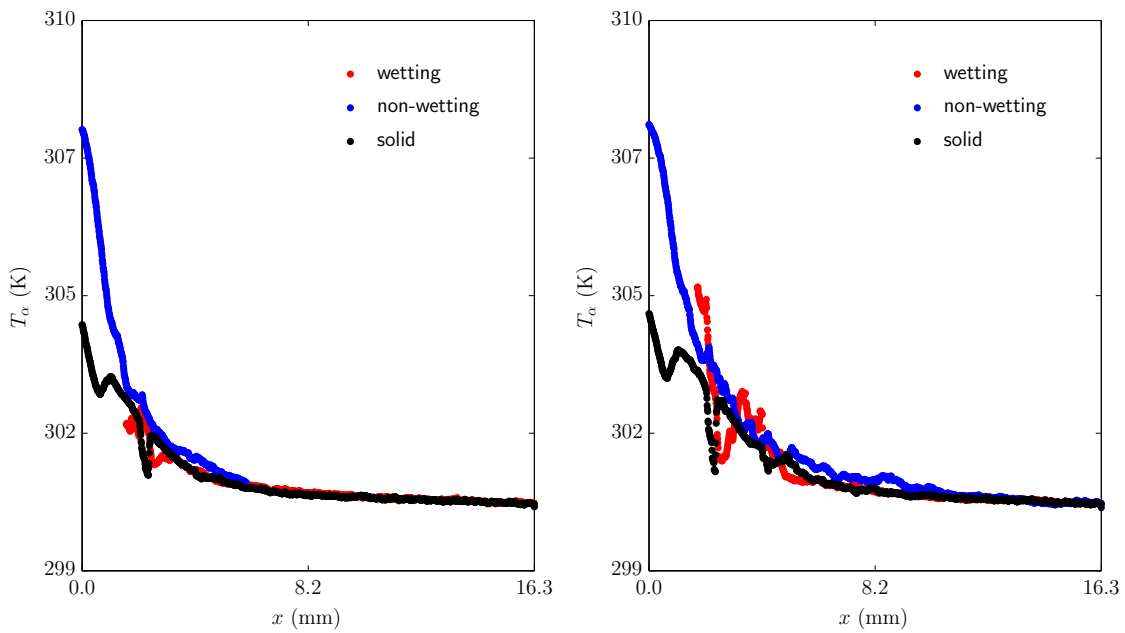


Figure 7.15: Experimental measurements, high-rate. **Left:** 5s after start of invasion, **Right:** 10s after start of invasion, see movie Chapter7_5.avi.

7 Estimating Transfer Coefficients: Simulation of the Experiment

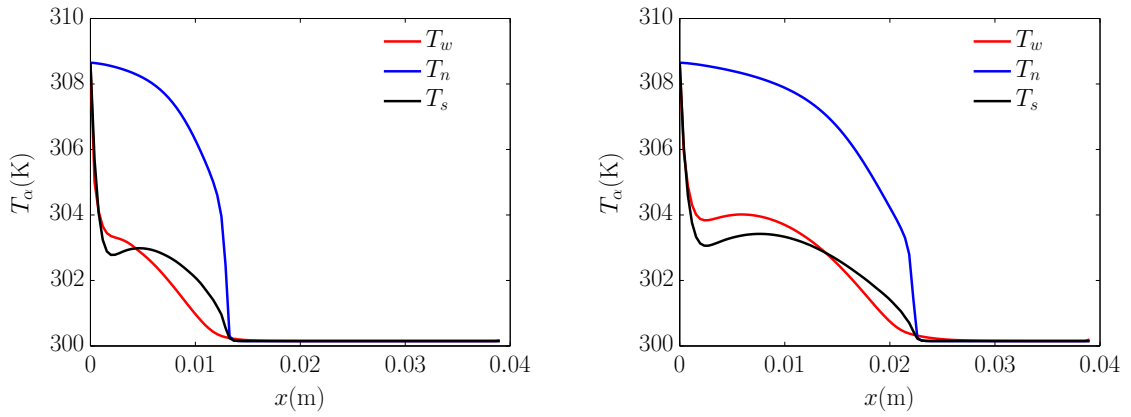


Figure 7.16: Simulation of the experiment, high-rate. **Left:** 5 s after start of invasion, **Right:** 10 s after start of invasion, $f_e = 0.1$.

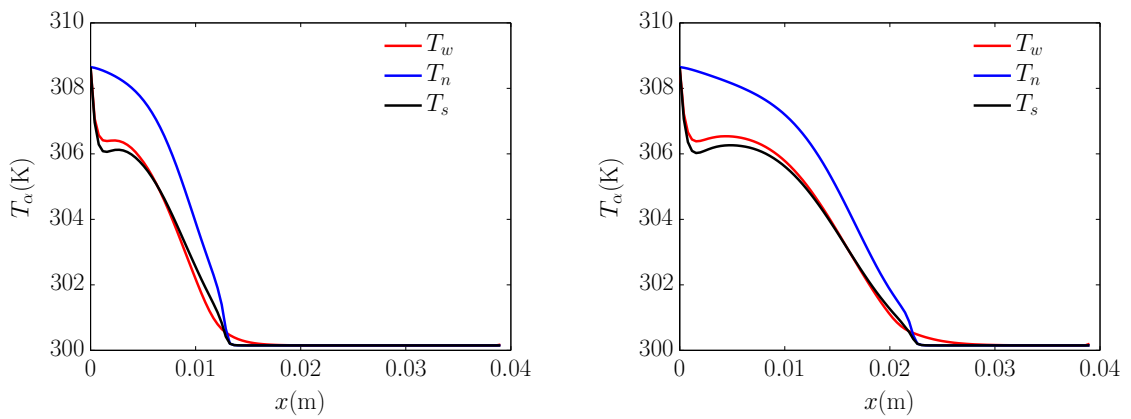


Figure 7.17: Simulation of the experiment, high-rate. **Left:** 5 s after start of invasion, **Right:** 10 s after start of invasion, $f_e = 0.5$.

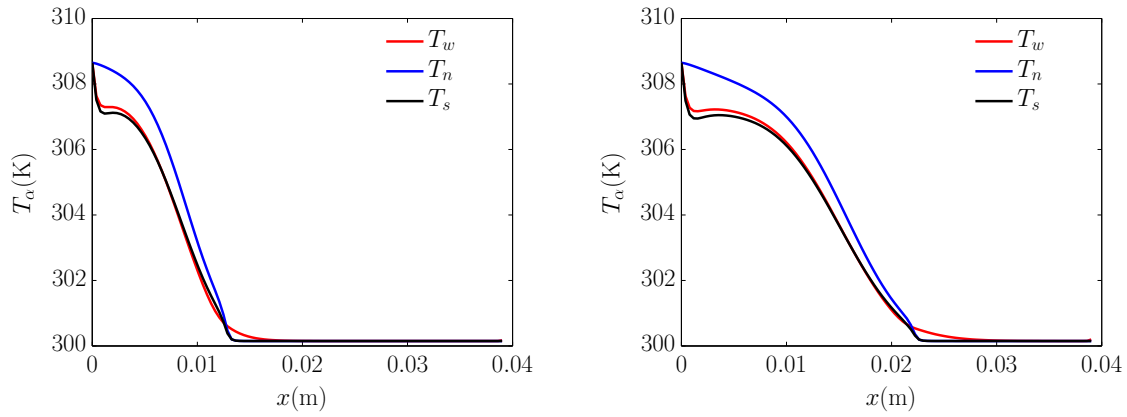


Figure 7.18: Simulation of the experiment, **high-rate**. **Left:** 5 s after start of invasion, **Right:** 10 s after start of invasion, $f_e = 1$.

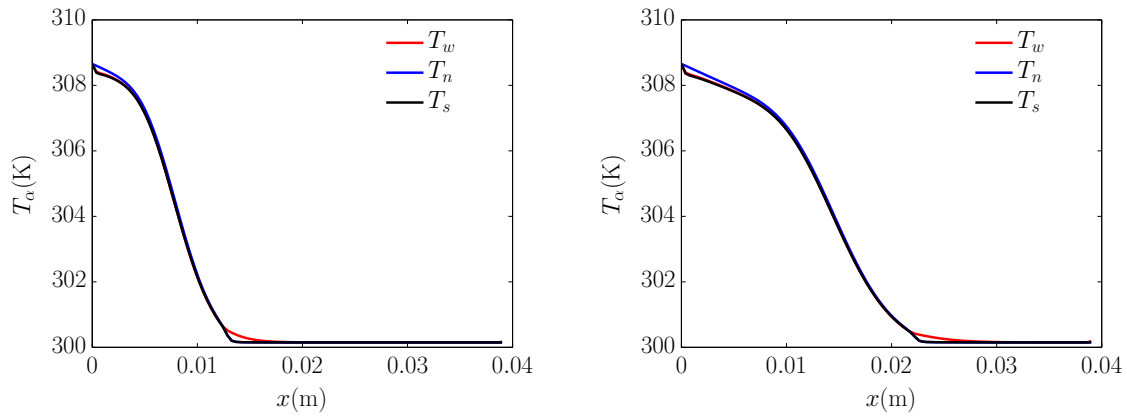


Figure 7.19: Simulation of the experiment, **high-rate**. **Left:** 5 s after start of invasion, **Right:** 10 s after start of invasion, $f_e = 10$.

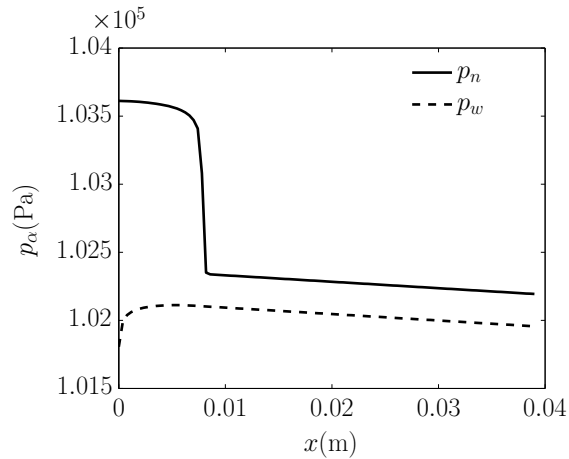


Figure 7.20: Pressure distribution in the simulated experiment. Capillary pressure causes an unintended pressure gradient to the left in the wetting phase.

7.5.3 Limitations of the Chosen Boundary Conditions

Figure 7.20 shows the pressure distribution of the `low-rate` simulation after 2 s simulated time. As explained in Section 7.4, on the left boundary a `DIRICHLET` value of $S_w = 0$ and in the domain an initial saturation of $S_w = 0.999$ is set. In other words: two adjacent nodes have states corresponding to the very ends of the capillary pressure – saturation curve (Figure 7.4). This leads to a big gradient in capillary pressure and thus in the wetting phase pressure. This gradient causes a flux of wetting phase leaving the left-hand side of the domain. This happens regardless of the zero mobility of the wetting phase on the left-hand boundary: Mobilities are either upwinded or obtained by central spatial weighting. This way, the non-zero upstream mobility is transferred to the boundary node. In order to fulfill mass conservation, more mass of the non-wetting phase has to enter the domain than caused by the `NEUMANN` boundary condition on the right-hand side alone.

Although this behavior fulfills the physical constraints (conservation equations, constitutive relations) formulated in the model, it leads to a behavior which is not observed in the experiment. The main result of the described effect is that too much mass of the non-wetting phase is in the system and the front locations cannot be exactly matched between simulation and experiment.

7.6 Summary & Conclusion

In this chapter, the experiment described in Chapter 6 was successfully simulated by means of a one-dimensional macro-scale model.

We provided detailed information about the simulation setup and employed material parameters. In order to obtain relevant input parameters to the macro-scale model, new image analysis algorithms have been developed and provided under a free license.

A number of issues remain unsolved in this context or had to be roughly approximated. First, and most notably, this is the role of heat losses to the environment. We chose an empirical formula, valid for free convection from a horizontal plate. However, the accuracy of such a formula remains open to validation in view of the given dimensions of the micro-model. The best approach would be to place the micro-model in a vacuum during the experiment in order to have good control over boundary conditions.

The role of residuals, and their associated interfacial areas, during kinetic energy exchange is to the best of our knowledge poorly understood. Up to now, residual interfacial areas and bulk phase interfacial areas are treated identically although residuals are not connected to bulk phases. Under the given flow conditions, they remain immobile and should therefore be treated differently from the bulk phases.

With respect to the imaging setup, the weakest points remain the synchronization of image streams (see Section 6.2.1) and the limited field of view of the infrared camera. In Section 7.5.3, we pointed out that the chosen boundary conditions do not perfectly match the observed behavior of the system.

In spite of the listed limitations of the presented model, the novelty and scientific contribution of the presented work are substantial. This is the first time for phase specific energy balances to be used in the simulation of an actual experiment. Furthermore, the experimental setup is new in its accessibility to optical and thermal observation. This is remarkable as it allows the phase specific attribution of temperatures. In other experimental setups in multiphase flow in porous media,

7 Estimating Transfer Coefficients: Simulation of the Experiment

it is often unclear or hard to control which temperature is actually measured. The detailed information as well as the decision to employ free and open-source software development strategies make our results open for testing and continuation.

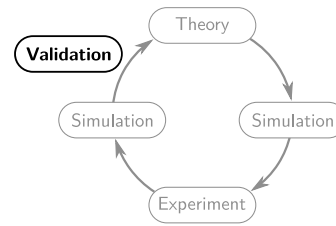
We give an order of magnitude estimate of the alleged heat transfer scaling factor of $f_e = 0.5$ for this setup.

The ultimate goal of this work is to study the correctness and applicability of the local thermal equilibrium assumption in multiphase flow in porous media. Therefore, the reasonable reproduction of the experimental observations can be taken as the point of origin for multiple further paths of research.

First of all, it has to be clearly stated that local thermal non-equilibrium is not of major importance for the given setup and boundary conditions. Therefore, either temperature differences between phases could be increased or, more interestingly, heat sources should be introduced in one of the present phases. This can be motivated by chemical reactions taking place or by the cooling of a severely damaged nuclear reactor core.

Another interesting direction of research is the study of averaging and the choice of appropriate models. The choice of using a one-dimensional model could be questioned. Beyond this question, the applicability of macro-scale models to this type of problem could be challenged. Interesting tools in this respect are pore-network models which can be seen as tools for volume averaging.

By the provided experimental, analysis and modelling tools, we give a solid foundation for the further study of local equilibrium assumptions in multiphase flow in porous media.



8

Forced Evaporation: Model Comparison for a Highly Non-Isothermal System⁸

Up to now, we developed a model and calibrated it to experimental observations. In another effort to increase confidence in model results, a comparison study of two independently developed numerical simulators is conducted in this chapter.

The second distinction of this chapter is the physical setup, which is to be simulated. We simulate a technical application: Metallic or ceramic evaporators are used for fuel pre-evaporation before combustion (Brandauer et al., 2002) or burners with small thermal output, see Figure 8.1. For a good overview of literature and applications see Wang and Cheng (1997).

For the sake of model comparison, the developed fully implicit macro-scale model is adapted to the problem at hand. The standard local chemical equilibrium module is combined with a local thermal non-equilibrium module. However, differently to the model presented so far, local thermal equilibrium is still assumed *between the fluid phases*. This results in *two* energy balance equations and temperatures: The temperatures in void space and solid phase are distinguished.

⁸This chapter is published in

Lindner, F., Nuske, P., Helmig, R., Mundt, C., and Pfitzner, M. (2014a). Transpiration cooling with local thermal non-equilibrium: Model comparison in multiphase flow in porous media. *Journal of Porous Media*. submitted

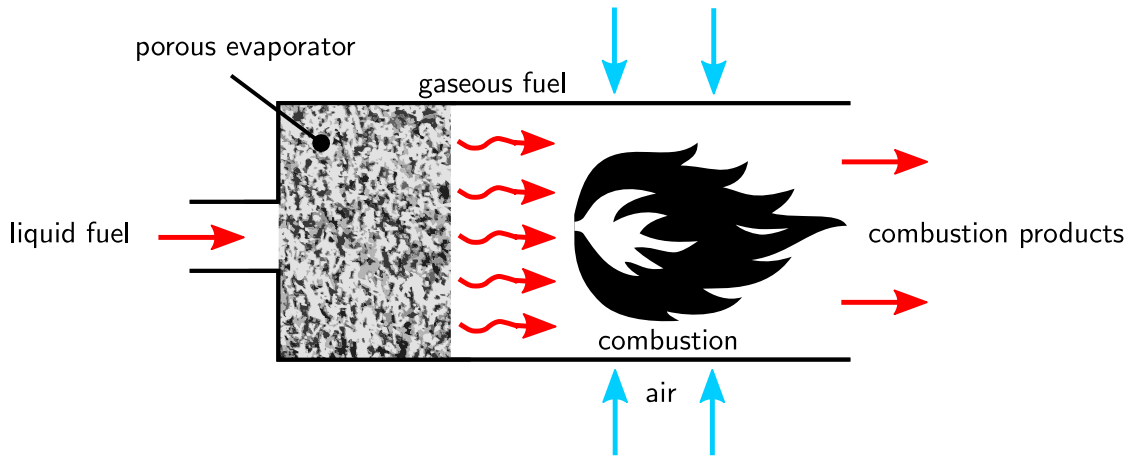


Figure 8.1: Schematic of a burner for small thermal output which utilizes a porous evaporator.

Bau and Torrance (1982) experimentally show for boiling in a vertical, porous medium filled cylinder which is heated from below and cooled from above that the evaporation process within the porous matrix can be divided into three zones: liquid region, two-phase region and superheated region. This is the physical setting which will be studied in this chapter. Therefore, we can benefit from the exact knowledge of the physical processes and apply energy transfer functions for boiling in the two-phase region and single-phase relations for the gas and liquid saturated parts.

Theoretically, for these three zones, three sets of energy equations could be solved according to the thermodynamic state of the fluid with separate phase models (SPM). The SPM require coupling of solutions through boundary conditions at the transition between the respective zones (macroscopic phase boundaries). Drawbacks of this approach are the need for tracking the interface between the zones and a large number of coupled conservation equations.

An alternative to this approach was presented in the work of Wang and Beckermann (1993) and Wang and Cheng (1996) who solved one set of conservation equations only for mixture variables using a volume averaging method. They developed a general set of conservation equations for the multiphase mixture and solved for enthalpy instead of temperature. These multiphase mixture models have been described and used in the literature (Wang, 1997; Li et al., 2010a,b,c; Yuki et al.,

2008; Xue, 2008; Wang et al., 1994; Wang, 1996; He et al., 2013; Lindner et al., 2014b).

For some cases, the local temperature difference between the fluid and the porous matrix cannot be neglected. In the case of heat sources or sinks in the solid matrix, fluid- and solid-phase temperatures may locally differ significantly (Wakao et al., 1979). In the following work, we use the term local thermal (non-) equilibrium indicating whether the local temperature difference between solid and fluid is (not) negligible. In the case of the local thermal equilibrium assumption breaking down, the individual compartments (solid – void) need to be described by individual energy balance equations leading to an increased number of unknowns.

Even without such sources or sinks, as Wang and Wang (2006) showed for gaseous fluids, the fluid mass flow rate (i.e. PECELET number) and the BIOT number in the pores are the most important parameters influencing the applicability of local thermal equilibrium (LTE) or non-equilibrium (LTNE) assumption. Using a two-energy equation approach to compute the temperatures of the fluid and the porous matrix, Shi and Wang (2011) have generalized the two-phase mixture model (TPMM) for local thermal non-equilibrium.

We aim to further discuss the numerical simulations of transpiration cooling with LTNE by showing the results of two models and comparing them to the results of Shi and Wang (2011). On the one hand, we show a newly developed fully coupled non-equilibrium model, which was implemented in DuMu^x (Flemisch et al., 2011). On the other hand, we show the results from a newly developed solver in Matlab (MATLAB, 2013), which uses the multiphase mixture model in LTNE. The solver in Matlab is verified by using the same set of equations and constitutive relations in Comsol (COMSOL, 2013).

This chapter is divided into six parts. First, the different models are introduced and discussed. We show differences and common features from the physical, as well as from the numerical point of view. Then, we discuss the numerical solution process for both concepts. Furthermore, we show the problem setup and boundary conditions which are taken from Shi and Wang (2011). Eventually, we show the numerical results and discuss similarities and deviations of the respective models.

8.1 Mathematical Models

In this section, we briefly introduce the governing equations of the presented models. First, in Section 8.1.1, the fully coupled system of equations, implemented in DuMu^x (Flemisch et al., 2011), will be presented. In Section 8.1.2, the two-phase mixture model will be explained. We conclude the section by showing common features and differences between the two mathematical models.

8.1.1 Fully Coupled Model

The balance equations constituting the fully coupled model are shown in Table 8.1. All presented conservation equations consist of a storage, a flux and a source/sink term. The storage terms will be further discussed in Section 8.1.3.

Equation 8.1 represents the mass conservation equation of a one component (water in liquid and gaseous state), two-phase system. It is a standard formulation for mass conservation in multiphase porous media flow (Helmig, 1997). All terms are described phase specifically and are subsequently summed up, because the mass of the considered component is conserved regardless of its phase state. This leads to one conservation equation as only one component is present in the system.

In order to capture local thermal non-equilibrium, i.e. the potentially differing temperatures in the solid phase and void space, at least two distinct energy conservation equations are needed. Equation 8.2 allows to calculate the temperature in the void space, i.e. an average temperature of up to two fluid phases. In fluids, energy can either be transported without the movement of mass (conduction) or it can be transported by the associated mass flux (advection). In the same sense, on the right-hand side, energy can either be provided associated with a mass flux (\dot{q}_{conv}) or directly (\dot{q}_{heat}).

The fluid and solid phases are (in an averaged sense) present at the same point. Therefore, the right-hand side of the equation has to capture sources and sinks as well as an exchange term (\dot{q}_{sf}) between the solid and fluid phases. The exchange

Table 8.1: Conservation equations of the fully coupled model. Momentum descriptions of the two models are discussed in Section 8.1.3.

Conservation of mass	$\sum_{\alpha} \frac{\partial (\phi S_{\alpha} \rho_{\alpha})}{\partial t} + \sum_{\alpha} \nabla \cdot (\rho_{\alpha} \mathbf{v}_{\alpha}) = \sum_{\alpha} \dot{q}_{\alpha} \quad (8.1)$
-------------------------	---

Conservation of fluid energy	$\sum_{\alpha} \frac{\partial (\phi \rho_{\alpha} S_{\alpha} h_{\alpha})}{\partial t} + \sum_{\alpha} \nabla \cdot (\rho_{\alpha} \mathbf{v}_{\alpha} h_{\alpha}) - \nabla \cdot (\lambda_{f \text{ eff}} \nabla T_f) =$ $+ \dot{q}_{\text{conv}} + \dot{q}_{f \text{ heat}} + \dot{q}_{sf} \quad (8.2)$
---------------------------------	--

Conservation of solid energy	$\frac{\partial ((1 - \phi) \rho_s c_s T_s)}{\partial t} - \nabla \cdot (\lambda_{s \text{ eff}} \nabla T_s) = \dot{q}_{s \text{ heat}} - \dot{q}_{sf} \quad (8.3)$
---------------------------------	---

term is identical for the two presented models and will therefore be explained in Section 8.1.3.

Equation 8.3 is the energy conservation equation for the solid phase. Here, energy can only be transported via conduction and sources / sinks can only be represented by direct input of energy. This means that we only allow energy but not mass flux into the solid phase.

In e.g. Crone et al. (2002) a similar implicit model, capturing the temperature difference between fluid phases and a coarse porous medium, is described. However, in their work the heating of a porous medium by an inflowing hot fluid phase is studied.

8.1.2 Two-Phase Mixture Model in Local Thermal Non-Equilibrium

In the following, the governing equations of the two-phase mixture model in local thermal non-equilibrium (TPMM-LTNE) are shown. The term mixture is used here with respect to fluid phases inside a control volume.

Table 8.2: Conservation equations of the TPMM-LTNE model (Shi and Wang, 2011). Momentum descriptions of the two models are discussed in Section 8.1.3.

Conservation of mass	$\nabla \cdot (\varrho \mathbf{v}) = \dot{q}$	(8.4)
-------------------------	---	-------

Conservation of fluid energy	$\nabla \cdot (\gamma_h \mathbf{v} H) - \nabla \cdot (\Gamma_h \nabla H) - \nabla \cdot \left[f(S_w) \frac{\mathbf{K} \Delta \varrho \Delta h_v}{\nu_n} \mathbf{g} \right] =$ $\dot{q}_{f \text{ heat}} + \dot{q}_{\text{conv}} + \dot{q}_{sf}$	(8.5)
---------------------------------	--	-------

Conservation of solid energy	$-\nabla \cdot (\lambda_{s \text{ eff}} \nabla T_s) = \dot{q}_{s \text{ heat}} - \dot{q}_{sf}$	(8.6)
---------------------------------	--	-------

In other words, not the properties of the individual phases are resolved, but properties of the mixture of the gas and liquid phases. Therefore, the variables ϱ, \mathbf{v}, H stand for the properties of the *mixture* of the liquid and gas phases (Wang, 1997; Wang and Beckermann, 1993) and will be called mixture variables in the scope of this chapter.

The formulation is used as presented by Shi and Wang (2011) who based their work on Wang (1997): Balance equations are formulated on the macro scale in a volume-averaged setting and capillary pressure is included as the macroscopic phase pressure difference. I.e. taking the energy conservation equation for the fluid at steady state, we sum up over the phases α and get:

$$\sum_{\alpha} \nabla \cdot (\varrho_{\alpha} \mathbf{v}_{\alpha} h_{\alpha}) - \nabla \cdot (\lambda_{f \text{ eff}} \nabla T_f) = \dot{q}_{\text{conv}} + \dot{q}_{f \text{ heat}} + \dot{q}_{sf}. \quad (8.7)$$

Instead of using the sum in the first term of Equation 8.7, the volumetric mixture enthalpy H is used (Wang and Beckermann, 1993). Introducing more mixture terms and rearranging Equation 8.7, we solve an energy conservation equation for the fluid mixture. Temperature differences between solid and fluid are allowed, leading to two energy conservation equations. The conservation equations for steady flow are summarized in Table 8.2, i.e. conservation of mass as well as fluid and solid energy.

The properties of the phases are captured by mixture variables. Having a look at Equation 8.5, the first term accounts for advective fluxes of the energy of the phases. Energy fluxes due to relative phase motion can be capillary diffusion due to capillary pressure and density-driven gravity effects. The former is captured by the second term and the latter is implemented in the third term. Heat conduction is also accounted for by the second term as a sub-term in the effective diffusion coefficient Γ_h .

For brevity, the mixture variables and properties as well as the supplemental equations for enthalpy (H) and the hindrance function (f) are not discussed here, and the reader is referred to the literature (Wang, 1997; Wang and Beckermann, 1993).

8.1.3 Common Features and Differences

The two models presented above are two ways to look at the same thing, i.e. energy and mass conservation in a porous medium without assuming local thermal equilibrium between fluid and solid phases and including capillary pressure.

Therefore, several aspects of the two models are identical, as the same physics are to be captured. These will be explained first.

Energy Transfer

Both models apply the heat transfer relation proposed by Shi and Wang (2011) for the case of evaporative cooling by an external heat source. It is based on the phase state as well as flow and fluid properties:

$$\dot{q}_{sf} = \bar{h}_{sw} a_s (T_s - T_f) \quad \text{for } S_w = 1, \quad (8.8)$$

$$\dot{q}_{sf} = (1 - S_w) \bar{h}_{sn} a_s (T_s - T_f) + S_w a_s \dot{q}_{\text{boil}} \quad \text{for } 0 < S_w < 1, \quad (8.9)$$

$$\dot{q}_{sf} = \bar{h}_{sn} a_s (T_s - T_f) \quad \text{for } S_w = 0, \quad (8.10)$$

where

$$\dot{q}_{\text{boil}} = \mu_w \Delta h_v \left[\frac{g(\rho_w - \rho_n)}{\sigma} \right]^{0.5} \left[\frac{c_w(T_s - T_{\text{sat}})}{b_{sf} \Delta h_v \text{Pr}_w^{1.7}} \right]^3 \quad (8.11)$$

is the heat which is exchanged between solid and fluid for boiling processes (Rohsenow, 1952; Clark and Rohsenow, 1954). The factor b_{sf} represents a constant for a unique combination of fluid and solid surface, $b_{sf} = 0.006$ for water and bronze is chosen. T_{sat} is the temperature of the boiling component for a given pressure.

In the one-phase liquid region ($S_w = 1$), heat transfer is a function of the temperature difference between solid and fluid phases, see Equation 8.8, which describes the sensible heat flux. However, in the two-phase regime ($1 > S_w > 0$), the heat transfer function is more complex as the boiling process influences the heat transfer. This is captured by the contribution of \dot{q}_{boil} in Equation 8.9, which accounts for the latent heat flux. Potentially, in this region, there is energy transfer without a temperature difference between the phases.

Heat transfer in the single-phase gaseous region ($S_w = 0$) is again a function of the temperature difference between solid and fluid phases, see Equation 8.10.

The mean heat transfer coefficient between the solid and the respective fluid phase α , $\bar{h}_{s\alpha}$, is calculated by means of the NUSSELT number

$$\text{Nu}_\alpha = \frac{\bar{h}_{s\alpha} L}{\lambda_\alpha} \quad \alpha = w, n \quad (8.12)$$

and a NUSSELT-correlation (Wakao and Kagei, 1982) for the case of heat transfer in a porous medium under single-phase conditions

$$\text{Nu}_\alpha = 2 + 1.1 \text{Pr}_\alpha^{1/3} \text{Re}_\alpha^{3/5}. \quad (8.13)$$

As characteristic length L , the characteristic size of the porous medium d_P is chosen.

Phase specific REYNOLDS numbers are computed by means of the respective phase velocities \mathbf{v}_α

$$\text{Re} = \frac{|\mathbf{v}_\alpha| L}{\nu_\alpha}. \quad (8.14)$$

In the case of the TPMM model, velocities have to be extracted from the mixture velocity, taking into account the diffusive mass flux (Wang, 1997). The fully coupled

model obtains volume-averaged velocities by averaging the phase velocities defined on the faces of the control volumes.

Capillary Pressure Relation & Relative Permeability

The two presented models have a different notion of phase pressure. However, the same function for the macroscopic phase pressure difference (p_c) is applied (Udell, 1985)

$$p_c = \sigma \sqrt{\frac{\phi}{K}} \left(1.263(1 - S_w)^3 - 2.120(1 - S_w)^2 + 1.417(1 - S_w) \right). \quad (8.15)$$

This function incorporates the influence of surface tension (σ) as well as permeability (K) and porosity (ϕ) on capillary pressure. Also based on Udell (1985) the relative permeabilities in both models are chosen as

$$k_{rw} = S_w^3 \quad (8.16)$$

$$k_{rn} = (1 - S_w)^3. \quad (8.17)$$

Average Conductivities & Remaining Quantities

Both models use the same average conductivities

$$\lambda_{f \text{ eff}} = \phi \lambda_f \quad \text{with } \lambda_f = S_w \lambda_w + (1 - S_w) \lambda_n \quad (8.18)$$

$$\lambda_{s \text{ eff}} = (1 - \phi) \lambda_s. \quad (8.19)$$

Volume changing work is neglected and fluid properties are assumed constant as listed in Table 8.4 and in more detail in Shi and Wang (2011).

Time Discretization

The TPMM, presented here, is stationary in time. It can describe problems which are known a priori to have a steady solution. The fully coupled model, on the other hand, is transient. It cannot only resolve a stationary final state of a problem, but also the transition from the initial state to a potentially stationary state.

One could argue that the given problem is stationary in time and therefore a stationary model is the appropriate choice. However, in DuMu^x we generally strive for the highest possible generality and re-usability of code. Therefore, the non-steady model described in Table 8.1 is applied and the desired stationary state is identified from analysis of the result. When variables do not change over time any more, the solution is considered stationary and results are compared to the TPMM model results.

Treatment of Components

The TPMM model treats a mixture of different phases. In the case of multicomponent flow, the distribution of the respective components between the phases, present at a point, has to be determined by extra conservation equations for components and computation of the vapor liquid equilibria in the two-phase zone.

The fully coupled model, on the other hand, bases the mass conservation on component balances. Each component has its own balance equation, which allows a straight forward extension to more considered components.

In this chapter, we only deal with a single-component flow setup for the fluid. Therefore, this difference is not of major importance. However, in Appendix A the extension to two components is discussed.

Momentum Description

Both Models apply extended DARCY's law, although in different notions. In the case of the TPMM model, a mixture pressure p drives a mixture velocity \mathbf{v}

$$\mathbf{v} = -\frac{K}{\mu} (\nabla p - \rho_k \mathbf{g}) . \quad (8.20)$$

The fully coupled model, on the other hand, calculates phase velocities \mathbf{v}_α which

are based on phase pressures p_α

$$\mathbf{v}_\alpha = -\frac{Kk_{r\alpha}(S_w)}{\mu_\alpha} (\nabla p_\alpha - \varrho_\alpha \mathbf{g}). \quad (8.21)$$

Further Differences

In Section 8.2, the numerical solution schemes of the two models will be explained in more detail. Section 8.3 will present model specific adaptations of the boundary conditions, necessary in order to simulate the given problem.

8.2 Numerical Solution

In this section, the numerical procedures, used to solve the fully coupled as well as the TPMM model, are presented. Naturally, the degree of detail varies, as the fully coupled model is part of a bigger endeavor (DuMu^x) which is documented elsewhere (Flemisch et al., 2011; Nuske et al., 2014a). DuMu^x is free and open-source software, published under the GPL (Free Software Foundation, 1991), see Section 3.5 for details. Therefore, also the source code can be directly studied.

8.2.1 Numerical Solution Fully Coupled Model

Space discretization is accomplished by a vertex centered finite volume (Huber and Helmig, 2000) scheme. As mentioned earlier, although the problem in this chapter is stationary, the fully coupled model, presented in Table 8.1, is non-steady. In terms of time discretization, a fully implicit scheme is chosen. The resulting set of partial differential equations is linearized by means of numerical forward differentiation and a NEWTON-scheme. Full upwinding is used for all simulations.

The only adaptation in terms of numerical solution which had to be applied was a regularization of the energy transfer function (\dot{q}_{sf}). As explained in Section 8.1.3, the approach for energy transfer is different in the single-phase and two-phase regions.

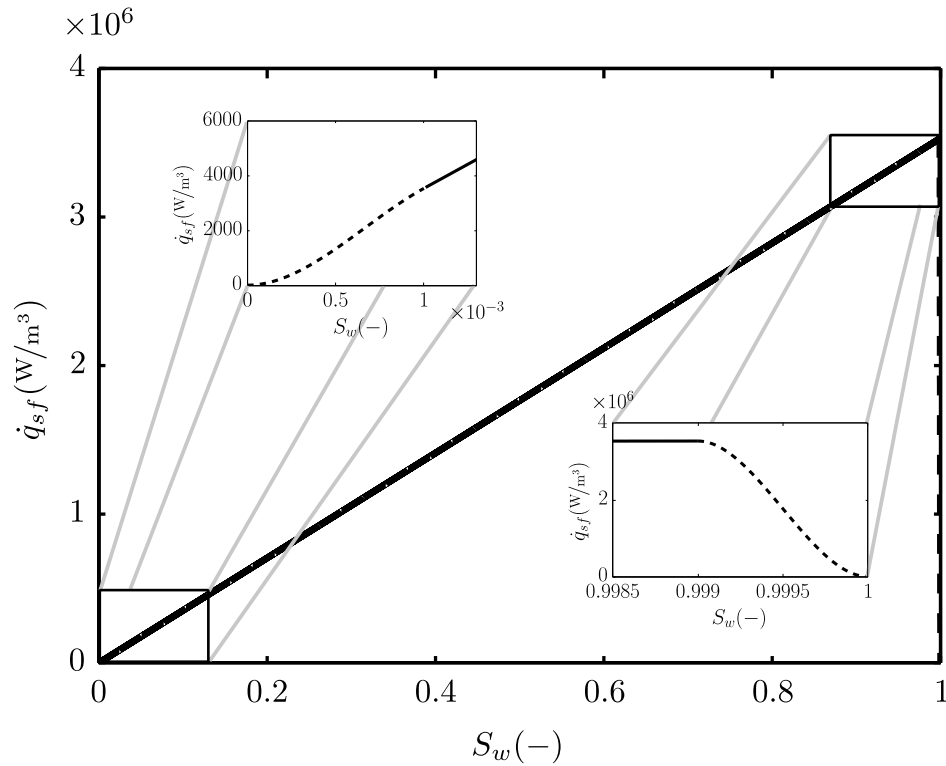


Figure 8.2: Heat transfer function in the two-phase region for a fixed temperature difference $T_s - T_{\text{sat}} = 1$ K. The regularized parts are depicted as dashed lines.

Actually, there is a kink in the energy transfer function at the transition from a gaseous to a two-phase state and it is even non-continuous with respect to saturation at the transition from two-phase to liquid state. The problem of interest is stationary in time and exhibits sharp gradients in saturation. Therefore, the described transitions lead to numerical problems.

These problems are counteracted by regularizing the energy transfer function by means of a third order spline for low ($S_w < 10^{-3}$) and high ($S_w > 0.999$) saturations, see Figure 8.2.

8.2.2 Numerical Solution TPMM-LTNE

Two different solvers were used in order to verify simulation results. First, the in-house developed Matlab solver, based on R2013a, is explained (Solver 1) followed

by the description of the Comsol implementation (Solver 2).

Solver 1 implements the equation system of Table 8.2 by means of a cell centered finite volume scheme. It is solved in an iterative manner:

1. Initialize: $S_w, T_f(\rightarrow H), T_s, \mathbf{v}$
2. Compute mixture variables
3. Compute velocity field
4. Compute heat transfer coefficients with phase velocities
5. Compute temperature fields for the coupled energy equations
6. Compute residuum for energy field and continue with step 2 if convergence criterion is not met

As a convergence criterion, it is demanded that temperatures do not vary between iterations any more. Numerically, this means that the root mean square of the relative difference of temperatures T_f and T_s at all cells i between successive iterations, n and $n + 1$, should be below 10^{-5} :

$$\sqrt{\frac{1}{2n} \sum_i \left[\left(\frac{T_{si}^{n+1} - T_{si}^n}{T_{si}^n} \right)^2 + \left(\frac{T_{fi}^{n+1} - T_{fi}^n}{T_{fi}^n} \right)^2 \right]} < 10^{-5}. \quad (8.22)$$

It was tested and made sure that this criterion goes along with a converged saturation distribution. Under-relaxation iteration is used for the coupled energy equations.

Inserting the momentum conservation equation of the TPMM into the mass conservation equation, i.e. Equation 8.20 into Equation 8.4 leads to:

$$\nabla \cdot \left(\varrho \left(-\frac{\mathbf{K}}{\mu} (\nabla p - \varrho_k \mathbf{g}) \right) \right) = \dot{q}. \quad (8.23)$$

Comparing Equation 8.23 with single-phase flow conservation equations, e.g. as used in MRST (Lie et al., 2012),

$$\nabla \cdot \left(-\frac{\mathbf{K}}{\mu_w} (\nabla p_w - \varrho_w \mathbf{g}) \right) = \dot{q} / \varrho_w, \quad (8.24)$$

one can see that their mathematical structure is identical.

Pressure is differently defined in MRST (global pressure) and TPMM (mixture pressure). Since the mixture pressure is just used as an auxiliary variable to compute the mixture velocity, the single-phase formulation (Equation 8.24) can be used in MRST, if one incorporates the variable mixture density ϱ in the cells. This is done by solving for the velocity field with a hybrid solver in MRST v. 2013a with an extension for variable density, i.e. implementing the mixture density in the transmissibility matrix.

In other words, the driving potential gradient of fluid flow for MRST can be exchanged by a mixture pressure gradient, if you consider mixture variables instead of single-phase variables. In a mathematical sense, these two are identical.

Grid convergence was investigated with different grid resolutions of 1000, 1500 and 2000 cells. Independence of the grid was found with choosing 1500 cells, with the maximum difference (to the finer grid) of the solid temperature of less than 1%.

The convective fluxes are stored at the cell interfaces. A Power-Law is used for treatment of the advective and diffusive fluxes (Patankar, 1980). For large advective fluxes at cell interfaces, a numerical upwinding scheme is used for stability reasons.

The switch between these discretization schemes is based on a PécLET number (Pe) related criterion, which will be explained in the following. The PécLET number at the cells is defined inspired by Patankar (1980) with the cell width Δx and the velocity \mathbf{v} as

$$\text{Pe} := \frac{\gamma_h |\mathbf{v}|}{\Gamma_h / \Delta x}. \quad (8.25)$$

Using this definition, upwinding is used for $\text{Pe} \geq 10$. Note that for this distinction, the advective and diffusive fluxes in a mathematical sense, according to Table 8.2,

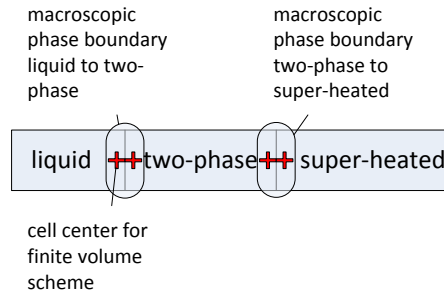


Figure 8.3: Macroscopic phase boundaries and position of cell centers for finite volume scheme. See porous evaporator in Figure 8.1.

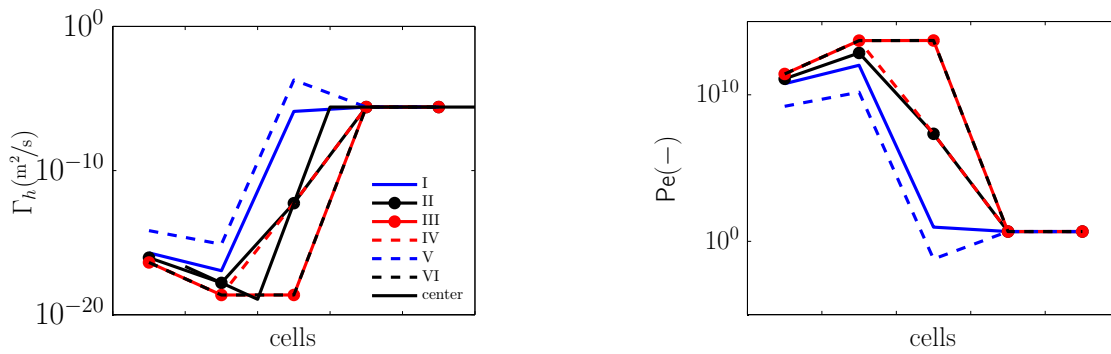


Figure 8.4: Γ_h and Pe for a generic transition between two-phase and super-heated region. The solid black lines (without markers) represent the actual values at cell centers, while the other lines indicate approximated values at cell interfaces.

are used. In other words, the diffusive fluxes consist of capillary and conductive fluxes.

As Γ_h degenerates at macroscopic phase boundaries, Pe tends to infinity. See Figure 8.3 for definitions of the terms macroscopic phase boundary and the position of cell centers for the finite volume scheme. Degenerating diffusive fluxes can introduce numerical instability. Thus, we examined different possibilities of evaluating the effective diffusion coefficient, Γ_h . It is needed at cell interfaces and therefore needs to be obtained by averaging cell values. However, the method of averaging for the diffusion coefficient at the cell interfaces has an influence of several orders of magnitude on Γ_h itself.

In the following, we will show the influence of several prominent averaging schemes on Γ_h , namely:

8 Forced Evaporation: Model Comparison for a Non-Isothermal System

- I arithmetic mean
- II geometric mean
- III harmonic mean
- IV harmonic mean with arithmetic mean of $\log_{10} \Gamma_h$ at macroscopic phase boundaries
- V modified Kirchhoff-method (Voller and Swaminathan, 1993)
- VI modified Kirchhoff-method with arithmetic mean of $\log_{10} \Gamma_h$ at macroscopic phase boundaries

Using the Kirchhoff approximation (cases V and VI), an additional nested iteration has to be used:

1. given H_i , compute Γ_{hi} at cell centers i
2. compute $\Gamma_{hi\pm 1/2}$ at cell interfaces $i \pm 1/2$
3. solve energy equations $\rightarrow H_i$
4. compute Γ_{hi} with mixture variables
5. compute residuum for energy field and $\Gamma_{hi\pm 1/2}$ and continue with step 1 if convergence criterion is not met

In Figure 8.4, we show Γ_{hi} at the cell centers and the corresponding $\Gamma_{hi\pm 1/2}$ at the cell interfaces for cases I to VI for a generic shift of two-phase to super-heated zone according to Figure 8.3. We also show the corresponding Pe numbers for these cell interfaces. As the effective diffusion coefficient varies by several orders of magnitude, depending on the method of computation at the cell interfaces, the Péclet number also varies in several orders of magnitude.

For cases V and VI, the values after the first iteration are shown. Clearly, using the Kirchhoff-method, the computational effort is larger. The influence of the methods for computation of Γ_h at the cell interfaces on simulation results is discussed in Section 8.4.2. To evaluate Pe at the cell interfaces, γ_h has to be interpolated at

the cell interfaces. The same procedure as for Γ_h is used. For the following results, case IV was used.

Solver 2 solves the same equations with a finite element scheme in Comsol v. 3.5a. In Comsol, the mass and momentum conservation equations are solved using the Subsurface Flow module, and the energy conservation equations are solved using the PDE module. The results of Solver 1 and Solver 2 are almost identical. Thus, the differences between the results from the solvers are not discussed here but are taken as cross-validation of model implementation and numerics. In the following sections, only results from Solver 1 are shown.

8.2.3 Differences in Numerics

The main difference, with respect to numerics, is the order in which the formulated balance equations are solved. The fully coupled model solves all given balance equations simultaneously. As it is not stationary, it can be added that all unknowns are solved for at the new time-level (fully implicit).

The TPMM model, on the other hand, solves the equations iteratively. Starting from an initial condition, the given equations are solved consecutively and solutions are used in the next iteration. In that sense, the numerical solution of the TPMM model can be called a decoupled scheme.

8.3 Problem Setup & Boundary Conditions

In this section, we first describe the physical problem setup which is simulated in this context. Next, we will explain the boundary conditions implemented in the respective models.

We simulate the complete evaporation of a liquid within a porous medium, see Figure 8.1. The liquid phase enters the domain over one boundary with a given mass flux. On the other boundary of the porous medium there is energy supply to the solid phase, atmospheric pressure conditions prevail and all fluid mass can

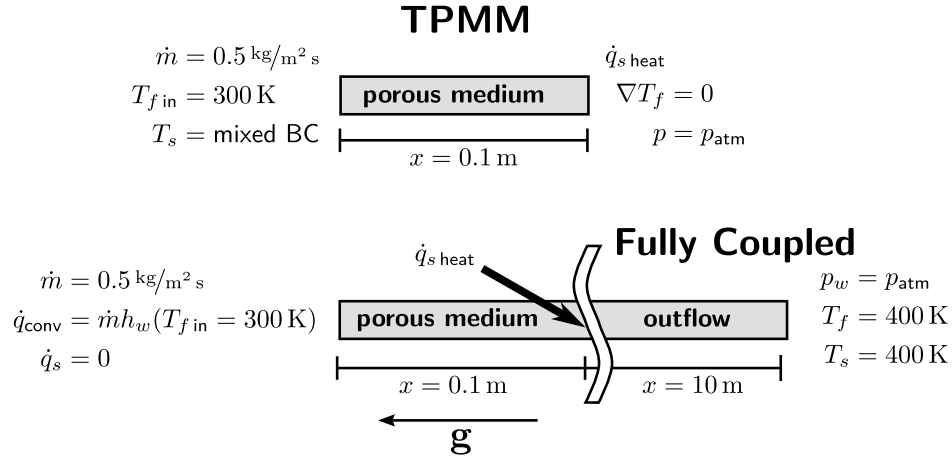


Figure 8.5: Problem setup and boundary conditions for the two models. More implementation related details are adapted as described in Shi and Wang (2011).

leave the system. The heat is exclusively provided to the solid phase because the gas phase is assumed to be transparent to radiation.

The solid phase consists of a metallic material with a high heat conductivity. This leads to complete evaporation of the injected fluid before reaching the exit of the porous medium. Liquid water is the wetting phase and water vapor is the non-wetting phase in this context.

Three regions can be distinguished in the domain. First, the fluid is heated up in a single-phase liquid region. Upon reaching boiling conditions, a two-phase region, with gas and liquid present, follows. In this region, capillary forces act on fluid movement. After the liquid is completely evaporated, a single-phase gas region starts where the gas is further heated up, until reaching the exit of the porous domain, see Figure 8.3. This setup is known in literature as transpiration cooling (Kaviany, 2002). However, the work presented in this chapter is motivated by the mathematically identical application of porous evaporators, see Figure 8.1.

In this chapter, we will only treat single-component (water) flow. This has two reasons. We want to limit the degrees of freedom and keep the system as simple as possible in order to compare the two presented models. Secondly, there are published simulation results (Shi and Wang, 2011) for the described setup, allowing comparison of our models to these results. Parameter values, describing the fluids

8.3 Problem Setup & Boundary Conditions

Table 8.3: Properties of the porous medium.

Property	Value	Unit
K	$1.69 \cdot 10^{-10}$	m ²
ϕ	0.35	-
λ_s	30	W/mK

as well as the porous medium, are shown in Tables 8.3 and 8.4.

The boundary conditions, implemented in order to simulate the above described physical setup, are summarized in Figure 8.5. The numerical boundary conditions on the left-hand side of the domain are almost identical for the mass conservation of the coupled and the TPMM model. Water enters the simulation domain via a NEUMANN boundary condition.

In the TPMM model, temperature is fixed with a DIRICHLET boundary condition for the fluid and the solid phase is covered by the same mixed boundary condition, as Shi and Wang (2011) are using. This is a mixed boundary condition of third order taken from Wang and Shi (2008)

$$\lambda_{s \text{ eff}} \frac{\partial T_s}{\partial x} + \Gamma_h \frac{\partial H}{\partial x} + f \frac{K \Delta \rho \Delta h_v}{\nu_n} g = \bar{h}_{\text{in}} (T_s - T_{f \text{ in}}). \quad (8.26)$$

The fully coupled model injects the energy flux associated with the given mass flux and the DIRICHLET temperature of the TPMM model ($T_{f \text{ in}} = 300$ K) in the fluid balance equation. NEUMANN no-flow is set for the solid phase.

Table 8.4: Main fluid properties as used in both models.

Property	Liquid	Gas	Unit
ρ_α	1044	1.679	kg/m ³
c_α	$4.217 \cdot 10^3$	$2.029 \cdot 10^3$	J/kgK
ν_α	$2.694 \cdot 10^{-7}$	$7.16 \cdot 10^{-6}$	m ² /s
λ_α	0.68	0.0248	W/mK
σ		0.0589	N/m
Δh_v		$2.257 \cdot 10^6$	J/kg
T_{sat}		373	K

On the right-hand side, different approaches had to be chosen. The TPMM model prescribes a zero gradient in fluid temperature, allows mass to freely leave the domain and injects energy into the solid phase.

However, this was not straight forward to implement in DuMu^x. Therefore, an approach mimicking the described physical setup was chosen. The simulation domain is extended (outflow region) in the direction of flow and atmospheric pressure prevails at the end of the extended domain. Heating was implemented as a source term to the solid phase at $x = 0.1$ m, see Figure 8.5.

In the outflow region, material properties were adapted such that they have as little influence on simulation results as possible. Permeability is set to a value four orders of magnitudes above the value of the porous medium in order to keep the pressure gradient in the outflow region as small as possible. The heat conductivity in the outflow region is two orders of magnitudes smaller than in the porous medium such that as little heat as possible is lost to the outflow region.

All simulations are carried out in 1d. The stationary state of the described models is used for comparison.

8.4 Results and Discussion

In this section, we will present results of the models explained in Section 8.1. First, an analytical calculation of the outlet temperature is presented. Next, results from the two models for different boundary conditions are compared to one another and to values found in the literature. Finally, the influence of key parameters on simulation results is analyzed.

8.4.1 Analytical Outlet Temperature

In order to get a priori knowledge about the system described above, we analytically estimate the temperature of the fluid phase at the exit of the porous domain. A typical case, according to Figure 8.5, can be divided into three regions, which

correspond to the heating of liquid fluid to saturation state, complete evaporation until dry steam conditions are reached and further heating of the super-heated vapor:

$$\underbrace{\text{liquid} \longrightarrow \text{start of two-phase}}_{\Delta\dot{q}_1 = \dot{m}c_w(T_{\text{sat}} - T_{\text{in}})} \underbrace{\text{phase change}}_{\Delta\dot{q}_2 = \dot{m}\Delta h_v} \underbrace{\text{end of two-phase} \longrightarrow \text{super-heated}}_{\Delta\dot{q}_3 = \dot{m}c_n(T_{\text{ex}} - T_{\text{sat}})}.$$

$\dot{q}_{\text{dryout}} = \dot{m} [c_w(T_{\text{sat}} - T_{\text{in}}) + \Delta h_v]$ is the minimal heat flux to completely evaporate the fluid mass flux. The fluid exit temperature T_{ex} can be calculated analytically with the heat flux boundary condition $\dot{q}_{s \text{ heat}}$

$$T_{\text{ex}} = \begin{cases} T_{\text{in}} + \frac{\dot{q}_{s \text{ heat}}}{\dot{m}c_w}, & \text{if } \dot{q}_{s \text{ heat}} \leq \dot{m}c_w(T_{\text{sat}} - T_{\text{in}}) \\ T_{\text{sat}}, & \text{if } \dot{m}c_w(T_{\text{sat}} - T_{\text{in}}) < \dot{q}_{s \text{ heat}} < \dot{q}_{\text{dryout}} \\ T_{\text{sat}} + \frac{\dot{q}_{s \text{ heat}} - \dot{q}_{\text{dryout}}}{\dot{m}c_n}, & \text{if } \dot{q}_{\text{dryout}} \leq \dot{q}_{s \text{ heat}} \end{cases} \quad (8.27)$$

This is of course only true, if the solid is not conducting any heat at the inlet:

$$\lambda_{s \text{ eff}} \left. \frac{\partial T_s}{\partial x} \right|_{\text{in}} = 0 \quad (8.28)$$

Furthermore, heat conduction of the fluid should be zero or negligible at the inlet and exit, which we assume by choosing the boundary conditions mentioned in Section 8.3.

Table 8.5 shows results of the TPMM presented in this work (Solver 1 and Solver 2) and the fully coupled model, in comparison with the values found in the literature. Both results from the TPMM, as well as the coupled model, are in good agreement with the analytical solution.

8.4.2 Results and Model Comparison

Both solvers for the TPMM (Matlab and Comsol, see Section 8.2.2) show almost the same fluid exit temperatures for the same set of boundary conditions. To

Table 8.5: Comparison of the outlet fluid-temperature between Shi and Wang (2011), the Matlab and Comsol solvers of the TPMM (Solver 1 and Solver 2) and the fully coupled model.

boundary conditions	$\frac{T_{f, \text{num}} _{y=L}}{T_{f, \text{analyt}} _{y=L}}$		
	Shi	Solver 1, Solver 2	fully coupled model
$\dot{m} = 0.3 \text{ kg/m}^2 \text{ s}, \dot{q}_{s \text{ heat}} = 10^6 \text{ W/m}^2$	0.944	0.994	1.000
$\dot{m} = 0.5 \text{ kg/m}^2 \text{ s}, \dot{q}_{s \text{ heat}} = 1.5 \cdot 10^6 \text{ W/m}^2$	0.992	1.000	1.000
$\dot{m} = 0.5 \text{ kg/m}^2 \text{ s}, \dot{q}_{s \text{ heat}} = 2 \cdot 10^6 \text{ W/m}^2$	0.981	1.000	1.000

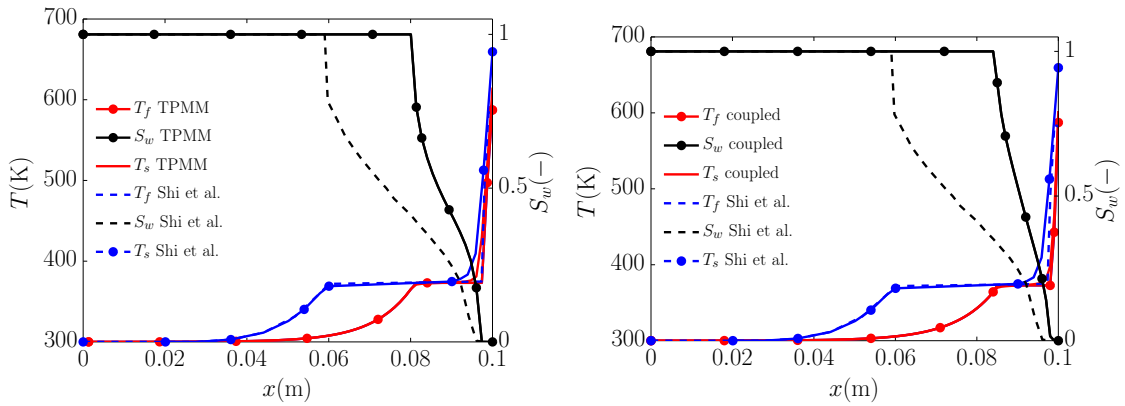


Figure 8.6: **Left:** Comparison between Solver 1 and Shi and Wang (2011). **Right:** Comparison between the fully coupled model and Shi and Wang (2011). Heat injection of $\dot{q}_{s \text{ heat}} = 1.5 \cdot 10^6 \text{ W/m}^2$.

enable a converging solution in Solver 2, smoothing of the degenerating diffusion coefficient Γ_h was necessary in Comsol. The relative length of the smoothing was set to 0.02. It is not necessary for Solver 1 to smooth Γ_h in order to achieve a converged solution.

The maximum difference of the solid temperature between the two solvers is less than 0.3%, the maximum difference of the fluid temperature is less than 0.4%. As the results of the two solvers are virtually identical, only results of Solver 1 will be used for model comparison.

Figures 8.6 and 8.7 show the comparison between the TPMM, the fully coupled model and Shi and Wang (2011). We chose the parameters specified in Tables 8.3

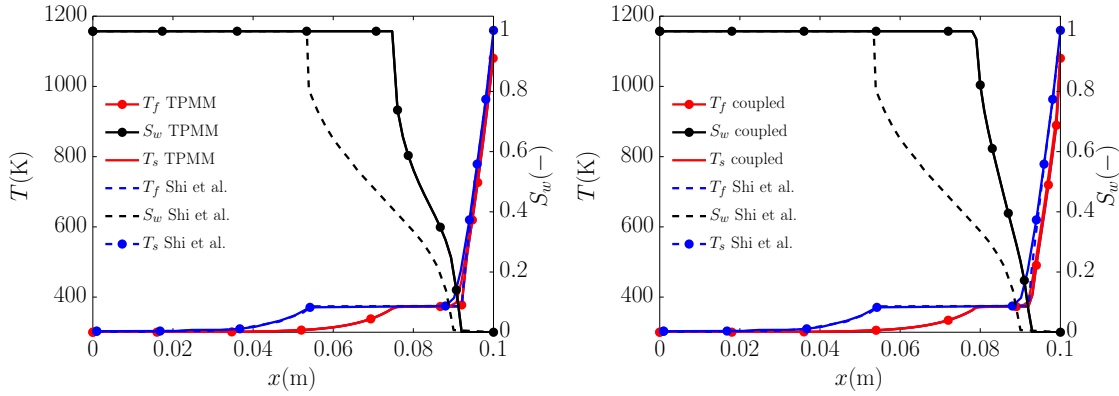


Figure 8.7: Left: Comparison between Solver 1 and Shi and Wang (2011). **Right:** Comparison between the fully coupled model and Shi and Wang (2011). Heat injection of $\dot{q}_{s\text{ heat}} = 2 \cdot 10^6 \text{ W/m}^2$.

and 8.4 as published in Shi and Wang (2011). The heat flux is varied between $\dot{q}_{s\text{ heat}} = 1.5 \cdot 10^6 \text{ W/m}^2$ (Figure 8.6) and $\dot{q}_{s\text{ heat}} = 2 \cdot 10^6 \text{ W/m}^2$ (Figure 8.7).

Lacking the raw data of Shi and Wang (2011), we have analyzed the graphs which were published. Within a reading accuracy of 5 K, the data points were extracted from the graphs.

Figure 8.8 shows only the saturation of the water phase obtained by Solver 1, the fully coupled model and the results from Shi and Wang (2011) for the same cases as in Figures 8.6 and 8.7. While the trend of the slope for the biphasic regime is similar for both results based on the TPMM, i.e. Solver 1 and the results from Shi and Wang (2011), the coupled model shows a more linear water phase distribution in the two-phase region. Having exactly the same correlations for relative permeability, capillary pressure and heat conductivities, we attribute this mainly to the differences in the calculation of velocities, see Section 8.1.3. As a consequence, one can observe a difference in the length of the two-phase region between the TPMM and the fully coupled model. However, it is remarkable that the two models presented in this work show very similar results. Considering that they are based on different mathematics, numerics and simulation environments, the degree of agreement is very good.

Considerable quantitative disagreement is found when comparing to the results of Shi and Wang (2011). The two-phase region of Shi and Wang (2011) is in

8 Forced Evaporation: Model Comparison for a Non-Isothermal System

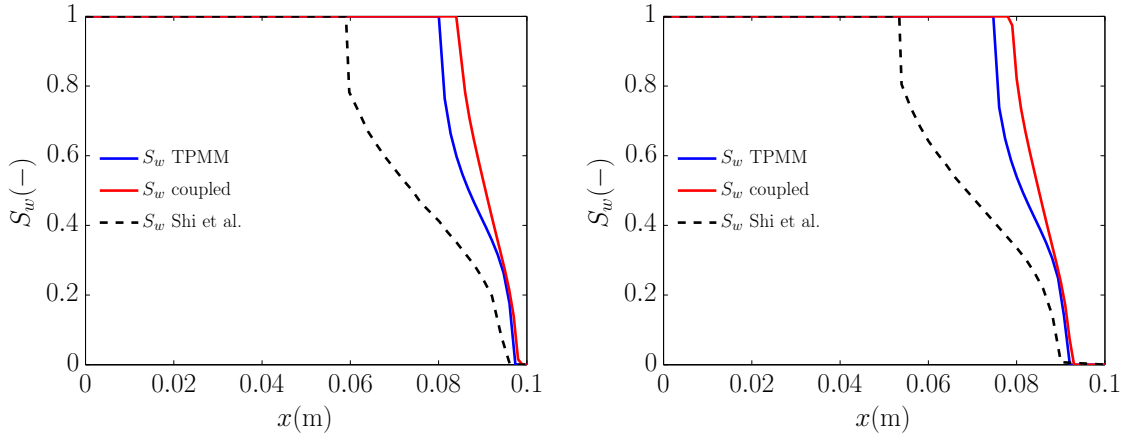


Figure 8.8: Saturation of the water phase for the cases with $\dot{q}_{s\text{ heat}} = 1.5 \cdot 10^6 \text{ W/m}^2$ (**left**) and $\dot{q}_{s\text{ heat}} = 2 \cdot 10^6 \text{ W/m}^2$ (**right**).

general further upstream. This leads to a drastically increased length of the two-phase region in comparison to the TPMM and the fully coupled model. Possible explanations are:

- Shi and Wang (2011) state that after a grid independence study a number of 100 cells is chosen. The TPMM model implemented in this work shows considerable changes in results for a refinement above 100 cells. Grid convergence is only found for 1500 cells, see Section 8.2.2. Therefore, a shift of the two-phase region might be observable for finer grids than used in Shi and Wang (2011).
- Smoothing of Γ_h by Shi and Wang (2011) at the macroscopic phase boundaries might have an influence on macroscopic phase boundaries, since smoothing introduces additional artificial diffusion to the enthalpy, see Section 8.4.2.
- A deviating ω for the relative permeability $k_r = S_w^\omega$ than given in the article by Shi and Wang (2011) could have been chosen. Relative permeabilities are known to have a very big influence, e.g. on macroscopic phase boundaries.
- The definition of fluid effective conductivity can have an influence on the solution. Since Shi and Wang (2011) do not define λ_f , we choose $\lambda_f = S_w \lambda_w + (1 - S_w) \lambda_n$.

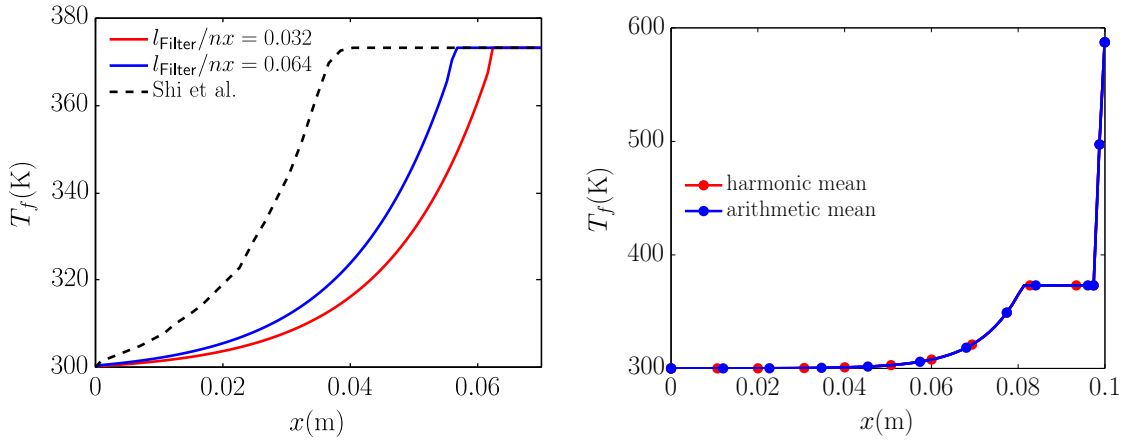


Figure 8.9: Left: Influence of smoothing Γ_h for $\dot{m} = 0.3 \text{ kg/m}^2\text{s}$, $\dot{q}_{s \text{ heat}} = 10^6 \text{ W/m}^2$. Right: Influence of approximation methods for the effective diffusion coefficient.

However, good qualitative agreement is found for all models with respect to the shift of the two-phase region when changing the heat input. All models match to a good degree the analytically provided outflow temperature.

In the following, we study the influence of varying a number of parameters on the results of the TPMM model.

Influence of Smoothing the Effective Diffusion Coefficient on Macroscopic Phase Boundary Position

Figure 8.9 (left) shows the shift of the two-phase region for a change in the smoothing of Γ_h . The Matlab function *smooth* is used applying a moving average filter. A filter length of l_{Filter}/nx , with nx as the number of cells, is used. For the two examples in Figure 8.9, nx is constant. At $l_{\text{Filter}}/nx = 0.032$, the position of the liquid macroscopic phase boundary is at $x = 0.0621$ m. At $l_{\text{Filter}}/nx = 0.064$, the position of the liquid macroscopic phase boundary is shifted to $x = 0.0561$ m. The super-heated macroscopic phase boundary remains unchanged for these examples. Although the liquid macroscopic phase boundary is sensitive to changes in the smoothing length, reproducing the liquid macroscopic phase boundary of Shi and Wang (2011) was not possible for bigger filter lengths for convergence reasons.

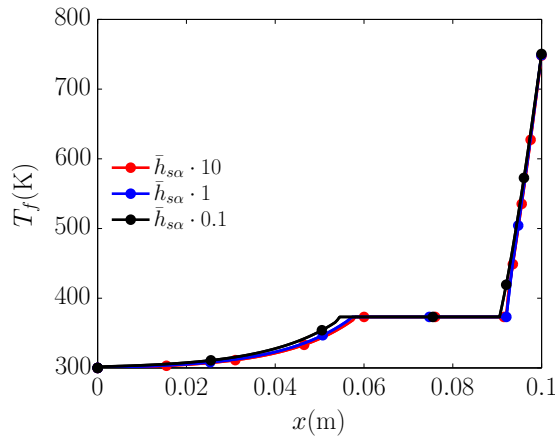


Figure 8.10: Influence of heat transfer coefficient on solution.

Influence of Approximation of the Effective Diffusion Coefficient on the Macroscopic Phase Boundary Position

The position of the macroscopic phase boundary, as well as the maximum fluid temperature, do not depend strongly on the approximation method for the effective diffusion coefficient, see Figure 8.9 (right). Depicted are the numerical results for the case already presented in Figure 8.6. In one case, Γ_h was approximated at the cell interfaces with a harmonic mean of the values in the neighboring cell centers. In the other case, an arithmetic mean was used. Other approximation methods for Γ_h show similar results. However, for numerical stability, we chose the approximation method number IV, as already explained in Section 8.2.2.

Influence of Nusselt Number on Macroscopic Phase Boundary Position

It is not clear which characteristic length was chosen for the REYNOLDS number by Shi and Wang (2011). This can influence the calculation of the NUSSELT number and in turn the heat transfer coefficient. The influence of $\bar{h}_{s\alpha}$ on the temperature difference between the fluid and solid phase, and therefore the degree of local thermal non-equilibrium, is substantial. The position of the macroscopic phase boundaries, however, is not very sensitive to changes in $\bar{h}_{s\alpha}$ (Figure 8.10).

8.5 Summary & Conclusion

In this chapter, we presented two different models to simulate the case of local thermal non-equilibrium between the fluid and solid phases in multiphase flow in porous media. One model is a two-phase mixture model (TPMM) implemented in Matlab and MRST (Solver 1), tested by a cross-validation in a Comsol implementation (Solver 2). The other model is a fully coupled transient model implemented in DuMu^x, a free and open source simulator for flow and transport processes in porous media. Both models were newly implemented.

We explained the mathematical background and the numerical schemes employed. Subsequently, common aspects as well as differences between the two mathematical and numerical approaches were discussed.

The configuration presented in this chapter is known in the literature as transpiration cooling. However, the same set of balance equations and boundary conditions can be used in order to simulate porous evaporators. We presented problem and simulation setup as well as the chosen boundary conditions.

Finally, we presented simulation results. The two models as well as a TPMM model found in the literature (Shi and Wang, 2011) were compared. All models matched the analytically approximated outflow temperature very well. Considerable differences in the length of the two-phase region compared to Shi and Wang (2011) were found.

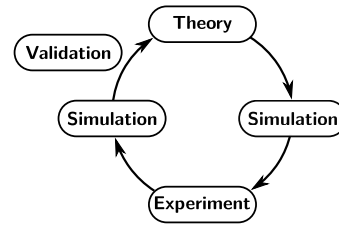
The sensitivity of a number of variables in the TPMM model is studied, but the difference to the literature results could not be reproduced. Therefore, we hypothesized that differences in relative permeability or an insufficiently refined grid are most likely the reason for the differences to the results presented in Shi and Wang (2011).

However, we have confidence in our models. We did not apply any calibration whatsoever and the results are very similar in terms of outflow temperature as well as saturation distribution. We find this remarkable, as the two models are based on very different mathematical descriptions, numerical discretizations and

simulation environments. The remaining difference between the TPMM model and the fully coupled model is attributed to differences in the calculation of velocities.

The strength of DuMu^x is in its generality and the possibility to implement very complex physical processes while still successfully dealing with the resulting highly non-linear systems. The free development concept of DuMu^x allows close collaboration and propels scientific progress. The TPMM model, on the other hand, is straight forward to implement and can benefit from existing projects, like the MRST. The TPMM is adapted to the stationary system at hand. Furthermore, it has the capability to directly implement the physically demanded boundary conditions. In this chapter, we have compared these two very different models. Such detailed comparisons are not very frequently conducted although they represent the foundation for confidently developing complex models in the absence of analytical solutions.

We find the presented results encouraging and will proceed with more complex physical settings. In a next step, water will be replaced by a mixture of components. Ultimately, we want to optimize the evaporator efficiency for highly complex fluid mixtures. The next step in this direction is presented in Appendix A.



9

Final Remarks

9.1 Summary

First, I presented a conceptual model describing those aspects of multiphase flow in porous media which are needed in this work. On this basis, a mathematical model, devoid of local thermal and chemical equilibrium assumptions, was developed. I discussed the limitations and capabilities of the mathematical model and gave a short summary of the numerical solution techniques applied. I implemented the newly developed model as part of the numerical framework DuMu^x, a free and open-source simulator for flow and transport processes in porous media. Following the ideas of free software, as well as reproducibility and accessibility, an infrastructure was developed in order to publish all the data and code used, along with scientific publications.

The macro-scale non-equilibrium model developed in this work was employed in a parameter study motivated by evaporation from porous media. A pore-network model was extended and used for generating input parameters. Volume-averaged interfacial areas, which are limiting factors to mass and energy transfer in multiphase flow in porous media, were obtained from this model. These interfacial areas and other quantities obtained from the pore-network model were used as input to the macro-scale non-equilibrium model. Subsequently, it was successfully applied to a simplified simulation of evaporation from a porous medium. In a parameter study, the unknown heat and mass transfer coefficients were scaled and reasonable limiting cases were obtained, i.e. no evaporation for low transfer coefficients and

9 Final Remarks

equilibrium for high transfer coefficients. Grid convergence was shown by means of a global as well as a local indicator. For the given setup and boundary conditions, it was found that chemical rather than thermal non-equilibrium is the limiting factor for evaporation.

On the basis of the parameter study, a new experimental setup allowing the simultaneous thermal and optical observation of multiphase flow in a micro-model was developed. Together with partners from the University of Utrecht, we successfully conducted experiments with this setup. I demonstrated how relevant information about phase presence and temperature distribution could be obtained by means of an image analysis procedure. I was able to show that temperature can be used as a flow path indicator and flow velocity does influence the extent of local thermal non-equilibrium.

In order to calibrate the macro-scale non-equilibrium model to the experimental data, all relevant input parameters needed to be obtained by means of additional measurements and a newly developed image analysis pipeline. In this way, for the first time, all interfacial areas could be obtained from micro-model data. I conducted simulations of two different experimental runs. In both cases, the best agreement between simulation and experiment was found for the same value of the introduced scaling factor $f_e = 0.5$. The simulation of an experiment under non-equilibrium conditions with individual temperatures assigned to the respective phases is novel and has not been accomplished before.

For cross-validation of numerical implementations and to show the applicability of the model to technical applications, a comparison study was conducted in a cooperative effort. In that context, the model developed in this work was compared with a model developed independently. The application of interest was the forced evaporation of a single component fluid in a metallic porous medium by means of huge temperature gradients. Although the two models compared did not reproduce literature values perfectly, they gave very similar results and possible explanations for the observed discrepancies were given.

In a follow-up work, the evaporation of a two-component mixture was successfully simulated by means of the model developed in this work. Robustness and flexibility

of the thermodynamics framework implemented in DuMu^x are demonstrated by this substantial step towards the simulation of a realistic fuel mixture. Beside the cross-validation by another model, this study can also be taken as proof of the successful modularization of the numerical model: different modules were combined and used jointly.

9.2 Future Research

In this section, I outline possible directions of future research as suggested by the results presented in this work. This outline does not follow the sequence of the chapters of this thesis but is structured according to theoretical, experimental and simulation aspects.

Theory Improvements So far, the approaches for describing energy and mass transfer are motivated by physical reasoning. More rigorous, but still practical, approaches are needed for predicting the limits of the standard model and for coming up with better founded and testable transfer relations.

Experimental Work In the parameter study motivated by evaporation from a porous medium, it became clear that more experimental work is needed. Measurements of the extent of local (non-) equilibrium as well as the calibration of the proposed transfer relations are reasonable further steps for studying local non-equilibrium in the field of evaporation from porous media.

To study local non-equilibrium experimentally, a setup including sources is highly interesting. The micro-model setup presented here could be extended by a heat source. This would improve the possibility of observing non-equilibrium effects.

The intrinsic experimental observation of the forced evaporation example is hard to realize, due to high temperatures and the small spatial extent of the porous medium. This is even more motivation for improvements in theory and simulation in this field.

Simulation Extensions To correctly describe evaporation from a porous medium in a non-equilibrium context, the description of the free-flow region needs to be improved. Most notably, turbulence needs to be accounted for and the momentum description needs to be improved.

The decision to model the micro-model experiment by means of a macro-scale model needs to be better founded. Interesting tools in this regard are pore-network models, which can be seen as volume-averaging tools.

The extension of the forced evaporation example to more components and ultimately realistic fuel mixtures is the practical motivation for that line of research. The description of multicomponent mixtures is highly complicated but important in this regard. It may be necessary to include chemical non-equilibrium, e.g. if components with very small diffusion coefficients have to be represented as well.

Each result chapter contains an outlook section at the end. Please refer to them for more detailed information.

9.3 Conclusion

In this work, I closed the loop connecting theory, simulation, experiment and validation in the study of local non-equilibrium in multiphase flow in porous media, see Figure 9.1. In a modern research environment, knowledge gain is guided by powerful simulation tools, such as the macro-scale non-equilibrium model presented here. However, simulation technology is an extension to the interplay of theory and experiment and not a replacement.

I studied the consequences and implications of not making local thermal and chemical equilibrium assumptions in the simulation of multiphase flow in porous media. The chosen course of action was to develop a macro-scale model which allows different chemical potentials and temperatures in different phases. This came at the cost of an increased number of balance equations. Also, unknown heat and mass transfer coefficients arose. The standard model for non-isothermal

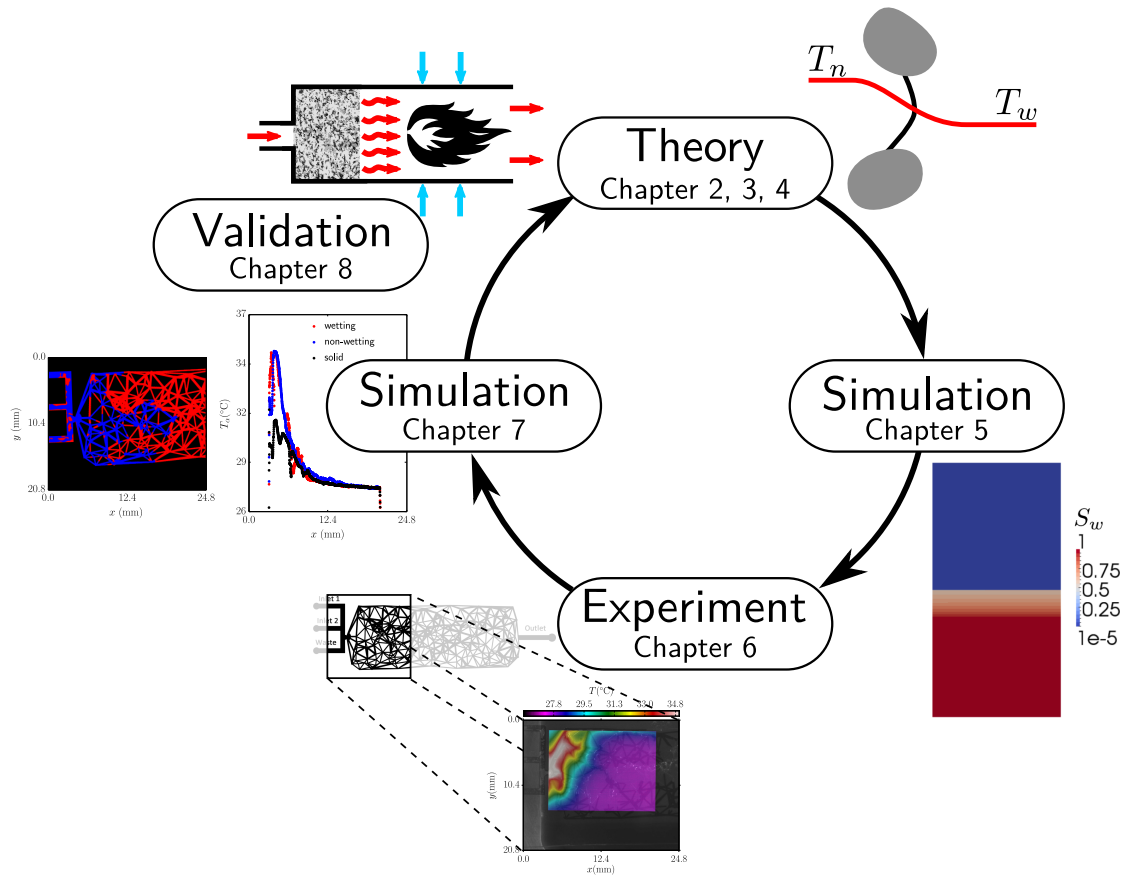


Figure 9.1: Closing the loop in this work.

compositional flow in porous media could be recovered by invoking local equilibrium assumptions and the execution of simple summations.

All in all, I presented a versatile and useable toolbox of methods and models: The non-equilibrium macro-scale model is applicable to very different and demanding applications. Amongst these are the simulation of experimental observations as well as the simulation of a technical application. Ways to calculate input parameters, whether numerically or experimentally, were developed if needed. In this way, a strong foundation for further studies of the assumption of local equilibrium in multiphase flow in porous media is given.

In other words: a model pointing beyond local equilibrium assumptions is presented.

List of Publications

- Philipp Nuske, Benjamin Faigle, Rainer Helmig, Jennifer Niessner and Insa Neuweiler (2010). Modeling gas-water processes in fractures with fracture flow properties obtained through upscaling. *Water Resources Research*, 46.
- Bernd Flemisch, Melanie Darcis, Karin Erbertseder, Benjamin Faigle, Andreas Lauser, Klaus Mosthaf, Steffen Müthing, Philipp Nuske, Alexandru Tatomir, Markus Wolff and Rainer Helmig (2011). DuMu^x: Dune for multi-{Phase, Component, Scale, Physics, ...} flow and transport in porous media. *Advances in Water Resources*, 34:1102–1112.
- Nikolaos K. Karadimitriou, Philipp Nuske, Pieter J. Kleingeld, S. Majid Hassanizadeh and Rainer Helmig (2014). Simultaneous thermal and optical imaging of two-phase flow in a micro-model. *Lab Chip*, 14:2515–2524.
- Franz Lindner, Philipp Nuske, Rainer Helmig, Christian Mundt and Michael Pfitzner (2014). Transpiration cooling with local thermal non-equilibrium: Model comparison in multiphase flow in porous media. *Journal of Porous Media*. Submitted.
- Philipp Nuske, Vahid Joekar-Niasar and Rainer Helmig (2014a). Non-equilibrium in multiphase multicomponent flow in porous media: An evaporation example. *International Journal of Heat and Mass Transfer*, 74(0):128–142.
- Philipp Nuske, Olaf Ronneberger, Nikolaos K. Karadimitriou, Rainer Helmig and S. Majid Hassanizadeh (2014b). Modelling multiphase flow in a micro-model with local thermal non-equilibrium on the darcy scale. *Water Resources Research*. Submitted.
- Alexandru Tatomir, Mario Schaffer, Alexander Kissinger, Johannes Hommel, Philipp Nuske, Tobias Licha, Rainer Helmig and Martin Sauter (2014). Novel approach for modeling kinetic interface-sensitive (KIS) tracers with respect to time-dependent interfacial area change for the optimization of supercritical carbon dioxide injection into deep saline aquifers. *International Journal of Greenhouse Gas Control*. Submitted.

A

Forced Evaporation: Compositional Effects

The design and optimization of complex systems demand the support and guidance by simulation tools. Especially systems which are not, or incompletely, accessible for measurements can be better understood by means of simulation. This way, new possibilities of optimization arise.

In this particular case, the evaporator located upstream of a burner is to be simulated, see Figure 8.1. The evaporator is treated as a porous medium. In practice, varying mixtures of many alkanes are to be vaporized before combustion. The combustion will power a heating system.

In a staggered approach, the development of appropriate models is conducted in consecutive levels. Building on the confidence and experience gained by the work presented in Chapter 8, we present in this appendix the simulation of a two-component mixture evaporation. This constitutes the extension towards multicomponent evaporation and is therefore a considerable step towards the simulation of realistic fuel mixtures. We choose two alkanes, heptane (exponent H) and dodecane (exponent D) as components.

This chapter is structured as follows: In Section A.1 the properties of the pure components heptane and dodecane are listed. From the properties of the pure components, the mixture properties are obtained in Section A.2. Some simulation results, employing the listed properties, are given in Section A.3. In Section A.4

we summarize and give an outlook.

A.1 Component Properties

Component properties are implemented as constant values, see Table A.1. This is a strong assumption, but main characteristics of the system are preserved.

The specific enthalpy of the individual components cannot be captured by constant values. They are described as linear functions of temperature and the enthalpy of vaporization. For example, the enthalpy of the component heptane in the liquid (index w) and gaseous (index n) state is given by:

$$h_w^H = c_{pw}^H (T - T_{\text{ref}}) \quad (\text{A.1})$$

$$h_n^H = c_{pw}^H (T_{\text{boil}} - T_{\text{ref}}) + \Delta h_v^H + c_{pn}^H (T - T_{\text{boil}}). \quad (\text{A.2})$$

Here, $c_{p\alpha}$ stands for the specific heat capacity of the pure component in the phase α . T , T_{boil} and T_{ref} are the actual, the boiling and the reference temperature of the respective pure components.

A.2 Fluidsystem

In a first approximation, all excess contributions are neglected. This means that the mixture properties of the respective phases are the mole fraction weighted averages of the pure component properties.

This is, especially for the enthalpy of the mixture, a rough approximation. Therefore, a reasonable next step is the implementation of more accurate caloric equations of state.

Equivalent to the system described in Chapter 8, local thermal non-equilibrium between fluids and solid and local chemical equilibrium are assumed. Equilibrium compositions of the respective phases are determined by applying DALTON's law and for each component RAOULT's law. Furthermore, the gas phase is assumed to behave ideally.

A.3 Simulation Results of the Two-Component Evaporation

Table A.1: Properties of the pure components heptane and dodecane. The indices w, n denote the liquid and gaseous properties, respectively.

Parameter	Dodecane	Heptane
M (kg/mol)	0.17	0.1002
T_{boil} (K)	487	371.2
p_{vap} (Pa)	331051.72	2738618.08
c_n (J/kg K)	2732	2772
c_w (J/kg K)	2211.59	2249.3
Δh_v (J/kg)	323000	316600
λ_n (W/m K)	0.025	0.018
λ_w (W/m K)	0.095	0.113
ρ_n (kg/m ³)	4.35	3.45
ρ_w (kg/m ³)	750	680
μ_n (Pa s)	$3.22 \cdot 10^{-5}$	$2.615 \cdot 10^{-5}$
μ_w (Pa s)	$1.52 \cdot 10^{-3}$	$1.83 \cdot 10^{-4}$

A.3 Simulation Results of the Two-Component Evaporation

The simulation setup was the same as described in Chapter 8: The actual simulation domain has a length of 0.1 m. Composition is according to equilibrium at the given pressure and temperature. Important parameters are given in Table A.2.

Over the left-hand side of the domain, a liquid mixture, consisting of equal amounts of heptane and dodecane, is injected. In order to represent the combustion in the motivating application, a heat flux is imposed on the right-hand side of the domain. In DuMu^x, the general and transient conservation equations are implemented, as explained in Chapter 8. However, the chosen examples have stationary final states, which are shown here.

Table A.2: Parameters of the simulated scenarios.

heat flux	mass flux	surface tension
$28e4$ W/m ²	0.3 kg/m ² s	0.05 N/m ²

A.3.1 Grid Convergence

In Figure A.1, saturation and composition of the liquid phase is shown as a function of grid resolution.

The development of the mole fraction of dodecane in the liquid phase needs further explanation. Dodecane is the component with the higher boiling temperature. However, the mole fraction of dodecane first goes down (red circles in Figure A.1) before increasing as expected. By means of the increasing grid resolution, depicted in Figure A.1, the decreasing section can be identified as an actually step-like behavior which happens in one cell. This is the first cell in direction of flow, accommodating two phases. Therefore, in this cell equilibrium compositions have to be met for the first time. Further downstream, temperature increases, and the mole fraction of dodecane increases according to equilibrium composition. Further explanations in that regard are given in Section A.3.3.

All further results are obtained with a grid resolution of 100 cells.

A.3.2 Composition

Figure A.2 shows a phase diagram of a heptane–dodecane mixture at 100000 Pa. It was calculated independently of the simulations presented in this chapter. The construction of the phase-diagram is based on the ANTOINE-parameters of the pure components, applying RAOULT’s law and assuming ideal behavior of the phases. It is in good agreement with simulation results, as will be more explicitly shown in Section A.3.3.

Figure A.3 shows the composition of the gas phase in the simulated domain. Although composition is also given in the one-phase liquid region, it only has physical meaning for regions where the gas phase is actually present, i.e. for $x > 0.07$ m.

In the two-phase region, composition is found according to the prevailing pressure and temperature, as local chemical equilibrium is assumed. No reactions are

A.3 Simulation Results of the Two-Component Evaporation

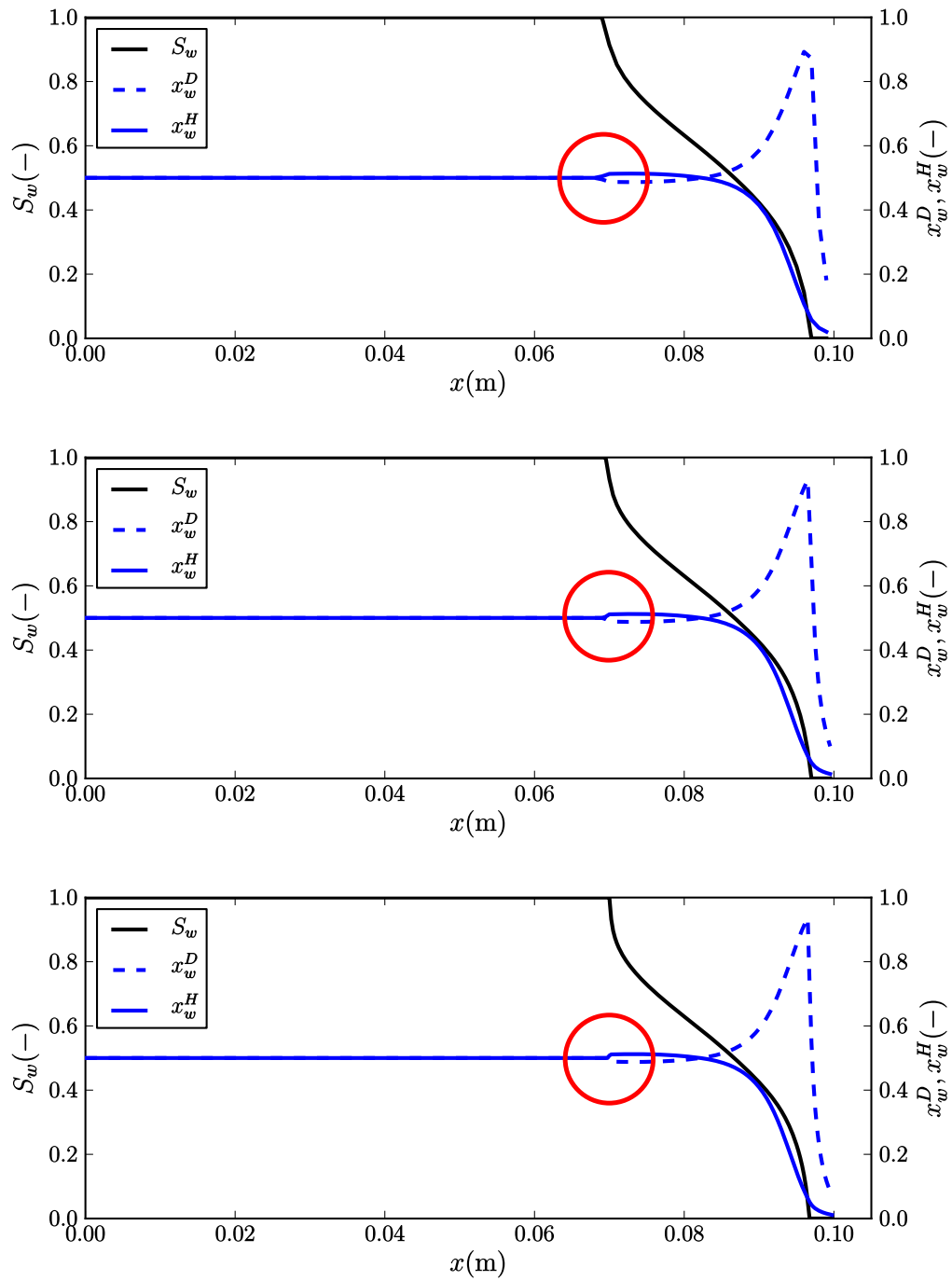


Figure A.1: Saturation of the wetting (liquid) phase and mole fractions of heptane and dodecane in the liquid phase. Resolutions of 100 (**top**), 200 (**middle**) and 400 (**bottom**) cells in the simulation domain. Mole fractions only have a physical meaning at those locations where the respective phase α actually exists ($S_\alpha > 0$).

A Forced Evaporation: Compositional Effects

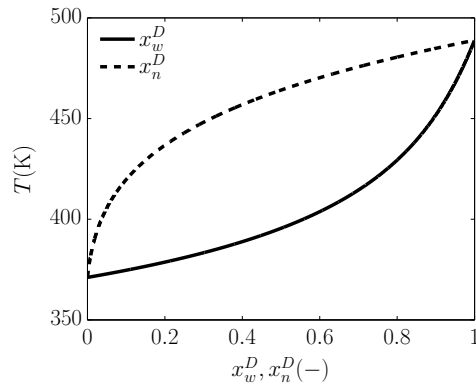


Figure A.2: Phase diagram of the heptane–dodecane mixture. It was calculated with a constant pressure of 100000 Pa and applying RAOULT’s law for both components. Vapor pressures are obtained from the ANTOINE-equation and the gas phase is assumed to behave ideally.

considered in this context. Therefore, the one-phase liquid region has the same composition as the one-phase gaseous region.

A.3.3 Composition in the Two-Phase Region: Factors of Influence

The mole fraction of dodecane shows a non-monotonic behavior in the direction of flow (see e.g. Figure A.1), which is not intuitive to understand. However, it can be explained. To be more precise: a monotonic trend in dodecane mole-fraction would violate model assumptions or physical constraints. In this section, we study the influence of varying a number of model parameters on the simulation results. This way, a better understanding of the simulation results is achieved.

For understanding the model results, the fully implicit character of the model has to be kept in mind: All balance equations have to be fulfilled simultaneously. Therefore, a temperature distribution fulfilling energy conservation and a saturation and mole-fraction distribution fulfilling mass conservation has to be found. This process does not happen in a static container, but under dynamic flow conditions.

Against this background, in the first cell in the direction of flow accommodating a two-phase system, temperatures are found. Composition of phases has to conform

A.3 Simulation Results of the Two-Component Evaporation

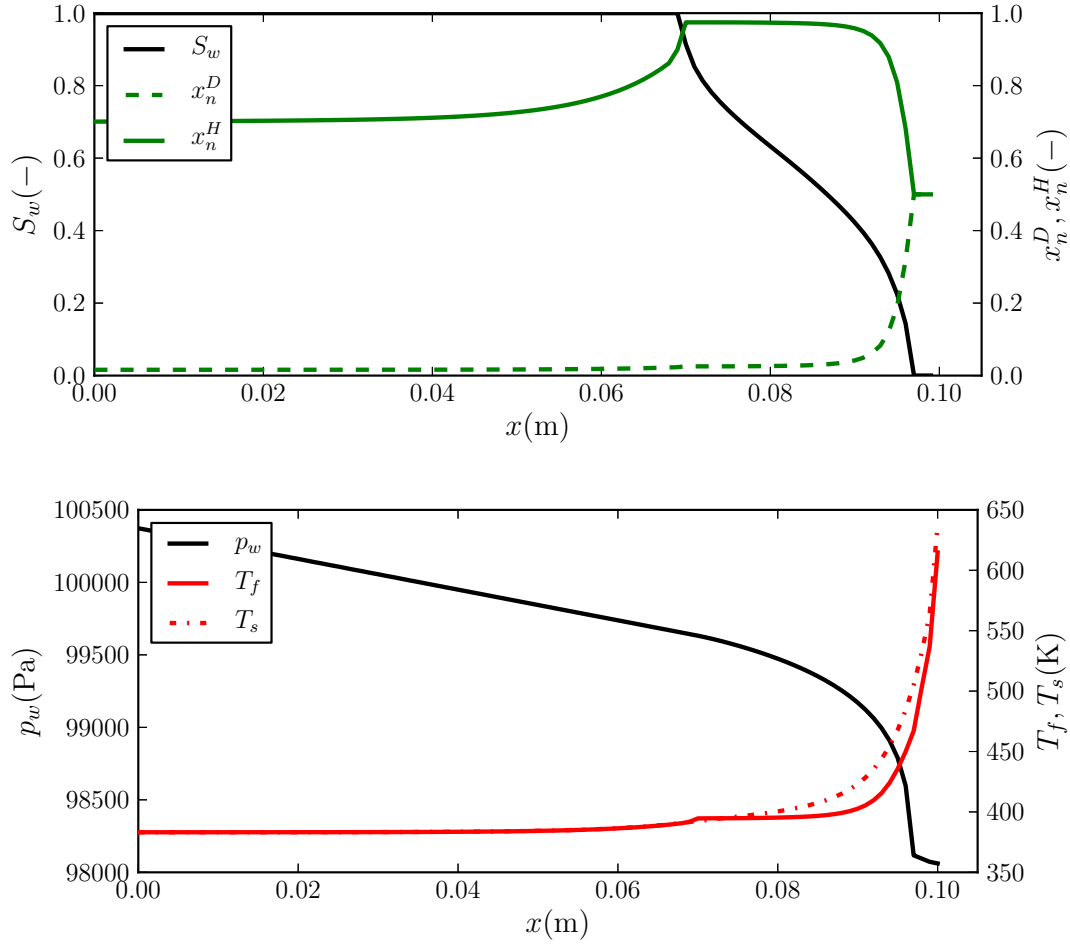


Figure A.3: Composition of the gas phase and saturation distribution (**top**), as well as temperature and pressure (**bottom**). Mole fractions only have a physical meaning at those locations where the respective phase α actually exists ($S_\alpha > 0$).

to pressure and temperature as local chemical equilibrium is assumed. All in all, this results in the step-like behavior of the composition distribution observed in Figure A.1. This step is not a numerical artifact, but physical in nature.

The above given explanations are backed by a couple of numerical values given in Table A.3. The table refers to the varying composition at the inflow, presented in Figure A.4. In the first column, the composition at the inflow to the simulation domain is given. Second and third column give temperature and composition in the first two-phase cell in the direction of flow, as calculated by DuMu^x. In the

Table A.3: Comparison between simulation results and read values from the phase diagram (Figure A.2). The simulation results (index DuMu^x) are given for the first cell in the direction of flow accommodating two phases.

$x_{w \text{ in}}^D$	$T_{f \text{ DuMu}^x}$	$x_{w \text{ DuMu}^x}^D$	$x_{w \text{ phase diagram}}^D(T_{f \text{ DuMu}^x})$
0.3	383.348	0.2999	0.2991
0.5	394.627	0.4876	0.4875
0.7	411.346	0.6734	0.6732

fourth column, the composition for the calculated temperature (second column), as read from Figure A.2, is given.

The phase diagram, shown in Figure A.2, is calculated independently of the simulation. Therefore, it can be concluded that composition and temperature fit. Demanding a monotone distribution of composition, would therefore violate the assumption of local chemical equilibrium.

The results presented in Figure A.5 back the above given explanations. In Figure A.5, results from varying the interfacial tension and therefore capillary pressure are shown. The lower the capillary pressure, the further downstream the start of the two-phase region moves. Therefore, temperature in the first two-phase cell is higher, resulting in according compositions.

A.3.4 Varying Heat Fluxes

Figure A.6 shows temperature and saturation distribution for two different heat fluxes imposed on the right-hand side. Both simulation results were obtained with the same injected mass flux. The higher heat flux results in a higher temperature at the exit and a longer one-phase gaseous region.

A.3 Simulation Results of the Two-Component Evaporation

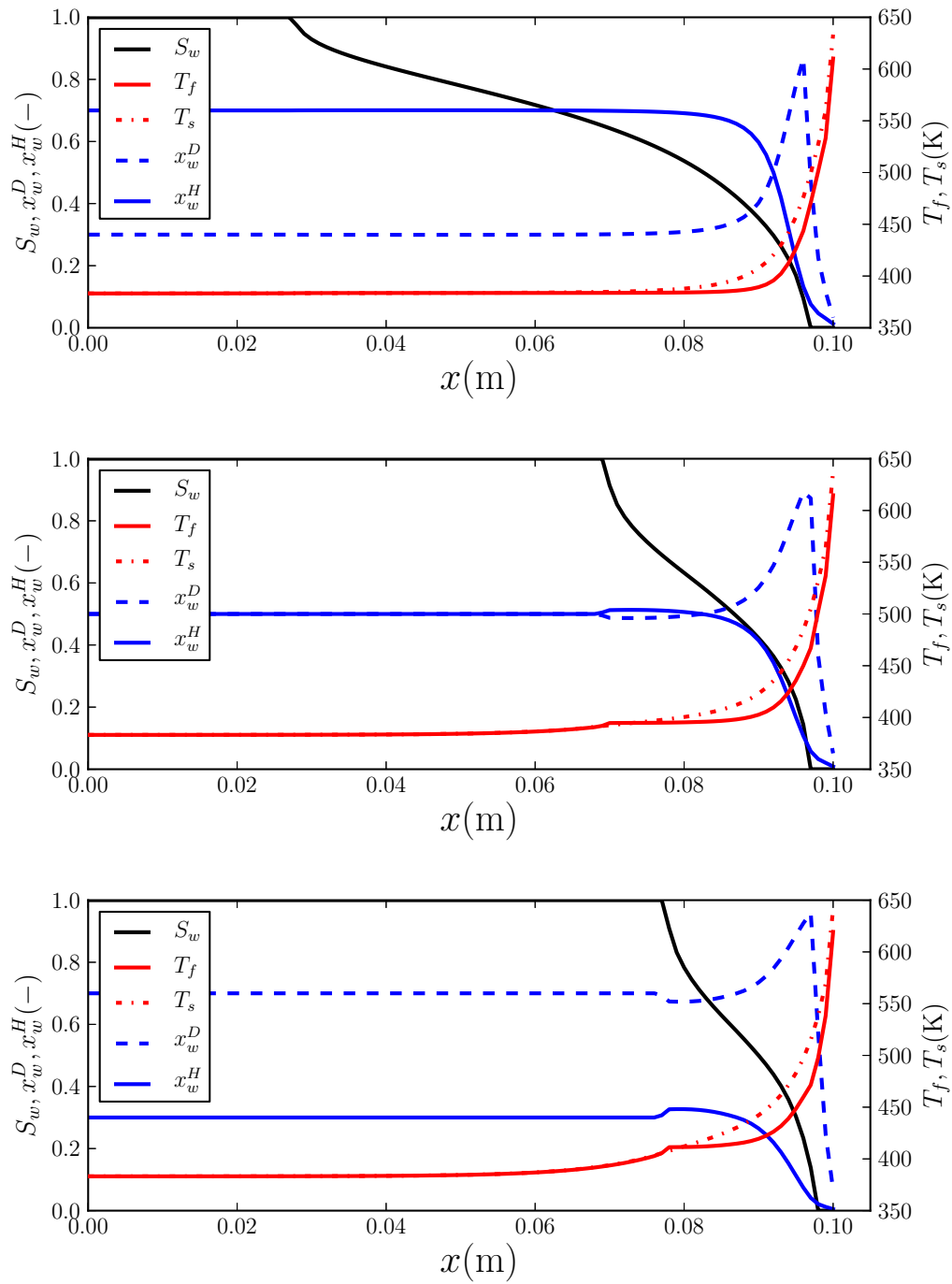


Figure A.4: Influence of varying compositions at the inflow. **Top:** $x_w^D = 0.3$, **Middle:** $x_w^D = 0.5$, **Bottom:** $x_w^D = 0.7$

A Forced Evaporation: Compositional Effects

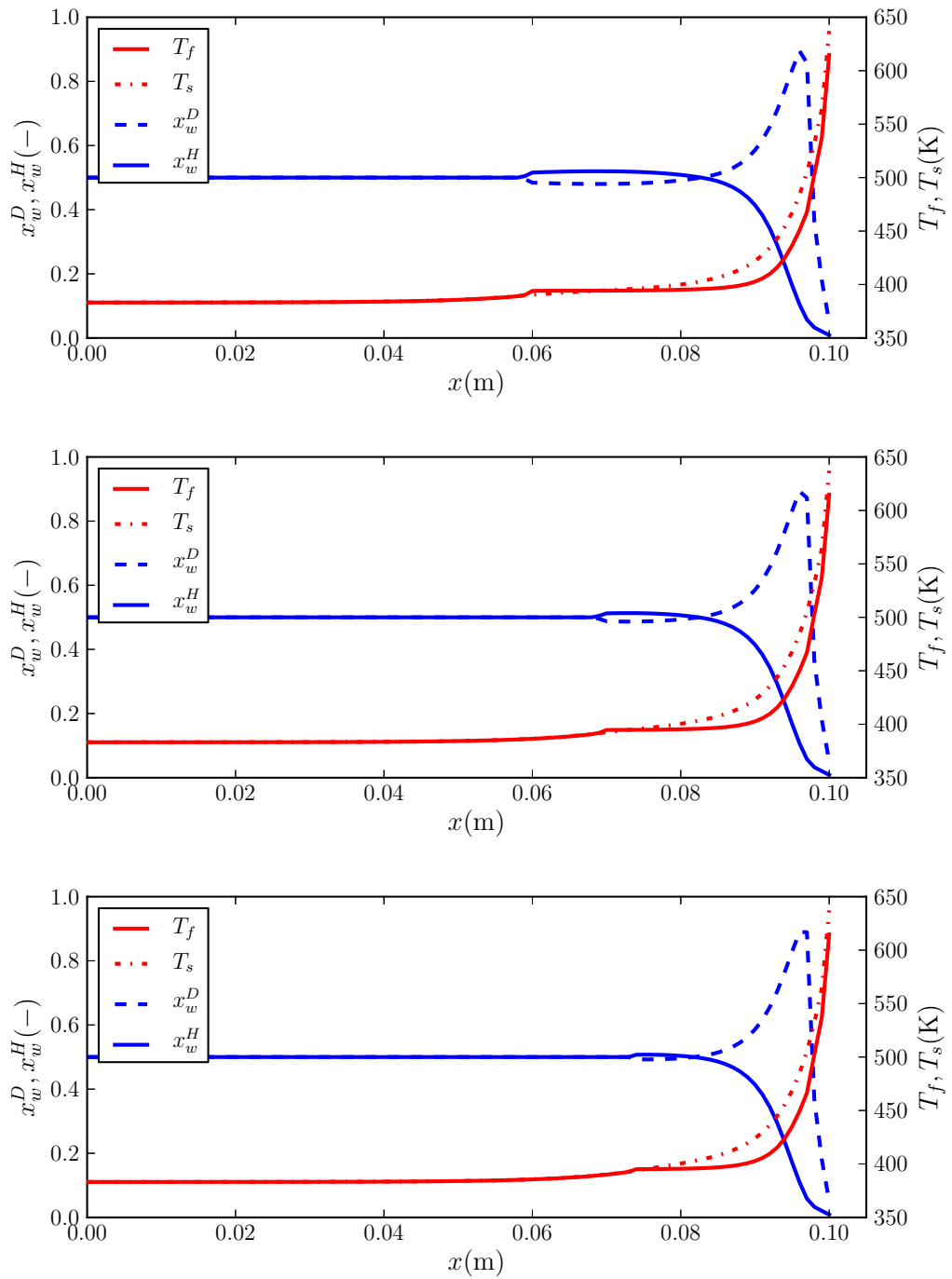


Figure A.5: Influence of scaling capillary pressure. **Top:** $\sigma = 0.1$, **Middle:** $\sigma = 0.05$, **Bottom:** $\sigma = 0.025$

A.3 Simulation Results of the Two-Component Evaporation

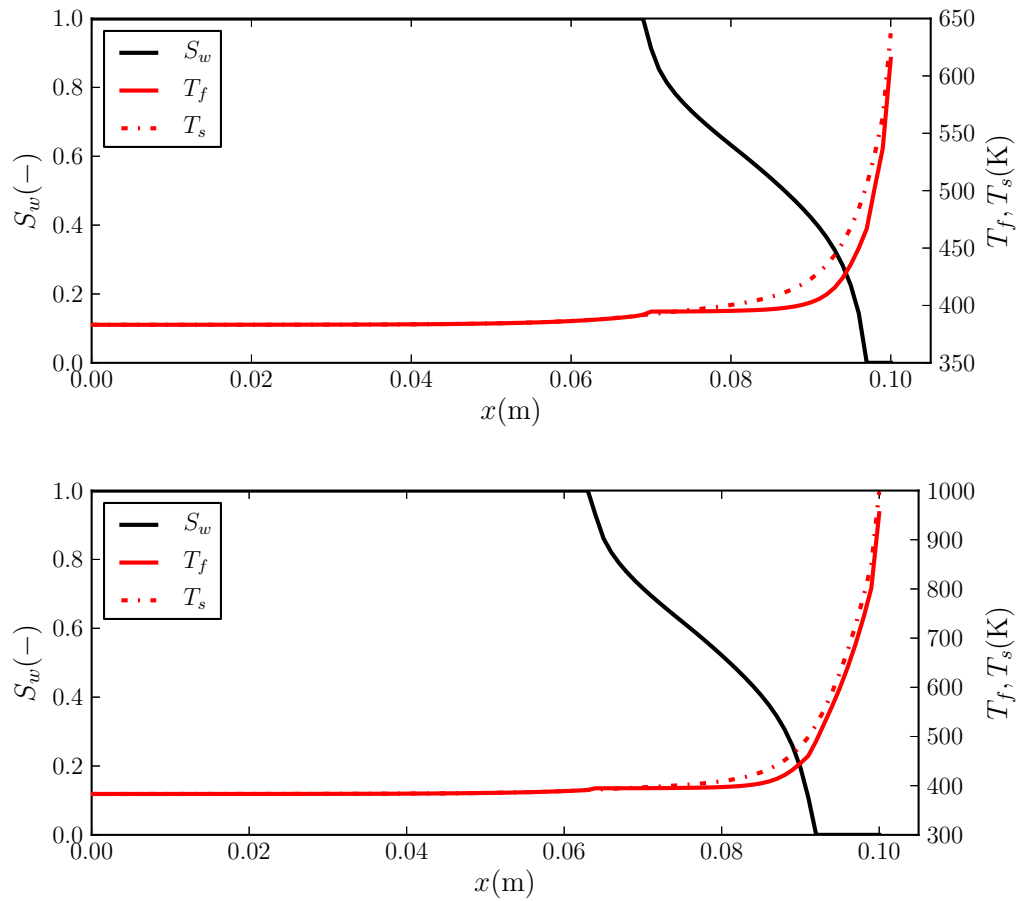


Figure A.6: Temperature and saturation distribution for het fluxes of $\dot{q} = 28e4 \text{ W/m}^2$ (**top**) and $\dot{q} = 56e4 \text{ W/m}^2$ (**bottom**).

A.4 Summary & Conclusion

The presented fluidsystem is novel to DuMu^x in two respects. First, it is a fluid system, which does not, at any point, make assumptions based on one component being the major one or neglecting a component. Second, it is the first fluid system implemented in DuMu^x to describe the composition of a liquid and a gas phase based on applying RAOULT's law twice. Although these are interesting new features, showcasing the versatility of the thermodynamics framework implemented in DuMu^x, they are no milestones with regards to content.

In that respect, the presented results are an important step towards simulating and designing realistic porous evaporators. These are strongly non-isothermal technical systems which inherit also complicated chemical composition. Both aspects can be captured by the design concept followed in DuMu^x. This is to strive for generality while providing adaptability.

Bibliography

- 3M (2013). Products, 3m™ fluorinert™ electronic liquid fc-43. online.
- Acosta, M., Merten, C., Eigenberger, G., Class, H., Helmig, R., Thoben, B., and Müller-Steinhagen, H. (2006). Modeling non-isothermal two-phase multi-component flow in the cathode of PEM fuel cells. *Journal of Power Sources*, 159(2):1123–1141.
- Ahrenholz, B., Niessner, J., Helmig, R., and Krafczyk, M. (2011). Pore-scale determination of parameters for macroscale modeling of evaporation processes in porous media. *Water Resources Research*, 47.
- Anzelius, A. (1926). Über Erwärmung vermittelt durchströmender Medien. *ZAMM - Journal of Applied Mathematics and Mechanics / Zeitschrift für Angewandte Mathematik und Mechanik*, 6(4):291–294.
- Armstrong, J. E., Frind, E. O., and McClellan, R. D. (1994). Nonequilibrium mass transfer between the vapor, aqueous, and solid phases in unsaturated soils during vapor extraction. *Water Resources Research*, 30:355–368.
- Atkins, P. and Julio, d. P. (2006). *Physical Chemistry*. Oxford University Press.
- Avraam, D. G., Kolonis, G. B., Roumeliotis, T. C., Constantinides, G. N., and Payatakes, A. C. (1994). Steady-state two-phase flow through planar and nonplanar model porous media. *Transport in Porous Media*, 16:75–101.
- Baehr, H. D. (2005). *Thermodynamik: Grundlagen und Technische Anwendungen*. Springer.
- Baouab, Z., Najjari, M., Ouerfelli, H., and Nasrallah, S. B. (2007). Experimental study of the effects of hydraulic gradient and injected-gas flow rate on fragmentation in porous media. *Journal of Petroleum Science and Engineering*, 59:250–256.
- Bastian, P., Blatt, M., Dedner, A., Engwer, C., Klöfkorn, R., Kornhuber, R., Ohlberger, M., and Sander, O. (2008). A Generic Grid Interface for Parallel and

Bibliography

- Adaptive Scientific Computing. Part II: Implementation and Tests in DUNE. *Computing*, 82(2–3):121–138.
- Bates, L. (1948). *Sir Alfred Ewing, A Pioneer in Physics and Engineering*. Longmans, Green & Co.
- Bau, H. H. and Torrance, K. (1982). Boiling in low-permeability porous materials. *International Journal of Heat and Mass Transfer*, 25(1):45–55.
- Baumann, T. and Werth, C. J. (2004). Visualization and modeling of polystyrol colloid transport in a silicon micromodel. *Vadose Zone Journal*, 3:434–443.
- Baytas, A. and Pop, I. (2002). Free convection in a square porous cavity using a thermal nonequilibrium model. *International Journal of Thermal Sciences*, 41(9):861–870.
- Berning, T., Odgaard, M., and Kær, S. K. (2010). A study of multi-phase flow through the cathode side of an interdigitated flow field using a multi-fluid model. *Journal of Power Sources*, 195(15):4842–4852.
- Bird, R. B., Stewart, W. E., and Lightfoot, E. N. (2002). *Transport phenomena*. John Wiley and Sons.
- Blatt, M. and Bastian, P. (2007). The iterative solver template library. In Kågström, B., Elmroth, E., Dongarra, J., and Waśniewski, J., editors, *Applied Parallel Computing. State of the Art in Scientific Computing*, volume 4699 of *Lecture Notes in Computer Science*, pages 666–675. Springer Berlin Heidelberg.
- Bookstein, F. L. (1989). Principal warps: thin-plate splines and the decomposition of deformations. *Pattern Analysis and Machine Intelligence, IEEE Transactions on*, 11(6):567–585.
- Brandauer, M., Schulz, A., and Wittig, S. (2002). Optimization of fuel prevaporization on porous surfaces for low-nox-combustion. In *Combustion Technology for a Clean Environment: Selected Papers for the Proceedings of the Third International Conference, Lisbon, Portugal, July 3-6, 1995*, volume 3, page 261. CRC Press.

- Brooks, R. H. and Corey, A. T. (1964). Hydraulic Properties of Porous Media. *Hydrology Papers, Colorado State University*.
- Burdine, N. (1953). Relative permeability calculations from pore size distribution data. *Journal of Petroleum Technology*.
- Bürger, M., Buck, M., Schmidt, W., and Widmann, W. (2006). Validation and application of the wabe code: Investigations of constitutive laws and 2d effects on debris coolability. *Nuclear Engineering and Design*, 236(19–21):2164 – 2188. Festschrift Edition Celebrating the 70th Birthday of Prof. Bal Raj Sehgal: Invited papers on - Core melt accidents in LWRs State of the art of coolability of porous media.
- Chang, L.-C., Tsai, J.-P., Shan, H.-Y., and Chen, H.-H. (2009). Experimental study on imbibition displacement mechanisms of two-phase fluid using micro model. *Environmental Earth Sciences*, 59:901–911.
- Chen, L. and Kibbey, T. C. G. (2006). Measurement of air–water interfacial area for multiple hysteretic drainage curves in an unsaturated fine sand. *Langmuir*, 22(16):6874–6880.
- Cheng, J.-T., Pyrak-Nolte, L. J., Nolte, D. D., and Giordano, N. J. (2004). Linking pressure and saturation through interfacial areas in porous media. *Geophysical Research Letters*, 31.
- Clark, J. and Rohsenow, W. (1954). Local boiling heat transfer to water at low reynolds numbers and high pressures. *Trans. ASME*, 76:554–562.
- Class, H. (2007). Models for non-isothermal compositional gas-liquid flow and transport in porous media. Habilitation thesis.
- Class, H., Ebigbo, A., Helmig, R., Dahle, H., Nordbotten, J., Celia, M., Audigane, P., Darcis, M., Ennis-King, J., Fan, Y., Flemisch, B., Gasda, S., Jin, M., Krug, S., Labregere, D., Naderi Beni, A., Pawar, R., Sbai, A., Thomas, S., Trenty, L., and Wei, L. (2009). A benchmark study on problems related to CO₂ storage in geologic formations. *Computational Geosciences*, 13:409–434.

Bibliography

- Class, H. and Helmig, R. (2002). Numerical simulation of non-isothermal multiphase multicomponent processes in porous media: 2. Applications for the injection of steam and air. *Advances in Water Resources*, 25(5):551–564.
- Class, H., Helmig, R., and Bastian, P. (2002). Numerical simulation of non-isothermal multiphase multicomponent processes in porous media: 1. An efficient solution technique. *Advances in Water Resources*, 25(5):533–550.
- COMSOL (2013). Comsol multiphysics® v. 3.5a. www.comsol.com. *COMSOL AB, Stockholm, Sweden*.
- Corapcioglu, M. Y., Yoon, S., and Chowdhury, S. (2009). Pore-scale analysis of NAPL blob dissolution and mobilization in porous media. *Transport in Porous Media*, 79(3):419–442.
- Crone, S., Bergins, C., and Strauss, K. (2002). Multiphase flow in homogeneous porous media with phase change. Part I: Numerical modeling. *Transport in Porous Media*, 49:291–312.
- Darcy, H. (1856). *Les Fontaines Publiques de la Ville de Dijon*, chapter Détermination des lois d’écoulement de l’eau à travers le sable, pages 590–594. Dalmon, Victor.
- Duan, Z. and Sun, R. (2003). An improved model calculating CO₂ solubility in pure water and aqueous NaCl solutions from 273 to 533 K and from 0 to 2000 bar. *Chemical Geology*, 193(3–4):257–271.
- Falta, R. W. (2000). Numerical modeling of kinetic interphase mass transfer during air sparging using a dual-media approach. *Water Resources Research*, 36:3391–3400.
- Ferer, M., Ji, C., Bromhal, G. S., Cook, J., Ahmadi, G., and Smith, D. H. (2004). Crossover from capillary fingering to viscous fingering for immiscible unstable flow: Experiment and modelling. *Physical Review E*, 70 (1):016303.
- Ferrell, R. T. and Himmelblau, D. M. (1967). Diffusion coefficients of nitrogen and oxygen in water. *Journal of Chemical & Engineering Data*, 12(1):111–115.

- Fichot, F., Duval, F., Trégourès, N., Béchaud, N., and Quintard, M. (2006). The impact of thermal non-equilibrium and large-scale 2d/3d effects on debris bed reflooding and coolability. *Nuclear Engineering and Design*, 236(19-21):2144–2163.
- Flemisch, B., Darcis, M., Erbertseder, K., Faigle, B., Lauser, A., Mosthaf, K., Müthing, S., Nuske, P., Tatomir, A., Wolff, M., and Helmig, R. (2011). DuMu^x: Dune for multi-{Phase, Component, Scale, Physics, ...} flow and transport in porous media. *Advances in Water Resources*, 34:1102–1112.
- Forchheimer, P. (1901). Wasserbewegung durch Boden. *VDI*.
- Free Software Foundation (1991). GNU general public license. <http://www.gnu.org/licenses/old-licenses/gpl-2.0.html>.
- Freeze, A. R. and Cherry, J. A. (1979). *Groundwater*. Prentice-Hall.
- Fuller, E. N., Schettler, P. D., and Giddings (1966). New method for prediction of binary gas-phase diffusion coefficients. *Industrial & Engineering Chemistry*, 58(5):18–27.
- Gervais, T., El-Ali, J., Günther, A., and Jensen, K. F. (2006). Flow-induced deformation of shallow microfluidic channels. *Lab Chip*, 6:500–507.
- Ghai, R. K., Ertl, H., and Dullien, F. A. L. (1973). Liquid diffusion of nonelectrolytes: Part I. *AIChE Journal*, 19:881–900.
- Grant, S. A. (2003). Extension of a temperature effects model for capillary pressure saturation relations. *Water Resources Research*, 39.
- Grate, J. W., Zhang, C., Wietsma, T. W., Warner, M. G. and Anheier Jr., N. C., Bernacki, B. E., Orr, G., and Oostrom, M. (2010). A note on the visualization of wetting film structures and a nonwetting immiscible fluid in a pore network micromodel using a solvatochromic dye. *Water Resources Research*, 46.
- Gutiérrez, B., Juárez, F., Ornelas, L., Zeppieri, S., and de Ramos, A. L. (2008). Experimental study of gas–liquid two-phase flow in glass micromodels. *International Journal of Thermophysics*, 29:2126–2135.

Bibliography

- Hassanizadeh, S. M. and Gray, William, G. (1980). General conservation equations for multi-phase systems: 3. Constitutive theory for porous media flow. *Advances in Water Resources*, 3:25–40.
- Hassanizadeh, S. M. and Gray, William, G. (1990). Mechanics and thermodynamics of multiphase flow in porous media including interphase boundaries. *Advances in Water Resources*, 13(4):169–186.
- Hassanizadeh, S. M. and Gray, William, G. (1993a). Thermodynamic basis of capillary pressure in porous media. *Water Resources Research*, 29(10):3389–3405.
- Hassanizadeh, S. M. and Gray, William, G. (1993b). Toward an improved description of the physics of two-phase flow. *Advances in Water Resources*, 16:53–67.
- He, F., Wang, J., Xu, L., and Wang, X. (2013). Modeling and simulation of transpiration cooling with phase change. *Applied Thermal Engineering*, 58:173–180.
- Heiba, A., Sahimi, M., Scriven, L., and Davis, H. (1992). Percolation theory of two-phase relative permeability. *presented at the 57th Annual Fall Meeting of the Society of Petroleum Engineers, New Orleans, LA.*
- Helmig, R. (1997). *Multiphase Flow and Transport Processes in the Subsurface: A Contribution to the Modeling of Hydrosystems*. Springer.
- Huber, M. L., Perkins, R. A., Friend, D. G., Sengers, J. V., Assael, M. J., Metaxa, I. N., Miyagawa, K., Hellmann, R., and Vogel, E. (2012). New international formulation for the thermal conductivity of H₂O. *Journal of Physical and Chemical Reference Data*, 41.
- Huber, M. L., Perkins, R. A., Laesecke, A., Friend, D. G., Sengers, J. V., Assael, M. J., Metaxa, I. N., Vogel, E., Mareš, R., and Miyagawa, K. (2009). New international formulation for the viscosity of H₂O. *Journal of Physical and Chemical Reference Data*, 38.
- Huber, R. and Helmig, R. (2000). Node-centered finite volume discretizations for the numerical simulation of multiphase flow in heterogeneous porous media. *Computational Geosciences*, 4:141–164.

- Hug, T. S., Parrat, D., Kunzi, P.-A., Staufer, U., Verpoorte, E., and de Rooij, N. F. (2003). Fabrication of nanochannels with PDMS, silicon and glass walls and spontaneous filling by capillary forces. *7th International Conference on Miniaturized Chemical and Biochemical Analysts Systems, California, USA*.
- Huh, D., Mills, K. L., Zhu, X., Burns, M. A., Thouless, M. A., and Takayama, S. (2007). Tuneable elastomeric nanochannels for nanofluidic manipulation. *Nature Materials*, 6:424–428.
- IAPWS (1994). Iapws release on surface tension of ordinary water substance. Technical report, International Association for the Properties of Water and Steam (IAPWS).
- Joback, K. (1984). A unified approach to physical property estimation using multivariate statistical techniques. Master’s thesis, Massachusetts Institute of Technology.
- Joekar-Niasar, V. (2010). *The immiscibles: Capillarity effects in porous media - pore-network modelling*. PhD thesis, University of Utrecht.
- Joekar-Niasar, V., Dijke, M., and Hassanizadeh, S. (2012). Pore-scale modeling of multiphase flow and transport: Achievements and perspectives. *Transport in Porous Media*, 94(2):461–464.
- Joekar-Niasar, V. and Hassanizadeh, S. M. (2011). Specific interfacial area: The missing state variable in two-phase flow equations? *Water Resources Research*, 47(5).
- Joekar-Niasar, V., Hassanizadeh, S. M., and Dahle, H. K. (2010). Non-equilibrium effects in capillarity and interfacial area in two-phase flow: dynamic pore-network modelling. *Journal of Fluid Mechanics*, 655:38–71.
- Joekar-Niasar, V., Hassanizadeh, S. M., and Leijnse, A. (2008). Insights into the relationship among capillary pressure, saturation, interfacial area and relative permeability using pore-network modeling. *Transport in Porous Media*, 74:201–219.

Bibliography

- Juanes, R., Spiteri, E., Orr, F., and Blunt, M. (2006). Impact of relative permeability hysteresis on geological CO₂ storage. *Water Resources Research*, 42.
- Karadimitriou, N. (2013). *Two-phase flow experimental studies in micro-models*. PhD thesis, University of Utrecht.
- Karadimitriou, N. K. and Hassanizadeh, S. M. (2012). A review of micromodels and their use in two-phase flow studies. *Vadose Zone Journal*, 11(3).
- Karadimitriou, N. K., Joekear-Niasar, V., Hassanizadeh, S. M., Kleingeld, P. J., and Pyrak-Nolte, L. J. (2012). A novel deep reactive ion etched (DRIE) glass micro-model for two-phase flow experiments. *Lab Chip*, 12:3413–3418.
- Karadimitriou, N. K., Musterd, M., Kleingeld, P., Kreutzer, M., Hassanizadeh, S., and Joekear-Niasar, V. (2013). On the fabrication of PDMS micromodels by rapid prototyping, and their use in two-phase flow studies. *Water Resources Research*, 49:2056–2067.
- Karadimitriou, N. K., Nuske, P., Kleingeld, P. J., Hassanizadeh, S. M., and Helmig, R. (2014). Simultaneous thermal and optical imaging of two-phase flow in a micro-model. *Lab Chip*, 14:2515–2524.
- Kaviany, M. (2002). *Principles of heat transfer in porous media*. Wiley, New York.
- Kumar Gunda, N. S., Bera, B., Karadimitriou, N. K., Mitra, S. K., and Hassanizadeh, S. M. (2011). Reservoir-on-a-chip (ROC): A new paradigm in reservoir engineering. *Lab Chip*, 11:3785–3792.
- Land, C. (1968). Calculation of imbibition relative permeabilities for two- and three-phase flow from rock properties. *Society of Petroleum Engineers Journal*, 243:149–156.
- Lauser, A., Hager, C., Helmig, R., and Wohlmuth, B. (2011). A new approach for phase transitions in miscible multi-phase flow in porous media. *Advances in Water Resources*, 34(8):957–966.
- Li, H., Leong, K., Jin, L., and Chai, J. (2010a). Three-dimensional numerical simulation of fluid flow with phase change heat transfer in an asymmetrically

- heated porous channel. *International Journal of Thermal Sciences*, 49(12):2363–2375.
- Li, H., Leong, K., Jin, L., and Chai, J. (2010b). Transient behavior of fluid flow and heat transfer with phase change in vertical porous channels. *International Journal of Heat and Mass Transfer*, 53(23–24):5209–5222.
- Li, H., Leong, K., Jin, L., and Chai, J. (2010c). Transient two-phase flow and heat transfer with localized heating in porous media. *International Journal of Thermal Sciences*, 49(7):1115–1127.
- Li, M., Wu, Y., Tian, Y., and Zhai, Y. (2007). Non-thermal equilibrium model of the coupled heat and mass transfer in strong endothermic chemical reaction system of porous media. *International Journal of Heat and Mass Transfer*, 50(15–16):2936–2943.
- Li, X. S. (2005). An overview of SuperLU: Algorithms, implementation, and user interface. *ACM Transactions on Mathematical Software*, 31(3):302–325.
- Lie, K. A., Krogstad, S., Ligaarden, I. S., Natvig, J. R., Nilsen, H. M., and Skaflestad, B. (2012). Open-source MATLAB implementation of consistent discretisations on complex grids. *Computational Geosciences*, 16:297–322.
- Lindner, F., Nuske, P., Helmig, R., Mundt, C., and Pfitzner, M. (2014a). Transpiration cooling with local thermal non-equilibrium: Model comparison in multiphase flow in porous media. *Journal of Porous Media*. submitted.
- Lindner, F., Pfitzner, M., and Mundt, C. (2014b). Fluid flow with phase change in vertical porous channels with local thermal non-equilibrium in a two-phase mixture model. In *Proceedings of the 5th International Conference on Porous Media and its Applications in Science and Engineering*.
- Manthey, S., Hassanizadeh, M. S., and Helmig, R. (2005). Macro-scale dynamic effects in homogeneous and heterogeneous porous media. *Transport in Porous Media*, 58(1-2):121–145.
- Mark, J. (1999). *Polymer Data Handbook*. Oxford University Press, Incorporated.

Bibliography

- MATLAB (2013). Matlab and image processing toolbox release 2013a. *The MathWorks, Inc., Natick, Massachusetts, United States*.
- McAdams, W. (1954). *Heat Transmission*. McGraw-Hill.
- Millington, R. and Quirk, J. (1960). Permeability of porous solids. *Transactions of the Faraday Society*, 57:1200–1207.
- Mosthaf, K., Baber, K., Flemisch, B., Helmig, R., Leijnse, A., Rybak, I., and Wohlmuth, B. (2011). A coupling concept for two-phase compositional porous-medium and single-phase compositional free flow. *Water Resources Research*, 47.
- Mualem, Y. (1976). A new model for predicting the hydraulic conductivity of unsaturated porous media. *Water Resources Research*, 12(3):513–522.
- Nam, J. H. and Kaviany, M. (2003). Effective diffusivity and water-saturation distribution in single- and two-layer {PEMFC} diffusion medium. *International Journal of Heat and Mass Transfer*, 46(24):4595–4611.
- Nield, D. A. and Bejan, A. (2006). *Convection in porous media*. Springer, New York, N.Y., 3. edition.
- Niessner, J. and Hassanizadeh, S. M. (2008). A model for two-phase flow in porous media including fluid–fluid interfacial area. *Water Resources Research*, 44.
- Nuske, P., Joekar-Niasar, V., and Helmig, R. (2014a). Non-equilibrium in multi-phase multicomponent flow in porous media: An evaporation example. *International Journal of Heat and Mass Transfer*, 74(0):128–142.
- Nuske, P., Ronneberger, O., Karadimitriou, N. K., Helmig, R., and Hassanizadeh, M. (2014b). Modelling multiphase flow in a micro-model with local thermal non-equilibrium on the darcy scale. *Water Resources Research*. submitted.
- Oliveira, A. and Kaviany, M. (2001). Nonequilibrium in the transport of heat and reactants in combustion in porous media. *Progress in Energy and Combustion Science*, 27(5):523–545.

- Parker, J. C., Lenhard, R. J., and Kuppusamy, T. (1987). A parametric model for constitutive properties governing multiphase flow in porous media. *Water Resources Research*, 23:618–624.
- Patankar, S. (1980). *Numerical heat transfer and fluid flow*. Series in computational methods in mechanics and thermal sciences. Taylor & Francis.
- Poling, B. E., Prausnitz, J. M., and O’Connell, J. P. (2001). *The Properties of Gases and Liquids (Fifth Edition)*. McGraw-Hill.
- Pop, I., van Duijn, C., Niessner, J., and Hassanizadeh, S. (2009). Horizontal redistribution of fluids in a porous medium: The role of interfacial area in modeling hysteresis. *Advances in Water Resources*, 32(3):383–390.
- Rashid, M., Kulenovic, R., and Laurien, E. (2012). Experimental results on the coolability of a debris bed with down comer configurations. *Nuclear Engineering and Design*, 249(0):104 – 110. The 8th International Topical Meeting on Nuclear Thermal-Hydraulics, Operation and Safety (NUTHOS-8).
- Rees, D., Bassom, A., and Siddheswar, P. (2008). Local thermal non-equilibrium effects arising from the injection of a hot fluid into a porous medium. *Journal of Fluid Mechanics*, 594:379–398.
- Reeves, P. C. and Celia, M. A. (1996). A functional relationship between capillary pressure, saturation, and interfacial area as revealed by a pore-scale network model. *Water Resources Research*, 32(8):2345–2358.
- Reid, R. C., Prausnitz, J. M., and Poling, B. E. (1987). *The Properties of Gases and Liquids (Fourth Edition)*. McGraw-Hill.
- Rohsenow, W. (1952). A method of correlating heat transfer data for surface boiling of liquids. *Trans. ASME*, 74:969–976.
- Rushton, A., Ward, A. S., and Holdich, R. G. (2000). *Solid-Liquid Filtration and Separation Technology*. Wiley-VCH.
- Schäfer, P., Groll, M., and Kulenovic, R. (2006). Basic investigations on debris cooling. *Nuclear Engineering and Design*, 236(19–21):2104 – 2116. Festschrift

Bibliography

- Edition Celebrating the 70th Birthday of Prof. Bal Raj Sehgal: Invited papers on - Core melt accidents in LWRs State of the art of coolability of porous media.
- Schäfer, P. and Lohnert, G. (2006). Boiling experiments for the validation of dryout models used in reactor safety. *Nuclear Engineering and Design*, 236(14-16):1511–1519.
- Schumann, T. (1929). Heat transfer: A liquid flowing through a porous prism. *Journal of the Franklin Institute*, 208(3):405–416.
- Shahraeeni, E. and Or, D. (2011). Quantification of subsurface thermal regimes beneath evaporating porous surfaces. *International Journal of Heat and Mass Transfer*, 54(19-20):4193–4202.
- Shi, J. and Wang, J. (2011). A numerical investigation of transpiration cooling with liquid coolant phase change. *Transport in Porous Media*, 87:703–716.
- Stingaciu, L. R., Weihermüller, L., Haber-Pohlmeier, S., Stapf, S., Vereecken, H., and Pohlmeier, A. (2010). Determination of pore size distribution and hydraulic properties using nuclear magnetic resonance relaxometry: A comparative study of laboratory methods. *Water Resources Research*, 46.
- Støverud, K., Darcis, M., Helmig, R., and Hassanizadeh, S. (2012). Modeling concentration distribution and deformation during convection-enhanced drug delivery into brain tissue. *Transport in Porous Media*, 92:119–143.
- Tolman, E., Kuan, P., and Broughton, J. (1988). Tmi-2 accident scenario update. *Nuclear Engineering and Design*, 108(1–2):45 – 54.
- Truong, H. and Zinsmeister, G. (1978). Experimental study of heat transfer in layered composites. *International Journal of Heat and Mass Transfer*, 21(7):905–909.
- Udell, K. S. (1985). Heat transfer in porous media considering phase change and capillarity — the heat pipe effect. *International Journal of Heat and Mass Transfer*, 28(2):485–495.

- van der Vorst, H. (1992). Bi-CGSTAB: A fast and smoothly converging variant of Bi-CG for the solution of nonsymmetric linear systems. *SIAM Journal on Scientific and Statistical Computing*, 13(2):631–644.
- van Genuchten, M. (1980). A closed-form equation for predicting the hydraulic conductivity of unsaturated soils. *Soil Sciences Society of America Journal*, 44(5):892–898.
- Visintin, A. (1994). *Differential models of hysteresis*. Springer.
- Voller, V. R. and Swaminathan, C. R. (1993). Treatment of discontinuous thermal conductivity in control-volume solutions of phase-change problems. *Numerical Heat Transfer, Part B: Fundamentals*, 24(2):161–180.
- Wagner, W., Cooper, J. R., Dittmann, A., Kijima, J., Kretzschmar, H. J., Kruse, A., Mareš, R., Oguchi, K., Sato, H., Stöcker, I., Šifner, O., Takaiishi, Y., Tanishita, I., Trübenbach, J., and Willkommen, T. (2000). The IAPWS Industrial Formulation 1997 for the Thermodynamic Properties of Water and Steam. *Journal of Engineering for Gas Turbines and Power*, 122(1):150–184.
- Wakao, N. and Kagei, S. (1982). *Heat and mass transfer in packed beds*. Topics in chemical engineering. Gordon and Breach Science Publishers.
- Wakao, N., Kaguei, S., and Funazkri, T. (1979). Effect of fluid dispersion coefficients on particle-to-fluid heat transfer coefficients in packed beds: correlation of nusselt numbers. *Chemical Engineering Science*, 34:325–336.
- Wang, C. (1996). Multi-dimensional modeling of steam injection into porous media. In *Proc. 2nd Euro. Therm. Sci., 14th UIT Natl. Heat Transfer Conf.*, Rome, Italy.
- Wang, C. (1997). A fixed-grid numerical algorithm for two-phase flow and heat transfer in porous media. *Numerical Heat Transfer, Part B: Fundamentals*, 32(1):85–105.
- Wang, C. and Beckermann, C. (1993). A two-phase mixture model of liquid-gas flow and heat transfer in capillary porous media - I. Formulation. *International Journal of Heat and Mass Transfer*, 36(11):2747–2758.

Bibliography

- Wang, C., Beckermann, C., and Fan, C. (1994). Numerical study of boiling and natural convection in capillary porous media using the two-phase mixture model. *Numerical Heat Transfer*, 26:375–398.
- Wang, C. and Cheng, P. (1996). A multiphase mixture model for multiphase, multicomponent transport in capillary porous media. Part I: Model development. *International Journal of Heat and Mass Transfer*, 39(17):3607–3618.
- Wang, C. and Cheng, P. (1997). Multiphase flow and heat transfer in porous media. In *Advances in Heat Transfer*, volume 30.
- Wang, J. and Shi, J. (2008). A discussion of boundary conditions of transpiration cooling problems using analytical solution of LTNE model. *ASME Journal of Heat Transfer*, 130(1).
- Wang, J. and Wang, H. (2006). A discussion of transpiration cooling problems through an analytical solution of local thermal nonequilibrium model. *Journal of Heat Transfer*, 128:1093–1098.
- Ward, J. (1965). *Turbulent Flow in Porous Media*. Journal of the Hydraulics Division. University of Arkansas, Engineering Experiment Station.
- Wessolek, G., Stoffregen, H., and Täumer, K. (2009). Persistency of flow patterns in a water repellent sandy soil – conclusions of {TDR} readings and a time-delayed double tracer experiment. *Journal of Hydrology*, 375(3–4):524 – 535.
- Whitaker, S. (1999). *The Method of Volume Averaging*. Theory and Applications of Transport in Porous Media. Springer.
- Wildenschild, D., Vaz, C., Rivers, M., Rikard, D., and Christensen, B. (2002). Using X-ray computed tomography in hydrology: systems, resolutions, and limitations. *Journal of Hydrology*, 267(3–4):285–297.
- Wu, Y.-S. (2002). Numerical simulation of single-phase and multiphase non-darcy flow in porous and fractured reservoirs. *Transport in Porous Media*, 49(2):209–240.
- Xue, G. (2008). *Numerical methods for multiphysics, multiphase, and multicomponent models for fuel cells*. PhD thesis, The Pennsylvania State University.

- Younglove, B. (1982). Thermophysical properties of fluids. I. argon, ethylene, parahydrogen, nitrogen, nitrogen trifluoride, and oxygen. *Journal of Physical and Chemical Reference Data*, 11:1–11.
- Yuki, K., Abei, J., Hashizume, H., and Toda, S. (2008). Numerical investigation of thermofluid flow characteristics with phase change against high heat flux in porous media. *Journal of heat transfer*, 13(1):012602.
- Zhang, C., Oostrom, M., Wietsma, T. W., Grate, J. G., and Warner, M. (2011). Influence of viscous and capillary forces on immiscible fluid displacement: Pore-scale experimental study in a water-wet micromodel demonstrating viscous and capillary fingering. *Energy and Fuels*, 25(8):3493–3505.
- Zhang, Q., Karadimitriou, N. K., Hassanizadeh, S. M., Klingeld, P. J., and Imhof, A. (2013). Study of colloids transport during two-phase flow using a novel polydimethylsiloxane micro-model. *Journal of Colloid and Interface Science*, 401(0):141–147.

Lebenslauf

Persönliche Daten

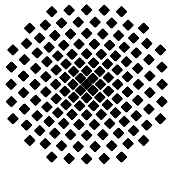
Name: Klaus Philipp Nuske
Geburtsdatum: 24.02.1983
Geburtsort: Berlin
Staatsangehörigkeit: deutsch

Ausbildung

1996 - 2002 Max-Planck-Gymnasium Göttingen
10/2003 - 05/2009 Studium der Umweltschutztechnik, Universität Stuttgart
Diplomarbeit: "Determination of Interfacial Area – Capillary Pressure – Saturation Relationships for a Single Fracture: Study, Upscaling, and Determination", AQUA-Studienpreis
09/2006 - 05/2007 Auslandsstudium, Department of Earth Sciences, University of Waterloo, Kanada
01/2013 - 03/2013 Forschungsaufenthalt, Department of Earth Sciences, Faculty of Geosciences, Utrecht University, Niederlande

Berufstätigkeit

seit 07/2009 Wissenschaftlicher Mitarbeiter am Institut für Wasser- und Umweltsystemmodellierung der Universität Stuttgart, Lehrstuhl für Hydromechanik und Hydrosystemmodellierung



Institut für Wasser- und Umweltsystemmodellierung Universität Stuttgart

Pfaffenwaldring 61
70569 Stuttgart (Vaihingen)
Telefon (0711) 685 - 64717/64749/64752/64679
Telefax (0711) 685 - 67020 o. 64746 o. 64681
E-Mail: iws@iws.uni-stuttgart.de
<http://www.iws.uni-stuttgart.de>

Direktoren

Prof. Dr. rer. nat. Dr.-Ing. András Bárdossy
Prof. Dr.-Ing. Rainer Helmig
Prof. Dr.-Ing. Silke Wieprecht

Vorstand (Stand 19.08.2013)

Prof. Dr. rer. nat. Dr.-Ing. A. Bárdossy
Prof. Dr.-Ing. R. Helmig
Prof. Dr.-Ing. S. Wieprecht
Prof. Dr. J.A. Sander Huisman
Jürgen Braun, PhD
apl. Prof. Dr.-Ing. H. Class
Dr.-Ing. H.-P. Koschitzky
Dr.-Ing. M. Noack
Jun.-Prof. Dr.-Ing. W. Nowak, M.Sc.
Dr. rer. nat. J. Seidel
Dr.-Ing. K. Terheiden

Emeriti

Prof. Dr.-Ing. habil. Dr.-Ing. E.h. Jürgen Giesecke
Prof. Dr.h.c. Dr.-Ing. E.h. Helmut Kobus, PhD

Lehrstuhl für Wasserbau und Wassermengenwirtschaft

Leiter: Prof. Dr.-Ing. Silke Wieprecht
Stellv.: Dr.-Ing. Kristina Terheiden
Versuchsanstalt für Wasserbau
Leiter: Dr.-Ing. Markus Noack

Lehrstuhl für Hydromechanik und Hydrosystemmodellierung

Leiter: Prof. Dr.-Ing. Rainer Helmig
Stellv.: apl. Prof. Dr.-Ing. Holger Class
**Jungwissenschaftlergruppe: Stochastische
Modellierung von Hydrosystemen**
Leiter: Jun.-Prof. Dr.-Ing. Wolfgang Nowak, M.Sc.

Lehrstuhl für Hydrologie und Geohydrologie

Leiter: Prof. Dr. rer. nat. Dr.-Ing. András Bárdossy
Stellv.: Dr. rer. nat. Jochen Seidel
Hydrogeophysik der Vadosen Zone
(mit Forschungszentrum Jülich)
Leiter: Prof. Dr. J.A. Sander Huisman

VEGAS, Versuchseinrichtung zur Grundwasser- und Altlastensanierung

Leitung: Jürgen Braun, PhD, AD
Dr.-Ing. Hans-Peter Koschitzky, AD

Verzeichnis der Mitteilungshefte

- 1 Röhnisch, Arthur: *Die Bemühungen um eine Wasserbauliche Versuchsanstalt an der Technischen Hochschule Stuttgart*, und Fattah Abouleid, Abdel: *Beitrag zur Berechnung einer in lockeren Sand gerammten, zweifach verankerten Spundwand*, 1963
- 2 Marotz, Günter: *Beitrag zur Frage der Standfestigkeit von dichten Asphaltbelägen im Großwasserbau*, 1964
- 3 Gurr, Siegfried: *Beitrag zur Berechnung zusammengesetzter ebener Flächen-tragwerke unter besonderer Berücksichtigung ebener Stauwände, mit Hilfe von Randwert- und Lastwertmatrizen*, 1965
- 4 Plica, Peter: *Ein Beitrag zur Anwendung von Schalenkonstruktionen im Stahlwasserbau*, und Petrikat, Kurt: *Möglichkeiten und Grenzen des wasserbaulichen Versuchswesens*, 1966

- 5 Plate, Erich: *Beitrag zur Bestimmung der Windgeschwindigkeitsverteilung in der durch eine Wand gestörten bodennahen Luftschicht, und*
Röhnisch, Arthur; Marotz, Günter: *Neue Baustoffe und Bauausführungen für den Schutz der Böschungen und der Sohle von Kanälen, Flüssen und Häfen; Gesteigungskosten und jeweilige Vorteile, sowie Unny, T.E.: Schwingungsuntersuchungen am Kegelstrahlschieber, 1967*
- 6 Seiler, Erich: *Die Ermittlung des Anlagenwertes der bundeseigenen Binnenschiffahrtsstraßen und Talsperren und des Anteils der Binnenschiffahrt an diesem Wert, 1967*
- 7 *Sonderheft anlässlich des 65. Geburtstages von Prof. Arthur Röhnisch mit Beiträgen von* Benk, Dieter; Breitling, J.; Gurr, Siegfried; Haberhauer, Robert; Honekamp, Hermann; Kuz, Klaus Dieter; Marotz, Günter; Mayer-Vorfelder, Hans-Jörg; Miller, Rudolf; Plate, Erich J.; Radomski, Helge; Schwarz, Helmut; Vollmer, Ernst; Wildenhahn, Eberhard; 1967
- 8 Jumikis, Alfred: *Beitrag zur experimentellen Untersuchung des Wassernachschubs in einem gefrierenden Boden und die Beurteilung der Ergebnisse, 1968*
- 9 Marotz, Günter: *Technische Grundlagen einer Wasserspeicherung im natürlichen Untergrund, 1968*
- 10 Radomski, Helge: *Untersuchungen über den Einfluß der Querschnittsform wellenförmiger Spundwände auf die statischen und rammtechnischen Eigenschaften, 1968*
- 11 Schwarz, Helmut: *Die Grenztragfähigkeit des Baugrundes bei Einwirkung vertikal gezogener Ankerplatten als zweidimensionales Bruchproblem, 1969*
- 12 Erbel, Klaus: *Ein Beitrag zur Untersuchung der Metamorphose von Mittelgebirgsschneedecken unter besonderer Berücksichtigung eines Verfahrens zur Bestimmung der thermischen Schneequalität, 1969*
- 13 Westhaus, Karl-Heinz: *Der Strukturwandel in der Binnenschiffahrt und sein Einfluß auf den Ausbau der Binnenschiffskanäle, 1969*
- 14 Mayer-Vorfelder, Hans-Jörg: *Ein Beitrag zur Berechnung des Erdwiderstandes unter Ansatz der logarithmischen Spirale als Gleitflächenfunktion, 1970*
- 15 Schulz, Manfred: *Berechnung des räumlichen Erddruckes auf die Wandung kreiszylindrischer Körper, 1970*
- 16 Mobasseri, Manoutschehr: *Die Rippenstützmauer. Konstruktion und Grenzen ihrer Standsicherheit, 1970*
- 17 Benk, Dieter: *Ein Beitrag zum Betrieb und zur Bemessung von Hochwasserrückhaltebecken, 1970*

- 18 Gàl, Attila: *Bestimmung der mitschwingenden Wassermasse bei überströmten Fischbauchklappen mit kreiszylindrischem Staublech*, 1971, vergriffen
- 19 Kuz, Klaus Dieter: *Ein Beitrag zur Frage des Einsetzens von Kavitationserscheinungen in einer Düsenströmung bei Berücksichtigung der im Wasser gelösten Gase*, 1971, vergriffen
- 20 Schaak, Hartmut: *Verteilleitungen von Wasserkraftanlagen*, 1971
- 21 *Sonderheft zur Eröffnung der neuen Versuchsanstalt des Instituts für Wasserbau der Universität Stuttgart mit Beiträgen von* Brombach, Hansjörg; Dirksen, Wolfram; Gàl, Attila; Gerlach, Reinhard; Giesecke, Jürgen; Holthoff, Franz-Josef; Kuz, Klaus Dieter; Marotz, Günter; Minor, Hans-Erwin; Petrikat, Kurt; Röhnisch, Arthur; Rueff, Helge; Schwarz, Helmut; Vollmer, Ernst; Wildenhahn, Eberhard; 1972
- 22 Wang, Chung-su: *Ein Beitrag zur Berechnung der Schwingungen an Kegelstrahlschiebern*, 1972
- 23 Mayer-Vorfelder, Hans-Jörg: *Erdwiderstandsbeiwerte nach dem Ohde-Variationsverfahren*, 1972
- 24 Minor, Hans-Erwin: *Beitrag zur Bestimmung der Schwingungsanfachungsfunktionen überströmter Stauklappen*, 1972, vergriffen
- 25 Brombach, Hansjörg: *Untersuchung strömungsmechanischer Elemente (Fluidik) und die Möglichkeit der Anwendung von Wirbelkammerelementen im Wasserbau*, 1972, vergriffen
- 26 Wildenhahn, Eberhard: *Beitrag zur Berechnung von Horizontalfilterbrunnen*, 1972
- 27 Steinlein, Helmut: *Die Eliminierung der Schwebstoffe aus Flußwasser zum Zweck der unterirdischen Wasserspeicherung, gezeigt am Beispiel der Iller*, 1972
- 28 Holthoff, Franz Josef: *Die Überwindung großer Hubhöhen in der Binnenschifffahrt durch Schwimmerhebwerke*, 1973
- 29 Röder, Karl: *Einwirkungen aus Baugrundbewegungen auf trog- und kastenförmige Konstruktionen des Wasser- und Tunnelbaues*, 1973
- 30 Kretschmer, Heinz: *Die Bemessung von Bogenstaumauern in Abhängigkeit von der Talform*, 1973
- 31 Honekamp, Hermann: *Beitrag zur Berechnung der Montage von Unterwasserpipelines*, 1973
- 32 Giesecke, Jürgen: *Die Wirbelkammertriode als neuartiges Steuerorgan im Wasserbau*, und Brombach, Hansjörg: *Entwicklung, Bauformen, Wirkungsweise und Steuereigenschaften von Wirbelkammerverstärkern*, 1974

- 33 Rueff, Helge: *Untersuchung der schwingungserregenden Kräfte an zwei hintereinander angeordneten Tiefschützen unter besonderer Berücksichtigung von Kavitation*, 1974
- 34 Röhnisch, Arthur: *Einpreßversuche mit Zementmörtel für Spannbeton - Vergleich der Ergebnisse von Modellversuchen mit Ausführungen in Hüllwellrohren*, 1975
- 35 *Sonderheft anlässlich des 65. Geburtstages von Prof. Dr.-Ing. Kurt Petrikat mit Beiträgen von:* Brombach, Hansjörg; Erbel, Klaus; Flinspach, Dieter; Fischer jr., Richard; Gàl, Attila; Gerlach, Reinhard; Giesecke, Jürgen; Haberhauer, Robert; Hafner Edzard; Hausenblas, Bernhard; Horlacher, Hans-Burkhard; Hutarew, Andreas; Knoll, Manfred; Krummet, Ralph; Marotz, Günter; Merkle, Theodor; Miller, Christoph; Minor, Hans-Erwin; Neumayer, Hans; Rao, Syamala; Rath, Paul; Rueff, Helge; Ruppert, Jürgen; Schwarz, Wolfgang; Topal-Gökceli, Mehmet; Vollmer, Ernst; Wang, Chung-su; Weber, Hans-Georg; 1975
- 36 Berger, Jochum: *Beitrag zur Berechnung des Spannungszustandes in rotations-symmetrisch belasteten Kugelschalen veränderlicher Wandstärke unter Gas- und Flüssigkeitsdruck durch Integration schwach singulärer Differentialgleichungen*, 1975
- 37 Dirksen, Wolfram: *Berechnung instationärer Abflußvorgänge in gestauten Gerinnen mittels Differenzenverfahren und die Anwendung auf Hochwasserrückhaltebecken*, 1976
- 38 Horlacher, Hans-Burkhard: *Berechnung instationärer Temperatur- und Wärmespannungsfelder in langen mehrschichtigen Hohlzylindern*, 1976
- 39 Hafner, Edzard: *Untersuchung der hydrodynamischen Kräfte auf Baukörper im Tiefwasserbereich des Meeres*, 1977, ISBN 3-921694-39-6
- 40 Ruppert, Jürgen: *Über den Axialwirbelkammverstärker für den Einsatz im Wasserbau*, 1977, ISBN 3-921694-40-X
- 41 Hutarew, Andreas: *Beitrag zur Beeinflußbarkeit des Sauerstoffgehalts in Fließgewässern an Abstürzen und Wehren*, 1977, ISBN 3-921694-41-8, vergriffen
- 42 Miller, Christoph: *Ein Beitrag zur Bestimmung der schwingungserregenden Kräfte an unterströmten Wehren*, 1977, ISBN 3-921694-42-6
- 43 Schwarz, Wolfgang: *Druckstoßberechnung unter Berücksichtigung der Radial- und Längsverschiebungen der Rohrwandung*, 1978, ISBN 3-921694-43-4
- 44 Kinzelbach, Wolfgang: *Numerische Untersuchungen über den optimalen Einsatz variabler Kühlsysteme einer Kraftwerkskette am Beispiel Oberrhein*, 1978, ISBN 3-921694-44-2
- 45 Barczewski, Baldur: *Neue Meßmethoden für Wasser-Luftgemische und deren Anwendung auf zweiphasige Auftriebsstrahlen*, 1979, ISBN 3-921694-45-0

- 46 Neumayer, Hans: *Untersuchung der Strömungsvorgänge in radialen Wirbelkammerverstärkern*, 1979, ISBN 3-921694-46-9
- 47 Elalfy, Youssef-Elhassan: *Untersuchung der Strömungsvorgänge in Wirbelkammerdiolen und -drosseln*, 1979, ISBN 3-921694-47-7
- 48 Brombach, Hansjörg: *Automatisierung der Bewirtschaftung von Wasserspeichern*, 1981, ISBN 3-921694-48-5
- 49 Geldner, Peter: *Deterministische und stochastische Methoden zur Bestimmung der Selbstdichtung von Gewässern*, 1981, ISBN 3-921694-49-3, vergriffen
- 50 Mehlhorn, Hans: *Temperaturveränderungen im Grundwasser durch Brauchwasseranleitungen*, 1982, ISBN 3-921694-50-7, vergriffen
- 51 Hafner, Edzard: *Rohrleitungen und Behälter im Meer*, 1983, ISBN 3-921694-51-5
- 52 Rinnert, Bernd: *Hydrodynamische Dispersion in porösen Medien: Einfluß von Dichteunterschieden auf die Vertikalvermischung in horizontaler Strömung*, 1983, ISBN 3-921694-52-3, vergriffen
- 53 Lindner, Wulf: *Steuerung von Grundwasserentnahmen unter Einhaltung ökologischer Kriterien*, 1983, ISBN 3-921694-53-1, vergriffen
- 54 Herr, Michael; Herzer, Jörg; Kinzelbach, Wolfgang; Kobus, Helmut; Rinnert, Bernd: *Methoden zur rechnerischen Erfassung und hydraulischen Sanierung von Grundwasserkontaminationen*, 1983, ISBN 3-921694-54-X
- 55 Schmitt, Paul: *Wege zur Automatisierung der Niederschlagsermittlung*, 1984, ISBN 3-921694-55-8, vergriffen
- 56 Müller, Peter: *Transport und selektive Sedimentation von Schwebstoffen bei gestautem Abfluß*, 1985, ISBN 3-921694-56-6
- 57 El-Qawasmeh, Fuad: *Möglichkeiten und Grenzen der Tropfbewässerung unter besonderer Berücksichtigung der Verstopfungsanfälligkeit der Tropfelemente*, 1985, ISBN 3-921694-57-4, vergriffen
- 58 Kirchenbaur, Klaus: *Mikroprozessorgesteuerte Erfassung instationärer Druckfelder am Beispiel seegangbelasteter Baukörper*, 1985, ISBN 3-921694-58-2
- 59 Kobus, Helmut (Hrsg.): *Modellierung des großräumigen Wärme- und Schadstofftransports im Grundwasser*, Tätigkeitsbericht 1984/85 (DFG-Forschergruppe an den Universitäten Hohenheim, Karlsruhe und Stuttgart), 1985, ISBN 3-921694-59-0, vergriffen
- 60 Spitz, Karlheinz: *Dispersion in porösen Medien: Einfluß von Inhomogenitäten und Dichteunterschieden*, 1985, ISBN 3-921694-60-4, vergriffen
- 61 Kobus, Helmut: *An Introduction to Air-Water Flows in Hydraulics*, 1985, ISBN 3-921694-61-2

- 62 Kaleris, Vassilios: *Erfassung des Austausches von Oberflächen- und Grundwasser in horizontalebene Grundwassermodellen*, 1986, ISBN 3-921694-62-0
- 63 Herr, Michael: *Grundlagen der hydraulischen Sanierung verunreinigter Porengrundwasserleiter*, 1987, ISBN 3-921694-63-9
- 64 Marx, Walter: *Berechnung von Temperatur und Spannung in Massenbeton infolge Hydratation*, 1987, ISBN 3-921694-64-7
- 65 Koschitzky, Hans-Peter: *Dimensionierungskonzept für Sohlbelüfter in Schußrinnen zur Vermeidung von Kavitationsschäden*, 1987, ISBN 3-921694-65-5
- 66 Kobus, Helmut (Hrsg.): *Modellierung des großräumigen Wärme- und Schadstofftransports im Grundwasser*, Tätigkeitsbericht 1986/87 (DFG-Forscherguppe an den Universitäten Hohenheim, Karlsruhe und Stuttgart) 1987, ISBN 3-921694-66-3
- 67 Söll, Thomas: *Berechnungsverfahren zur Abschätzung anthropogener Temperaturanomalien im Grundwasser*, 1988, ISBN 3-921694-67-1
- 68 Dittrich, Andreas; Westrich, Bernd: *Bodenseeufererosion, Bestandsaufnahme und Bewertung*, 1988, ISBN 3-921694-68-X, vergriffen
- 69 Huwe, Bernd; van der Ploeg, Rienk R.: *Modelle zur Simulation des Stickstoffhaushaltes von Standorten mit unterschiedlicher landwirtschaftlicher Nutzung*, 1988, ISBN 3-921694-69-8, vergriffen
- 70 Stephan, Karl: *Integration elliptischer Funktionen*, 1988, ISBN 3-921694-70-1
- 71 Kobus, Helmut; Zilliox, Lothaire (Hrsg.): *Nitratbelastung des Grundwassers, Auswirkungen der Landwirtschaft auf die Grundwasser- und Rohwasserbeschaffenheit und Maßnahmen zum Schutz des Grundwassers*. Vorträge des deutsch-französischen Kolloquiums am 6. Oktober 1988, Universitäten Stuttgart und Louis Pasteur Strasbourg (Vorträge in deutsch oder französisch, Kurzfassungen zweisprachig), 1988, ISBN 3-921694-71-X
- 72 Soyeaux, Renald: *Unterströmung von Stauanlagen auf klüftigem Untergrund unter Berücksichtigung laminarer und turbulenter Fließzustände*, 1991, ISBN 3-921694-72-8
- 73 Kohane, Roberto: *Berechnungsmethoden für Hochwasserabfluß in Fließgewässern mit überströmten Vorländern*, 1991, ISBN 3-921694-73-6
- 74 Hassinger, Reinhard: *Beitrag zur Hydraulik und Bemessung von Blocksteinrampen in flexibler Bauweise*, 1991, ISBN 3-921694-74-4, vergriffen
- 75 Schäfer, Gerhard: *Einfluß von Schichtenstrukturen und lokalen Einlagerungen auf die Längsdispersion in Porengrundwasserleitern*, 1991, ISBN 3-921694-75-2
- 76 Giesecke, Jürgen: *Vorträge, Wasserwirtschaft in stark besiedelten Regionen; Umweltforschung mit Schwerpunkt Wasserwirtschaft*, 1991, ISBN 3-921694-76-0

- 77 Huwe, Bernd: *Deterministische und stochastische Ansätze zur Modellierung des Stickstoffhaushalts landwirtschaftlich genutzter Flächen auf unterschiedlichem Skalenniveau*, 1992, ISBN 3-921694-77-9, vergriffen
- 78 Rommel, Michael: *Verwendung von Kluftdaten zur realitätsnahen Generierung von Kluftnetzen mit anschließender laminar-turbulenter Strömungsberechnung*, 1993, ISBN 3-92 1694-78-7
- 79 Marschall, Paul: *Die Ermittlung lokaler Stofffrachten im Grundwasser mit Hilfe von Einbohrloch-Meßverfahren*, 1993, ISBN 3-921694-79-5, vergriffen
- 80 Ptak, Thomas: *Stofftransport in heterogenen Porenaquiferen: Felduntersuchungen und stochastische Modellierung*, 1993, ISBN 3-921694-80-9, vergriffen
- 81 Haakh, Frieder: *Transientes Strömungsverhalten in Wirbelkammern*, 1993, ISBN 3-921694-81-7
- 82 Kobus, Helmut; Cirpka, Olaf; Barczewski, Baldur; Koschitzky, Hans-Peter: *Versuchseinrichtung zur Grundwasser und Altlastensanierung VEGAS, Konzeption und Programmrahmen*, 1993, ISBN 3-921694-82-5
- 83 Zang, Weidong: *Optimaler Echtzeit-Betrieb eines Speichers mit aktueller Abflußregenerierung*, 1994, ISBN 3-921694-83-3, vergriffen
- 84 Franke, Hans-Jörg: *Stochastische Modellierung eines flächenhaften Stoffeintrages und Transports in Grundwasser am Beispiel der Pflanzenschutzmittelproblematik*, 1995, ISBN 3-921694-84-1
- 85 Lang, Ulrich: *Simulation regionaler Strömungs- und Transportvorgänge in Karst-aquiferen mit Hilfe des Doppelkontinuum-Ansatzes: Methodenentwicklung und Parameteridentifikation*, 1995, ISBN 3-921694-85-X, vergriffen
- 86 Helmig, Rainer: *Einführung in die Numerischen Methoden der Hydromechanik*, 1996, ISBN 3-921694-86-8, vergriffen
- 87 Cirpka, Olaf: *CONTRACT: A Numerical Tool for Contaminant Transport and Chemical Transformations - Theory and Program Documentation -*, 1996, ISBN 3-921694-87-6
- 88 Haberlandt, Uwe: *Stochastische Synthese und Regionalisierung des Niederschlages für Schmutzfrachtberechnungen*, 1996, ISBN 3-921694-88-4
- 89 Croisé, Jean: *Extraktion von flüchtigen Chemikalien aus natürlichen Lockergesteinen mittels erzwungener Luftströmung*, 1996, ISBN 3-921694-89-2, vergriffen
- 90 Jorde, Klaus: *Ökologisch begründete, dynamische Mindestwasserregelungen bei Ausleitungskraftwerken*, 1997, ISBN 3-921694-90-6, vergriffen
- 91 Helmig, Rainer: *Gekoppelte Strömungs- und Transportprozesse im Untergrund - Ein Beitrag zur Hydrosystemmodellierung-*, 1998, ISBN 3-921694-91-4, vergriffen

- 92 Emmert, Martin: *Numerische Modellierung nichtisothermer Gas-Wasser Systeme in porösen Medien*, 1997, ISBN 3-921694-92-2
- 93 Kern, Ulrich: *Transport von Schweb- und Schadstoffen in staugeregelten Fließgewässern am Beispiel des Neckars*, 1997, ISBN 3-921694-93-0, vergriffen
- 94 Förster, Georg: *Druckstoßdämpfung durch große Luftblasen in Hochpunkten von Rohrleitungen* 1997, ISBN 3-921694-94-9
- 95 Cirpka, Olaf: *Numerische Methoden zur Simulation des reaktiven Mehrkomponententransports im Grundwasser*, 1997, ISBN 3-921694-95-7, vergriffen
- 96 Färber, Arne: *Wärmetransport in der ungesättigten Bodenzone: Entwicklung einer thermischen In-situ-Sanierungstechnologie*, 1997, ISBN 3-921694-96-5
- 97 Betz, Christoph: *Wasserdampfdestillation von Schadstoffen im porösen Medium: Entwicklung einer thermischen In-situ-Sanierungstechnologie*, 1998, ISBN 3-921694-97-3
- 98 Xu, Yichun: *Numerical Modeling of Suspended Sediment Transport in Rivers*, 1998, ISBN 3-921694-98-1, vergriffen
- 99 Wüst, Wolfgang: *Geochemische Untersuchungen zur Sanierung CKW-kontaminierter Aquifere mit Fe(0)-Reaktionswänden*, 2000, ISBN 3-933761-02-2
- 100 Sheta, Hussam: *Simulation von Mehrphasenvorgängen in porösen Medien unter Einbeziehung von Hysterese-Effekten*, 2000, ISBN 3-933761-03-4
- 101 Ayros, Edwin: *Regionalisierung extremer Abflüsse auf der Grundlage statistischer Verfahren*, 2000, ISBN 3-933761-04-2, vergriffen
- 102 Huber, Ralf: *Compositional Multiphase Flow and Transport in Heterogeneous Porous Media*, 2000, ISBN 3-933761-05-0
- 103 Braun, Christopherus: *Ein Upscaling-Verfahren für Mehrphasenströmungen in porösen Medien*, 2000, ISBN 3-933761-06-9
- 104 Hofmann, Bernd: *Entwicklung eines rechnergestützten Managementsystems zur Beurteilung von Grundwasserschadensfällen*, 2000, ISBN 3-933761-07-7
- 105 Class, Holger: *Theorie und numerische Modellierung nichtisothermer Mehrphasenprozesse in NAPL-kontaminierten porösen Medien*, 2001, ISBN 3-933761-08-5
- 106 Schmidt, Reinhard: *Wasserdampf- und Heißluftinjektion zur thermischen Sanierung kontaminierter Standorte*, 2001, ISBN 3-933761-09-3
- 107 Josef, Reinhold.: *Schadstoffextraktion mit hydraulischen Sanierungsverfahren unter Anwendung von grenzflächenaktiven Stoffen*, 2001, ISBN 3-933761-10-7

- 108 Schneider, Matthias: *Habitat- und Abflussmodellierung für Fließgewässer mit unscharfen Berechnungsansätzen*, 2001, ISBN 3-933761-11-5
- 109 Rathgeb, Andreas: *Hydrodynamische Bemessungsgrundlagen für Lockerdeckwerke an überströmbaren Erddämmen*, 2001, ISBN 3-933761-12-3
- 110 Lang, Stefan: *Parallele numerische Simulation instationärer Probleme mit adaptiven Methoden auf unstrukturierten Gittern*, 2001, ISBN 3-933761-13-1
- 111 Appt, Jochen; Stumpp Simone: *Die Bodensee-Messkampagne 2001, IWS/CWR Lake Constance Measurement Program 2001*, 2002, ISBN 3-933761-14-X
- 112 Heimerl, Stephan: *Systematische Beurteilung von Wasserkraftprojekten*, 2002, ISBN 3-933761-15-8, vergriffen
- 113 Iqbal, Amin: *On the Management and Salinity Control of Drip Irrigation*, 2002, ISBN 3-933761-16-6
- 114 Silberhorn-Hemming, Annette: *Modellierung von Kluftaquifersystemen: Geostatistische Analyse und deterministisch-stochastische Kluftgenerierung*, 2002, ISBN 3-933761-17-4
- 115 Winkler, Angela: *Prozesse des Wärme- und Stofftransports bei der In-situ-Sanierung mit festen Wärmequellen*, 2003, ISBN 3-933761-18-2
- 116 Marx, Walter: *Wasserkraft, Bewässerung, Umwelt - Planungs- und Bewertungsschwerpunkte der Wasserbewirtschaftung*, 2003, ISBN 3-933761-19-0
- 117 Hinkelmann, Reinhard: *Efficient Numerical Methods and Information-Processing Techniques in Environment Water*, 2003, ISBN 3-933761-20-4
- 118 Samaniego-Eguiguren, Luis Eduardo: *Hydrological Consequences of Land Use / Land Cover and Climatic Changes in Mesoscale Catchments*, 2003, ISBN 3-933761-21-2
- 119 Neunhäuserer, Lina: *Diskretisierungsansätze zur Modellierung von Strömungs- und Transportprozessen in geklüftet-porösen Medien*, 2003, ISBN 3-933761-22-0
- 120 Paul, Maren: *Simulation of Two-Phase Flow in Heterogeneous Poros Media with Adaptive Methods*, 2003, ISBN 3-933761-23-9
- 121 Ehret, Uwe: *Rainfall and Flood Nowcasting in Small Catchments using Weather Radar*, 2003, ISBN 3-933761-24-7
- 122 Haag, Ingo: *Der Sauerstoffhaushalt staugeregelter Flüsse am Beispiel des Neckars - Analysen, Experimente, Simulationen -*, 2003, ISBN 3-933761-25-5
- 123 Appt, Jochen: *Analysis of Basin-Scale Internal Waves in Upper Lake Constance*, 2003, ISBN 3-933761-26-3

- 124 Hrsg.: Schrenk, Volker; Batereau, Katrin; Barczewski, Baldur; Weber, Karolin und Koschitzky, Hans-Peter: *Symposium Ressource Fläche und VEGAS - Statuskolloquium 2003, 30. September und 1. Oktober 2003*, 2003, ISBN 3-933761-27-1
- 125 Omar Khalil Ouda: *Optimisation of Agricultural Water Use: A Decision Support System for the Gaza Strip*, 2003, ISBN 3-933761-28-0
- 126 Batereau, Katrin: *Sensorbasierte Bodenluftmessung zur Vor-Ort-Erkundung von Schadensherden im Untergrund*, 2004, ISBN 3-933761-29-8
- 127 Witt, Oliver: *Erosionsstabilität von Gewässersedimenten mit Auswirkung auf den Stofftransport bei Hochwasser am Beispiel ausgewählter Stauhaltungen des Oberrheins*, 2004, ISBN 3-933761-30-1
- 128 Jakobs, Hartmut: *Simulation nicht-isothermer Gas-Wasser-Prozesse in komplexen Kluft-Matrix-Systemen*, 2004, ISBN 3-933761-31-X
- 129 Li, Chen-Chien: *Deterministisch-stochastisches Berechnungskonzept zur Beurteilung der Auswirkungen erosiver Hochwasserereignisse in Flusstauhaltungen*, 2004, ISBN 3-933761-32-8
- 130 Reichenberger, Volker; Helmig, Rainer; Jakobs, Hartmut; Bastian, Peter; Niessner, Jennifer: *Complex Gas-Water Processes in Discrete Fracture-Matrix Systems: Upscaling, Mass-Conservative Discretization and Efficient Multilevel Solution*, 2004, ISBN 3-933761-33-6
- 131 Hrsg.: Barczewski, Baldur; Koschitzky, Hans-Peter; Weber, Karolin; Wege, Ralf: *VEGAS - Statuskolloquium 2004*, Tagungsband zur Veranstaltung am 05. Oktober 2004 an der Universität Stuttgart, Campus Stuttgart-Vaihingen, 2004, ISBN 3-933761-34-4
- 132 Asie, Kemal Jabir: *Finite Volume Models for Multiphase Multicomponent Flow through Porous Media*. 2005, ISBN 3-933761-35-2
- 133 Jacoub, George: *Development of a 2-D Numerical Module for Particulate Contaminant Transport in Flood Retention Reservoirs and Impounded Rivers*, 2004, ISBN 3-933761-36-0
- 134 Nowak, Wolfgang: *Geostatistical Methods for the Identification of Flow and Transport Parameters in the Subsurface*, 2005, ISBN 3-933761-37-9
- 135 Süß, Mia: *Analysis of the influence of structures and boundaries on flow and transport processes in fractured porous media*, 2005, ISBN 3-933761-38-7
- 136 Jose, Surabhin Chackiath: *Experimental Investigations on Longitudinal Dispersive Mixing in Heterogeneous Aquifers*, 2005, ISBN: 3-933761-39-5
- 137 Filiz, Fulya: *Linking Large-Scale Meteorological Conditions to Floods in Mesoscale Catchments*, 2005, ISBN 3-933761-40-9

- 138 Qin, Minghao: *Wirklichkeitsnahe und recheneffiziente Ermittlung von Temperatur und Spannungen bei großen RCC-Staumauern*, 2005, ISBN 3-933761-41-7
- 139 Kobayashi, Kenichiro: *Optimization Methods for Multiphase Systems in the Sub-surface - Application to Methane Migration in Coal Mining Areas*, 2005, ISBN 3-933761-42-5
- 140 Rahman, Md. Arifur: *Experimental Investigations on Transverse Dispersive Mixing in Heterogeneous Porous Media*, 2005, ISBN 3-933761-43-3
- 141 Schrenk, Volker: *Ökobilanzen zur Bewertung von Altlastensanierungsmaßnahmen*, 2005, ISBN 3-933761-44-1
- 142 Hundecha, Hirpa Yeshewatersfa: *Regionalization of Parameters of a Conceptual Rainfall-Runoff Model*, 2005, ISBN: 3-933761-45-X
- 143 Wege, Ralf: *Untersuchungs- und Überwachungsmethoden für die Beurteilung natürlicher Selbstreinigungsprozesse im Grundwasser*, 2005, ISBN 3-933761-46-8
- 144 Breiting, Thomas: *Techniken und Methoden der Hydroinformatik - Modellierung von komplexen Hydrosystemen im Untergrund*, 2006, 3-933761-47-6
- 145 Hrsg.: Braun, Jürgen; Koschitzky, Hans-Peter; Müller, Martin: *Ressource Untergrund: 10 Jahre VEGAS: Forschung und Technologieentwicklung zum Schutz von Grundwasser und Boden*, Tagungsband zur Veranstaltung am 28. und 29. September 2005 an der Universität Stuttgart, Campus Stuttgart-Vaihingen, 2005, ISBN 3-933761-48-4
- 146 Rojanschi, Vlad: *Abflusskonzentration in mesoskaligen Einzugsgebieten unter Berücksichtigung des Sickerraumes*, 2006, ISBN 3-933761-49-2
- 147 Winkler, Nina Simone: *Optimierung der Steuerung von Hochwasserrückhaltebecken-systemen*, 2006, ISBN 3-933761-50-6
- 148 Wolf, Jens: *Räumlich differenzierte Modellierung der Grundwasserströmung alluvialer Aquifere für mesoskalige Einzugsgebiete*, 2006, ISBN: 3-933761-51-4
- 149 Kohler, Beate: *Externe Effekte der Laufwasserkraftnutzung*, 2006, ISBN 3-933761-52-2
- 150 Hrsg.: Braun, Jürgen; Koschitzky, Hans-Peter; Stuhmann, Matthias: *VEGAS-Statuskolloquium 2006*, Tagungsband zur Veranstaltung am 28. September 2006 an der Universität Stuttgart, Campus Stuttgart-Vaihingen, 2006, ISBN 3-933761-53-0
- 151 Niessner, Jennifer: *Multi-Scale Modeling of Multi-Phase - Multi-Component Processes in Heterogeneous Porous Media*, 2006, ISBN 3-933761-54-9
- 152 Fischer, Markus: *Beanspruchung eingeeerdeter Rohrleitungen infolge Austrocknung bindiger Böden*, 2006, ISBN 3-933761-55-7

- 153 Schneck, Alexander: *Optimierung der Grundwasserbewirtschaftung unter Berücksichtigung der Belange der Wasserversorgung, der Landwirtschaft und des Naturschutzes*, 2006, ISBN 3-933761-56-5
- 154 Das, Tapash: *The Impact of Spatial Variability of Precipitation on the Predictive Uncertainty of Hydrological Models*, 2006, ISBN 3-933761-57-3
- 155 Bielinski, Andreas: *Numerical Simulation of CO₂ sequestration in geological formations*, 2007, ISBN 3-933761-58-1
- 156 Mödinger, Jens: *Entwicklung eines Bewertungs- und Entscheidungsunterstützungssystems für eine nachhaltige regionale Grundwasserbewirtschaftung*, 2006, ISBN 3-933761-60-3
- 157 Manthey, Sabine: *Two-phase flow processes with dynamic effects in porous media - parameter estimation and simulation*, 2007, ISBN 3-933761-61-1
- 158 Pozos Estrada, Oscar: *Investigation on the Effects of Entrained Air in Pipelines*, 2007, ISBN 3-933761-62-X
- 159 Ochs, Steffen Oliver: *Steam injection into saturated porous media – process analysis including experimental and numerical investigations*, 2007, ISBN 3-933761-63-8
- 160 Marx, Andreas: *Einsatz gekoppelter Modelle und Wetterradar zur Abschätzung von Niederschlagsintensitäten und zur Abflussvorhersage*, 2007, ISBN 3-933761-64-6
- 161 Hartmann, Gabriele Maria: *Investigation of Evapotranspiration Concepts in Hydrological Modelling for Climate Change Impact Assessment*, 2007, ISBN 3-933761-65-4
- 162 Kebede Gurmessa, Tesfaye: *Numerical Investigation on Flow and Transport Characteristics to Improve Long-Term Simulation of Reservoir Sedimentation*, 2007, ISBN 3-933761-66-2
- 163 Trifković, Aleksandar: *Multi-objective and Risk-based Modelling Methodology for Planning, Design and Operation of Water Supply Systems*, 2007, ISBN 3-933761-67-0
- 164 Götzing, Jens: *Distributed Conceptual Hydrological Modelling - Simulation of Climate, Land Use Change Impact and Uncertainty Analysis*, 2007, ISBN 3-933761-68-9
- 165 Hrsg.: Braun, Jürgen; Koschitzky, Hans-Peter; Stuhmann, Matthias: *VEGAS – Kolloquium 2007*, Tagungsband zur Veranstaltung am 26. September 2007 an der Universität Stuttgart, Campus Stuttgart-Vaihingen, 2007, ISBN 3-933761-69-7
- 166 Freeman, Beau: *Modernization Criteria Assessment for Water Resources Planning; Klamath Irrigation Project, U.S.*, 2008, ISBN 3-933761-70-0

- 167 Dreher, Thomas: *Selektive Sedimentation von Feinstschwebstoffen in Wechselwirkung mit wandnahen turbulenten Strömungsbedingungen*, 2008, ISBN 3-933761-71-9
- 168 Yang, Wei: *Discrete-Continuous Downscaling Model for Generating Daily Precipitation Time Series*, 2008, ISBN 3-933761-72-7
- 169 Kopecki, Ianina: *Calculational Approach to FST-Hemispheres for Multiparametrical Benthos Habitat Modelling*, 2008, ISBN 3-933761-73-5
- 170 Brommundt, Jürgen: *Stochastische Generierung räumlich zusammenhängender Niederschlagszeitreihen*, 2008, ISBN 3-933761-74-3
- 171 Papafotiou, Alexandros: *Numerical Investigations of the Role of Hysteresis in Heterogeneous Two-Phase Flow Systems*, 2008, ISBN 3-933761-75-1
- 172 He, Yi: *Application of a Non-Parametric Classification Scheme to Catchment Hydrology*, 2008, ISBN 978-3-933761-76-7
- 173 Wagner, Sven: *Water Balance in a Poorly Gauged Basin in West Africa Using Atmospheric Modelling and Remote Sensing Information*, 2008, ISBN 978-3-933761-77-4
- 174 Hrsg.: Braun, Jürgen; Koschitzky, Hans-Peter; Stuhmann, Matthias; Schrenk, Volker: *VEGAS-Kolloquium 2008 Ressource Fläche III*, Tagungsband zur Veranstaltung am 01. Oktober 2008 an der Universität Stuttgart, Campus Stuttgart-Vaihingen, 2008, ISBN 978-3-933761-78-1
- 175 Patil, Sachin: *Regionalization of an Event Based Nash Cascade Model for Flood Predictions in Ungauged Basins*, 2008, ISBN 978-3-933761-79-8
- 176 Assteerawatt, Anongnart: *Flow and Transport Modelling of Fractured Aquifers based on a Geostatistical Approach*, 2008, ISBN 978-3-933761-80-4
- 177 Karnahl, Joachim Alexander: *2D numerische Modellierung von multifraktionalem Schwebstoff- und Schadstofftransport in Flüssen*, 2008, ISBN 978-3-933761-81-1
- 178 Hiester, Uwe: *Technologieentwicklung zur In-situ-Sanierung der ungesättigten Bodenzone mit festen Wärmequellen*, 2009, ISBN 978-3-933761-82-8
- 179 Laux, Patrick: *Statistical Modeling of Precipitation for Agricultural Planning in the Volta Basin of West Africa*, 2009, ISBN 978-3-933761-83-5
- 180 Ehsan, Saqib: *Evaluation of Life Safety Risks Related to Severe Flooding*, 2009, ISBN 978-3-933761-84-2
- 181 Prohaska, Sandra: *Development and Application of a 1D Multi-Strip Fine Sediment Transport Model for Regulated Rivers*, 2009, ISBN 978-3-933761-85-9

- 182 Kopp, Andreas: *Evaluation of CO₂ Injection Processes in Geological Formations for Site Screening*, 2009, ISBN 978-3-933761-86-6
- 183 Ebigbo, Anozie: *Modelling of biofilm growth and its influence on CO₂ and water (two-phase) flow in porous media*, 2009, ISBN 978-3-933761-87-3
- 184 Freiboth, Sandra: *A phenomenological model for the numerical simulation of multiphase multicomponent processes considering structural alterations of porous media*, 2009, ISBN 978-3-933761-88-0
- 185 Zöllner, Frank: *Implementierung und Anwendung netzfreier Methoden im Konstruktiven Wasserbau und in der Hydromechanik*, 2009, ISBN 978-3-933761-89-7
- 186 Vasin, Milos: *Influence of the soil structure and property contrast on flow and transport in the unsaturated zone*, 2010, ISBN 978-3-933761-90-3
- 187 Li, Jing: *Application of Copulas as a New Geostatistical Tool*, 2010, ISBN 978-3-933761-91-0
- 188 AghaKouchak, Amir: *Simulation of Remotely Sensed Rainfall Fields Using Copulas*, 2010, ISBN 978-3-933761-92-7
- 189 Thapa, Pawan Kumar: *Physically-based spatially distributed rainfall runoff modeling for soil erosion estimation*, 2010, ISBN 978-3-933761-93-4
- 190 Wurms, Sven: *Numerische Modellierung der Sedimentationsprozesse in Retentionsanlagen zur Steuerung von Stoffströmen bei extremen Hochwasserabflussereignissen*, 2011, ISBN 978-3-933761-94-1
- 191 Merkel, Uwe: *Unsicherheitsanalyse hydraulischer Einwirkungen auf Hochwasserschutzdeiche und Steigerung der Leistungsfähigkeit durch adaptive Strömungsmodellierung*, 2011, ISBN 978-3-933761-95-8
- 192 Fritz, Jochen: *A Decoupled Model for Compositional Non-Isothermal Multiphase Flow in Porous Media and Multiphysics Approaches for Two-Phase Flow*, 2010, ISBN 978-3-933761-96-5
- 193 Weber, Karolin (Hrsg.): *12. Treffen junger WissenschaftlerInnen an Wasserbauinstituten*, 2010, ISBN 978-3-933761-97-2
- 194 Bliedernicht, Jan-Geert: *Probability Forecasts of Daily Areal Precipitation for Small River Basins*, 2011, ISBN 978-3-933761-98-9
- 195 Hrsg.: Koschitzky, Hans-Peter; Braun, Jürgen: *VEGAS-Kolloquium 2010 In-situ-Sanierung - Stand und Entwicklung Nano und ISCO -*, Tagungsband zur Veranstaltung am 07. Oktober 2010 an der Universität Stuttgart, Campus Stuttgart-Vaihingen, 2010, ISBN 978-3-933761-99-6

- 196 Gafurov, Abror: *Water Balance Modeling Using Remote Sensing Information - Focus on Central Asia*, 2010, ISBN 978-3-942036-00-9
- 197 Mackenberg, Sylvia: *Die Quellstärke in der Sickerwasserprognose: Möglichkeiten und Grenzen von Labor- und Freilanduntersuchungen*, 2010, ISBN 978-3-942036-01-6
- 198 Singh, Shailesh Kumar: *Robust Parameter Estimation in Gauged and Ungauged Basins*, 2010, ISBN 978-3-942036-02-3
- 199 Doğan, Mehmet Onur: *Coupling of porous media flow with pipe flow*, 2011, ISBN 978-3-942036-03-0
- 200 Liu, Min: *Study of Topographic Effects on Hydrological Patterns and the Implication on Hydrological Modeling and Data Interpolation*, 2011, ISBN 978-3-942036-04-7
- 201 Geleta, Habtamu Itefa: *Watershed Sediment Yield Modeling for Data Scarce Areas*, 2011, ISBN 978-3-942036-05-4
- 202 Franke, Jörg: *Einfluss der Überwachung auf die Versagenswahrscheinlichkeit von Staustufen*, 2011, ISBN 978-3-942036-06-1
- 203 Bakimchandra, Oinam: *Integrated Fuzzy-GIS approach for assessing regional soil erosion risks*, 2011, ISBN 978-3-942036-07-8
- 204 Alam, Muhammad Mahboob: *Statistical Downscaling of Extremes of Precipitation in Mesoscale Catchments from Different RCMs and Their Effects on Local Hydrology*, 2011, ISBN 978-3-942036-08-5
- 205 Hrsg.: Koschitzky, Hans-Peter; Braun, Jürgen: *VEGAS-Kolloquium 2011 Flache Geothermie - Perspektiven und Risiken*, Tagungsband zur Veranstaltung am 06. Oktober 2011 an der Universität Stuttgart, Campus Stuttgart-Vaihingen, 2011, ISBN 978-3-933761-09-2
- 206 Haslauer, Claus: *Analysis of Real-World Spatial Dependence of Subsurface Hydraulic Properties Using Copulas with a Focus on Solute Transport Behaviour*, 2011, ISBN 978-3-942036-10-8
- 207 Dung, Nguyen Viet: *Multi-objective automatic calibration of hydrodynamic models – development of the concept and an application in the Mekong Delta*, 2011, ISBN 978-3-942036-11-5
- 208 Hung, Nguyen Nghia: *Sediment dynamics in the floodplain of the Mekong Delta, Vietnam*, 2011, ISBN 978-3-942036-12-2
- 209 Kuhlmann, Anna: *Influence of soil structure and root water uptake on flow in the unsaturated zone*, 2012, ISBN 978-3-942036-13-9

- 210 Tuhtan, Jeffrey Andrew: *Including the Second Law Inequality in Aquatic Ecodynamics: A Modeling Approach for Alpine Rivers Impacted by Hydropeaking*, 2012, ISBN 978-3-942036-14-6
- 211 Tolossa, Habtamu: *Sediment Transport Computation Using a Data-Driven Adaptive Neuro-Fuzzy Modelling Approach*, 2012, ISBN 978-3-942036-15-3
- 212 Tatomir, Alexandru-Bodgan: *From Discrete to Continuum Concepts of Flow in Fractured Porous Media*, 2012, ISBN 978-3-942036-16-0
- 213 Erbertseder, Karin: *A Multi-Scale Model for Describing Cancer-Therapeutic Transport in the Human Lung*, 2012, ISBN 978-3-942036-17-7
- 214 Noack, Markus: *Modelling Approach for Interstitial Sediment Dynamics and Reproduction of Gravel Spawning Fish*, 2012, ISBN 978-3-942036-18-4
- 215 De Boer, Cjstmir Volkert: *Transport of Nano Sized Zero Valent Iron Colloids during Injection into the Subsurface*, 2012, ISBN 978-3-942036-19-1
- 216 Pfaff, Thomas: *Processing and Analysis of Weather Radar Data for Use in Hydrology*, 2013, ISBN 978-3-942036-20-7
- 217 Lebreuz, Hans-Henning: *Addressing the Input Uncertainty for Hydrological Modeling by a New Geostatistical Method*, 2013, ISBN 978-3-942036-21-4
- 218 Darcis, Melanie Yvonne: *Coupling Models of Different Complexity for the Simulation of CO₂ Storage in Deep Saline Aquifers*, 2013, ISBN 978-3-942036-22-1
- 219 Beck, Ferdinand: *Generation of Spatially Correlated Synthetic Rainfall Time Series in High Temporal Resolution - A Data Driven Approach*, 2013, ISBN 978-3-942036-23-8
- 220 Guthke, Philipp: *Non-multi-Gaussian spatial structures: Process-driven natural genesis, manifestation, modeling approaches, and influences on dependent processes*, 2013, ISBN 978-3-942036-24-5
- 221 Walter, Lena: *Uncertainty studies and risk assessment for CO₂ storage in geological formations*, 2013, ISBN 978-3-942036-25-2
- 222 Wolff, Markus: *Multi-scale modeling of two-phase flow in porous media including capillary pressure effects*, 2013, ISBN 978-3-942036-26-9
- 223 Mosthaf, Klaus Roland: *Modeling and analysis of coupled porous-medium and free flow with application to evaporation processes*, 2014, ISBN 978-3-942036-27-6
- 224 Leube, Philipp Christoph: *Methods for Physically-Based Model Reduction in Time: Analysis, Comparison of Methods and Application*, 2013, ISBN 978-3-942036-28-3
- 225 Rodríguez Fernández, Jhan Ignacio: *High Order Interactions among environmental variables: Diagnostics and initial steps towards modeling*, 2013, ISBN 978-3-942036-29-0

- 226 Eder, Maria Magdalena: *Climate Sensitivity of a Large Lake*, 2013, ISBN 978-3-942036-30-6
- 227 Greiner, Philipp: *Alkoholinjektion zur In-situ-Sanierung von CKW Schadensherden in Grundwasserleitern: Charakterisierung der relevanten Prozesse auf unterschiedlichen Skalen*, 2014, ISBN 978-3-942036-31-3
- 228 Lauser, Andreas: *Theory and Numerical Applications of Compositional Multi-Phase Flow in Porous Media*, 2014, ISBN 978-3-942036-32-0
- 229 Enzenhöfer, Rainer: *Risk Quantification and Management in Water Production and Supply Systems*, 2014, ISBN 978-3-942036-33-7
- 230 Faigle, Benjamin: *Adaptive modelling of compositional multi-phase flow with capillary pressure*, 2014, ISBN 978-3-942036-34-4
- 231 Oladyshkin, Sergey: *Efficient modeling of environmental systems in the face of complexity and uncertainty*, 2014, ISBN 978-3-942036-35-1
- 232 Sugimoto, Takayuki: *Copula based Stochastic Analysis of Discharge Time Series*, 2014, ISBN 978-3-942036-36-8
- 233 Koch, Jonas: *Simulation, Identification and Characterization of Contaminant Source Architectures in the Subsurface*, 2014, ISBN 978-3-942036-37-5
- 234 Zhang, Jin: *Investigations on Urban River Regulation and Ecological Rehabilitation Measures, Case of Shenzhen in China*, 2014, ISBN 978-3-942036-38-2
- 235 Siebel, Rüdiger: *Experimentelle Untersuchungen zur hydrodynamischen Belastung und Standsicherheit von Deckwerken an überströmbaren Erddämmen*, 2014, ISBN 978-3-942036-39-9
- 236 Baber, Katherina: *Coupling free flow and flow in porous media in biological and technical applications: From a simple to a complex interface description*, 2014, ISBN 978-3-942036-40-5
- 237 Nuske, Klaus Philipp: *Beyond Local Equilibrium — Relaxing local equilibrium assumptions in multiphase flow in porous media*, 2014, ISBN 978-3-942036-41-2

Die Mitteilungshefte ab der Nr. 134 (Jg. 2005) stehen als pdf-Datei über die Homepage des Instituts: www.iws.uni-stuttgart.de zur Verfügung.